ABSTRACT

Title of dissertation: DESIGN, DEVELOPMENT, AND EVALUATION OF A TELEOPERATED MASTER-SLAVE SURGICAL SYSTEM FOR BREAST BIOPSY UNDER CONTINUOUS MRI GUIDANCE

Bo Yang, Doctor of Philosophy, 2013

Dissertation directed by: Professor Jaydev P. Desai
Department of Mechanical Engineering

The goal of this project is to design and develop a teleoperated master-slave surgical system that can potentially assist the physician in performing breast biopsy with a magnetic resonance imaging (MRI) compatible robotic system. MRI provides superior soft-tissue contrast compared to other imaging modalities such as computed tomography or ultrasound and is used for both diagnostic and therapeutic procedures. The strong magnetic field and the limited space inside the MRI bore, however, restrict direct means of breast biopsy while performing real-time imaging. Therefore, current breast biopsy procedures employ a blind targeting approach based on magnetic resonance (MR) images obtained *a priori*. Due to possible patient involuntary motion or inaccurate insertion through the registration grid, such approach could lead to tool tip positioning errors thereby affecting diagnostic accuracy and leading to a long and painful process, if repeated procedures

are required. Hence, it is desired to develop the aforementioned teleoperation system to take advantages of real-time MR imaging and avoid multiple biopsy needle insertions, improving the procedure accuracy as well as reducing the sampling errors.

The design, implementation, and evaluation of the teleoperation system is presented in this dissertation. A MRI-compatible slave robot is implemented, which consists of a 1 degree of freedom (DOF) needle driver, a 3-DOF parallel mechanism, and a 2-DOF X-Y stage. This slave robot is actuated with pneumatic cylinders through long transmission lines except the 1-DOF needle driver is actuated with a piezo motor. Pneumatic actuation through long transmission lines is then investigated using proportional pressure valves and controllers based on sliding mode control are presented. A dedicated master robot is also developed, and the kinematic map between the master and the slave robot is established. The two robots are integrated into a teleoperation system and a graphical user interface is developed to provide visual feedback to the physician. MRI experiment shows that the slave robot is MRI-compatible, and the *ex vivo* test shows over 85% success rate in targeting with the MRI-compatible robotic system. The success in performing *in vivo* animal experiments further confirm the potential of further developing the proposed robotic system for clinical applications.

DESIGN, DEVELOPMENT, AND EVALUATION OF A TELEOPERATED MASTER-SLAVE SURGICAL SYSTEM FOR BREAST BIOPSY UNDER CONTINUOUS MRI GUIDANCE

by

Bo Yang

Dissertation submitted to the Faculty of the Graduate School of the
University of Maryland, College Park in partial fulfillment
of the requirements for the degree of
Doctor of Philosophy
2013

Advisory Committee:
Professor Jaydev P. Desai, Chair / Advisor
Professor Inderjit Chopra, Dean's Representative
Professor Amr Baz
Professor Nikhil Chopra
Professor Rao Gullapalli

Acknowledgments

I would like to express my gratitude to all the people who have supported me through my Ph.D. studies over the past four years. Without their kind assistance this dissertation would not have been possible.

First and foremost, I would like to thank my advisor, Dr. Jaydev P. Desai, for giving me the opportunity to work in the Robotics, Automation, and Medical Systems (RAMS) Laboratory and work on this challenging and exciting project. He has made himself available for help at any time, even during Christmas. His continuous advice and guidance has kept me on track for my research project at all times. It has been an honor and pleasure to work with and learning form Dr. Desai over the past four years.

I would also like to thank Dr. U-Xuan Tan for his assistance and patience in this project. He has helped me preparing and conducting many of the MRI experiments and numerous discussions with him have inspired me a lot in the research work of the project. I have learned a lot from working closely with him.

Dr. Rao Gullapalli and Dr. Alan McMillan have been of great help to me with respect to the knowledge of MRI and the related experiments. These help are essential to build the MRI-compatible slave robot. Mr. Steven Roys and Mr. Mathew Philip have also been helpful in the MRI experiments on the evaluation of the integrated surgical system. We have spent many late nights working together to get the robotic system running properly and collect the experimental data needed. Thanks also goes to George Makris and Albert Kir for operating the MRI scanner many times. I would like to thank Dr. Howard Richard for the advises on developing the surgical system as well as performing the live

animal experiment, and Dr. Steven T. Shipley, Dr. Ivan Tatarov, and Ms. Theresa Alexander for taking care of the subjects of the live animal experiments. Thanks also goes to Joseph Rosenberg for preparing the revised protocol of the live animal experiments for timely approval by Institutional Animal Care and Use Committee (IACUC).

Thanks are also due to Dr. Rao Gullapalli, Dr. Amr Baz, Dr. Inderjit Chopra, and Dr. Nikhil Chopra for agreeing to serve on my dissertation committee and for sparing their invaluable time reviewing this dissertation.

My colleagues at the RAMS Lab have enriched my graduate studies in many ways. Dr. Zhan Gao was instrumental in the first couple of years of my study, mentoring me how to thrive as a Ph.D. student. Yoann Piriou provided help by performing preliminary design and analysis on the parallel mechanism of the slave robot. Peter M. Phelps assisted me in the machining and assembling of the needle driver for the master robot. Yalun Wu helped me start-off the interface implementation of the teleoperation system by writing the basic graphical user interface (GUI) code. Dr. Kevin Lister and Mingyen Ho have always been helpful on mechanical design and machining skills, and my interaction with Elif Ayvali, Rajarshi Roy, Chad Kessens, Professor Jianyu Yang, Dr. Hardik J. Pandya, and Hyuntae Kim has also been very helpful. I am really grateful to have everyone in the RAMS Lab making the lab a fun and exciting place to work during the past years.

I would like to acknowledge the help from Ms. Lee Harper for processing the documents assigning me as a teaching assistant in the fall of 2012, and the help of Professor Jungho Kim, Dr. Xinan Liu, and Dr. James R. Borrelli during this semester of my teaching assistant responsibilities.

I would also like to acknowledge the help and support from some of the staff mem-

bers here at the University of Maryland. Thanks go to Dr. Hugh Bruck for his support as the director of graduate studies and to Mr. Amarildo Damata for keeping me on track as the graduate studies coordinator. Ms. Penny Komsat and Ms. Janet Woolery have helped pushing through my numerous purchase requests so quickly throughout the project, and both Mr. Steve Wicker and Ms. Lita Brown have provided support for payroll, healthcare benefit, and tax return, as well as the travel reimbursement. I would also like to thank Mr. Melvin Fields for his prompt support with my computer issues, Mr. Majid Aroom for helping me to use the machine shop of the mechanical engineering department, and Ms. Felicia Stephenson for helping me to apply the after-hour parking permit. Thanks also goes to Ms. Sharon von Bergener from writing center for proofreading the very first draft of this dissertation in a very short time, and to Ms. Susan Hindle for her valuable advice on my career development after my Ph.D. study. Finally, I would like to thank Mr. Howard Grossenbacher for his assistance in machining many of the components of the surgical system described in this dissertation, as well as discussions on component design. Help and support from other staff members are also greatly appreciated.

I owe my deepest thanks to my parents. They have always stood by me, encouraged and supported me by all means possible throughout my entire life. I know they are always there backing me up, and I am eternally grateful for that. Thanks go to my fiancee Xiaoxiao and thank you for being patient with me at all times. Without you I would not need to work till the last minute for many times but I am also not able to get the work done at the last minute without your help. You have your sweat and effort in this dissertation as well. I would also like to thank all my friends who make my life at Maryland an enjoyable experience.

I would like to acknowledge the financial support from the National Institutes of Health (NIH) for the research presented herein, and the travel support from the National Science Foundation (NSF) that makes my attending the 2011 International Conference on Robotics and Automation possible.

Lastly, I would like to apologize to those I've inadvertently left out. Thank you all for your help!

Table of Contents

List of Tables viii

List of Figures ix

List of Abbreviations xi

1 Introduction 1
- 1.1 Background for Breast Cancer . . . 1
- 1.2 Robot-Assisted Surgery and Percutaneous Intervention . . . 6
- 1.3 Robot-Assisted Surgery under Continuous MRI Guidance . . . 11
- 1.4 Solution for Breast Biopsy under Continuous MRI Guidance . . . 17

2 Design and Development of the MRI-Compatible Slave Robot 22
- 2.1 Challenges to Develop MRI-Compatible Robots . . . 23
- 2.2 Design and Implementation of the MRI-Compatible Prototype Robot . . . 28
  - 2.2.1 Parallel Mechanism of the Prototype Robot . . . 29
  - 2.2.2 Needle Driver of the Robot Prototype . . . 35
- 2.3 MRI-Compatibility Evaluation of the Robot Prototype . . . 38
- 2.4 Design and Implementation of the MRI-Compatible Slave Robot . . . 42
  - 2.4.1 Parallel Mechanism of the Slave Robot . . . 43
  - 2.4.2 Needle Driver of the Slave Robot . . . 46
  - 2.4.3 X-Y Stage of the Slave Robot . . . 48
- 2.5 MRI-Compatibility Evaluation of the Slave Robot . . . 49
- 2.6 Kinematic Analysis of the Slave Robot . . . 54
  - 2.6.1 Inverse Kinematics of the Parallel Mechanism . . . 56
  - 2.6.2 Forward Kinematics of the Parallel Mechanism . . . 65
  - 2.6.3 Kinematics of the Slave Robot . . . 69
- 2.7 Control Scheme of the Slave Robot . . . 71
- 2.8 Summary . . . 72

3 Modeling and Control of Pneumatic Actuation in the Slave Robot 74
- 3.1 Background of Pneumatic Actuation . . . 75
- 3.2 Design and Development of the 1-DOF Prototype Device . . . 80
- 3.3 Modeling of the Pneumatic Actuation System . . . 83
  - 3.3.1 Pneumatic Valve Model . . . 83
  - 3.3.2 Pneumatic Transmission Line Model . . . 84
  - 3.3.3 Cylinder Piston-Load Model . . . 88
  - 3.3.4 Friction Model . . . 90
- 3.4 Design of the Pneumatic Controller . . . 95
  - 3.4.1 SMC-I . . . 97
  - 3.4.2 SMC-II . . . 101
  - 3.4.3 SMC-III . . . 101
- 3.5 Experimental Evaluation of the SMC Controllers . . . 102

3.6 MRI-Compatibility Evaluation of the 1-DOF Prototype Device 105
3.7 Pneumatic Control of the Cylinders of the Slave Robot 108
3.8 Summary 113

4 Design and Development of the Master Robot 114
4.1 Design and Implementation of the Master Robot 116
4.1.1 Needle Driver of the Master Robot 118
4.1.2 Parallel Mechanism of the Master Robot 119
4.2 Kinematic Map of the Master Robot to the Slave Robot 120
4.3 Control of the Master Robot 123
4.4 Summary 125

5 Teleoperation Integration and the Graphic User Interface of the System 126
5.1 Integration of the Master System 127
5.2 Control Strategy for the Teleoperation System 129
5.3 Experimental Evaluation of the Teleoperation System 134
5.4 Development of the GUI 137
5.5 Summary 140

6 Experimental Evaluation of the Master-Slave System 141
6.1 MRI-Compatibility Evaluation under Dynamic MR Imaging 142
6.2 *Ex Vivo* Targeting Test under MR Guidance 150
6.3 *In Vivo* Targeting Test under MR Guidance 162
6.4 Summary 166

7 Conclusions and Future Works 168
7.1 Conclusions 168
7.2 Contributions 170
7.3 Future Works 172

A CAD Drawings of the Slave Robot 173

B CAD Drawings of the Master Robot 196

Bibliography 216

List of Tables

2.1 SNRs of the MR images with the robot prototype 41
2.2 SNRs of the MR images with the slave robot 53

3.1 SNRs of the MR images with the 1-DOF prototype device 108

5.1 Experimental result of the network communication time delay 132

6.1 SNRs of the dynamic MR images 145
6.2 Summary of the evaluation tests 161

List of Figures

1.1 The envisioned system scheme 19

2.1 Photo of the breast biopsy slave robot prototype 30
2.2 Schematic of the parallel mechanism 33
2.3 The 4-DOF breast biopsy slave robot prototype 34
2.4 Photo of the needle driver prototype attached with a force sensor 37
2.5 Experimental setup for the MRI evaluation of the robot prototype 39
2.6 MR images of the phantom with the robot prototype and its actuation . . . 40
2.7 Photo of the actual MRI-compatible slave robot 44
2.8 The new needle driver that can advance the needle without rotation 47
2.9 Experimental setup for the MRI-compatibility evaluation of the slave robot 50
2.10 MR images of phantoms with slave robot and its various actuation 52
2.11 Overview of the control scheme of the slave robot 71

3.1 MRI-compatible 1-DOF prototype device 81
3.2 Step response comparison for the pressure valve 84
3.3 Schematic of the pneumatic transmission line 85
3.4 Step response comparison for the long transmission line 88
3.5 Schematic representation of the piston-load subsystem 89
3.6 Experimental setup for the friction measurement of the 1-DOF device . . 92
3.7 Measured friction force data for the 1-DOF prototype device 94
3.8 Control diagram of the pneumatic system 96
3.9 Experimental evaluation results of the SMC controllers 103
3.10 MR images of phantom to evaluate pneumatic actuation accuracy 107
3.11 Experimental result of a brass cylinder 110
3.12 Experimental result of the x-direction cable cylinder 112

4.1 Photo of the actual master robot 117
4.2 Schematic of the parallel mechanism of the master robot 121

5.1 The control scheme of the master-slave teleoperation system 130
5.2 Experimental result of the teleoperation system for needle orientation . . 135
5.3 Experimental result of the teleoperation system for needle insertion 136
5.4 The graphical user interface of the teleoperation system 138

6.1 The modified needle driver that can mount the EndoScout® MR sensor . 144
6.2 Experimental setup for the MRI-compatibility evaluation in the MRI . . . 145
6.3 Dynamic MR images in a needle insertion task. (continued) 146
6.3 (continued) Dynamic MR images in a needle insertion task. 147
6.4 The SNR curve of the dynamic MR images 148
6.5 Phase images with the slave robot at various distances from the phantom . 149
6.6 Sagittal, coronal, and axial MR images of a pig's thigh 151
6.7 Selected nine MR frames as the needle approaches the target 152
6.8 MR images for the first insertion trial 154

6.9 MR images for the second insertion trial 155
6.10 MR images for the third insertion trial 156
6.11 MR images for the fourth insertion trial 157
6.12 MR images for the fifth insertion trial 158
6.13 MR images for the sixth insertion trial 160
6.14 Insertion force profile measured in the *ex vivo* experiments 161
6.15 *In vivo* experimental setup in the MRI targeting the femoral bone 163
6.16 High-resolution spot images at different phases of targeting 164
6.17 Dynamic images as the needle is advanced towards the target 165
6.18 Insertion force profile measured in the *in vivo* experiments 166

List of Abbreviations

CAD computer-aided design 42
CBE clinical breast examination 1
CPI cycles per inch 80
CT computed tomography 2
DCIS ductal carcinoma in situ 1
DOF degree of freedom 9
DAQ data acquisition 82
DICOM digital imaging and communications in medicine 41
EMI electromagnetic interference 13
EM electromagnetic 42
ERP event-related potential 17
FDA Food and Drug Administration 8
fMRI functional magnetic resonance imaging 17
GUI graphical user interface 21
ID inner diameter 3
IACUC Institutional Animal Care and Use Committee 162
LCIS lobular carcinoma in situ 1
LPR light puncture robot 16
MIS minimally invasive surgery 7
MRI magnetic resonance imaging 2
MR magnetic resonance 3
NMR nuclear magnetic resonance 23
OD outer diameter 35
OpenGL Open Graphics Library 137
P proportional 77
PD proportional derivative 91
PI proportional integral 77
PID proportional integral derivative 78
PAM pneumatic artificial muscle 75
ppm part per million 148
PWM pulse-width modulation 76
RF radio frequency 3

RFA radiofrequency ablation 10
ROI region of interest 3
SMA shape memory alloy 12
SMC sliding mode control 77
SNR signal-to-noise ratio 13
TRUS trans-rectal ultrasound 10
US ultrasound 2

Chapter 1

Introduction

1.1 Background for Breast Cancer

Breast cancer is a class of malignant tumors that begin in the cells of the breast. It can be noninvasive or invasive. The noninvasive breast cancers, also called “in situ”, originate from the ducts (ductal carcinoma in situ (DCIS)) or lobules (lobular carcinoma in situ (LCIS)), within which they are confined before invading other breast tissue. The invasive breast cancers, on the other hand, have broken through the duct or glandular walls from the sites of origin inside the ducts or lobules and spread to the surrounding breast tissue.

In American women, breast cancer is the most frequently diagnosed cancer, excluding cancers of the skin. According to the American Cancer Society, every one in eight of American women will be diagnosed with breast cancer in her lifetime, and that accounts for nearly one in three cancers diagnosed, excluding cancers of the skin [3]. It is also the second leading cause of cancer death among American women, following the lung cancer [4]. Those figures and facts evidently show that breast cancer is severely affecting the quality of life of women. Compared to its high mortality at a later stage, breast cancer, when at its early stage and the tumor is still small, usually does not cause symptoms and is more treatable. Hence, it is desirable to detect and treat the breast cancer at the early stage.

The traditional means for early detection of breast cancer are mammography and

clinical breast examination (CBE). Mammography uses low-energy X-rays to examine the breast while CBE is done by a health professional using palpation. Both means are used mainly as screening tools, and further diagnostic techniques are needed, including ultrasound (US), computed tomography (CT), as well as magnetic resonance imaging (MRI). US is typically used for further evaluation of the positive diagnosis found in mammography or CBE, yet it can only provide images with limited resolution and low quality. CT can provide images in 3D space with high resolution, but it relies on multiple X-ray scans, and the significant amount of ionizing radiation can adversely induce cancer.

On the contrary, MRI can provide high quality images with superior soft-tissue contrast [5] but without employing ionizing radiation. Further, it is able to provide temperature mapping, which can potentially be used to assess the result of thermal treatment. Hence, MRI has been gaining popularity in recent years, especially in clinical tumor diagnosis. A recent study reported in [6] concluded that MRI is able to detect cancer in the contralateral breast that is otherwise missed by mammography and CBE at the time of initial diagnosis of breast cancer (and the negative predictive value of the cancer using MRI is 99%). Another study shows that MRI can improve the ability of diagnosing DCIS, especially DCIS with high nuclear grade [7]. These studies strongly support the application of MRI as a detection tool for breast cancer.

Though MRI, along with other clinical detection and assessment means including CBE and other imaging techniques such as CT and US, may provide strongly suggestive clues of a cancer diagnosis, microscopic analysis of the suspicious breast tissue is necessary for a definitive diagnosis of breast cancer and, if positive, to acquire further information and help determine the appropriate treatment [3]. The suspicious breast tissue

sample for the microscopic analysis is usually obtained via a needle biopsy, yet it requires a reliable and accurate means of guidance so that the tissue sampled is actually biopsied from the suspicious region of interest (ROI). With its superior soft-tissue contrast to identify the tumor boundary while avoiding the harmful ionizing radiation of mammography and CT or the poor image quality of US, MRI has also been more widely used as guidance for the breast biopsy procedures.

To take full advantage of the unparalleled image quality and soft-tissue contrast of MRI, special care has to be taken to comply with the restrictions MRI has posed. MRI is an imaging technique that can acquire the detailed cross-sectional images of human body, just as CT could, but it is based on a harmless strong magnetic field rather than the harmful ionizing radiation that CT requires. The static magnetic field strength is typically $1.5\,\mathrm{T}$ to $3.0\,\mathrm{T}$, and the technology development is pushing this number up to $7.0\,\mathrm{T}$ [8]. While requiring the strong static magnetic field to be homogeneous to acquire high-quality images, MRI also applies changing magnetic gradient field and strong radio frequency (RF) magnetic field for image acquisition [5]. The high magnetic fields of MRI make constrains severe as described below:

- The strong magnetic fields needed for magnetic resonance (MR) imaging can only be created and maintained in a limited spatial volume, with little room for the physician to maneuver inside. To achieve high in-bore magnetic fields essential to acquire high-quality MR images, most commonly used MRI scanners in recent years adopt small closed bore design of cylindrical shape. The inner diameter (ID) of those cylindrical scanner bores is generally $70\,\mathrm{cm}$. Such a small space has to fit in

the patient along with an appropriate imaging coil, which is used to enhance the image quality. Little room will be left for the physician to perform any procedure or treatment while the patient is inside the scanner bore.

- The strong in-bore magnetic fields limit the equipment that can be used inside the scanner bore. The high static and changing magnetic gradient fields preclude the use of ferromagnetic or paramagnetic materials, since they can be attracted by the magnetic fields and become dangerous projectiles, damaging the MRI scanner as well as harming the personnel. Should anything be used inside the MRI bore, it has to be MRI safe, i.e., presenting no additional risk to the patient [9]. In the meanwhile, the equipment used should not interfere with the magnetic fields. To be more specific, neither the operation of the equipment should be affected by the strong magnetic fields nor the homogeneous distribution of the static magnetic field, which determines the quality of the diagnostic information of the MR images, should be significantly affected by the operation of the equipment or the MRI-safe materials used to build it. That is defined as MRI compatible [9]. The strong RF field applied for image acquisition would also discourage the use of bulky non-magnetic metal materials close to the scanner center, as eddy current could be generated inside those bulky metal and distort the magnetic fields.

With the above constraints, breast biopsies are currently performed manually outside of the MRI bore based on MR images obtained *a priori* through a blind targeting approach. It is comprised of the following steps:

(1) Put the patient inside the MRI scanner and obtain MR images of the breast to iden-

tify the suspicious breast tissue;

(2) Slide the patient out of the MRI scanner bore;

(3) Insert the MRI-compatible coaxial breast biopsy needle with the plastic guiding cannula to a predetermined depth into the breast towards the suspicious tissue site. The insertion is performed using a blind targeting approach and is based on the MRI images acquired *a priori*;

(4) Remove the trocar needle but leave the guiding cannula in place and insert the plastic blunt obturator (also known as stylet). The blunt obturator acts as a MRI marker and can enhance the visibility of the guiding cannula in the MR images;

(5) Slide the patient back into the MRI scanner bore and take MR images to verify if the tip of the guiding cannula is at the desired location;

(6) Slide the patient out of the MRI scanner bore;

(7) If the tip position of the guiding cannula is not satisfactory, remove the guiding cannula and the blunt obturator. Then repeat steps (3)–(6);

(8) If the tip position of the guiding cannula is right at the desired tissue site, remove the blunt obturator only and insert the biopsy gun through the guiding cannula;

(9) Perform breast biopsy operation with the biopsy gun and acquire breast core sample of the suspicious breast tissue for later microscopic analysis;

(10) Remove the breast biopsy gun only and plant small MRI visible markers through the guiding cannula for future reference;

(11) Remove the guiding cannula from the patient.

The trial-and-error approach described above is a compromise of the aforementioned restrictions posed by the MRI scanner. It moves the patient to the MRI scanner bore so that procedures with intra-operative MRI guidance is possible. However, this approach can lead to positioning error of the tool tip due to the patient being slided into and out of the scanner multiple times during the repeated biopsy attempts. This could result in a long and painful process and could cause undue trauma to the patient. To take the challenge, Sutherland et al. proposed to move the magnet of the MRI towards the patient, and a mobile $1.5\,\mathrm{T}$ MRI system was developed [10]. With such system, 46 neurosurgical patients were treated successfully with traditional neurosurgical, nursing, and anesthetic techniques. Effective as it has demonstrated, this system puts additional time to the procedures, and is vulnerable to patient involuntary motion. The ultimate solution is to develop a diagnostic capability whereby the biopsy can be guided and performed accurately while the patient is inside the MRI bore under continuous MRI guidance. This calls for a robotic surgical system that could perform the desired operation inside the MRI bore by the teleoperation of the physician.

1.2 Robot-Assisted Surgery and Percutaneous Intervention

The concept of robot-assisted surgery dated back into 1980s with the initial motivation of taking advantage of the reliability and precision of the robotic device to carry out surgical procedures requiring accurate execution. The first robot-assisted surgery with human subject was performed on April 11, 1985 to obtain a tissue sample from a suspicious brain

lesion [11]. The procedure carried out successfully and a positive biopsy was confirmed on the first sample. In this very procedure, a Unimation PUMA 200 robot was used to work under the CT guidance and place the probe guide, through which the probe was inserted to a certain depth for tissue biopsy. In 1992, the ROBODOC from Integrated Surgical System was introduced and successfully performed the cementless hip replacement surgery by precisely milling out a cavity in the femur, which is very challenging to achieve manually [12]. Such success also benefited from the careful planning based on images acquired via CT scans. The combination of robotic techniques and medical imaging guidance led to the means of performing many surgical procedures in a faster, more accurate, reliable, and flexible way, and the initial success greatly motivated the development of robot-assisted surgery under image guidance.

Along with the fast development of robot-assisted surgery was the advent of minimally invasive surgery (MIS) in surgical techniques. The idea of MIS was to carried out medical surgeries in such ways that would minimize the trauma resulted form the large incisions of conventional open surgery. This would generally be achieved by entering the body through the skin or through the body cavity or anatomical openings and with minimal damage to those structures. It could minimize the trauma to the patient, so that the patient would suffer less pain from the procedure and would recover in a much shorter time [13] with less morbidity than open surgery [14]. For patients who could not withstand conventional open surgery, MIS could also provide a viable means of treatment. Martínez-Monge et al. reported that a patient with lung cancer could not undergo regular treatment of surgical resection benefited from the treatment of brachytherapy with radiation therapy [15]. Attractive and promising as it showed, however, MIS greatly increased

the technology complexities for the surgeon, making procedures traditionally done in open procedures challenging or even unapproachable, since many of the surgical sites are difficult to access due to the presence of bones, nerves, or blood vessels [14].

With the development and application of robot-assisted surgery, more and more MIS procedures were made possible and less challenging to perform. Degani et al. developed a highly articulated robotic probe (HARP) for cardiac surgery [16]. It used cable actuation and could enter the pericardial cavity through a subxiphoid port without disturbing the surrounding tissues and organs. Preliminary *in vivo* animal trials showed the validation of the idea and the effectiveness of the device. Tadano and Kawashima developed a master slave system for laparoscopic surgery using pneumatic actuation [17]. Force sensing scheme was adopted in this surgical system for safer and more precise operations, and experiments had been conducted to verify the implemented haptic interface.

While most of those robots and devices were developed under ongoing research projects and some of them had even gone through clinical trials, none of them had been approved in clinical settings by regulatory agencies and were not available in the market, with only a couple of exceptions: the ZEUS™ robotic surgical system and the *da Vinci*® surgical system.

The ZEUS™ robotic surgical system was developed by Computer Motion, Inc. and consisted of three robotic arms mounted on the operating table, with two arms acting as the extension of the surgeon's two hands. It had been cleared by the Food and Drug Administration (FDA) in 1994 to assist the surgeon in MIS and was used in clinical surgeries. Marescaux et al. applied the system in a transatlantic robot-assisted telesurgery, and the laparoscopic cholecystectomy were carried out in a 68-year-old female success-

fully [18]. The use of the ZEUS™ system was also reported in research field by Trejos et al. in [19], where the proposed approach of percutaneous brachytherapy for lung cancer treatment was experimentally validated. In 2003, the ZEUS™ system discontinued due to the merge of Computer Motion, Inc. and Intuitive Surgical®, which was the manufacturer of the *da Vinci*® surgical system.

The *da Vinci*® surgical system was made up of mainly two subsystems: the surgeon's console and the patient side system, and would create an immersive operating environment for the surgeon [13]. It could scale down the motion of the surgeon into micro-motion while reducing the tremors at the surgeon's hands. As the ZEUS™ system, the *da Vinci*® surgical system had been approved for clinical application, and one of its application was reported by Pisch et al. [20]. In this feasibility study, the surgical system was used to place and suture radioactive seeds on the resection margin after the tumor had been surgically removed. The procedure was performed easily and precisely without any complications. The latest model of the *da Vinci*® surgical systems features six manipulator arms with a total of 41 degrees of freedom (DOFs), along with a stereo endoscope and 3D video display. To date, the *da Vinci*® surgical system has over $2,000$ installations worldwide and is the only robotic surgical system sold [14] on the market. It has been widely used in various surgical procedures, including cardiothoracic procedure, gynecologic surgery, urologic surgery, head and neck procedure, and general surgery.

Among various procedures in MIS, the percutaneous intervention attracted most attention from the researchers of the robot-assisted surgical systems for its relative simple procedures. It would perform local treatment on internal organs by introducing an appropriate needle instrument through skin [21], and those treatment could include tis-

sue biopsy, brachytherapy (place radiative seeds in close proximity to the tumor), and radiofrequency ablation (RFA) (apply heat generated from the high frequency alternating current to ablate the tumor). Numerous robotic surgical systems targeting on percutaneous interventions have been reported.

Stoianovici et al. developed the PAKY needle driver that could provide efficient needle injection based on friction transmission and was one of the most advanced solutions at the time [22]. A simple and cost-effective robotic system based on this needle driver was optimized for percutaneous access of the kidney along with radiological image guidance [23]. This could improve both the safety and accuracy of the procedure. With the same PAKY needle driver, AcuBot was developed for percutaneous interventions under CT or fluoroscopy guidance [24]. It had six DOFs with decoupled motion, and had gone through cadaver study. Being able to be teleoperated to hold, orient, and advance a needle under CT fluoroscopic guidance, AcuBot was used by Soloman et al. to avoid radiation exposure to the physician [25]. Twenty-three procedures including core needle biopsy and RFA had been performed in clinical trials without complications. Treatment planning software was then developed to register and select the target, ensuring the accurate placement of the needle instrument [26]. It was used to develop overlapping treatment plans for RFA, and results from clinical trials confirmed its effectiveness. Wei et al. presented a robotic system for dynamic intra-operative prostate brachytherapy using 3D trans-rectal ultrasound (TRUS) imaging guidance [27]. A commercial robot was used in this system, and the software tools developed with dynamic re-planning and verification enabled sub-millimeter targeting accuracy in a phantom study.

Besides execution accuracy, robot-assisted surgery could also extend the surgeon's

capability by facilitating access to hard-to-reach locations or providing additional diagnostic and/or manipulation information, without elongating the procedure time. Maurin et al. proposed a robotic system that would be teleoperated with haptic feedback under CT guidance, and a prototype had been implemented for validation test [21]. Phee et al. implemented a robotic system prototype that was for prostate needle biopsy under TRUS guidance [28]. As a first prototype, only one axis was motorized, and the clinical trials were performed by manipulating the robot as a passive device. Salcudean et al. designed and built a four DOFs robot that could be mounted on a standard brachytherapy stepper and translate a needle guide for precise needle insertion into tumors located in the prostate [29]. The robot was guided with TRUS, and the radiation oncologist could accomplish a 26 needles with 136 seeds implant in only 32 minutes with the help of such robotic system. More image-guided robotic surgical systems were reviewed in [30], including the aforementioned AcuBot.

1.3 Robot-Assisted Surgery under Continuous MRI Guidance

It is advantageous to use robots in surgical procedures, but the robotic devices have to be designed and implemented carefully according to their targeting applications, due to the natural complexity of each surgical procedure. That is especially true when developing robotic devices under MRI environment since additional strict space constraint should be taken into consideration. At the same time, developing such a teleoperated robotic surgical system could be beneficial as it would extend the capability of the physician to reach the hard-to-access space inside the MRI bore. Extra care also has to be taken when devel-

oping MRI-compatible robot to address the additional challenging restrictions posed by the MRI machine. Other than material consideration of their magnetic susceptibility, special MRI-compatible actuation techniques have to be employed. Due to those challenges, despite the fact that the first robotic prototype system for MRI guided stereotactic neurosurgery was implemented by Masamune et al. as early as 1995 [31], only recently have the MRI-compatible robotic technology and applications gone through a rapid evolution [32].

The basis for developing MRI-compatible robotic systems is the MRI-compatible actuation technique. Extensive work has been done to evaluate and compare various conventional actuation techniques and new actuation method, and new actuators have also been developed. After reviewing a number of MRI-compatible robotic systems and manipulators, Elhawary et al. summarized four main groups of MRI-compatible actuation techniques, i.e., piezo based ultrasonic motor actuation, hydraulic actuation, pneumatic actuation, and remote manual actuation [33]. Other MRI-compatible actuation techniques, such as shape memory alloy (SMA) actuation [34], are also under active exploration. The ultrasonic motor is a kind of electrical motor that is actuated by ultrasonic vibration of its actuating elements, which are commonly made of piezo/piezoelectric materials. One of its characteristics is the use of resonance phenomenon to amplify the vibration generated by the actuating elements. In comparison, motors of similar structure built with piezo/piezoelectric materials and under similar actuating technique could also generate motion with acoustic vibration. These motors are generally referred as piezo motors. Since most if not all of the ultrasonic motors used in the development of MRI-compatible robots use piezo/piezoelectric materials as their actuator elements, ultrasonic motor, piezo motor, and ultrasonic piezo motor can be used to refer to the same kind of

motor, and the term ultrasonic motor is used mainly to emphasize its reliance on ultrasonic vibration and resonance.

To validate the fitness of those actuation techniques for the purpose of application under MRI, numerous prototypes and robotic devices have been developed, and piezo motor is the most frequently tested due to its ease of control. Elhawary et al. used a non-magnetic linear piezoceramic motor to build a 1-DOF test rig for MRI application, and artifact in proximity area of the motor was observed with modest signal-to-noise ratio (SNR) loss of 14% [35] in the MR images. Fischer et al. evaluated one pneumatic cylinder actuator and two ultrasonic motors from different vendors and found that the pneumatic cylinder could be fully MRI compatible while the ultrasonic motors could lead to moderate or significant loss of SNR [36]. Goldenberg et al. reported the application of ultrasonic motors in the proposed robotic system for prostate intervention [37]. Significant SNR reduction was observed and was attributed to electromagnetic interference (EMI). Krieger et al. also reported the application of piezo-ceramic motors, and significant SNR loss were observed while the motors were being actuated [38]. A simple way of avoiding the side effects of using piezo motor was to place the motors at a distant away from the MRI scanning center [39]. This helped to minimize the substantial image artifacts due to the conducting motor casing if placed close to the scanning center. To acquire noise-free MR images with ultrasonic motors, Suzuki et al. developed a driving method that only actuated the ultrasonic motor during the "dead time", during which the MRI scanner stopped signal acquisition to wait for relaxation of protons [40]. Su et al. believed the SNR loss resulted by piezoelectric motor was due to the MRI frequency interference problem and mitigated the noise issue by customizing the motor driver board

to generate special waveform [41]. The comparison between pneumatic and hydraulic actuations conducted by Yu et al. showed that both techniques were MRI compatible with different actuation performance [42]. Generally, pneumatic actuation is more favorable for MRI-compatible application over hydraulic actuation, but with lower position accuracy and less smooth movement. To improve position accuracy of pneumatic actuation, a novel pneumatic step motor with complicated design was developed by Stoianovici et al. and could easily achieve $0.5\,\mathrm{mm}$ position accuracy [43]. Another pneumatic stepping actuator with simpler structure and fewer parts was designed by Sajima et al. and used in a 2-DOF non-metal manipulator, with a maximum positioning error of $0.8\,\mathrm{mm}$ [44].

With different choices of MRI-compatible actuation techniques and targeting at different surgical applications, various proof-of-concept prototypes and multi-DOF surgical robotic systems and manipulators have been designed and developed. Besides Masamune et al., Chinzei et al. were among the pioneers who introduced robotic surgical system under MRI environment. They had reported in 2000 the implementation of a MRI-compatible surgical assist robot with 5 DOFs [45]. However, the robot was only used for tool positioning in a double-doughnut open MRI system with a magnetic field strength of merely $0.5\,\mathrm{T}$. Most part of the robotic device was placed outside of the MRI scanner and only two arms were allowed to enter the imaging volume to minimize image distortion. Later, Krieger et al. reported for transrectal prostate imaging and intervention a novel remotely actuated manipulator with small fiducial markers at known locations on it [46]. Those fiducial markers would allow for MRI guidance in standard closed bore scanner. Based on this manipulator, a completely new design and implementation of a MRI-compatible robotic device actuated with piezo-ceramic-motor was presented in [38],

with significant SNR loss while the motors were being actuated. Moser and Gassert et al. developed a 1-DOF proof-of-concept MRI-compatible master slave system using hydraulic transmission and achieved a manipulation accuracy of a few micrometers over a range of several centimeters [47, 48]. Elhawary et al. designed a 5-DOF prostate biopsy manipulator using piezoceramic motors and the feasibility was shown with a 1-DOF test rig implementing closed loop position control [35]. Goldenberg et al. developed a 6-DOF MRI-compatible robotic system for prostate interventions using ultrasonic motors and had achieved less than $2\,\mathrm{mm}$ positioning accuracy [37]. Sutherland et al. adopted the dexterous manipulator design for the International Space Station and implemented the MRI-compatible neuroArm, which had 7 DOFs and was manufactured primarily of titanium and some hard plastic material [49]. With ultrasonic piezoelectric actuators, the neuroArm was able to perform microsurgery at a spatial resolution of 50 to $100\,\mu m$, yet more validation studies should be conducted to quantify the system performance. Su et al. also used piezoelectric actuators and developed for prostate brachytherapy a 6-DOF prototype with a high-resolution fiber optic force sensor and only 2% SNR loss was observed in the MRI-compatibility test [41]. Based on the novel pneumatic step motor design [43], Stoianovici et al. developed an MRI-unperceivable robot, MrBot, to carry out transperineal needle insertions for prostate intervention [50]. Fischer et al. initially developed a 4-DOF MRI-compatible needle placement robot for prostate interventions using pneumatic cylinders with only 2-DOF actively controlled as a proof-of-concept [51], and this work is continued by Song et al. with a new workspace-optimized 4-DOF robot for MRI-guided prostate biopsy and brachytherapy. The new robot was based on modular system design and utilized external damping mechanism to improve pneumatic cylinder

positioning accuracy [52].

While the development of MRI-compatible robotic devices for prostate interventions has attracted most attention, robotic devices for breast lesions are also under active development. The first robotic system for biopsy and therapy of breast lesions under a $1.5\,\mathrm{T}$ high-field whole-body MRI unit has been developed by Kaiser et al., and the *in vitro* experiment showed the feasibility of a combination of imaging with biopsy and subsequent therapy [53], though the needle approach direction in their system was limited. Larson et al. developed a 5-DOF ultrasonic motor actuated robotic stereotactic device for minimally invasive interventions in the breast with real-time MRI-guidance, and submillimeter repeatability of the probe tip for same-direction point-to-point movement was achieved [39, 54]. Kokes et al. developed a 1-DOF MRI-compatible robot for RFA of the breast tumors with hydraulic actuation and interfaced it with a PHANToM haptic feedback device controlled from outside of the MRI room [55, 56]. That is the pioneer work based on which the work documented here developed.

There are also ongoing research to develop MRI-compatible surgical robots for other interventional procedures. Raoufi et al. presented a novel modular robot design to perform neurosurgery guided by MRI with ultrasonic motor actuation [57], and its control paradigm as well as two proposed brain biopsy procedures using MRI guidance was detailed in [58]. The design was further revised to replace the ultrasonic motors using either hydraulic cylinders or pneumatic motors in [59]. Zemiti et al. developed based on specially designed pneumatic motor a light puncture robot (LPR) that was both CT and MRI-compatible and could perform abdominal and thoracic punctures [60]. Pappafotis et al. reported a preliminary design of a 6-DOF highly dexterous MRI-compatible robot, and

actuation with SMA was proposed and verified in one of its links [61]. Ho et al. continued that work and redesigned the robot to have it actuated with SMA wires for each of its links, and showed good controllability of that robot under real-time MRI guidance [34]. The systems mentioned here are far from exhaustive, and more MRI-compatible robotic and mechatronic systems can be found in [33] and [62].

Robotic devices for non-surgical purpose have also been developed. Hou et al. implemented a MRI-compatible force feedback system that could be used both in functional magnetic resonance imaging (fMRI) and event-related potential (ERP) [63]. This device was then applied in hand-grip tasks and finger movement experiments to explore the relationship between force output and brain activation mode in normal subject and stroke patient. With custom-developed pneumatic air motor, Tse et al. developed a 3-DOF MRI-compatible mechatronic system and used it to position a variety of limbs at the magic angle inside closed-bore MRI scanner [64]. It helped to take advantage of the "magic angle" effect and increase the signal intensity observed at the tendon or cartilage in the MR images. These MRI-compatible devices were simple in their functionality compared to those surgical systems, yet they were developed in ways that would conform to the restrictions posed by the MRI environment.

1.4 Solution for Breast Biopsy under Continuous MRI Guidance

With the space constraint of the MRI machine, the breast biopsy under continuous MR imaging guidance inside the MRI scanner bore has to be performed by a robotic device; and the magnetic fields inside the scanner bore require that the robot be built with MRI-

safe materials and actuated with MRI-compatible actuation techniques. Such a robot would be teleoperated by the physician who stays inside the MRI control room to access the MR images acquired in real-time and ensures that the breast biopsy needle will be inserted into the target lesion. Hence, a "one-sitting procedure" is pursued, whereby identification of tumor boundaries, placement of the needle, assessment of placement accuracy, and even treatment such as RFA and its assessment can be done in one sitting, without removing the patient from the MRI scanner or disrupting tumor location. The envisioned scheme is shown in Figure 1.1.

The MRI-compatible robot shown in Figure 1.1 would have multiple DOFs and should be able to access various tumor locations in the breast. It can be fitted into the MRI machine and fixed at the back of the scanner bore or on the MRI bed. Teleoperated by the physician who accesses the real-time MR images inside the MRI control room, this slave robot could maneuver underneath the headrest while the patient lies on the MRI bed and perform needle insertion task through the front opening of the breast coil. With such surgical setup, the breast biopsy procedure can be reformed as follows:

(1) Prepare the teleoperated surgical system with the MRI-compatible slave robot;

(2) Put the patient inside the MRI scanner and take MR images of the breast to locate the suspicious breast tissue;

(3) Teleoperate the MRI-compatible slave robot while watching the MR images acquired in real time to prepare for needle insertion by moving the needle close to the breast and adjusting the needle orientation;

(4) Perform the needle insertion task with real-time MR imaging monitoring and insert

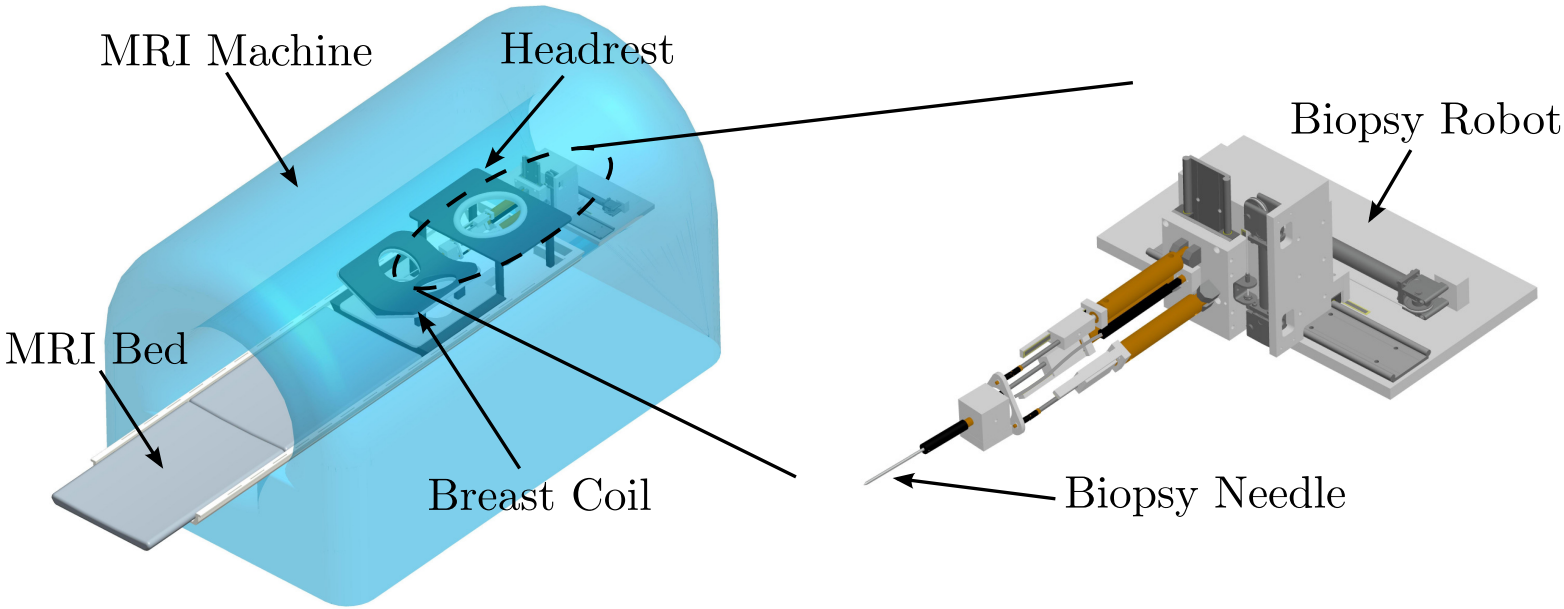

Figure 1.1: The envisioned scheme of the MRI-compatible robot inside the MRI bore

the coaxial breast biopsy needle with the plastic guiding cannula to the target location in one single insertion. The needle orientation can be re-adjusted as needed during insertion;

(5) Slide the patient out of the MRI scanner bore;

(6) Remove the trocar needle only and leave the guiding cannula, and then insert the biopsy gun through the guiding cannula;

(7) Perform breast biopsy with the biopsy gun and acquire breast core specimen of the suspicious breast tissue for microscopic analysis;

(8) Remove the biopsy gun and/or perform immediate treatment accordingly if needed;

(9) Plant small MRI visible markers through the guiding cannula for future reference, and remove the cannula from the breast of the patient.

The above procedure simplifies and speeds up the current breast biopsy procedure by eliminating the "trial and error" phase while taking advantage of the execution precision of the robotic device, performing breast biopsy right on the lesion.

The goal of the project described in this dissertation is to develop a teleoperated master-slave surgical system with a MRI-compatible slave robot that can perform breast biopsy needle insertion under continuous MRI guidance. The slave robot is built with MRI-safe material and MRI-compatible actuators, i.e., pneumatics and piezo motors, and its design, development and analysis is presented in Chapter 2. The modeling and control

of the pneumatic actuation system is detailed in Chapter 3. The design and implementation of the master manipulator is covered in Chapter 4. The system integration and teleoperation as well as a graphical user interface (GUI) is described in Chapter 5, and the result of the *ex vivo* phantom test and *in vivo* live swine test is discussed in Chapter 6. Finally, concluding remarks and discussions for future work are presented in Chapter 7.

Chapter 2

Design and Development of the MRI-Compatible Slave Robot

To achieve the goal of developing a teleoperated master-slave surgical system that can perform breast biopsy needle insertion under continuous MRI guidance, it is imperative to develop a slave robot that is MRI-compatible and can perform the needle insertion tasks for breast biopsy. Unlike conventional surgical environments, MRI imposes strong magnetic fields that rule out the possibility of utilizing most commercially available equipment as well as the traditional actuators. Hence, it requires special care to use appropriate raw materials and actuators to implement the slave robot.

This chapter presents in detail the design and development of the MRI-compatible slave robot and is organized as follows. The challenges posed by the MRI environment are reviewed in Section 2.1. Then, a 4-DOF MRI-compatible slave robot prototype is designed and built in Section 2.2, followed by a MRI-compatibility evaluation experiment in Section 2.3. Based on the result of that preliminary study, a slave robot is designed and implemented in Section 2.4, and the evaluation result of its MRI-compatibility is presented in Section 2.5. The kinematic analysis of the developed slave robot is then described in Section 2.6, and its control scheme is briefly described in Section 2.7. This chapter summarizes in Section 2.8.

2.1 Challenges to Develop MRI-Compatible Robots

Magnetic resonance imaging (MRI) is an imaging technique that uses the nuclear magnetic resonance (NMR) property to image the nuclei of atoms and hence reconstructs the inner structure of a biological body. The MRI machine employs a very strong static and homogeneous magnetic field ranging from $1.5\,\mathrm{T}$ to $7.0\,\mathrm{T}$ to align the magnetic moments of certain kinds of atoms, such as hydrogen ($^1\mathrm{H}$), which is highly abundant in biological body. Those kinds of atoms have unpaired protons and neutrons and, hence, exhibit net magnetic effect under the strong magnetic field. When a pulsed RF magnetic field is applied, energy at a certain frequency that is proportional to the strength of the applied static magnetic field will be absorbed. The absorbed energy rotates the net magnetic moments of those atoms away from their previously aligned axis to a certain angle, which is called the flip angle. Such flip angle is proportional to the strength and the duration of the applied RF pulse. Upon removal of the pulsed RF magnetic field, the magnetic moments restore to their original direction and energy absorbed is emitted in the form of RF signals at the corresponding frequency. Meanwhile, a gradient magnetic field is applied and used to shift the RF frequency that stimulates the tissues so that the frequency of the emitted RF signals is also shifted accordingly and corresponds to the specific location of the tissues. Those RF signals are picked up by the MRI scanner and analyzed to reconstruct the chemical composition of the tissues being scanned and form the MR images that will be used for clinical diagnosis.

The imaging process described above involves a strong static and homogeneous magnetic field, a gradient magnetic field, and a pulsed RF magnetic field that together

determine the final emitted RF signals. Therefore, to ensure high-quality RF signals be generated and used to synthesize high-quality MR images, the interference on those three magnetic fields should be kept minimal if not completely avoided.

With such a magnetic environment, it is challenging to safely place a robot inside the MRI bore and operate it therein, without interfering with the strong but delicate magnetic fields inside.

Firstly, the robot has to be built with appropriate materials. Ferromagnetic materials are strictly prohibited inside the MRI since they can be attracted by the strong magnetic fields and become dangerous projectiles that can damage the MRI machine or even hurt the personnel nearby (missile effect). Apart from ferromagnetic materials, many other metals are also not encouraged for use inside the MRI bore, since significant artifacts can be produced in the images due to the eddy current induced by either the changing magnetic field during scanning or the motion of the robot.

Ideally, polymer materials such as Delrin® and Teflon® are preferred construction materials since they are both nonmagnetic and dielectric. While polymer materials are used for as many parts as possible, however, metal materials are at times required for structural parts that require higher mechanical stiffness and strength that polymer materials cannot provide [65]. Under those circumstances, nonmagnetic metals are used and those metallic parts would be placed as far away from the target lesion as allowed to minimize the possible artifacts and image quality degradation.

Titanium is the most ideal material for use in MRI-compatible robots since it is strong, light-weight, corrosion-resistant, and most importantly, MRI-safe. However, it is rarely used in MRI-compatible robotic research and development since the final mecha-

tronic system is a balance of desired function, MRI-compatibility, and the manufacturing cost [65] while titanium is expensive and challenging to machine.

Nonmagnetic metals such as brass and aluminum are thus most commonly used for customized parts due to their cost and machinability; while the 300 series stainless steel, or more specifically, the 316 stainless steel, is more commonly seen in the nonmagnetic version of some commercially available products. Nevertheless, nonmagnetic products built with 316 stainless steel have to be tested carefully after the manufacturing process since the magnetic susceptibility of the 316 stainless steel can increase from 0.003 to 9 when heavily cold worked [66], rendering it unfit for use in MRI. The brass and aluminum do not exhibit such behavior and MRI tests have shown that Alloy 360 (brass) and Alloy 3601 (aluminum) render modest magnetic field interference and are hence used as the primary nonmagnetic metal materials.

Secondly, the actuation techniques that would be used to actuate the robot have to be MRI-compatible. That essentially means that not only the materials used to build the actuator have to be MRI-safe, but also the actuation itself should not introduce any artifacts in the MR images, nor its operation be affected by the presence of the strong magnetic fields. The well-developed electrical motors can no longer be utilized in such scenarios as they are based on the electro-magnetic effect. The magnetic field generated during motor operation can interfere with the homogeneous magnetic field inside the MRI bore, significantly degrading the image quality, not to mention the fact that the materials used to build them are usually ferromagnetic or even include magnets that are strictly prohibited inside the MRI environment. Review of the actuation techniques that can be used under the MRI environment has been performed by various researchers and Elhawary et al. summarized

the major MRI-compatible actuation techniques into four categories, i.e., remote manual actuation, ultrasonic motors based on piezoceramic principle, hydraulic transmission, and pneumatic transmission [33], while the potential of other MRI-compatible actuation techniques such as SMA is under active investigation.

Among all the aforementioned actuation techniques, remote manual actuation provides an inexpensive method to achieve MRI-compatible actuation, but at the cost of slower procedure and lower resolution than the motorized actuation [33], and hence are less popular than other actuation techniques.

Ultrasonic piezo motor has the advantage of being inherently safe with respect to power failure as it does not need electrical power to keep the posture of the manipulator [67]. However, the MR image quality cannot be ensured with ultrasonic piezo motor actuation since the piezoceramic elements are often embedded inside ferrous materials [33]. Also, the choice of the high-frequency actuating electrical signals that the ultrasonic piezo motor actuation relies on does not taken into account the frequency band the MRI machine operates on, and that could lead to severe signal interference and would cause moderate to significant image quality degradation when in actuation [36, 38, 50, 51]. Therefore, it is not recommended to operate the ultrasonic piezo motor while the MRI scanning is taking place [37]. Despite all those limitations, ultrasonic piezo motor actuation is still widely used due to its analogous structure to traditional motors and convenience of application, and they should be carefully chosen before usage to avoid ferrous materials and be placed away from the scanning target to minimize the effect of any electrical noise introduced from its electrical driver.

The actuation of SMA, though with a large force density and is potentially MRI-

compatible, provides limited force and/or displacement output and can only generate force from milli-newtons [61] up to a few newtons [34] unless complicated configuration is arranged. Therefore, the actuation of SMA is more suitable for micro- to meso-scale robots.

In comparison, hydraulic and pneumatic actuation techniques offer the advantage of maintaining high SNRs [42] or even no negative impact in all configurations [36] at a closer location to the scanning target. Due to the compressibility of air, pneumatic actuation is back drivable and natural impedance, which makes it more favorable for fast or force-control applications. Also, pneumatic systems are easier to maintain compared to hydraulic systems, since hydraulic systems can suffer from cavitation and fluid leakage. Further, pneumatic systems are clean and safe even with a transmission fluid spill condition that could compromise the sterility condition of the surgical environment in the case of hydraulic actuation [50, 68, 69].

Therefore, pneumatic actuation has been chosen as the primary means of actuation for the slave robot implementation, with piezo motor actuation as the supplemental method.

Thirdly, the sensors used in the robot implementation should be MRI-compatible. A good review of the sensing techniques that are suitable for MRI application has been presented by Gassert et al. with the categorization of electrically active sensors, electrically passive sensors, and nonmagnetic non-conducting sensors [70]. The electrically active sensors are electrically powered and include strain gauge as well as potentiometers. Some of those sensors can be used but require proper shielding to retain their nominal functions. Yang et al. has reported that without shielding, the reading of a commercially

available nonmagnetic force sensor was compromised by the MRI scanning sequence [2]. The electrically passive sensors are those using passive electrodes to measure potentials of the targeting physical quantity. However, those sensors are mostly used to measure biological body potentials and are not very appropriate for robot implementation. The nonmagnetic non-conducting sensing approach utilizes fluid or light to transmit the power and is the most preferred for MRI application. Force sensors based on fiber-optic techniques have been developed with good MRI evaluation results reported in [70, 71]. In the systems developed in the ensuing sections, a customized fiber-optic force sensor as well as potentiometers and optical encoders are used with caution.

2.2 Design and Implementation of the MRI-Compatible Prototype Robot

Other than the material and actuation / sensing restrictions described in Section 2.1, the MRI machine also poses space constraints to the robot. The standard MRI scanner bore is generally $70\,\mathrm{cm}$ in diameter and has to fit in the patient along with the appropriate imaging coil that is essential for high quality image acquisition, leaving little space to the robot. Hence, the slave robot must have a compact footprint that can not only fit into the limited space available but also be able to maneuver and achieve a workspace that can include most of the possible sites of breast tumor.

Given such significant in-bore space constraint, a compact design with parallel mechanism has been proposed as a key subsystem. The parallel mechanism pursued in this section has three DOFs in total, with one DOF in translation and the other two in rotation. Along with a needle driver that provides the fourth DOF and advances the nee-

dle, a 4-DOF MRI-compatible breast biopsy slave robot is designed and implemented as a prototype to validate the feasibility of building a robot that can assist performing breast biopsies under continuous MRI guidance. The parallel mechanism is actuated with pneumatic cylinders and the needle driver is actuated with a piezo motor placed away from the scanning target. Figure 2.1 shows the implemented robot prototype and the detailed design of the parallel mechanism as well as the needle driver is described in the following subsections.

2.2.1 Parallel Mechanism of the Prototype Robot

Parallel mechanism is a kind of mechanism whose end effector is connected to its base through a number of similar and independent linkages in parallel, and is more rigid and compact compared to serial manipulators. It can also provide a very good absolute as well as repetitive positioning of its end-effector [21]. Therefore, parallel mechanism has been a popular choice and has been used in various industrial and research applications [72–83].

Among all kinds of parallel mechanism, the 6-DOF Stewart platform structure is the most popular and has found wide applications. Salcudean et al. designed and implemented an inverted, ceiling-mounted Stewart platform with hydraulic actuation and used it as a one person motion simulator [74]. The modeling, simulation, and control of such Stewart platform was presented in detail in [84]. A novel design of a hydraulic actuated Stewart platform has been reported by van Silfhout to support scientific instruments that would require a stable alignment base with high-precision motion [76]. The implemented manipulator could deal with loads up to $20\,\mathrm{kN}$ and had a resolution of $1\,\mu\mathrm{m}$. Hadden et

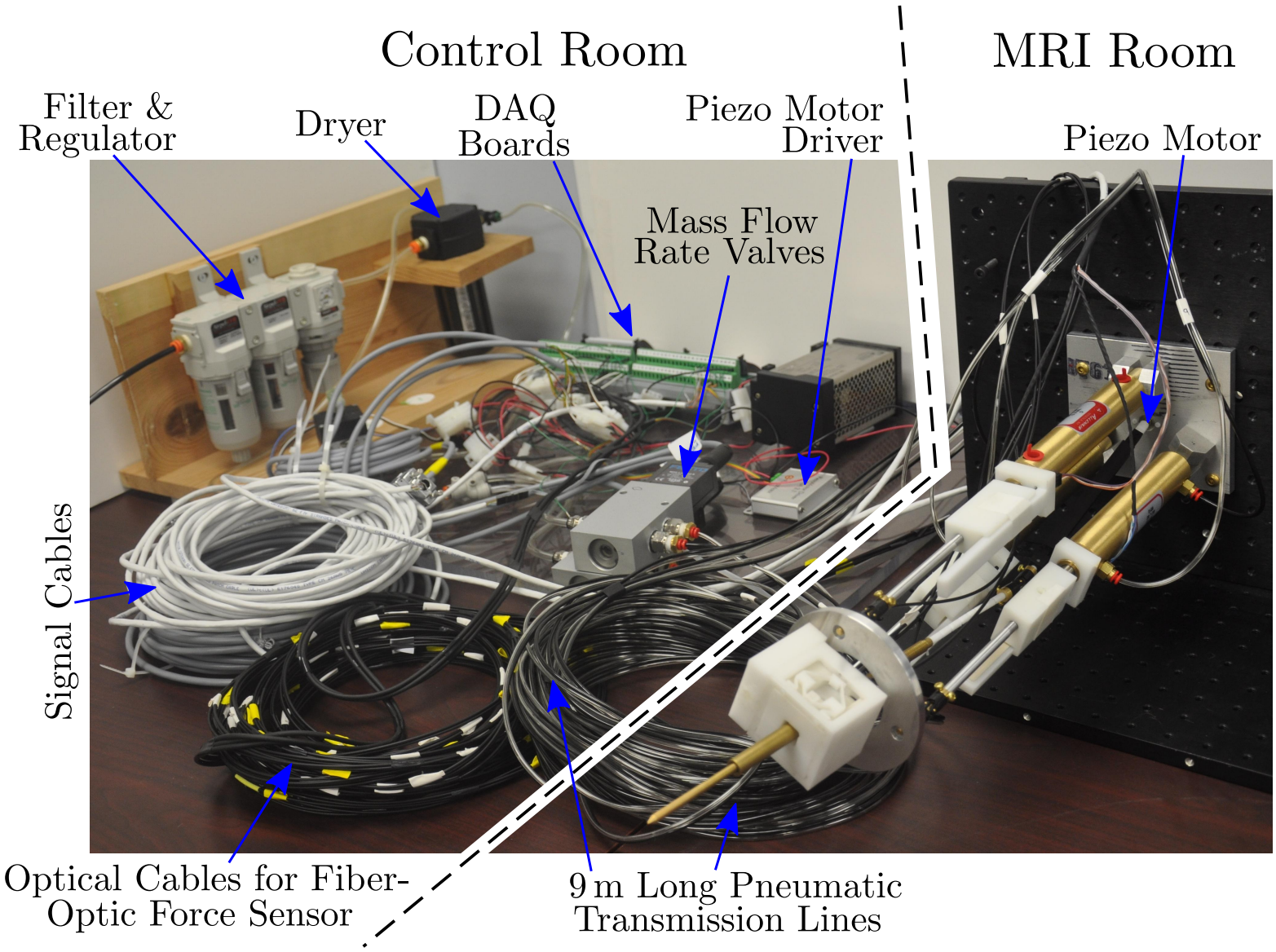

Figure 2.1: Photo of the breast biopsy slave robot prototype: The optical cables and pneumatic lines pass through the waveguide while signal cables and piezo motor driving cable pass through the filter panel of the MRI room.

al. built a Stewart platform with pneumatic struts and applied it to achieve heavy load vibration isolation for airborne payloads [77]. Aracil et al. used the Stewart platform structure in a different way and built a parallel robot for autonomous climbing along tubular structures [78] while Tanaka et al. developed a force-driven joystick based on Stewart structure with pneumatic actuation [82]. Also, based on the six-link Stewart platform structure, Burdea et al. developed the pneumatically actuated "Rutgers Ankle" [85–87], and the control of such devices was investigated in detail by Yoon et al. [88]. They were than applied in ankle and gait rehabilitation [79, 80] with preliminary case study results reported in [89]. In addition to applying Stewart platform into various applications, Nanua et al. reported a forward kinematics solution for a six-link platform [90], while Liu et al. performed thorough kinematic analysis and proposed a simple algorithm to solve the forward kinematics [91]. Yurt et al. performed error analysis and motion determination on a flight simulator modeled as a Stewart platform, and Ukidev et al. studied the fault tolerance property of the manipulators and applied redundency to optimize the manipulability of the Stewart platforms.

In cases where less maneuverability were required, parallel mechanisms with less complicated structures had been designed and applied. Pfreundschuh, Kumar and Sugar developed a 3-DOF in-parallel manipulator with pneumatic actuation to serve as a wrist of a robot arm or an ankle for a walking robot, and the detailed study on the kinematics, control, dynamics behaviour of the device were presented in [72, 73, 75]. Ning et al. designed and developed a new wire-driven 3-DOF parallel manipulator that potentially could find wide applications in industries due to its simple structure and low cost [81], and a similar mechanical structure was reported by Raparelli et al. but with smart wire actuation

(SMA) [92]. D'Angelle et al. developed a new parallel robot called PmarNeedle and the targeting application would be needle surgery [83].

The parallel mechanism utilized in the prototype design comprises of three RPS (Revolute, Prismatic, and Spherical) joint structures spaced evenly in 120° increment along each circle on the two platforms, as shown schematically in Figure 2.2. By changing the lengths of its three independent extensible links, L_i ($i = 1, 2, 3$), the orientation of the top mobile platform, to which the mobile frame F^m ($o_m x_m y_m z_m$) attaches, can be adjusted, and the spatial position of the mobile platform center o_m is changed accordingly. The rotation of the mobile platform along its z-axis, z_m, is not implemented since the needle is axially symmetric and aligned to that axis, and is unnecessary. Its three DOFs combined with the insertion DOF provided by the needle driver that is discussed later in Section 2.2.2 together enable the positioning of the needle tip at any point in 3-D space. A similar mechanism has also been explored by other researchers and some of them can be found in [75] and [93].

The parallel mechanism, as shown in Figure 2.1, is attached horizontally to a vertical plate, which will later be replaced with an X-Y stage that is discussed in Section 2.4.3 to enable position adjustment in the vertical plane, as illustrated in the envisioned system scheme in Figure 1.1. The parallel mechanism is designed to move underneath the headrest and reach the target lesion inside the breast coil; therefore, the parallel mechanism is relatively compact in the radial direction and long in the longitudinal direction. Each of its extensible links has a minimum length of $400\,\mathrm{mm}$ and is attached to both platforms along the circumferences of an r-radius and an R-radius circle, respectively. Though the radii of the top mobile platform and the base platform do not necessarily need to be equivalent,

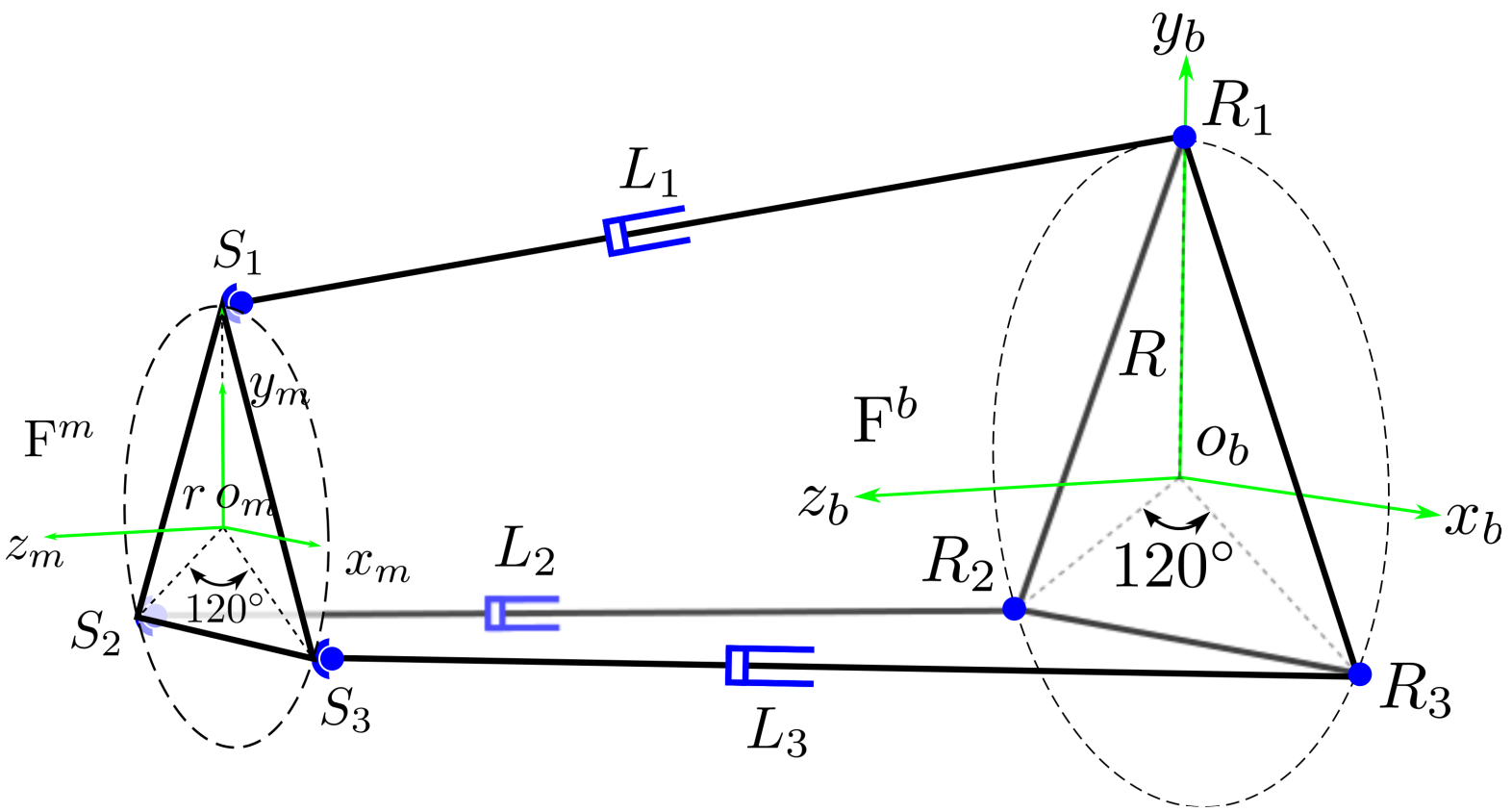

Figure 2.2: Schematic of the parallel mechanism: S_is represent the spherical joints on the mobile platform, R_is represent the revolute joints on the base platform, and L_is are the lengths of the extensible links, ($i = 1, 2, 3$). Frame F^m ($o_m x_m y_m z_m$) attaches to the mobile platform on the $S_1S_2S_3$ plane while frame F^b ($o_b x_b y_b z_b$) attaches to the base platform on $R_1R_2R_3$ plane.

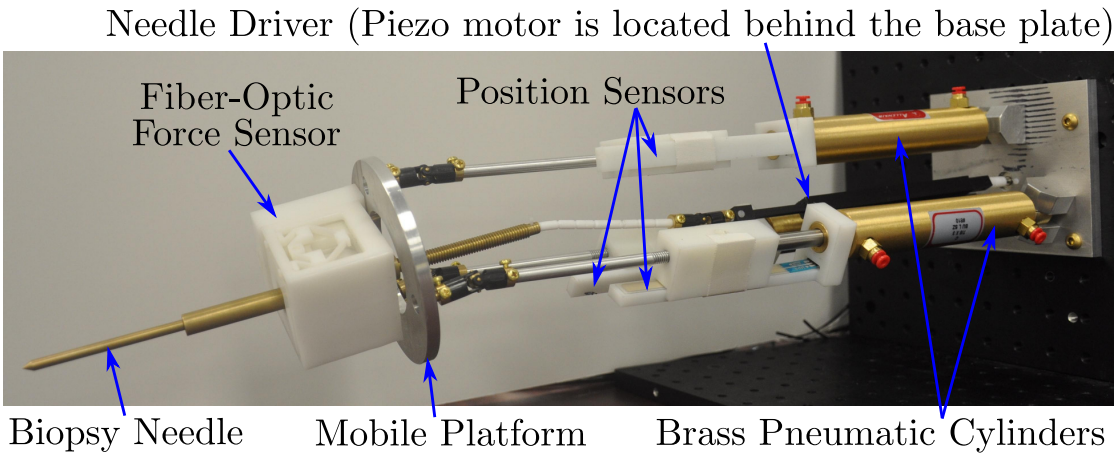

(a) Assembly of the 3-DOF parallel mechanism and the needle driver

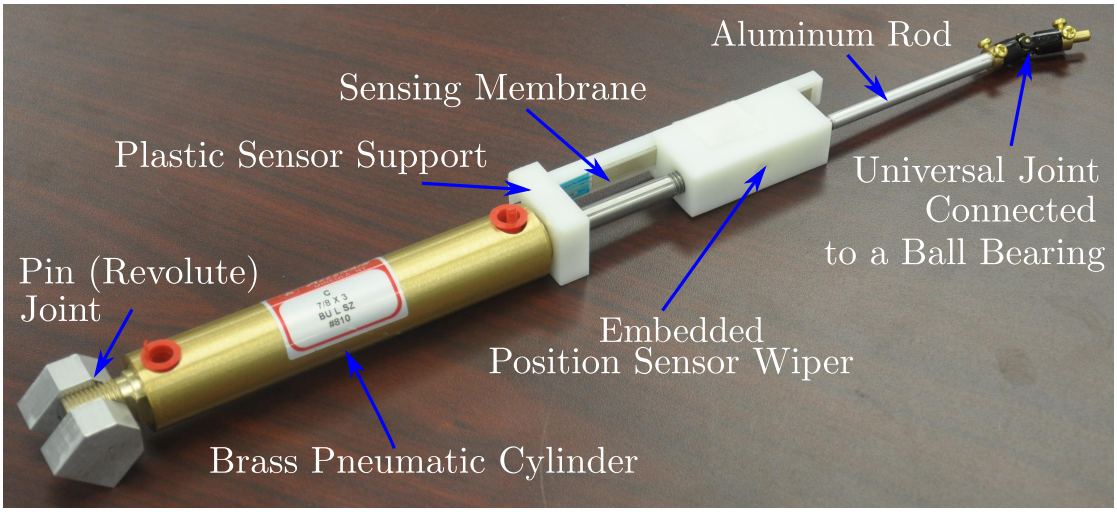

(b) Detailed view of an individual link of the parallel mechanism

Figure 2.3: The 4-DOF breast biopsy slave robot prototype

and the kinematic derivation in Section 2.6 will show that the kinematic constraint of the parallel mechanism depends only on the circle radius of the top mobile platform, identical radius has been chosen for both the top mobile platform and the base platform to make the parallel mechanism more compact, with $r = R = 38.1\,\mathrm{mm}$. The entire prototype robot and one link of the parallel mechanism are shown in Figure 2.3.

The key component of each extensible link is the brass pneumatic cylinder (Allenair Brass Cylinder, C-7/8x3-BU-L-SZ), which is chosen for its high strength and being non-

magnetic at the expense of higher stiction force. It provides $76.2\,\mathrm{mm}$ ($3"$) stroke and attaches to the base platform via two aluminum blocks that support a $1/4"$ outer diameter (OD) brass pin (McMaster, 97325A185), about which the link rotates. The link is extended to the desired length with a thin aluminum rod to reach the targeting space so that sufficient room near the mobile platform would be provided for the needle driver to manipulate. The rod of the brass cylinder and the aluminum rod are attached together with a Delrin® block which also houses the position sensor wiper (spectrasymbol, WP-M1-01-03-014-DI). The wiper and the sensing membrane potentiometer (spectrasymbol, TSP-L-0100-103-1%-RH) attached to the plastic sensor support together provide the position information of the cylinder with a resolution of less than $0.1\,\mathrm{mm}$. At the other end of the aluminum rod is a universal joint (Small Parts, UJD-3/3-01) that is made of brass and Delrin® and holds a $3/16"$ OD brass pin (McMaster, 97325A165). This pin is glued to a plastic ball bearing (McMaster, 6455K7) that is embedded into the aluminum mobile platform. The universal joint, with its two rotational DOFs, and the ball bearing that provides the third rotational DOF orthogonal to the previous two DOFs together behave kinematically as a spherical joint, and the pivot point of such spherical joint is at the rotation center of the universal joint.

2.2.2 Needle Driver of the Robot Prototype

With the target application of percutaneous intervention, the design and implementation of the needle driver is crucial to achieve the desired functionality. The PARK needle driver developed by Stoianovici et al. takes advantage of the friction force to perform

needle insertion and the exertable insertion force is inherently limited due to its reliance on the friction [22]. Trejos et al. has developed a needle driver device for brachytherapy, yet it can only retract the hollow needle loaded with radioactive seeds to place the seeds into the tissue, and the needle insertion should be performed by the robotic manipulator that holds such needle driver [14]. Shah et al. developed a novel rotating needle driver with complicated design [94]. This needle driver could spin the needle at different speed and has the safety feature to release the needle when the sensed force exceeds a predetermined limit; however, it is expected to work with the AcuBot under CT guidance, and is not appropriate to perform breast biopsy needle insertion under continuous MRI guidance.

The needle driver designed and implemented for the prototype robot is shown in Figure 2.4. A fiber-optic force sensor is attached to the needle driver and is used to sense the interaction force between the needle and the soft-tissue. Such force information could be provided to the physician during the procedure and facilitate the detection of transitions between tissue layers, thus reducing needle placement error [95]. The force sensor was developed by Tan et al. and measures the force by monitoring the intensity change of the light reflected from an elastic frame structure, which would deform under external load. For detailed design and implementation of the force sensor, please refer to [71].

The needle can be advanced using screw motion by rotating the one-end threaded biopsy needle about the fixture. This fixture is fixed to the fiber-optic force sensor that attaches to the aluminum mobile platform through a Delrin® block. MR markers are embedded inside this block to provide the position and orientation information of the mobile platform. Based on the design constraints, motors that are small enough to mount on the

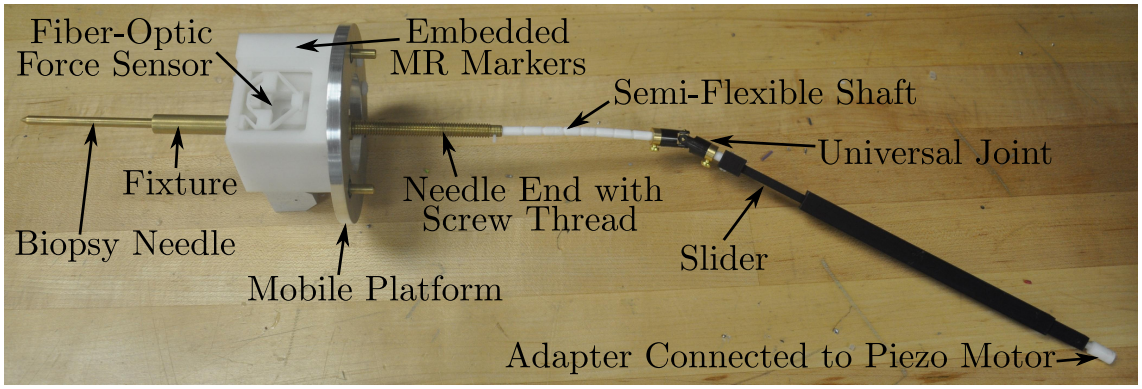

Figure 2.4: Photo of the needle driver prototype attached with a force sensor

mobile platform cannot provide sufficient torque to advance the needle. In addition, it is necessary to mount the motor at a distance away from the mobile platform to minimize its negative impact on the MR images. In the design shown in Figure 2.3(a), the motor utilized is a piezo motor (LEGS-R01NM-10 from PiezoMotors, Sweden) and is mounted at the base of the robot, which is over $400\,\mathrm{mm}$ away from the scanning target. The remaining challenge is to reliably transmit the rotational power and drive the biopsy needle without hindering the mobile platform to move in the 3-D space.

Due to the space constraint, a compact mechanism is needed to transmit the rotational power and has to be able to translate in the lateral directions as the mobile platform re-orientates or the needle advances. The conventional method of using rigid shaft is no longer appropriate since the mobile platform can be manipulated to arbitrary orientation with respect to the base platform with slight offsets in both horizontal and vertical directions. Therefore, the flexible transmission approached is proposed and implemented. A slider, as shown in Figure 2.4, is incorporated in the design to provide the required translational DOF when either the mobile platform translates or the needle advances. The slider is able to positively transmit the rotational power with a special rectangular shape.

Two rotational DOF are provided by connecting a universal joint (Small Parts, UJD-3/3-01) in series with the slider, and higher orders of bending that is required while actuating the pneumatic cylinders to operate the parallel mechanism are supplemented by a semi-flexible Teflon® shaft that joins the universal joint and the biopsy needle.

The drawback of this approach is the drilling effect when the needle is inserted into the tissue with rotation. This could cause extra damage to the tissue due to unusual dimension of a standard biopsy needle (8 gauge, or $4.191\,\mathrm{mm}$ in diameter). This issue is addressed later in the revised implementation discussed in Section 2.4.2.

2.3 MRI-Compatibility Evaluation of the Robot Prototype

To verify the MRI-compatibility of the slave robot prototype, MRI tests have been conducted under the experimental setup shown in Figure 2.5. The robot prototype was mounted on the black aluminum frame and was placed inside the MRI bore pointing to a homemade phantom, which consisted of a mixture of $200\,\mathrm{ml}$ boiling water with $7\,\mathrm{g}$ gelatin powder (Knox gelatin, Kraft Foods Global Inc.).

Testing was performed using a Siemens $3\,\mathrm{T}$ Tim Trio MR scanner (Siemens Medical Solutions; Malvern, PA) and the phantom was imaged using a T_1-weighted gradient echo acquisition with $T_\mathrm{E}/T_\mathrm{R} = 9.4/500\,\mathrm{ms}$, flip angle $= 75^\circ$, bandwidth $= 200\,\mathrm{Hz/pixel}$, FoV $= 120 \times 120\,\mathrm{mm}$, matrix $= 512 \times 512$, and slice thickness $= 3\,\mathrm{mm}$. A T_2-weighted imaging sequence would generally generate a sharper image, but the T_1-weighted imaging sequence was used because future experiments involving dynamic imaging would be based on T_1-weighted sequences. To examine the effect of each fac-

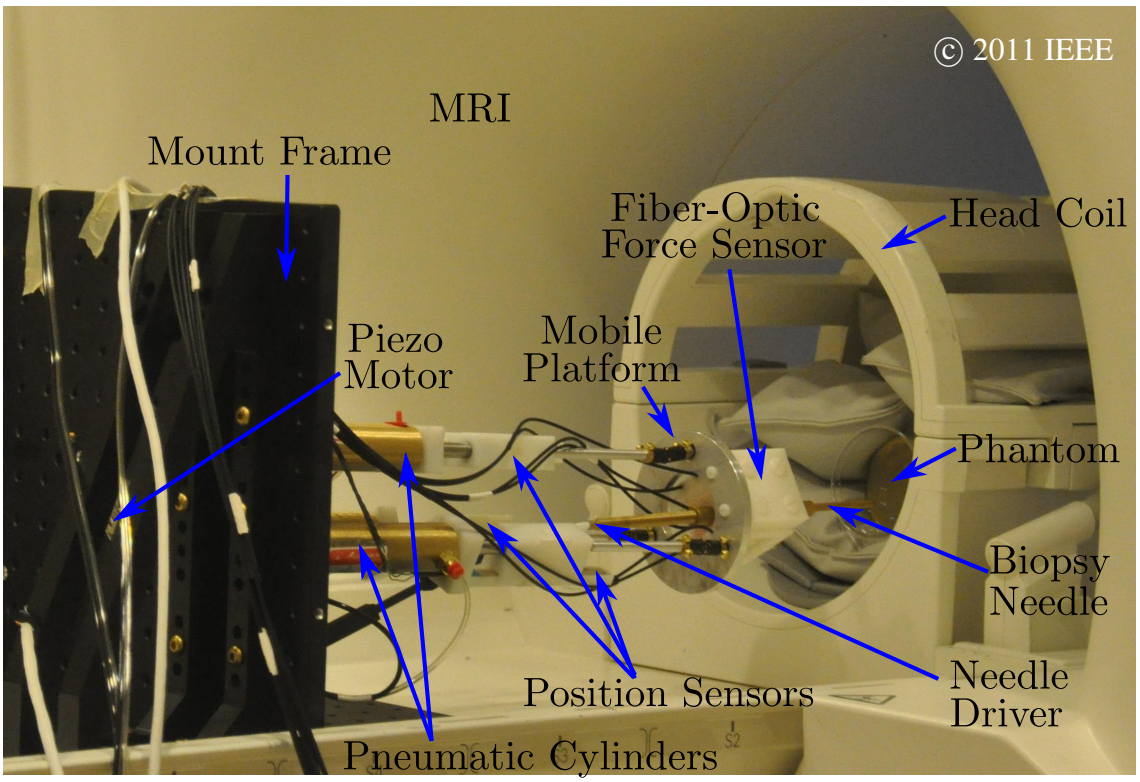

Figure 2.5: Experimental setup for the MRI evaluation of the robot prototype. Reprint from [2], © IEEE.

tor on the MR image quality, the phantom was imaged under four different conditions as listed below:

1. Imaging the phantom without the presence of the robot prototype and the images acquired would serve as the ground truth;

2. Imaging the phantom with the robot but without actuation;

3. Imaging the phantom with pneumatic actuation but without piezo motor actuation;

4. Imaging the phantom without pneumatic actuation but with piezo motor actuation.

The MR images acquired under the aforementioned conditions are shown in Figure 2.6. Figure 2.6(a) shows the MR image of the phantom without the robot while

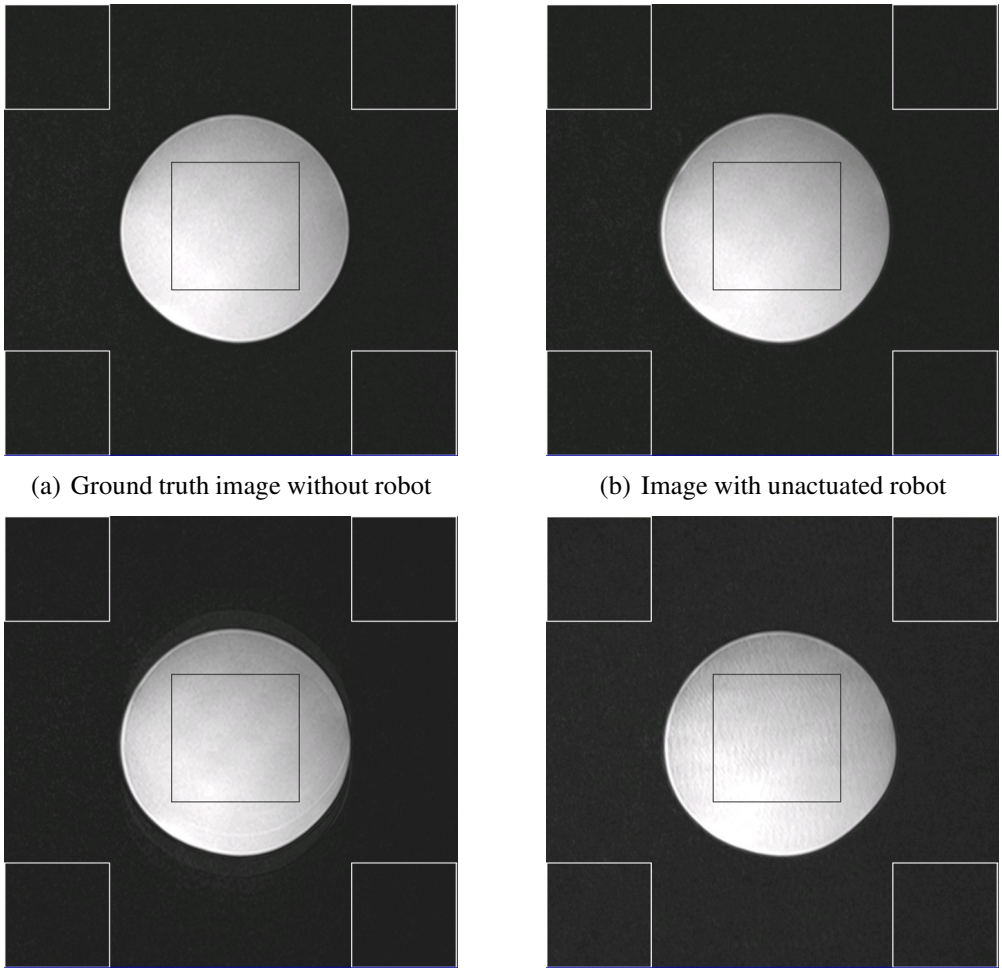

(a) Ground truth image without robot

(b) Image with unactuated robot

(c) Image with only pneumatic actuation

(d) Image with only piezo motor actuation

Figure 2.6: MR images of the phantom with the robot prototype and its actuation. The four corners and the center square of each image are the ROIs used to calculate the SNR for the noise and the signal, respectively.

Figure 2.6(b) is with the robot but without any actuation. The MR images acquired with pneumatic and piezo motor actuation are shown in Figure 2.6(c) and Figure 2.6(d), respectively. The phantom can be seen clearly from Figure 2.6(b)-2.6(d), which shows that the robot prototype is not producing significant artifacts or image distortion. If needed, better images can be acquired with proper shielding of the robot.

To further determine the degree of MRI-compatibility using quantitative measure-

Table 2.1: SNRs of the MR images with the robot prototype

Experimental Setup	SNR Values
Ground truth without robot	109.36
With robot but without actuation	105.99
With pneumatic actuation only	112.24
With piezo motor actuation only	98.04

ments, signal-to-noise ratio (SNR), defined as the ratio of the mean pixel value of the signal to the standard deviation of the pixel value of the background noise, is adopted. SNR is a relative measurement to evaluate the influence of the robot prototype and its actuation and such measurement is heavily observer dependant. The images acquired under different imaging sequence could result widely spanned SNR values depending on the choices of the imaging parameters. Likewise, choosing various subjects can also lead to large SNR variation of the MR images. Hence, the comparison of SNR values is meaningful only within the same study using the same imaging sequence, and significant difference should be expected between SNRs of a high-resolution diagnostic image, based on which the radiologist would make a medical decision, and that of the images for navigation purpose as used in this evaluation experiment. The SNR computation of the four MR images are performed on the original digital imaging and communications in medicine (DICOM) images and the SNR values are summarized in Table 2.1. Only modest SNR variation has been observed.

Figure 2.6(c) is one of the 22 MRI slice images taken in 122 seconds while the robot was actuated pneumatically to move in a periodical way by sending sinusoidal position signals with 120° phase lag to two of the links. As a result of such periodic motion, eddy

current was induced in the aluminum mobile platform along with other metal parts of the robot prototype and created magnetic field disturbance accordingly, which rendered overlapping phantom images in the MR image. Those false signals in turn lead to a slightly higher SNR value. In practical application, however, the slave would either stand still to take a static image with long scanning time for registration as the case of the image shown, or move under real-time dynamic imaging guidance with very short scanning time for each image. Therefore, the phenomenon shown in Figure 2.6(c) is not expected to be observed in practical application and such image SNR change will not be experienced.

Piezo motors, even carefully built with nonmagnetic material and actuated with relative low-frequency electrical signal, could still introduce electromagnetic (EM) noise from the driving electronics and cause interference at the MRI acquisition band. Such interference cannot be removed completely despite using shielded power cable and passing it through the filter panel. Hence, they should be placed a distance away from the scanning target, as required in the needle driver design in Section 2.2.2. By placing the motor at the very back behind the base platform of the parallel mechanism, clear MR phantom images with minimal distortion and modest SNR loss have been obtained. One such example is shown in Figure 2.6(d).

2.4 Design and Implementation of the MRI-Compatible Slave Robot

Based on the design and evaluation result in Section 2.2 and 2.3, the design and implementation of a multi-DOF MRI-compatible slave robot that has full motion capability is presented in this section. The computer-aided design (CAD) drawing of the robot inside

the MRI bore can be found in Figure 1.1 and a photo of the actual robot is shown in Figure 2.7. The detailed CAD drawing of each component is listed in Appendix A. Similar to its prototype, this robot maneuvers under the headrest and access from the front opening of the breast coil, on which the patient lies. With continuous MR imaging guidance and the physician in the loop to manipulate the slave robot and compensate for the positioning error, the targeting error due to patient involuntary motion in between scans could be significantly minimized. This version of robot consists of a 1-DOF piezo motor actuated needle driver that has been redesigned based on its previous version, a 3-DOF pneumatically actuated parallel mechanism with minor modifications, and a new 2-DOF X-Y stage that is actuated with two pneumatic cable cylinders. Comparing with its prototype, the newly implemented X-Y stage provides gross positioning and is used to support and move the parallel mechanism. This represents the macro-micro robotic system design concept. The novel 3-D ultrasound guided robotic system for prostate brachytherapy developed by Yousef et al. follows this concept [96]. The ZEUS™ surgical system and the *da Vinci*® surgical system can also be considered to have such macro-mirco architecture. The detailed design of each subsystem or the revisions based on the previous prototype is described in the following subsections.

2.4.1 Parallel Mechanism of the Slave Robot

For the implementation of the slave robot, the design of the parallel mechanism in the robot prototype has been adopted with minor modifications. The newly implemented parallel mechanism consists mainly of three $76.2\,\mathrm{mm}$ ($3"$) stroke brass pneumatic cylinders

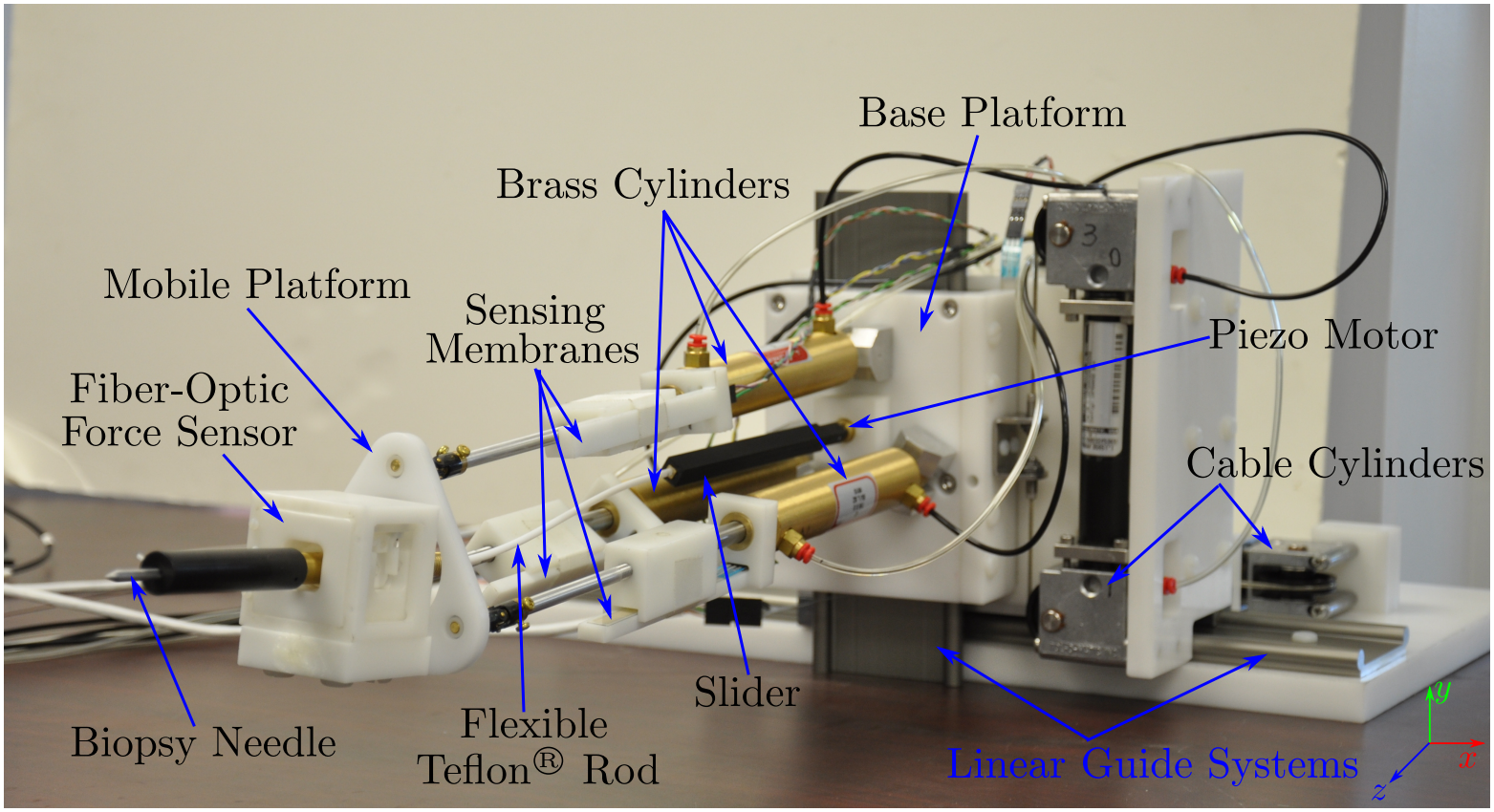

Figure 2.7: Photo of the actual MRI-compatible slave robot [97].

(Allenair Brass Cylinder, C-7/8x3-BU-L-SZ). One ends of those brass cylinders connect to the mobile platform with kinematically equivalent ball joints (using serial connection of a universal joint (Small Parts, UJD-3/3-01) and a ball bearing (McMaster, 6455K7)). On the other ends, those cylinders connect to the base platform with pin joints. These three cylinders are evenly spaced with 120° increments and are attached to both platforms on circles. By controlling the cylinder lengths with mass flow rate valves placed inside the control room through long pneumatic transmission lines, one translational and two rotational DOFs are achieved.

In this implementation, both platforms have been redesigned and built. The new mobile platform is made of Delrin®, and that is to avoid the overlapping artifacts or other artifacts created by the induced eddy current as observed in Figure 2.6(c) of Section 2.3. The mobile platform is almost orthogonal to the static magnetic field inside the MRI bore and is relatively close to the scanning target; therefore, if made of metal, it is the part that is most likely to generate eddy current once in motion and contribute most to the MR image quality degradation, which should be avoided. The effective of this material change to avoid the possible influence has been verified by MRI experiments, as described in Section 2.5. The shape of the mobile platform has also been changed from circular shape to triangle shape with rounded corners to reduce chances of coalition with the breast coil. The base platform has also been re-engineered to house the piezo motor while being able to attach to the X-Y stage. This base platform is also made of Delrin® to avoid potential influence on the MR image quality. For details about the design and implementation of other parts, please refer to Section 2.2.

2.4.2 Needle Driver of the Slave Robot

Despite the fact that by controlling the rotation and translation of the needle the friction force between the needle and tissue can be greatly minimized to reduce the undesired tissue deformation [98], the new needle driver would advance the needle without rotary motion. This is to avoid the "drilling effect" that could cause extra damage to the tissue and hence is undesired in breast biopsy, given the unusual dimension of a standard biopsy needle (8 gauge, or $4.191\,\mathrm{mm}$ in diameter). To use the same actuation mechanism of screw motion as that of its previous prototype, ball bearings are introduced to isolate such rotation. The CAD drawing of the revised design is shown in Figure 2.8(a) with the photo of the actual mechanism shown in Figure 2.8(b).

As in its previous prototype, the needle is driven by converting the rotary motion of the piezo motor (LEGS-R01NM-10 from PiezoMotors, Sweden) into translational motion using a screw structure. The rotation power generated by the distal piezo motor is transmitted via a flexible Teflon® rod to the threaded needle base to generate translational motion. The universal joint used in the previous prototype has been removed for simplicity and could be easily included if necessary. Different from its previous prototype, the rotary motion at the biopsy needle has to be removed; therefore, two ceramic bearings (VXB, Kit8707) are incorporated and press-fitted into the needle base to hold the needle adapter. With such design, the biopsy needle can rotate freely relative to the needle base and the friction force between the needle and the tissue during needle insertion are sufficient to prevent the needle from rotating; thus, pure translational motion can be achieved at the biopsy needle.

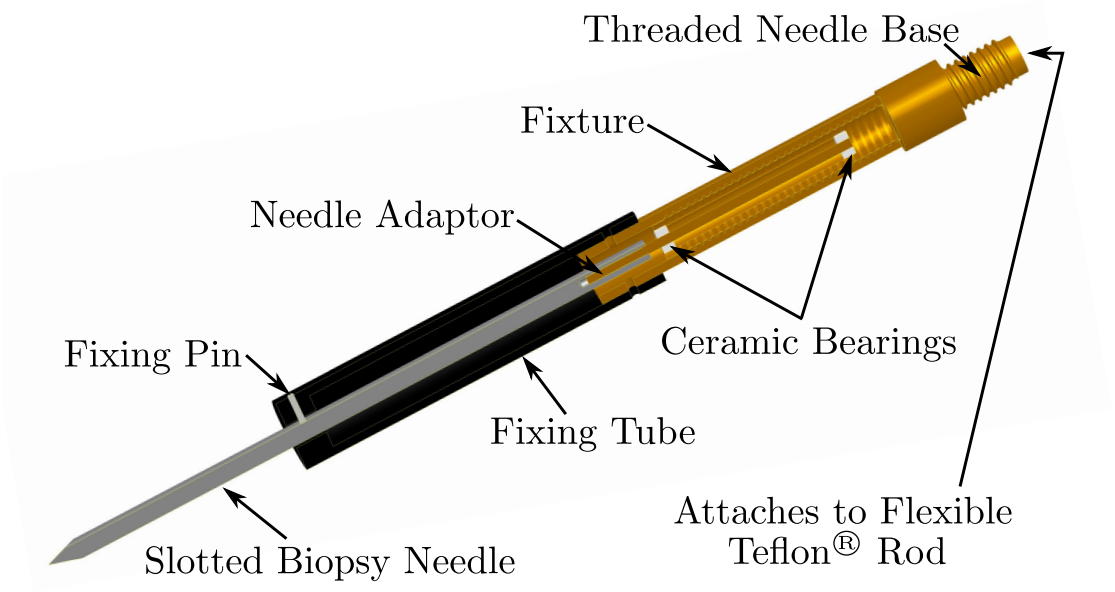

(a) The CAD drawing of the new needle driver

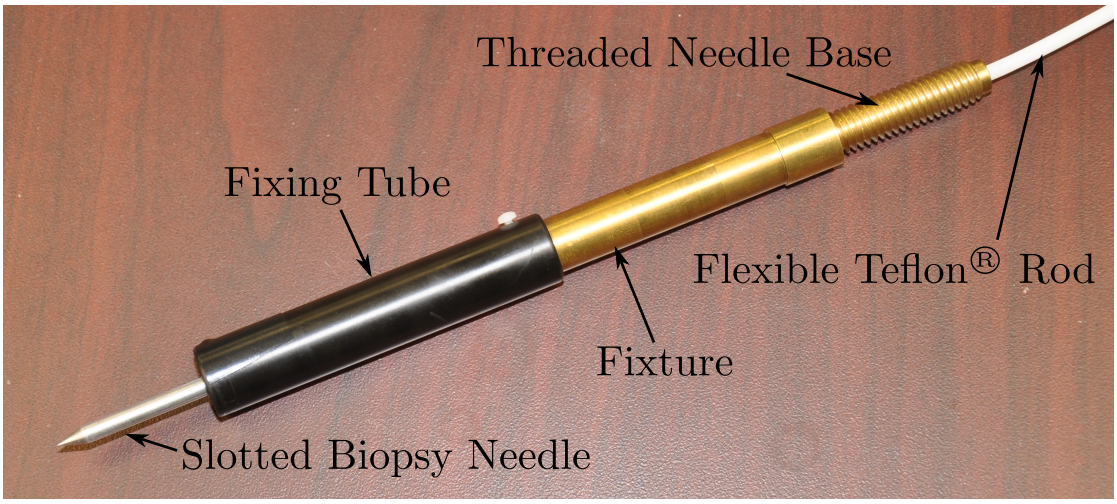

(b) The actual photo of the new needle driver

Figure 2.8: The new needle driver that can advance the needle without rotation [97].

A plastic fixing tube is also included and attached to the outside of the fixture. This fixing tube serves dual purposes: to further ensure the removal of needle rotation without relying on the needle-tissue interaction friction force by press-fitting a pin to mate with the customized slot on the needle, and as a support structure to enhance the rigidity of the needle and minimize its bending effect by supporting the needle and greatly reducing its unsupported length [28]. Furthermore, this new design of the needle driver mechanism allows the use of needles of various sizes, since the needles would attach to the needle driver by the threaded needle adaptor, as shown in Figure 2.8(a).

As its previous prototype, the new needle driver attaches with its fixture to the MRI-compatible fiber-optic force sensor [71] that is used to sense the needle insertion force and the force sensor is mounted on the mobile platform of the parallel mechanism, as shown in Figure 2.7.

2.4.3 X-Y Stage of the Slave Robot

The newly implemented X-Y stage extends the workspace of the slave robot by enabling it to move in the vertical plane (both horizontally and vertically). It can also compensate for the ensuing offsets of the mobile platform in x_b and y_b directions as the needle orientation is adjusted by manipulating the parallel mechanism, which is later shown in Section 2.6.

The X-Y stage, as shown in Figure 2.7, is the subsystem behind the base platform and holds the parallel mechanism. It implements two independent DOFs using two linear guide systems purchased from igus® (DryLin® WK-10-80-20-01-450 and WK-

10-80-10-01-250). Each of the linear guide system is actuated with a cable cylinder, which can provide larger strokes in a given limited space, such as inside of the MRI bore. Both cylinders are of the nonmagnetic version of the CC07 series cable cylinders from Tolomatic, Inc. Along the x_b direction the cable cylinder with $228.6\,\mathrm{mm}$ ($9"$) stroke (Tolomatic 10760032 SK9) is used, and its position feedback is obtained from a sensing membrane (spectrasymbol, TSP-L-0300-103-1%-RH) that attaches to the robot base and can measure up to $300\,\mathrm{mm}$; along the y_b direction, the cable cylinder with $101.6\,\mathrm{mm}$ ($4"$) stroke (Tolomatic 10760032 SK4) is used, and its position information is provided by another sensing membrane (spectrasymbol, TSP-L-0150-103-1%-RH) that can measure up to $150\,\mathrm{mm}$.

With such design and implementation, the parallel mechanism can be moved from the base in the horizontal (x_b) and vertical (y_b) directions. Hence, before performing needle insertion with the needle driver mechanism, the biopsy needle can be positioned coarsely at the appropriate location prior to engaging the parallel mechanism. This is followed by a fine repositioning after manipulating the parallel mechanism to adjust the needle orientation.

2.5 MRI-Compatibility Evaluation of the Slave Robot

To verify the MRI-compatibility of the slave robot implemented in Section 2.4, two MRI tests have been performed. Both tests were conducted using a Siemens $3\,\mathrm{T}$ Tim Trio MR scanner (Siemens Medical Solutions; Malvern, PA) and the experimental setup was shown in Figure 2.9.

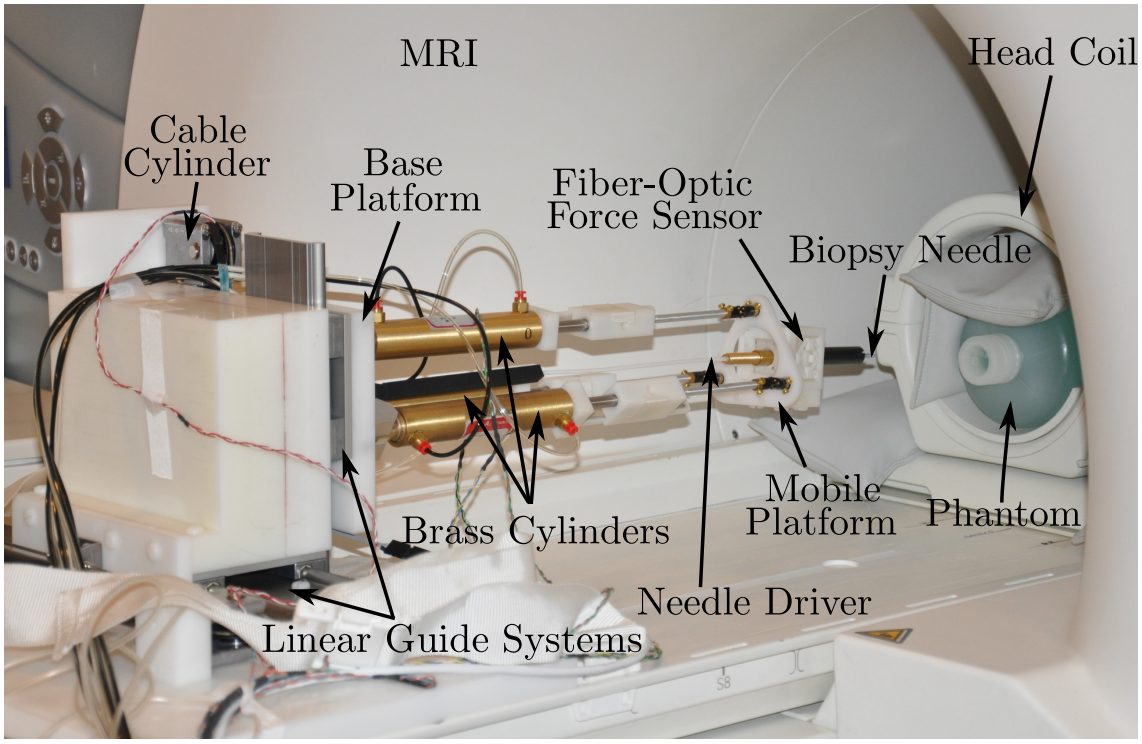

Figure 2.9: Experimental setup for the MRI-compatibility evaluation of the slave robot

In the first test, the phantom imaged was a standard cylindrical bottle, and the imaging sequence used was a gradient echo acquisition with $T_{\mathrm{E}}/T_{\mathrm{R}} = 1.63/354.24\,\mathrm{ms}$, flip angle $= 20^{\circ}$, bandwidth $= 870\,\mathrm{Hz/pixel}$, FoV $= 160 \times 160\,\mathrm{mm}$, matrix $= 128 \times 128$, and slice thickness $= 3\,\mathrm{mm}$. This first test was to verify the MRI-compatibility of the slave robot at resting state and the influence of the pneumatic actuation on the quality of the MR images. The phantom used in the second test was a homemade phantom, which was made of a mixture of $200\,\mathrm{ml}$ boiling water and $7\,\mathrm{g}$ gelatin powder (Knox gelatin, Kraft Foods Global Inc.) with an extra $2\,\mathrm{ml}$ Omniscan™ (gadodiamide – $287\,\mathrm{mg/ml}$) (GE Healthcare; Waukesha, WI) to increase the T_1-weighted signal intensity. The imaging sequence used was a gradient echo acquisition with $T_{\mathrm{E}}/T_{\mathrm{R}} = 1.81/388.8\,\mathrm{ms}$, flip

angle $= 20^{\circ}$, bandwidth $= 870\,\mathrm{Hz/pixel}$, FoV $= 120 \times 120\,\mathrm{mm}$, matrix $= 128 \times 128$, and slice thickness $= 3\,\mathrm{mm}$. The influence of the piezo motor actuation on the MR image quality was studied in this second test. The MR images acquired are shown in Figure 2.10.

The first image of the standard cylindrical bottle phantom was acquired while the slave robot was still outside of the MRI room and is shown in Figure 2.10(a), which is used as the ground truth in the first test. Then, the second MR image, as shown in Figure 2.10(b), was taken when the slave robot was placed inside the MRI bore but without any actuation. Figure 2.10(c) was obtained when the three brass cylinders of the parallel mechanism were actuated to repeat a predefined motion pattern, while Figure 2.10(d) and Figure 2.10(e) were taken when the slave robot was actuated moving back and forth along the direction of x_b and y_b, respectively. Figure 2.10(f) shows the image of the gelatin phantom under the second imaging sequence when the robot was put inside the MRI bore but without any actuation. Figure 2.10(g) was taken when the piezo motor was actuated to advance the needle towards the phantom, and Figure 2.10(h) was obtained when the needle was inserted into the phantom with piezo motor actuation. All images can be clearly depicted with no visually detectable artifact.

To further quantify the effect of the slave robot on the MR image quality, SNR was calculated using the definition of the ratio of the mean pixel value of the signal to the standard deviation of the pixel value of the background noise. All computations were performed on the original DICOM images and the ROIs used for this calculation were indicated on the images with rectangles as shown in Figure 2.10, and the calculated SNRs are summarized in Table 2.2.

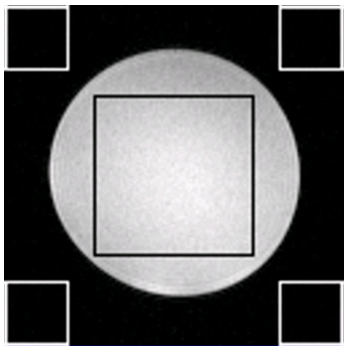

(a) Ground truth image of the first test without robot

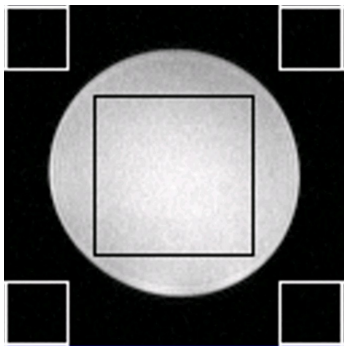

(b) Image of the first test with unactuated robot

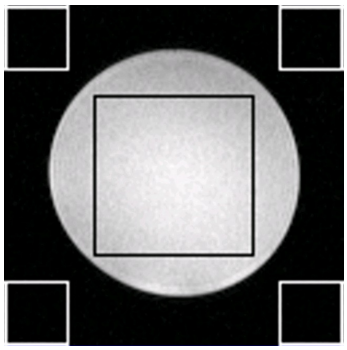

(c) Image of the first test with parallel mechanism actuated

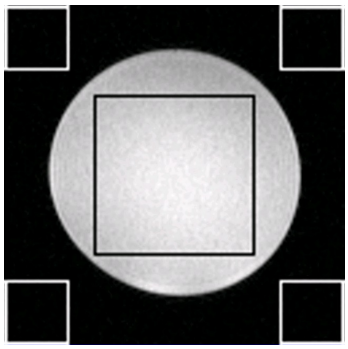

(d) Image of the first test with horizontal cable cylinder actuated

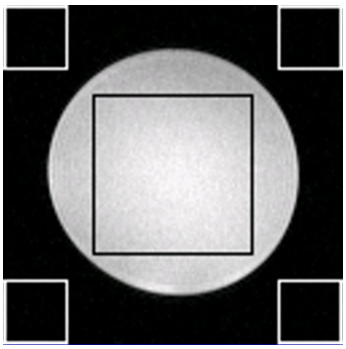

(e) Image of the first test with vertical cable cylinder actuated

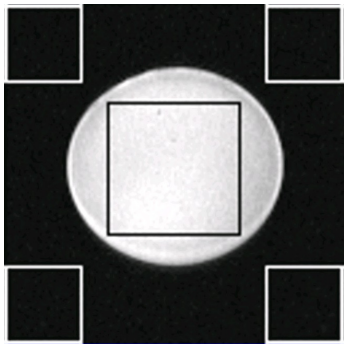

(f) Image of the second test with unactuated robot

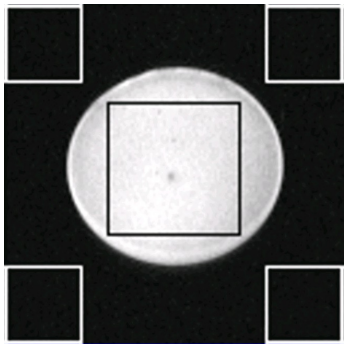

(g) Image of the second test with piezo motor actuated and advancing the needle towards the phantom

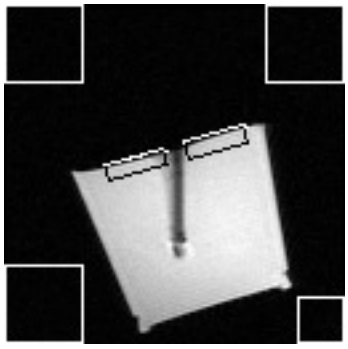

(h) Image of the second test with needle inserted into the phantom and piezo motor actuated

Figure 2.10: MR images of the two MRI tests. (a)–(e) are the images for the first test while (f)–(h) are the images for the second test. The rectangles indicate the ROIs used to calculate the SNR for each image [97].

Table 2.2: SNRs of the MR images with the slave robot

(a) SNRs of the MR images of the first test

Experimental Setup	SNR Values
Ground truth without robot presence	78.58
With robot but without any actuation	73.91
With pneumatic actuation of the parallel mechanism	76.03
With pneumatic actuation of the horizontal cable cylinder	77.00
With pneumatic actuation of the vertical cable cylinder	74.65

(b) SNRs of the MR images of the second test

Experimental Setup	SNR Values
With robot but without any actuation	75.97
With piezo motor actuated advancing the needle towards the phantom	77.48
With piezo motor actuated and the needle inserted into the phantom	71.27

The SNR values listed in Table 2.2(a) show a small SNR loss when the robot was placed inside the MRI bore. This could be attributed to the nonmagnetic metal parts used to implement this slave robot and would not be an issue since the image still maintained a high SNR with no visually detectable artifact or distortion. When the slave robot was actuated pneumatically, the SNR values varied by very small amounts and that could be attributed to the false signal generated by the metal parts of the slave robot. In the second test when the robot was actuated with piezo motor, a slight SNR increase was also observed as in the case of pneumatic actuation, as shown in Table 2.2(b). The resulting images were still of good quality with high SNRs.

Again, it is necessary to point out that SNR values are not comparable between

scans of different imaging parameters or on different subjects. In this evaluation experiment, the T_1 constant of the standard cylinder bottle phantom and the homemade gelatin phantom are different due to their different solution composition. Differences also exist in the voxel size as well as the scanning parameters of the two imaging sequences. Therefore, the SNR values are not comparable between the first and the second test, though the resulted numbers are quite close. Also notice that the ROIs of the signal used for computing the SNR of Figure 2.10(h) is different from those used in the SNR computation of Figure 2.10(f) and Figure 2.10(g). This is primarily due to the different choice of the image plane and its relative position with respect to the imaging subject (gelatin phantom only): the imaging plane used to take Figure 2.10(f) and Figure 2.10(g) is at the edge of the phantom to monitor the contact of the needle with the phantom and only partial volume has been imaged. Hence, the ROIs of the signal for Figure 2.10(h) is chosen at the edge of the phantom accordingly avoiding the needle and comparable SNR value as those for Figure 2.10(f) and Figure 2.10(g) is obtained.

The acquired MR images and SNR analysis show that the slave robot does not induce image artifact or distortion that can cause significant degradation in the image quality. Hence, the slave robot can be safely operated inside the scanner with only minimal influence on SNR.

2.6 Kinematic Analysis of the Slave Robot

The design and implementation of the slave robot has been presented in the previous sections, and the MRI-compatibility evaluations done in Section 2.5 has verified that the

robot can be safely operated inside the MRI bore and perform breast biopsy under continuous MR imaging guidance. In this section, the kinematics of the slave robot, including both inverse and forward kinematics, will be studied in detail, which would help understand its kinematic characteristics, workspace, and method of manipulation.

As described in Section 2.4, the slave robot consists of three subsystems, i.e., the X-Y stage, the needle driver, and the parallel mechanism. The X-Y stage moves the parallel mechanism in two orthogonal directions in a decoupled manner, while the needle driver always advances the needle in perpendicular to the mobile platform of the parallel mechanism, and hence, is relatively easy to describe kinematically. On the contrary, the parallel mechanism changes the orientation and translation of its mobile platform relative to the base by changing the lengths of the three brass cylinders, which is not intuitive and will be the focus of this section. The kinematic analysis of the three-link parallel mechanism has also been studied in the literatures [75, 99, 100], and a different approach using screw theory has been adopted in this section. The dynamic analysis of such platform is available in [101].

To reduce the total number of geometric parameters and simplify the derivation, the coordinates of the parallel mechanism have been defined as shown in Figure 2.2. The base frame F^b ($o_b x_b y_b z_b$) that attaches to the base platform is defined to have its $o_b x_b y_b$ plane coincide with the plane determined by the three revolute joints R_1, R_2, and R_3. The origin o_b lies at the center of the three joints with the y_b-axis pointing to R_1 while its z_b-axis pointing towards the mobile platform. Similarly, the mobile frame F^m ($o_m x_m y_m z_m$) that attaches to the mobile platform is defined to have its $o_m x_m y_m$ plane coincide with the plane determined by the three spherical joints S_1, S_2, and S_3. The origin o_m lies at

the center of the three joints with the y_m-axis pointing to S_1 while its z_m-axis pointing outwards of the parallel mechanism. The radii of the circles where the revolute joints lie on the base platform and the spherical joints lie on the mobile platform are denoted by R and r, respectively. L_1, L_2, and L_3 are used to denote the lengths of the links of the parallel mechanism.

2.6.1 Inverse Kinematics of the Parallel Mechanism

The inverse kinematics is to solve the actuated link variables, i.e., L_1, L_2, and L_3, given the spatial orientation and position of the end effector, that is, the mobile platform. To derive the inverse kinematics of the parallel mechanism using screw theory, each of the three extensible links will be treated as an independent 2-DOF serial manipulator with one revolute joint and one prismatic joint. Then, the homogeneous coordinates of the prismatic joint tips, which are the spherical joints S_1, S_2, and S_3, can be computed using forward kinematic derivation of those simple 2-DOF manipulators. Those coordinates can also be computed using homogeneous transformation given the spatial orientation and position of the mobile platform, on which those spherical joints are physically fixed with known geometric relation. By equating these three points' corresponding coordinates that are computed in two different ways, the mathematical relation between the actuating link variables and the spatial orientation and position of the end effector can be acquired, and hence the inverse kinematics can be solved.

Under the predefined coordinate system, the homogeneous coordinates of the revolute joints R_i^b and those of the spherical joints S_i^m ($i = 1, 2, 3$) in their respective frames,

F^b and F^m, can be written as:

$$R_1^b = \begin{bmatrix} 0 \\ R \\ 0 \\ 1 \end{bmatrix}, \quad R_2^b = \begin{bmatrix} -\frac{\sqrt{3}}{2}R \\ -\frac{1}{2}R \\ 0 \\ 1 \end{bmatrix}, \quad R_3^b = \begin{bmatrix} \frac{\sqrt{3}}{2}R \\ -\frac{1}{2}R \\ 0 \\ 1 \end{bmatrix} \tag{2.1}$$

$$S_1^m = \begin{bmatrix} 0 \\ r \\ 0 \\ 1 \end{bmatrix}, \quad S_2^m = \begin{bmatrix} -\frac{\sqrt{3}}{2}r \\ -\frac{1}{2}r \\ 0 \\ 1 \end{bmatrix}, \quad S_3^m = \begin{bmatrix} \frac{\sqrt{3}}{2}r \\ -\frac{1}{2}r \\ 0 \\ 1 \end{bmatrix} \tag{2.2}$$

The forward kinematics of each link can be computed by first rotating about its revolute joint and then extending its prismatic joint. The initial configuration of each link is chosen such that the three links are aligned with z_b-axes and the prismatic joints are fully retracted to their minimum lengths, and the corresponding transformation between the link tips and the base frame is given by:

$$g_{st,1}(0) = \begin{bmatrix} 1 & 0 & 0 & 0 \\ 0 & 1 & 0 & R \\ 0 & 0 & 1 & 0 \\ 0 & 0 & 0 & 1 \end{bmatrix} \tag{2.3}$$

$$g_{st,2}(0) = \begin{bmatrix} 1 & 0 & 0 & -\frac{\sqrt{3}}{2}R \\ 0 & 1 & 0 & -\frac{1}{2}R \\ 0 & 0 & 1 & 0 \\ 0 & 0 & 0 & 1 \end{bmatrix} \tag{2.4}$$

$$g_{st,3}(0) = \begin{bmatrix} 1 & 0 & 0 & \frac{\sqrt{3}}{2}R \\ 0 & 1 & 0 & -\frac{1}{2}R \\ 0 & 0 & 1 & 0 \\ 0 & 0 & 0 & 1 \end{bmatrix} \tag{2.5}$$

To construct the twists for the revolute joints, the joint rotation axes as well as the coordinates of the corresponding reference points can be written as:

$$\omega_1 = \begin{bmatrix} 1 \\ 0 \\ 0 \end{bmatrix}, \quad \omega_2 = \begin{bmatrix} -\frac{1}{2} \\ \frac{\sqrt{3}}{2} \\ 0 \end{bmatrix}, \quad \omega_3 = \begin{bmatrix} -\frac{1}{2} \\ -\frac{\sqrt{3}}{2} \\ 0 \end{bmatrix} \tag{2.6}$$

$$q_1 = \begin{bmatrix} 0 \\ R \\ 0 \end{bmatrix}, \quad q_2 = \begin{bmatrix} -\frac{\sqrt{3}}{2}R \\ -\frac{1}{2}R \\ 0 \end{bmatrix}, \quad q_3 = \begin{bmatrix} \frac{\sqrt{3}}{2}R \\ -\frac{1}{2}R \\ 0 \end{bmatrix} \tag{2.7}$$

and the twists for the revolute joints can be computed by

$$\xi_{r,i} = [-\omega_i \times q_i,\, \omega_i]^T \tag{2.8}$$

as shown below:

$$\xi_{r,1} = \begin{bmatrix} 0 \\ 0 \\ -R \\ 1 \\ 0 \\ 0 \end{bmatrix}, \quad \xi_{r,2} = \begin{bmatrix} 0 \\ 0 \\ -R \\ -\frac{1}{2} \\ \frac{\sqrt{3}}{2} \\ 0 \end{bmatrix}, \quad \xi_{r,3} = \begin{bmatrix} 0 \\ 0 \\ -R \\ -\frac{1}{2} \\ -\frac{\sqrt{3}}{2} \\ 0 \end{bmatrix} \tag{2.9}$$

All the prismatic joints point in the z_b direction and have the same associated twist:

$$\xi_{p,1} = \xi_{p,2} = \xi_{p,3} = \begin{bmatrix} 0 & 0 & 1 & 0 & 0 & 0 \end{bmatrix}^T \tag{2.10}$$

Hence, the forward kinematic map of link i can be computed using the exponential of twists,

$$g_{st,i} = e^{\hat{\xi}_{r,i}\theta_i} e^{\hat{\xi}_{p,i}l_i} g_{st,i}(0) \tag{2.11}$$

and they are shown as:

$$g_{st,1} = \begin{bmatrix} 1 & 0 & 0 & 0 \\ 0 & c_{\theta_1} & -s_{\theta_1} & R - l_1 s_{\theta_1} \\ 0 & s_{\theta_1} & c_{\theta_1} & l_1 c_{\theta_1} \\ 0 & 0 & 0 & 1 \end{bmatrix} \tag{2.12}$$

$$g_{st,2} = \begin{bmatrix} \frac{1+3c_{\theta_2}}{4} & \frac{\sqrt{3}(-1+c_{\theta_2})}{4} & \frac{\sqrt{3}}{2}s_{\theta_2} & \frac{\sqrt{3}}{2}(-R+l_2 s_{\theta_2}) \\ \frac{\sqrt{3}(-1+c_{\theta_2})}{4} & \frac{3+c_{\theta_2}}{4} & \frac{1}{2}s_{\theta_2} & \frac{1}{2}(-R+l_2 s_{\theta_2}) \\ -\frac{\sqrt{3}}{2}s_{\theta_2} & -\frac{1}{2}s_{\theta_2} & c_{\theta_2} & l_2 c_{\theta_2} \\ 0 & 0 & 0 & 1 \end{bmatrix} \tag{2.13}$$

$$g_{st,3} = \begin{bmatrix} \frac{1+3c_{\theta_3}}{4} & -\frac{\sqrt{3}(-1+c_{\theta_3})}{4} & -\frac{\sqrt{3}}{2}s_{\theta_3} & \frac{\sqrt{3}}{2}(R-l_3 s_{\theta_3}) \\ -\frac{\sqrt{3}(-1+c_{\theta_3})}{4} & \frac{3+c_{\theta_3}}{4} & \frac{1}{2}s_{\theta_3} & \frac{1}{2}(-R+l_3 s_{\theta_3}) \\ \frac{\sqrt{3}}{2}s_{\theta_3} & -\frac{1}{2}s_{\theta_3} & c_{\theta_3} & l_3 c_{\theta_3} \\ 0 & 0 & 0 & 1 \end{bmatrix} \tag{2.14}$$

where θ_i is the rotation variable and l_i is the translation variable for link i, and $s_{\theta_i} = \sin\theta_i$ and $c_{\theta_i} = \cos\theta_i$ (i = 1, 2, 3). The homogeneous coordinates of the end effectors in the base frame, i.e., S_1^b, S_2^b, and S_3^b, correspond to the 4$^{\text{th}}$ column of each forward kinematics

map given by (2.12)-(2.14), and can be written as:

$$S_1^b = \begin{bmatrix} 0 \\ R - l_1 s_{\theta_1} \\ l_1 c_{\theta_1} \\ 1 \end{bmatrix}, \quad S_2^b = \begin{bmatrix} \frac{\sqrt{3}}{2}(-R + l_2 s_{\theta_2}) \\ \frac{1}{2}(-R + l_2 s_{\theta_2}) \\ l_2 c_{\theta_2} \\ 1 \end{bmatrix}, \quad S_3^b = \begin{bmatrix} \frac{\sqrt{3}}{2}(R - l_3 s_{\theta_3}) \\ \frac{1}{2}(-R + l_3 s_{\theta_3}) \\ l_3 c_{\theta_3} \\ 1 \end{bmatrix} \tag{2.15}$$

Now the homogeneous coordinates of the same points in the base frame will be computed with the spatial orientation and position of the mobile platform using homogeneous transformation. The spatial orientation of the mobile platform can be described with Z-Y-Z Euler angles of α, β, γ, and its position can be determined by an arbitrary point on it. For derivation simplicity, this point is chosen to be the origin of frame F^m, o_m, and its homogeneous coordinates is denoted as $(x_{o_m}^b,\, y_{o_m}^b,\, z_{o_m}^b,\, 1)^T$. Hence, the transformation matrix, T_m^b, that maps coordinates from the mobile frame F^m to the base frame F^b, can be derived as:

$$T_m^b = \begin{bmatrix} c_\alpha c_\beta c_\gamma - s_\alpha s_\gamma & -c_\alpha c_\beta s_\gamma - s_\alpha c_\gamma & c_\alpha s_\beta & x_{o_m}^b \\ s_\alpha c_\beta c_\gamma + c_\alpha s_\gamma & -s_\alpha c_\beta s_\gamma + c_\alpha c_\gamma & s_\alpha s_\beta & y_{o_m}^b \\ -s_\beta c_\gamma & s_\beta s_\gamma & c_\beta & z_{o_m}^b \\ 0 & 0 & 0 & 1 \end{bmatrix} \tag{2.16}$$

The homogeneous coordinates of the spherical joints in the base frame now can be computed by applying the transformation matrix to their coordinates in the mobile frame,

$S_i^b = T_m^b S_i^m$, ($i = 1, 2, 3$), as:

$$
\begin{aligned}
S_1^b &= \begin{bmatrix} -r(c_\alpha c_\beta s_\gamma + s_\alpha c_\gamma) + x_{o_m}^b \\ r(-s_\alpha c_\beta s_\gamma + c_\alpha c_\gamma) + y_{o_m}^b \\ r s_\beta s_\gamma + z_{o_m}^b \\ 1 \end{bmatrix} \\
S_2^b &= \begin{bmatrix} -\frac{\sqrt{3}}{2} r(c_\alpha c_\beta c_\gamma - s_\alpha s_\gamma) + \frac{1}{2} r(c_\alpha c_\beta s_\gamma + s_\alpha c_\gamma) + x_{o_m}^b \\ -\frac{\sqrt{3}}{2} r(s_\alpha c_\beta c_\gamma + c_\alpha s_\gamma) + \frac{1}{2} r(s_\alpha c_\beta s_\gamma - c_\alpha c_\gamma) + y_{o_m}^b \\ \frac{\sqrt{3}}{2} r s_\beta c_\gamma - \frac{1}{2} r s_\beta s_\gamma + z_{o_m}^b \\ 1 \end{bmatrix} \\
S_3^b &= \begin{bmatrix} \frac{\sqrt{3}}{2} r(c_\alpha c_\beta c_\gamma - s_\alpha s_\gamma) + \frac{1}{2} r(c_\alpha c_\beta s_\gamma + s_\alpha c_\gamma) + x_{o_m}^b \\ \frac{\sqrt{3}}{2} r(s_\alpha c_\beta c_\gamma + c_\alpha s_\gamma) + \frac{1}{2} r(s_\alpha c_\beta s_\gamma - c_\alpha c_\gamma) + y_{o_m}^b \\ -\frac{\sqrt{3}}{2} r s_\beta c_\gamma - \frac{1}{2} r s_\beta s_\gamma + z_{o_m}^b \\ 1 \end{bmatrix}
\end{aligned}
\tag{2.17}
$$

By comparing the homogeneous coordinates of the spherical joints expressed in both (2.15) and (2.17), nine equations with twelve variables can be acquired. This shows that the mechanism has only three DOFs. These nine equations are:

$$0 = -r(c_\alpha c_\beta s_\gamma + s_\alpha c_\gamma) + x_{o_m}^b \tag{2.18}$$

$$R - l_1 s_{\theta_1} = r(-s_\alpha c_\beta s_\gamma + c_\alpha c_\gamma) + y_{o_m}^b \tag{2.19}$$

$$l_1 c_{\theta_1} = r s_\beta s_\gamma + z_{o_m}^b \tag{2.20}$$

$$\frac{\sqrt{3}}{2}(-R + l_2 s_{\theta_2}) = -\frac{\sqrt{3}}{2} r(c_\alpha c_\beta c_\gamma - s_\alpha s_\gamma) + \frac{1}{2} r(c_\alpha c_\beta s_\gamma + s_\alpha c_\gamma) + x^b_{o_m} \tag{2.21}$$

$$\frac{1}{2}(-R + l_2 s_{\theta_2}) = -\frac{\sqrt{3}}{2} r(s_\alpha c_\beta c_\gamma + c_\alpha s_\gamma) + \frac{1}{2} r(s_\alpha c_\beta s_\gamma - c_\alpha c_\gamma) + y^b_{o_m} \tag{2.22}$$

$$l_2 c_{\theta_2} = \frac{\sqrt{3}}{2} r s_\beta c_\gamma - \frac{1}{2} r s_\beta s_\gamma + z^b_{o_m} \tag{2.23}$$

$$\frac{\sqrt{3}}{2}(R - l_3 s_{\theta_3}) = \frac{\sqrt{3}}{2} r(c_\alpha c_\beta c_\gamma - s_\alpha s_\gamma) + \frac{1}{2} r(c_\alpha c_\beta s_\gamma + s_\alpha c_\gamma) + x^b_{o_m} \tag{2.24}$$

$$\frac{1}{2}(-R + l_3 s_{\theta_3}) = \frac{\sqrt{3}}{2} r(s_\alpha c_\beta c_\gamma + c_\alpha s_\gamma) + \frac{1}{2} r(s_\alpha c_\beta s_\gamma - c_\alpha c_\gamma) + y^b_{o_m} \tag{2.25}$$

$$l_3 c_{\theta_3} = -\frac{\sqrt{3}}{2} r s_\beta c_\gamma - \frac{1}{2} r s_\beta s_\gamma + z^b_{o_m} \tag{2.26}$$

Dividing (2.21) by (2.22) with some manipulation results in:

$$\begin{aligned} &-\frac{\sqrt{3}}{2} r(c_\alpha c_\beta c_\gamma - s_\alpha s_\gamma) + \frac{1}{2} r(c_\alpha c_\beta s_\gamma + s_\alpha c_\gamma) + x^b_{o_m} \\ =&\sqrt{3}\left[-\frac{\sqrt{3}}{2} r(s_\alpha c_\beta c_\gamma + c_\alpha s_\gamma) + \frac{1}{2} r(s_\alpha c_\beta s_\gamma - c_\alpha c_\gamma) + y^b_{o_m}\right] \end{aligned} \tag{2.27}$$

Similarly, dividing (2.24) by (2.25) with some manipulation results in:

$$\begin{aligned} &\frac{\sqrt{3}}{2} r(c_\alpha c_\beta c_\gamma - s_\alpha s_\gamma) + \frac{1}{2} r(c_\alpha c_\beta s_\gamma + s_\alpha c_\gamma) + x^b_{o_m} \\ =&-\sqrt{3}\left[\frac{\sqrt{3}}{2} r(s_\alpha c_\beta c_\gamma + c_\alpha s_\gamma) + \frac{1}{2} r(s_\alpha c_\beta s_\gamma - c_\alpha c_\gamma) + y^b_{o_m}\right] \end{aligned} \tag{2.28}$$

Summing up (2.27) and (2.28) leads to:

$$2x^b_{o_m} + r(c_\alpha c_\beta s_\gamma + s_\alpha c_\gamma) = -\sqrt{3} \cdot \sqrt{3} r(s_\alpha c_\beta c_\gamma + c_\alpha s_\gamma) \tag{2.29}$$

Now substitute (2.18) into the above equation with manipulation and finally get:

$$(c_\beta + 1)s_{\alpha+\gamma} = 0 \tag{2.30}$$

Considering the physical constraints that rule out the case when $\beta = \pi$ and require $-\frac{\pi}{2} < \alpha,\ \gamma < \frac{\pi}{2}$, and the following relation is acquired:

$$\gamma = -\alpha \tag{2.31}$$

Furthermore, from (2.18) and (2.28) $x^b_{o_m}$ and $y^b_{o_m}$ can be solved respectively as:

$$x^b_{o_m} = \frac{r}{2}(1 - c_\beta)s_{2\alpha} \tag{2.32}$$

$$y^b_{o_m} = \frac{r}{2}(1 - c_\beta)c_{2\alpha} \tag{2.33}$$

Thus α, $\beta(-\frac{\pi}{2} < \beta < \frac{\pi}{2})$ and $z^b_{o_m}$ are independent variables and can be used to determine $x^b_{o_m}$, $y^b_{o_m}$, and γ. This further verifies that the mechanism has only three DOFs. However, such parallel mechanism can still move in x_b, y_b, and γ about F^b in a constrained way when it is being actuated, generating motion in the 6-DOF space. When those three independent variables are given, the transformation matrix T^b_m is determined, and $S^b_i(i = 1,\ 2,\ 3)$ can be computed using (2.17). Then the link length $L_i(i = 1,\ 2,\ 3)$ can be calculated with the coordinates given in (2.1) and (2.17) as:

$$L_i = \sqrt{(S^b_{ix} - R^b_{ix})^2 + (S^b_{iy} - R^b_{iy})^2 + (S^b_{iz} - R^b_{iz})^2} \tag{2.34}$$

where subscripts x, y, z are used to denote the x, y, z coordinates of each point.

2.6.2 Forward Kinematics of the Parallel Mechanism

The forward kinematics is to compute the spatial position and orientation of the end effector with known link variables, and is helpful to study the workspace of the manipulator. Unlike the forward kinematics of serial manipulators, the forward kinematics of parallel mechanisms generally do not have simple explicit form, and only numerical solutions are possible. In the case of this parallel mechanism, it is to solve α, β, γ, $x^b_{o_m}$, $y^b_{o_m}$, and $z^b_{o_m}$, with known L_i ($i = 1, 2, 3$). The variable definition in the previous section is adopted in the derivation of the forward kinematics here.

The inverse kinematics derived in the previous section showed that the three-link parallel mechanism has three DOFs. It is also shown in the derivation that complicated relation exists between the independent configuration variables α, β, and $z^b_{o_m}$ and the link lengths L_i ($i = 1, 2, 3$). However, if using intermediate variables θ_i ($i = 1, 2, 3$), which are defined to be the angles subtended between the i^{th} link and the z_b-axis in the previous section, equations with simpler form can be derived. These equations can be used to solve θ_i with numerical methods, and the solution can be applied to determine α, β, and $z^b_{o_m}$.

Let the link variables of the prismatic joints be the actual link lengths, i.e., $l_i = L_i$ ($i = 1, 2, 3$). The coordinates of the spherical joints in the base frame F^m are available

in (2.15) and are rewritten here as:

$$S_1^b = \begin{bmatrix} 0 \\ R - L_1 s_{\theta_1} \\ L_1 c_{\theta_1} \\ 1 \end{bmatrix}, \quad S_2^b = \begin{bmatrix} \frac{\sqrt{3}}{2}(-R + L_2 s_{\theta_2}) \\ \frac{1}{2}(-R + L_2 s_{\theta_2}) \\ L_2 c_{\theta_2} \\ 1 \end{bmatrix}, \quad S_3^b = \begin{bmatrix} \frac{\sqrt{3}}{2}(R - L_3 s_{\theta_3}) \\ \frac{1}{2}(-R + L_3 s_{\theta_3}) \\ L_3 c_{\theta_3} \\ 1 \end{bmatrix} \tag{2.35}$$

Notice that these three points are the vertices of an equilateral triangle with side length of $\sqrt{3}r$, the following three equations can be derived as:

$$\begin{cases} \frac{3}{4}\left(R - L_2 s_{\theta_2}\right)^2 + \left(\frac{3}{2}R - L_1 s_{\theta_1} - \frac{1}{2}L_2 s_{\theta_2}\right)^2 + \left(L_1 c_{\theta_1} - L_2 c_{\theta_2}\right)^2 = 3r^2 \\ \frac{3}{4}\left(R - L_3 s_{\theta_3}\right)^2 + \left(\frac{3}{2}R - L_1 s_{\theta_1} - \frac{1}{2}L_3 s_{\theta_3}\right)^2 + \left(L_1 c_{\theta_1} - L_3 c_{\theta_3}\right)^2 = 3r^2 \\ \frac{3}{4}\left(-2R + L_2 s_{\theta_2} + L_3 s_{\theta_3}\right)^2 + \left(\frac{1}{2}L_2 s_{\theta_2} - \frac{1}{2}L_3 s_{\theta_3}\right)^2 + \left(L_2 c_{\theta_2} - L_3 c_{\theta_3}\right)^2 = 3r^2 \end{cases} \tag{2.36}$$

Equations (2.36) can be simplified as:

$$\begin{cases} 3R^2 + L_1^2 + L_2^2 - 3RL_1 s_{\theta_1} - 3RL_2 s_{\theta_2} + L_1 L_2 s_{\theta_1} s_{\theta_2} - 2L_1 L_2 c_{\theta_1} c_{\theta_2} = 3r^2 \\ 3R^2 + L_1^2 + L_3^2 - 3RL_1 s_{\theta_1} - 3RL_3 s_{\theta_3} + L_1 L_3 s_{\theta_1} s_{\theta_3} - 2L_1 L_3 c_{\theta_1} c_{\theta_3} = 3r^2 \\ 3R^2 + L_2^2 + L_3^2 - 3RL_2 s_{\theta_2} - 3RL_3 s_{\theta_3} + L_2 L_3 s_{\theta_2} s_{\theta_3} - 2L_2 L_3 c_{\theta_2} c_{\theta_3} = 3r^2 \end{cases} \tag{2.37}$$

which can be used to solve θ_i numerically using iterations. Summing up each equations in (2.37) and dividing by 2, then subtracting each equations respectively, the equations

can be rewritten as:

$$\begin{cases} \theta_1^{(k)} = \arcsin \dfrac{f_1(L_1,\, L_2,\, L_3,\, \theta_1^{(k-1)},\, \theta_2^{(k-1)},\, \theta_3^{(k-1)})}{3RL_1} \\ \theta_2^{(k)} = \arcsin \dfrac{f_2(L_1,\, L_2,\, L_3,\, \theta_1^{(k-1)},\, \theta_2^{(k-1)},\, \theta_3^{(k-1)})}{3RL_2} \\ \theta_3^{(k)} = \arcsin \dfrac{f_3(L_1,\, L_2,\, L_3,\, \theta_1^{(k-1)},\, \theta_2^{(k-1)},\, \theta_3^{(k-1)})}{3RL_3} \end{cases} \tag{2.38}$$

where

$$\begin{aligned} f_1(L_1,\, L_2,\, L_3,\, \theta_1,\, \theta_2,\, \theta_3) = \;& \frac{3}{2}(R^2 - r^2) + L_1^2 \\ & + \frac{1}{2}(L_1 L_2 s_{\theta_1} s_{\theta_2} + L_1 L_3 s_{\theta_1} s_{\theta_3} - L_2 L_3 s_{\theta_2} s_{\theta_3}) \\ & - (L_1 L_2 c_{\theta_1} c_{\theta_2} + L_1 L_3 c_{\theta_1} c_{\theta_3} - L_2 L_3 c_{\theta_2} c_{\theta_3}) \\ f_2(L_1,\, L_2,\, L_3,\, \theta_1,\, \theta_2,\, \theta_3) = \;& \frac{3}{2}(R^2 - r^2) + L_2^2 \\ & + \frac{1}{2}(L_1 L_2 s_{\theta_1} s_{\theta_2} + L_2 L_3 s_{\theta_2} s_{\theta_3} - L_1 L_3 s_{\theta_1} s_{\theta_3}) \\ & - (L_1 L_3 c_{\theta_1} c_{\theta_3} + L_2 L_3 c_{\theta_2} c_{\theta_3} - L_1 L_3 c_{\theta_1} c_{\theta_3}) \\ f_3(L_1,\, L_2,\, L_3,\, \theta_1,\, \theta_2,\, \theta_3) = \;& \frac{3}{2}(R^2 - r^2) + L_3^2 \\ & + \frac{1}{2}(L_1 L_3 s_{\theta_1} s_{\theta_3} + L_2 L_3 s_{\theta_2} s_{\theta_3} - L_1 L_2 s_{\theta_1} s_{\theta_2}) \\ & - (L_2 L_3 c_{\theta_2} c_{\theta_3} + L_1 L_3 c_{\theta_1} c_{\theta_3} - L_1 L_2 c_{\theta_1} c_{\theta_2}) \end{aligned} \tag{2.39}$$

Now with the previous configuration of the parallel mechanism known, and by substituting the previous θ_i into (2.39) and (2.38), the current values of $\theta_i^{(k)}$ can be computed with the given L_i. Then, the spatial position of the spherical joints S_i^b can be computed with (2.35), and the spatial position of the center of the mobile platform, o_m^b, is:

$$x_{o_m}^b = \frac{1}{3}\left(\frac{\sqrt{3}}{2} L_2 s_{\theta_2} - \frac{\sqrt{3}}{2} L_3 s_{\theta_3}\right) \tag{2.40}$$

$$y^b_{o_m} = \frac{1}{3}\left(-L_1 s_{\theta_1} + \frac{1}{2}L_2 s_{\theta_2} + \frac{1}{2}L_3 s_{\theta_3}\right) \tag{2.41}$$

$$z^b_{o_m} = \frac{1}{3}\left(L_1 c_{\theta_1} + L_2 c_{\theta_2} + L_3 c_{\theta_3}\right) \tag{2.42}$$

Comparing the z coordinates of S^b_1 and S^b_2 expressed in (2.17) and those in (2.35) leads to:

$$z^b_{o_m} - L_1 c_{\theta_1} = -r s_\beta s_\gamma = r s_\beta s_\alpha \tag{2.43}$$

$$z^b_{o_m} - L_2 c_{\theta_2} = \frac{1}{2} r s_\beta s_\gamma - \frac{\sqrt{3}}{2} r s_\beta c_\gamma = -r s_\beta s_{\alpha+\pi/3} \tag{2.44}$$

Combining with the result of inverse kinematics derivation in (2.32) and (2.33), and hence $\gamma = -\alpha$, and β can be solved under different conditions:

- If $x^b_{o_m} = y^b_{o_m} = 0$, then $1 - c_\beta = 0$; hence, $\beta = 0$, and α and γ are taken as 0;
- If $x^b_{o_m} = 0$ but $y^b_{o_m} \neq 0$, then $s_{2\alpha} = 0$; hence, $\alpha = \frac{\pi}{4} - \frac{\pi}{4}\text{sgn}\left(y^b_{o_m}\right)$, and β can be determined by

$$\beta = \arctan2\left(\frac{L_2 c_{\theta_2} - z^b_{o_m}}{r s_{\alpha+\pi/3}},\, 1 - \frac{2y^b_{o_m}}{r c_{2\alpha}}\right) \tag{2.45}$$

- If $x^b_{o_m} \neq 0$ but $y^b_{o_m} = 0$, then $c_{2\alpha} = 0$; hence, $\alpha = \frac{\pi}{4}\text{sgn}\left(x^b_{o_m}\right)$, and β can be determined by

$$\beta = \arctan2\left(\frac{L_2 c_{\theta_2} - z^b_{o_m}}{r s_{\alpha+\pi/3}},\, 1 - \frac{2x^b_{o_m}}{r s_{2\alpha}}\right) \tag{2.46}$$

- If $x^b_{o_m} \neq 0$ and $y^b_{o_m} \neq 0$, then:

$$\alpha = \frac{1}{2}\text{arctan2}\left(x^b_{o_m},\, y^b_{o_m}\right) \tag{2.47}$$

$$\beta = \begin{cases} \text{arctan2}\left(\dfrac{z^b_{o_m} - L_1 c_{\theta_1}}{r s_\alpha},\, 1 - \dfrac{2x^b_{o_m}}{r s_{2\alpha}}\right), & \text{if } \alpha = -\dfrac{1}{3}\pi \text{ or } \dfrac{2}{3}\pi \\ \text{arctan2}\left(\dfrac{L_2 c_{\theta_2} - z^b_{o_m}}{r s_{\alpha+\pi/3}},\, 1 - \dfrac{2x^b_{o_m}}{r s_{2\alpha}}\right), & \text{if } \alpha = \text{other} \end{cases} \tag{2.48}$$

That completes the forward kinematics derivation for the parallel mechanism.

2.6.3 Kinematics of the Slave Robot

With the coordinate definition and the kinematics result of the parallel mechanism, the kinematics of the slave robot can be studied. Since the X-Y stage is used to hold the parallel mechanism at its base and moves in the $o_b x_b y_b$ plane, the global world frame F^0 ($oxyz$) can be defined to align with frame F^b, with its origin at the lower left corner of the X-Y stage's workspace, as shown in Figure 2.7. The offsets from the origin of frame F^0 to the origin of frame F^b are denoted by X_{offset} and Y_{offset} and correspond to the link variables of the two cable cylinders, respectively. Also, the needle depth or needle length, noted as l_N, can be defined as the distance from the needle tip to the origin of the mobile platform of the parallel mechanism. It is worth noting that the rotational DOF of the needle is intentionally neglected during design, and hence, the slave robot has one redundant DOF between the needle depth l_N, and the mobile platform translation $z^b_{o_m}$. In practice, the needle depth l_N will be specified accordingly when performing insertion tasks.

The desired robot configuration can be described by the needle orientation α and β, needle tip spatial position $(x_N,\, y_N,\, z_N)^T$, and the needle depth l_N. The needle orientation parameters α and β are identical to that of the parallel mechanism since the needle driver is attached to the mobile platform and only advances the needle along z_m direction. Therefore, the needle position can be computed with the same homogeneous transformation matrix, T_m^b, derived as in (2.16). The homogeneous coordinate of the needle tip in the mobile frame F^m is $\mathrm{Tip}^m = (0,\, 0,\, l_N,\, 1)^T$, and after being transformed to the base frame, it can be written as:

$$\mathrm{Tip}^b = T_m^b \mathrm{Tip}^m = \begin{bmatrix} x_{o_m}^b + l_N c_\alpha s_\beta \\ y_{o_m}^b + l_N s_\alpha s_\beta \\ z_{o_m}^b + l_N c_\beta \\ 1 \end{bmatrix} \tag{2.49}$$

and further mapping such coordinate into frame F^0 can lead to:

$$\mathrm{Tip} = \begin{bmatrix} x_{o_m}^b + l_N c_\alpha s_\beta + X_{\text{offset}} \\ y_{o_m}^b + l_N s_\alpha s_\beta + Y_{\text{offset}} \\ z_{o_m}^b + l_N c_\beta \\ 1 \end{bmatrix} = \begin{bmatrix} x_N \\ y_N \\ z_N \\ 1 \end{bmatrix} \tag{2.50}$$

Now the value for $z_{o_m}^b$ is available as $z_N - l_N c_\beta$. Combined with α and β, the inverse kinematics of the parallel mechanism can be used to solve the inverse kinematic of the slave robot by first computing $x_{o_m}^b$ and $y_{o_m}^b$ with (2.32) and (2.33), then getting X_{offset} and

Y_{offset} from (2.50), and S_i^b from (2.17), and finally getting L_i from (2.34).

Similarly, we can solve the forward kinematics of the slave robot using the result derived for the parallel mechanism in Section 2.6.2. With L_i^b given, the intermediate variables θ_i can be computed with (2.38) and (2.39). Then $x_{o_m}^b$, $y_{o_m}^b$, and $z_{o_m}^b$ can be calculated with (2.40)-(2.42), and α and β can be calculated with (2.45)-(2.48). Finally, the spatial position of the needle can be acquired from (2.50).

2.7 Control Scheme of the Slave Robot

The overall control scheme of the slave robot is shown in Figure 2.11.

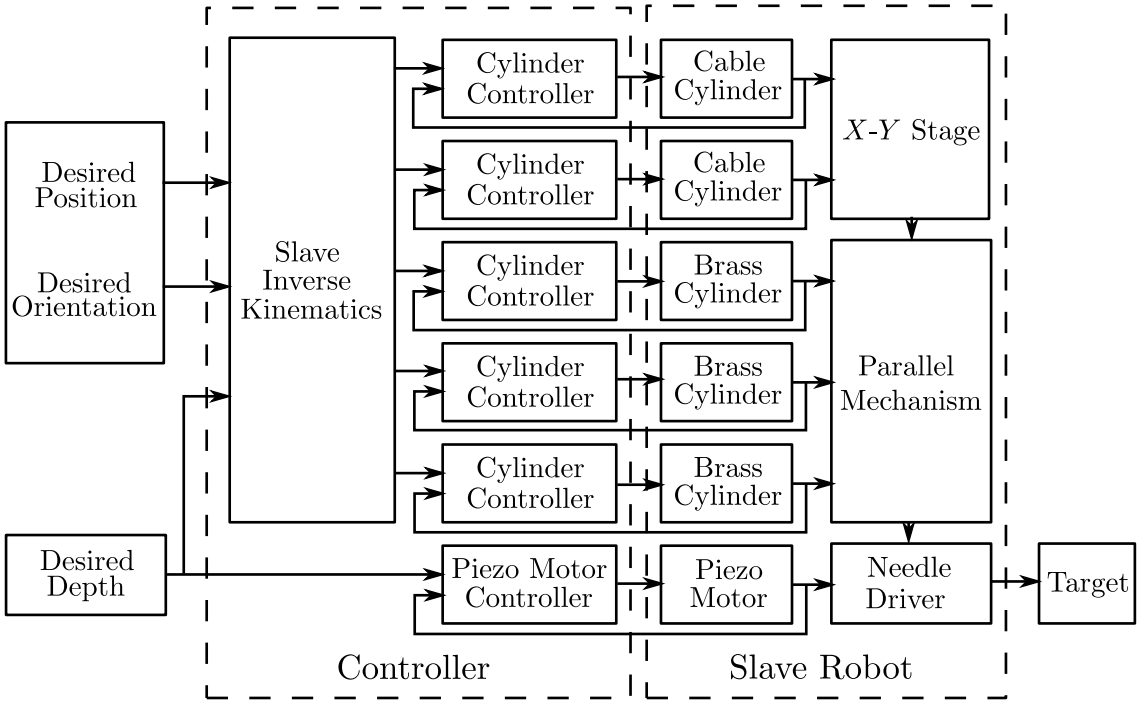

Figure 2.11: Overview of the control scheme of the slave robot

The robot will be commanded by the desired needle tip position along with its orientation and insertion depth. The needle insertion depth is independently controlled with the needle driver using the piezo motor. With given needle tip position, however, the

kinematics derivation in Section 2.6 shows that the needle depth also affects the spatial position and orientation of both the parallel mechanism and the X-Y stage. Hence, it should be fed into the inverse kinematics of the slave robot so that the lengths of the parallel mechanism's three brass cylinders and the X-Y stage's two cable cylinders can be computed. These cylinders are then controlled by their corresponding controllers with closed loop control so that each actuator attains its desired configuration. With appropriate actuation on each link, the slave robot adjusts its configuration and finally reaches the target position. In the envisioned application procedure, the robot will firstly be directed to a desired position at a given orientation but with the needle fully retracted; only after the desired position and orientation of the robot is achieved, the needle will be advanced to the pre-planned depth by actuating the piezo motor only.

2.8 Summary

In this chapter, two iterations of the design and implementation of a slave robot that is to perform breast biopsy needle insertion under continuous MRI guidance has been presented, along with the necessary MRI-compatibility evaluation of each version under various test scenarios. The experimental results show that the robot is MRI-compatible with modest influence on the SNR values and no visually detectable distortion when being actuated. Hence, the implemented slave robot will potentially enable the breast biopsy procedure to be carried out without the need of removing the patient from the MRI bore and avoid multiple needle insertion iterations while also minimizing the sampling errors during biopsy. The kinematics of the robot has been analyzed in detail, and the control

scheme proposed can be used to manipulate the robot to perform the desired needle insertion task. Challenges including space constraints and actuation techniques to maintain high image quality have been overcome in the presented work.

With the currently implemented MRI-compatible slave robot, further work on pneumatic control, design and implementation of a master manipulator, as well as the master-slave teleoperation control can be carried out. In the next chapter, the pneumatic control of the pneumatic cylinders used to actuate the slave robot will be investigated.

Chapter 3

Modeling and Control of Pneumatic Actuation in the Slave Robot

The MRI-compatible slave robot implemented in Chapter 2 has adopted pneumatic actuation and used pneumatic cylinders for five out of its six DOFs. As the primary actuation technique, the position control of pneumatic cylinders has to be studied in detail, since the pneumatic control problem is very challenging due to the inherent nonlinearity introduced by the compressible air. It is further complicated by the introduction of long pneumatic transmission lines that are necessary to use the pneumatic valves placed inside the control room to control the cylinders inside the MRI scanner bore.

In this chapter, the modeling and position control of the MRI-compatible pneumatic system have been studied with proportional pressure valves as well as proportional mass flow rate valves. Started with a brief review on the application, modeling and control of pneumatic systems in Section 3.1, a 1-DOF MRI-compatible pneumatically actuated prototype device is designed and implemented in Section 3.2. This is followed by the modeling of the implemented pneumatic actuation system in Section 3.3. Controllers are then designed in Section 3.4 and their evaluation results as well as the device MRI-compatibility test result using long transmission lines are presented in Section 3.5 and Section 3.6, respectively. Preliminary controller design and evaluation on the actual brass cylinder used in the slave robot using proportional mass flow rate valve is then presented in Section 3.7, and summaries are made in Section 3.8.

3.1 Background of Pneumatic Actuation

The pneumatic actuation is one of the traditional actuation techniques and it uses the compressed air to induce mechanical motion. The common ways of using pneumatics for linear actuation are applying either pneumatic cylinder or pneumatic artificial muscle (PAM). Due to its low-cost, reliability, ease of maintenance, and high-power output, pneumatic actuation has been widely applied in many applications.

Ben-Dov and Salcudean implemented a force-controlled pneumatic actuator using cylinders and customized flapper valves with targeting application of teleoperation masters [102, 103]. Salcudean et al. developed a six DOFs fine-motion device using PAM for applications requiring high position resolution and force control [104]. Adopted the structure of six-link Stewart platform, Girone and Burdea et al. developed the "Rutgers Ankle" using pneumatic cylinders [85–87]. Verrelst et al. developed the second generation PAM and applied it in the implementation of the biped robot, Lucy, as well as an operator assisting manipulator [105]. Zhang et al. designed and implemented a series of climbing robots actuated with pneumatic cylinders for glass-wall cleaning of high-rise buildings [106]. Durbha and Li applied pneumatic actuators in the implementation of a passive bilateral teleoperation system with human force amplification [107]. Narilka and Hosoda built up a musculoskeletal infant robot with PAM to study the mechanism of an infant's locomotive development [108], and Wait and Goldfrab designed and implemented a quadrupedal walking robot with pneumatic cylinders [109].

The pneumatic actuation requires complicated control techniques, due to the compressible nature of air that results in nonlinear dynamic response, and sophisticated sens-

ing and valve mechanisms are needed for accurate and repeatable positioning [110]. To take advantage of pneumatic actuation in more applications, the challenging pneumatic control has been studied in detail on the pneumatic system modeling as well as its control techniques.

The model for the pneumatic system is highly nonlinear as a result of the air compressibility and the nonlinear airflow. Richer and Hurmuzlu developed a detailed mathematical model based on the principle of physics and the model parameters were identified experimentally [111]. Barth et al. proposed to use the state-space averaging approach to model a pulse-width modulation (PWM)-based pneumatic system [112]. Such method provided the analytic machinery to remove the discontinuities associated with switching so that standard nonlinear control design techniques could be applied. Zhao et al. presented the method of using orthogonal polynomials for pneumatic system identification [113]. It was to avoid the commonly used pseudo-random binary sequences that could potentially damage the pneumatic system. By modeling the main internal mechatronic devices, Sorli et al. formulated a nonlinear dynamic model of a pneumatic proportional pressure valve so that both the time-domain and the frequency-domain dynamic behavior of the valve can be simulated [114]. Lu et al. studied a pneumatic contstant pressure system and established a complete dynamic model, which was used in a zero gravity simulation [115].

Substantial work has also been done to investigate the control techniques for the pneumatic systems. Using an adaptive approach, Bobrow and Jabbari studied the force and position control for a pneumatic cylinder [116], and McDonell and Bobrow studied the tracking control of a pneumatic cylinder that was to be applied in an air powered

robot [117]. Hamiti et al. presented a double-loop control scheme for pneumatic servo systems [118]. It used analog proportional (P) control for the inner loop to stabilize the system and digital proportional integral (PI) control for the outer loop to specify whole system characteristics. The integral gain of the outer loop controller could also be decreased to eliminate the limit cycles due to stick-slip friction. Brun et al. applied some linear and nonlinear control laws on an electropneumatic positioning system and compared the positioning and tracking performance in [119]. To address the pneumatic control problem for systems with connection port restriction, modified feedback linearization method was proposed by Bigras et al. to work with the singularity observed in a regular feedback linearization controller [120]. With friction compensation, Ning and Bone used PVA / PV control and achieved high steady-state positioning accuracy for a pneumatic cylinder [121]. To enhance the dynamic performance of McKibben PAM, Davis et al. showed that the bandwidth limit could be greatly increased by reducing dead volume in the pneumatic systems and ensuring effective air flow rate [122]. By taking advantages of the natural compliance of pneumatic actuators, Zhu and Barth developed an impedance controller for a pneumatic actuator for contact tasks but without the need to use a load cell [123].

To address the uncertainties in the complicated highly nonlinear pneumatic system, sliding mode control (SMC) technique has been adopted in multiple applications. Based on the developed model in [111], Richer and Hurmuzlu developed two high performance pneumatic force controllers using SMC theory to account for the modeling error of pneumatics [124]. Lilly and Quesada developed a trajectory tracking controller for a planar arm actuated with PAM groups [125]. Multiple-input sliding mode tech-

nique was used to account for parameter variation of the PAM as well as the mass change of the manipulator arm. Along with friction compensation, Zhao et al. developed a two-layer sliding mode electro-pneumatic synchro position system with feedback linearization and achieved accurate and robust performance under varying external force [126]. Van Damme et al. applied SMC technique on a 2-DOF planar pneumatic manipulator after feedback linearization to account for the model approximation error [127].

Attempts have also been made to reduce the cost of the pneumatic system, by replacing the expensive pressure sensors with nonlinear observers or replacing the servo valves with on / off solenoid valves. Based on the work in [128] that studied the role of pressure sensors in pneumatic servo control, Gulati and Barth developed a Lyapunov-based pressure observer [129]. That observer was then used to develop a robust controller [130], and the improved robust controller with globally stable load-independent pressure observer was presented in [131]. With on / off solenoid valves, van Varseveld and Bone developed a novel PWM valve pulsing algorithm and used proportional integral derivative (PID) control with added friction compensation and position feed-forward to achieve on a pneumatic system comparable overall performance to those using servo valves [132]. Chen et al. developed a hybrid fuzzy controller for an Arm-Exoskeleton using on / off valves and achieved precise force-feedback control [133]. Le et al. proposed to use a predictive hybrid control law to implement a pneumatic teleoperation system using on / off valves [134]. Comparison study showed better tracking and dynamic performance with this control approach than that with PWM control [135];

The aforementioned research work focuses on the nonlinearity of the airflow with either the traditional proportional mass flow rate valve or the on / off solenoid valves, or on

the nonlinearity of the pressure dynamics in the actuator chambers. Their targeting pneumatic systems have valves placed close to the actuators to avoid the influence of transmission line dynamics. The longest transmission lines used is mentioned in [124] as 2 meters, and the performance difference is significant compared to that using transmission lines of 0.5 meters. Also, some of the controllers aimed at force control, and the complicated friction force on the cylinder piston is hence neglected. To develop a MRI-compatible pneumatic actuation system for the MRI-compatible slave robot developed in Chapter 2, the parts intended to be used inside the MRI bore have to be chosen to be made of MRI-safe materials with MRI-compatible actuation, and the non-MRI-compatible parts have to be placed outside of the MRI room inside the control room. Since the commercially available pressure sensors as well as the proportional valves are not MRI-compatible, they have to be placed inside the MRI control room and are distant away from the pneumatic cylinders located inside the MRI bore. Hence, long pneumatic transmission lines up to 9 meters are unavoidable. The presence of such long transmission lines can significantly affect the system performance, by slowing down the pressure response from the valve output ports to the corresponding cylinder chambers. This is partially because it takes a non-negligible amount of time for the pressure waves to travel from one side of the transmission line to the other, and partially because the non-negligible volume of the transmission lines along with the limited mass flow rate delivery capability of the compressed air supply lead to a non-negligible pressure build-up time. Also, the material limitation requires as many as possible parts of the pneumatic device be built with high-strength polymer material. However, due to the inherent material characteristics of polymers, non-uniform (position dependent) friction with static friction significantly

higher than dynamic friction, is present in the device implemented. This makes precise position control extremely challenging.

3.2 Design and Development of the 1-DOF MRI-Compatible Pneumatically Actuated Prototype Device

To evaluate the feasibility of MRI-compatible pneumatic actuation inside the MRI environment, a 1-DOF pneumatically actuated prototype device has been built with MRI-compatible materials and parts, as shown in the top image of Figure 3.1.

As mentioned previously in Section 2.1, this prototype device has to be built with MRI-compatible materials. The key component, i.e., the pneumatic cylinder, is a non-magnetic anti-stiction plastic cylinder (Airpot®, AC-13270-3) with a stroke of $152.4\,\mathrm{mm}$ ($6"$). It is actuated by two pressure valves through two 9 meters long pneumatic transmission lines with $3.175\,\mathrm{mm}$ ($1/8"$) ID. It is made mainly of plastic material with the only exception being its cylinder rod, which is made of brass (Alloy 360) and renders no significant image distortion when tested inside the MRI bore. The brass cylinder rod is attached to the Delrin® made slider block, which is guided by two guiding rods. The two guiding rods are initially made of carbon fiber tubes. Since the two carbon fiber tubes are not rigid enough to provide parallel guidance and induce wedging effect that keeps the slider from moving smoothly along the guiding rods, they are later replaced with two titanium rods, which are tested to be MRI-compatible. To ensure the smooth motion of the slider, the iglide® M250 linear bearings are also used. On the top of the slider sits the optical encoder (US Digital, LIN-500-10-N, EM1-0-500) with a resolution of 500 cycles

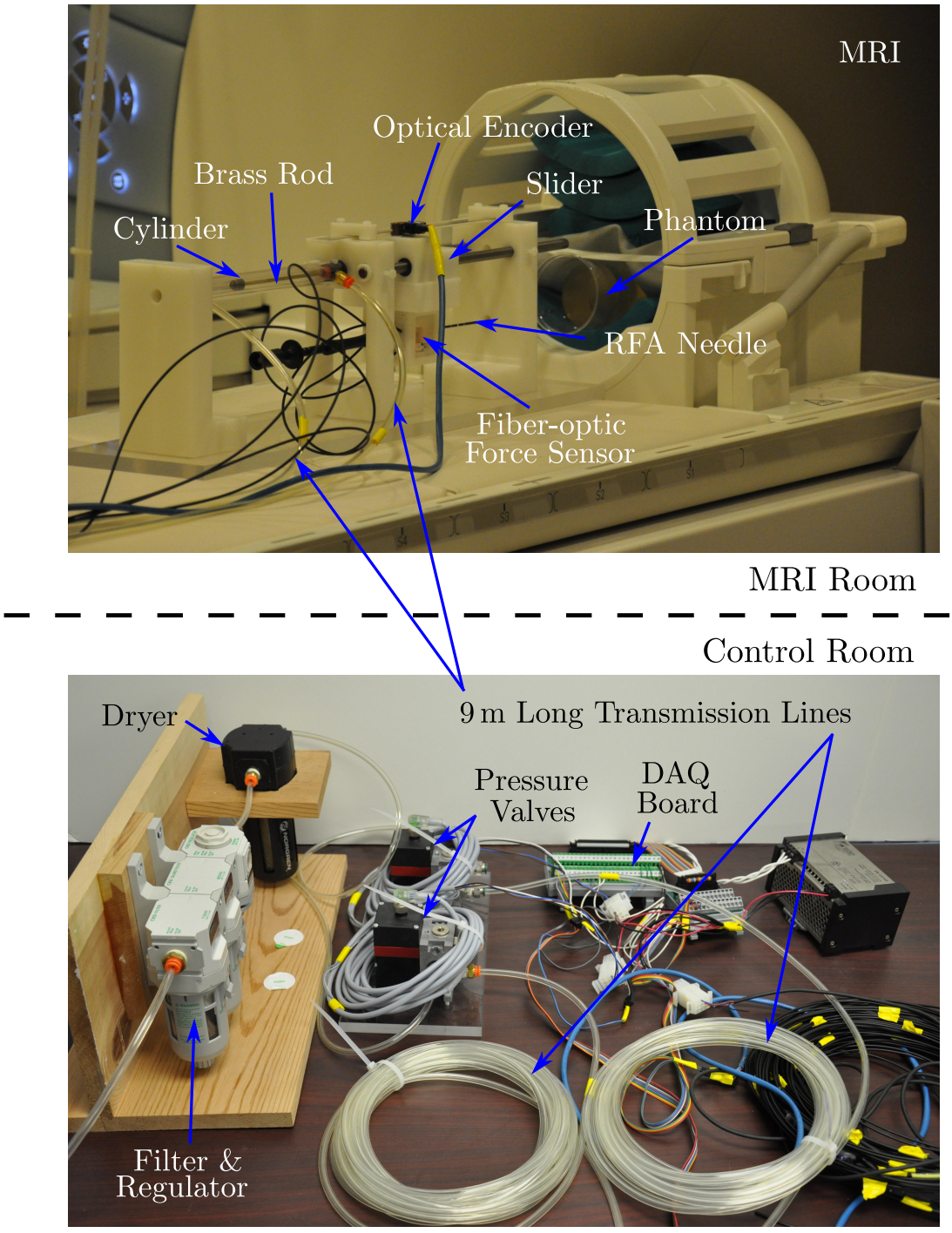

Figure 3.1: MRI-compatible 1-DOF pneumatically actuated prototype device. The top image shows the experimental setup inside the MRI; all equipment that is not MRI-compatible has been placed inside the control room.

per inch (CPI). It is used to indirectly measure the position of the pneumatic cylinder by measuring the relative position of the slider along the guiding rods. The encoder signals are transmitted with a cable driver (US Digital, PC5-H10) through a long shielded cable and the cable passes through the filter panel of the MRI room to avoid picking up RF noise that could degrade the MR image quality. Beneath the slider, a specially designed MRI-compatible 3-DOF fiber-optic force sensor is attached, which is developed by Tan et al. [71] and has been used in the slave robot implementation in Chapter 2. A MRI-compatible RFA needle is attached to the force sensor so that the needle insertion force can be measured inside the MRI bore. All other parts of the prototype device are built with Delrin® to ensure MRI-compatibility of the pneumatic actuation system. The total mass load of the pneumatic system including the cylinder piston-rod, the slider, the force sensor, the optical encoder, and the RFA needle is measured to be $0.675\,\mathrm{kg}$.

The two pressure valves are proportional piezo pressure valves purchased from Hoerbiger™ (Tecno plus, PS120100-080-036) with nominal reaction time of less than $10\,\mathrm{ms}$. They are placed inside the control room along with other non-MRI-compatible components including the air filter & regulator system, the air dryer, and the data acquisition (DAQ) system, as shown in the bottom image of Figure 3.1. All measurements of the pneumatic actuation system are taken through the Sensoray DAQ cards (Model 626) and the controller has been implemented in a Linux PC (Intel® P4 $1.8\,\mathrm{GHz}$ CPU and $512\,\mathrm{MB}$ Memory) with $500\,\mathrm{Hz}$ sampling rate.

3.3 Modeling of the Pneumatic Actuation System

The system modeling of the pneumatic actuation system is essential to the controller design as well as its evaluation. The model of the pneumatic actuation system consists of four subsystems: the valve model, the transmission line model, the piston-load model, and the friction model. These four models are described in detail in the following subsections.

3.3.1 Pneumatic Valve Model

The pneumatic valves used for the 1-DOF prototype device are a pair of proportional pressure valves. By commanding analog voltage signal to the valve, proportional pressure output can be expected at the respective valve output port. This, in a way, avoids the nonlinearity of the orifice mass flow rate of the proportional mass flow rate valves by the inner pressure feedback mechanism of the pressure valves. Another advantage of using pressure valves is that it could eliminate the need of pressure sensors or pressure observers for cylinder chamber pressure information, should the valves be placed close enough to the cylinder or only the static state of the pressure is concerned. By approximating the valve as a first order system based on experimental data, the model is established without disassembling the expensive pressure valve. The transfer function of the pressure valve is thus given by:

$$\frac{P_v(s)}{u(s)} = \frac{0.8s + 50}{s + 50} \tag{3.1}$$

where P_v is the valve output pressure and u is the valve input voltage. This model gives a good approximation of the actual valve step response, as shown in Figure 3.2.

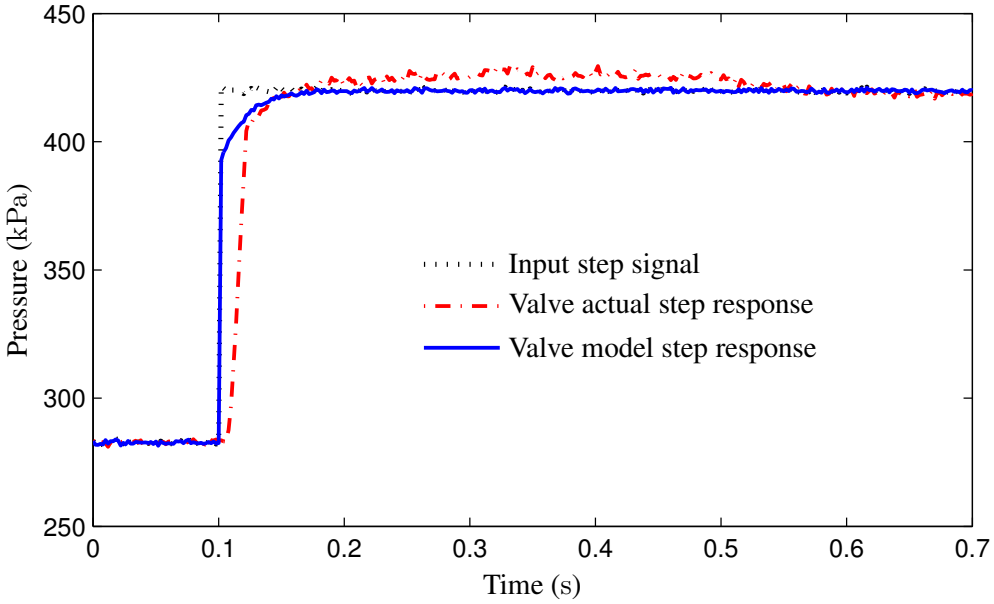

Figure 3.2: Actual and model step response comparison for the proportional pressure valve

3.3.2 Pneumatic Transmission Line Model

As the long pneumatic transmission lines are necessary in this application to achieve MRI-compatible actuation and such long pneumatic transmission lines play a significant role on the pneumatic actuation performance, its dynamic behavior should be studied and its model has to be established. A schematic of the pneumatic transmission line can be described in Figure 3.3, with $P(l,\, t)$ denoting the dynamic air pressure distribution along the lengthwise direction l of the transmission line at time instance t. L_t, A_t are the transmission line parameters with the physical meaning of the total length and effective cross-sectional area of the transmission line. $p(t)$ is the input pressure function at the transmission line inlet from the valve.

Using Newton's second law and the law of conservation of mass, Schuder and Binder first derived the partial differential equations governing the airflow along the trans-

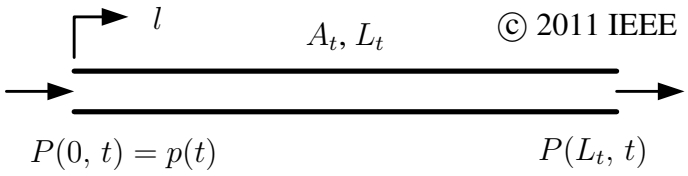

Figure 3.3: Schematic of the pneumatic transmission line. Reprint from [2], © IEEE.

mission line [136], which are written as:

$$\frac{\partial P}{\partial l} = -R_t v - \rho \frac{\partial v}{\partial t} \tag{3.2}$$

$$\frac{\partial v}{\partial l} = -\frac{1}{\rho c^2} \frac{\partial P}{\partial t} \tag{3.3}$$

where v and ρ are the air velocity and density distribution along the transmission line and are functions of both the transmission line position l and the time t; R_t denotes the transmission line resistance, and c is the constant of sound speed.

With appropriate algebraic manipulation, it is shown that both the pressure distribution $P(l, t)$ and the airflow velocity distribution $v(l, t)$ are constrained by a same second-order partial differential equation with different initial values and boundary conditions:

$$\frac{\partial^2 z}{\partial l^2} - \frac{1}{c^2} \frac{\partial^2 z}{\partial t^2} - \frac{R_t}{\rho c^2} \frac{\partial z}{\partial t} = 0 \tag{3.4}$$

where z denotes either the pressure distribution $P(l, t)$ or the airflow velocity distribution $v(l, t)$. The transmission dynamics of the pressurized airflow along the transmission lines can then be obtained by solving this equation given the actual initial values and the boundary conditions.

The equation (3.4), however, is the famous telegraph equation. The general ana-

lytical solution of the telegraph equation is not available despite decades of effort, and only analytical solutions under certain initial and boundary conditions or some numerical solutions have been achieved [137–144]. By studying the physical phenomenon of diffusion with discontinuous movements, Goldstein successfully found two analytical solutions to the telegraph equation under the same zero initial condition [137]. The two solutions correspond to two different boundary conditions: one is with a step boundary condition while the other is with a pulse boundary condition. This is analogous to the basic pressure dynamic response of the transmission line given a step pressure input or an impulse pressure input; however, both solutions are too complicated to evaluate in practice either analytically or numerically, and hence, are only meaningful in theory. Besides the attempts to solve the telegraph equation analytically, numerical algorithms have also been developed, yet none of those solutions available are simple enough to be used for controller design or simulation evaluation purposes [138, 144].

Although extensive work has been done for the solution of the telegraph equation, acquiring such solution alone does not necessarily lead to the dynamic air pressure characterization along the transmission line for three reasons. First of all, the telegraph equation is a derivation of the partial differential equations (3.2) and (3.3), which is based on the assumption that there is no reflection or resonance in the transmission line. This could be justifiable with an open-ended transmission line, but would conceivably lead to incorrect results in an application where the transmission line is connected to a small and closed volume, i.e., the cylinder chamber. Second, the partial differential equations (3.2) and (3.3) also indicate a fixed boundary condition at the end of the transmission line. In practice, however, the transmission line connects to the cylinder chamber, at which the

air flowing through the transmission line accumulates and results in the pressure increase that changes the boundary condition. Finally, the coefficients of the telegraph equation contain the air density ρ, which is a function of both the time t and the location l, due to the pressure variation along the transmission line. This could lead to a higher order partial differential equation or a telegraph equation with varying coefficients that are dependent on the solution itself. Although Aloy et al. attempted to compute a variable coefficient telegraph equation, that coefficient variation was not dependent on the solution [142] and their method cannot be applied here.

Due to the aforementioned challenges and concerns and considering the result derived in [111], the dynamics of the 9 meters transmission line is modeled with a first-order system with a constant time delay, which represents the pressure build-up process at the end of the transmission line and the pressure propagation process along the transmission line, respectively. The model with its estimated parameters based on experimental data is given by:

$$\frac{P_o(s)}{P_i(s)} = \frac{0.25s + 32}{s + 32} e^{-0.0265s} \tag{3.5}$$

where P_o and P_i are the respective input and output pressures. The time delay is determined as the ratio of the transmission line length and the air propagation speed. When using flexible tubing, the effects due to the elasticity of the conduit wall can be account for by estimating the propagation speed based on the effective bulk modulus of the fluid (air in this case) and the tube [145]. For simplicity of approximation, however, the speed of sound is used as the propagation speed, and the time delay is computed as L_t/c. This model closely characterizes the actual transmission line step response, as is shown in

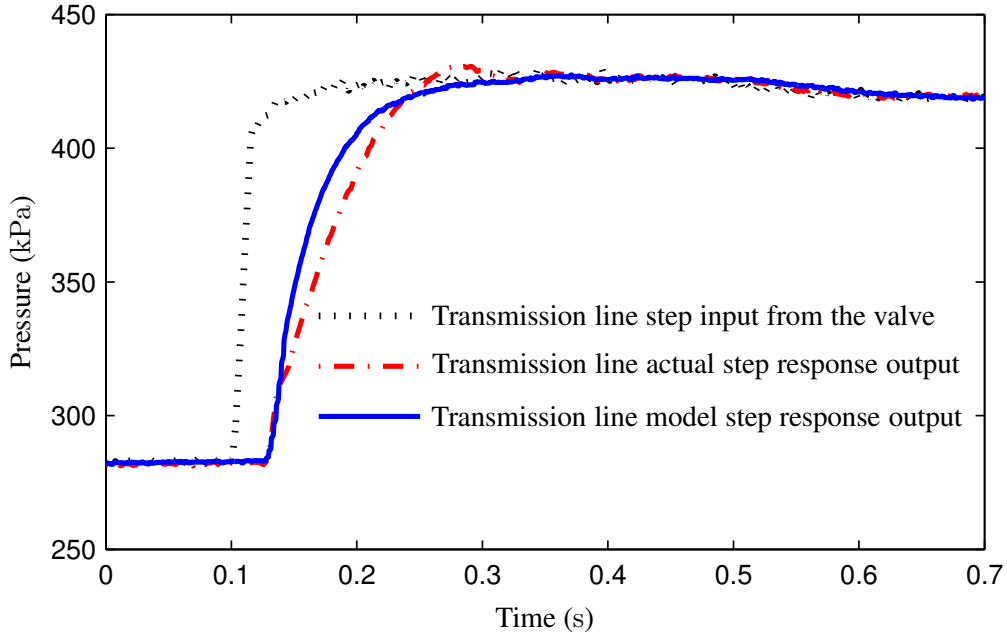

Figure 3.4: Actual and model step response comparison for the 9 meters pneumatic transmission line

Figure 3.4.

3.3.3 Cylinder Piston-Load Model

The mechanical structure of a typical double-acting cylinder is shown in Figure 3.5, and its dynamical model can be written as:

$$M\ddot{x} = P_1 A_1 - P_2 A_2 - P_a A_r + F_L + F_f \tag{3.6}$$

where M is the total mass of the piston-rod, the slider, the force sensor and other loads attached; x is the position of the slider; P_1, A_1 and P_2, A_2 are the pressure and the effective cross-sectional area of each cylinder chamber, respectively; P_a is the atmosphere pressure; A_r is the effective cross-sectional area of the cylinder rod; F_L is the external

force, and F_f is the total frictional force.

Since the proportional pressure valves are selected to control the position of the cylinder, the two chamber pressures P_1 and P_2 can be directly used as the control variables, and the only command input in (3.6) will be the desired cylinder position. Now the problem expression can be simplified by maintaining an average chamber pressure of $275.8\,\mathrm{kPa}$ $(40\,\mathrm{psi})$ at steady state and using the pressure difference as the only control output for this cylinder:

$$P_1 = 275.8 + \Delta P \tag{3.7}$$

$$P_2 = 275.8 - \Delta P \tag{3.8}$$

where ΔP is the pressure difference between the two cylinder chamber pressures. Now the cylinder piston-load dynamic equation can be rewritten as:

$$M\ddot{x} = (A_1 + A_2)\Delta P + (275.8 - P_a)A_r + F_L + F_f \tag{3.9}$$

Note that the term $(275.8 - P_a)A_r$ is a known constant determined by the cross-

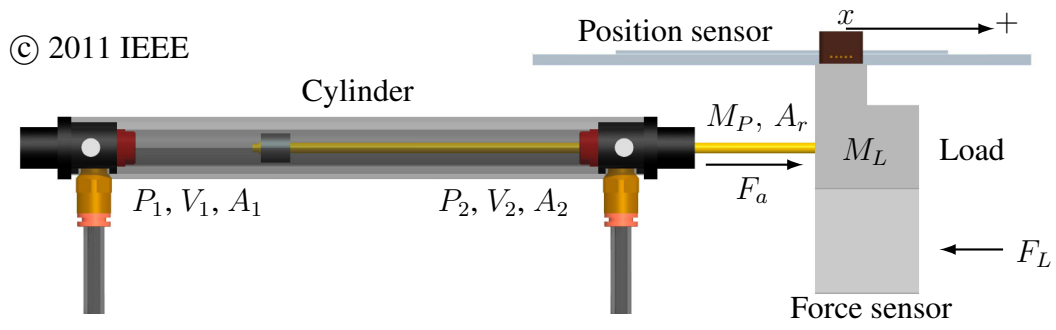

Figure 3.5: Schematic representation of the piston-load subsystem. Reprint from [2], © IEEE.

sectional area of the cylinder rod A_r and the atmosphere pressure P_a, and that the external force F_L can be measured by the force sensor, the model can be further simplified as:

$$M\ddot{x} = (A_1 + A_2)u + F_f \tag{3.10}$$

and $\Delta P = u - u_0$ with $u_0 = \dfrac{(275.8 - P_a)A_r + F_L}{A_1 + A_2}$ is a known offset.

3.3.4 Friction Model

Friction force reflects the interacting behavior of objects in contact with relative motion and can directly affect the system positioning accuracy or even the stability in applications where the friction effect cannot be neglected. Hence, researchers have studied the friction phenomenon in detail, and various friction models have been established, along with numerous control techniques based on friction model compensation.

Walrath investigated the dynamic friction characteristics of a gimbal bearing and created a friction model that could adjust its parameters adaptively and predict the real-time friction torque [146]. Armstrong-Hélouvry applied dimensional and perturbation analysis to study the stick-slip problem and established an exact model of the nonlinear friction force [147]. Dupont and Bapna presented the result on how the normal force dependant friction force would affect the stability of low-velocity motion [148], and Dupont and Dunlap proposed to include a frictional lag in the negatively-sloped friction velocity curve and eliminated stick-slip by stiffening the system [149]. Generally, friction can be modeled with a combination of seven distinct phenomena, which are named as: static friction (the force required to initiate the motion), coulomb friction (also known as kinetic

friction and is the friction force component independent of velocity), viscous friction (the velocity dependent friction force component), Stribeck friction (the phenomenon that describes the friction variation with respect to velocity change), rising static friction (the static friction component that increases as the dwell time increases), frictional memory (the friction force component that will not change at the instance the velocity changes), and the Dahl effect (also known as the pre-sliding displacement and states that the interacting surface of two objects behaves like a spring before the force exerted in the tangential direction reaches the static force, and exhibits small displacement that is proportional to the exerted force). A detailed discussion on those friction phenomena can be found in [150], and the analysis tools and compensation methods for the automatic control of systems with friction are presented in [151]. Ehrich reviewed several different friction models, based on which adaptive friction compensation controllers were designed for bi-directional low-velocity position tracking systems [152, 153]. With an observer to estimate the Coulomb friction, Friedland and Park presented a method to adaptively compensate the friction in control systems [154]. Dupont compared two experimentally-based dynamic friction models using a linearized stability analysis and achieved steady motion at very low velocities using proportional derivative (PD) control [155]. Using a nonlinear observer based on Dahl model, Kelly et al. proposed a smooth adaptive viscous friction compensator, and its control performance was illustrated on a direct-drive servo motor [156]. Based on dynamic friction model, Lee et al. presented a method to utilize a PD control structure and an adaptive estimation of the friction force to improve the tracking performance of the motion control system [157].

In the application of pneumatic cylinders, because of the need to overcome the

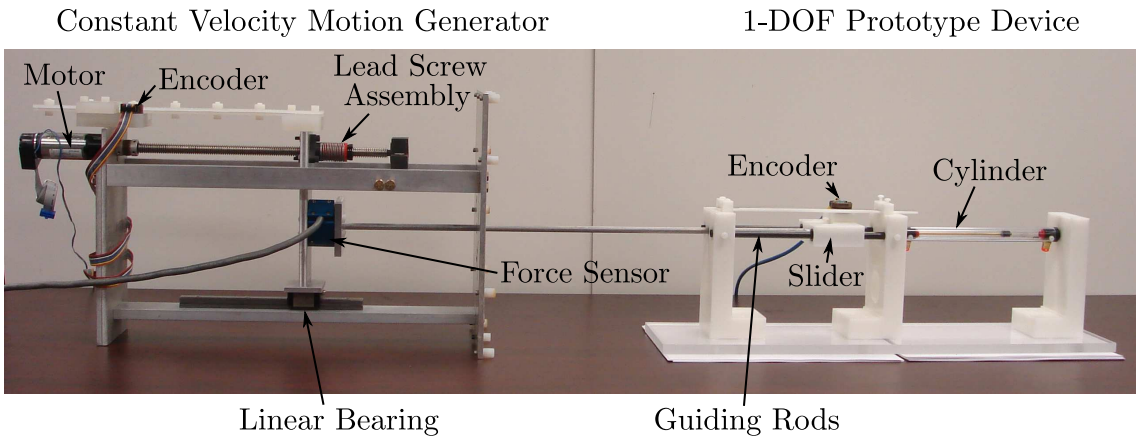

Figure 3.6: Experimental setup for the friction force measurement of the 1-DOF prototype device

friction or breakaway force between the piston seal and the cylinder barrel, erratic initial motion and stick-slip behavior can be resulted, which could greatly affect the system performance at low speed or in stop-start applications [110]. For the 1-DOF prototype device implemented in Section 3.2, the friction force is non-negligible and keeps the device from moving smoothly, and hence is studied and modeled in this subsection. To measure the friction force observed on this device, an experiment has been conducted using a constant velocity motion generating device, developed by Lister et al. [158]. The device and the experimental setup is shown in Figure 3.6.

The constant velocity generating device is attached to the slider of the 1-DOF prototype device via a force sensor, so that the friction force can be collected. Using an electrical motor along with a lead screw assembly and a linear bearing, this device can generate constant velocity motion along the horizontal direction. The velocity control of the device is based on position control; as the commanded velocity increases, the performance of its position controller deteriorates, causing small overshoots and oscillations. Such unstable behavior can be attributed to the friction force on the 1-DOF prototype de-

vice, since friction is known to affect the system stability to some extent. Therefore, only friction force data at 0.254, 0.508, 1.27, and $2.54\,\mathrm{mm/s}$ along both moving directions has been collected, as shown in Figure 3.7.

As observed in Figure 3.7, the friction force increases quickly at one end of the stroke compared to the relatively small friction force at the center part. This is likely due to the misalignment of the guiding rods and its resulting wedging effect. Also worth noting is that the trend of the friction force at different velocities is quite similar, and that the magnitude of the friction force (disregard of its direction) decreases as the velocity increases. This suggests that the static friction exhibited in this 1-DOF prototype device could be significantly higher than that when the device is in motion. This makes the system more likely to be unstable when precise positioning accuracy is desired and hence should be treated with care. To model such friction phenomenon, Stribeck friction has been used to characterize the friction force transient at low velocities continuously. This approach avoids the discontinuity caused by the simple friction combination model that only consists of static friction, coulomb friction, and viscous friction. Limited by the available experimental apparatus to capture other friction phenomena such as Dahl effect, rising static friction, and frictional memory, the following friction model is finally chosen to approximate the observed friction force:

$$F_f = 1.8\mathrm{sgn}(\dot{x}) + 2.5\dot{x} + 0.8e^{-(\dot{x}/0.04)^2}\mathrm{sgn}(\dot{x}) \tag{3.11}$$

The first term uses the signum function $\mathrm{sgn}(\cdot)$ to represent the coulomb friction while the proportional term corresponds to the viscous friction. The exponential term characterizes

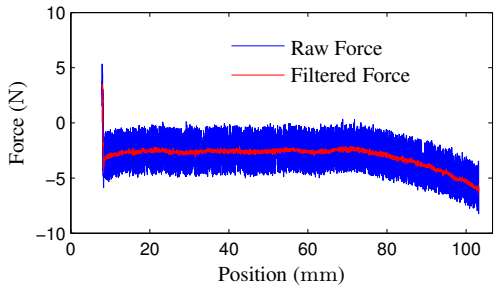

(a) Move from left to right at $0.254\,\mathrm{mm/s}$

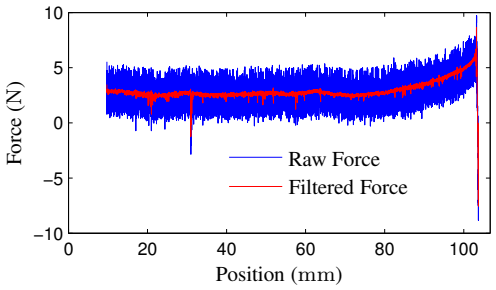

(b) Move from right to left at $0.254\,\mathrm{mm/s}$

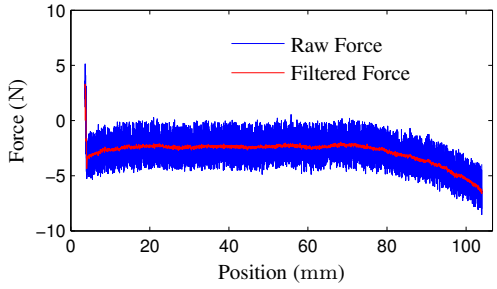

(c) Move from left to right at $0.508\,\mathrm{mm/s}$

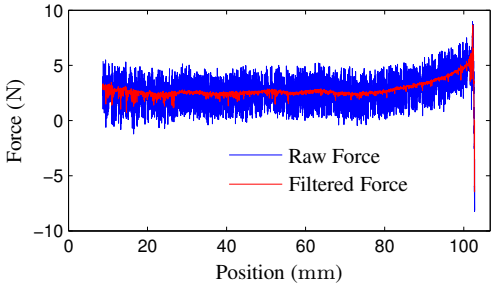

(d) Move from right to left at $0.508\,\mathrm{mm/s}$

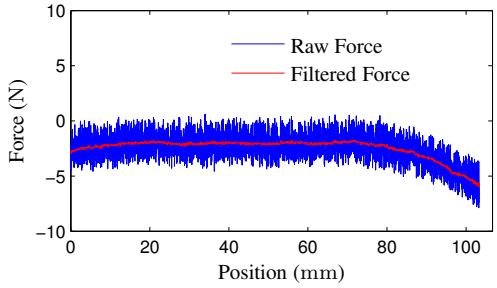

(e) Move from left to right at $1.27\,\mathrm{mm/s}$

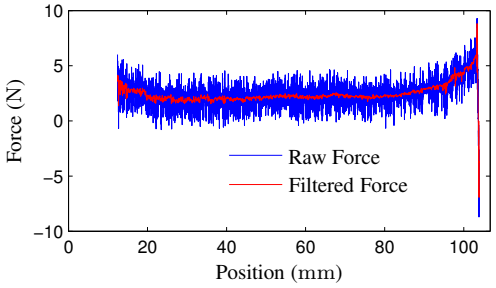

(f) Move from right to left at $1.27\,\mathrm{mm/s}$

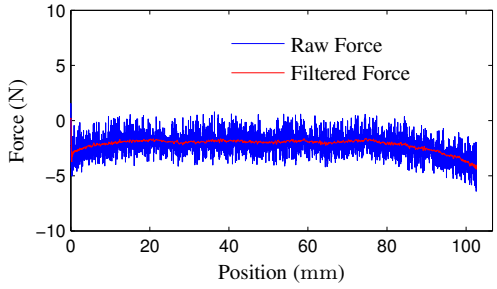

(g) Move from left to right at $2.54\,\mathrm{mm/s}$

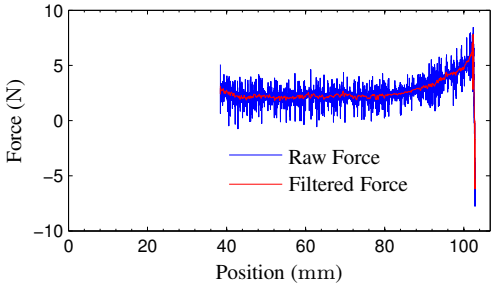

(h) Move from right to left at $2.54\,\mathrm{mm/s}$

Figure 3.7: Measured friction force data for the 1-DOF prototype device

the Stribeck friction and dominates mainly in the low-velocity region. The parameters used in (3.11) are rough estimates and serve primarily as qualitative descriptions. The rationale is that this friction model is intended to capture the structure of the friction force and will be used in simulation to verify the effectiveness of the controllers. Hence, it is not necessarily accurate enough to be used as a feed-forward compensation term. The discrepancy should be either accounted for by the controller robustness or cancelled with an adaptive term.

3.4 Design of the Pneumatic Controller

The controller design of the pneumatic actuation system is based on the pneumatic model developed in Section 3.3. The complete model of the pneumatic system can be described by (3.1), (3.5), and (3.10), and hence is a fourth-order system. Since there is no MRI-compatible pressure sensor that can be placed inside the MRI bore, the cylinder chamber pressure information will be unavailable to the controller. Therefore, it is not feasible to improve the pressure response of the valve-transmission line subsystem using feedback, not to mention the application of complicated control approaches that require full system state information. The velocity information will be deduced from the cylinder position that is measured by the optical encoder and transmitted by the shielded signal cable, and the controller will use both the position and the velocity to compute the valve commanded input, as shown in Figure 3.8. The SMC technique is applied in this section to design the **controller** block shown in the control diagram. The goal is to design controllers that could move the slider slowly, since the targeting application is to insert a needle in a slow and

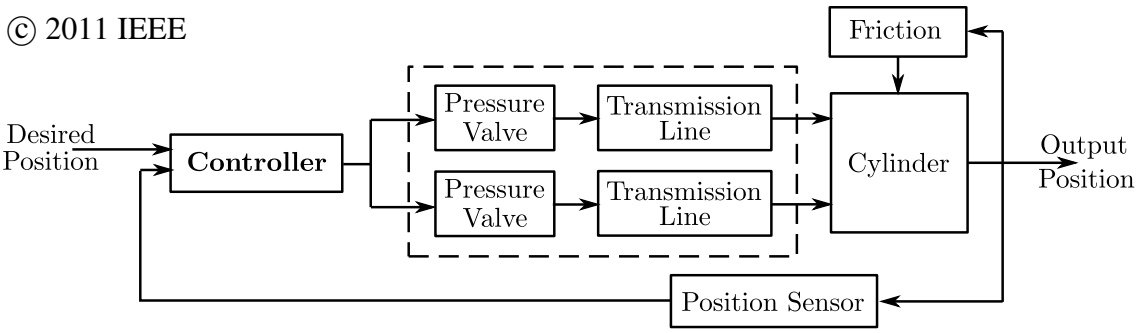

Figure 3.8: Control diagram of the pneumatic system. Reprint from [2], © IEEE.

controlled manner. This mitigates the challenges of using the relatively slow responded valve-transmission line with time delay, and hence, the valve-transmission line dynamics is intentionally neglected and treated as system disturbance, which is to be accounted for by the robustness of the SMC controllers.

The main objective of the controller is to overcome the influence of friction with slow actuators. The friction exhibited in this 1-DOF prototype device is of a complicated form and varies along the guiding rods; hence, it is treated as an uncertain term in the system, and such uncertainty will be tolerated by robust controllers to achieve reasonable performance. The sliding mode control approach, with the advantage of being robust to uncertainties, is adopted accordingly, and is used to design controllers without considering the valve-transmission line dynamics. The omission of the valve-transmission line dynamics reduces the system model to a second-order system, as described by (3.10). This would simplify the controller design process and enable the direct cancellation of the friction term. Attempt has also been made to design adaptive controllers that estimate and cancel the friction force; the designed adaptive controllers, however, are prone to overestimating the friction force due to its spatial variation and would lead to an unstable

system, and hence are abandoned.

The core of a SMC controller implementation is to design a sliding surface that characterizes the desired system dynamics disregard of system uncertainties. Then, the control output can be derived accordingly to drive the system states onto the designed sliding surface and maintain the desired system dynamics on the surface with the presence of system uncertainties. To start the controller design and simplify the control law derivation, the system equilibrium point should be shifted from its desired system states, $(x_d,\ 0)$, to the origin. Take position error $e = x_d - x$ and substitute it into the system model described by (3.10), the system model can be rewritten in the form of state space expression as:

$$\dot{e} = v \tag{3.12}$$

$$\dot{v} = \frac{1}{M}\left[(A_1 + A_2)u + F_f\right] \tag{3.13}$$

and SMC controllers based on this model will be derived in the following subsections.

3.4.1 SMC-I

To achieve a slow system response without overshoot, the sliding surface can be designed as $s = e + av = 0$, and the system dynamics governed by this sliding surface can be described as $\dot{e} = -\frac{1}{a}e$, independent of system uncertainties. By choosing a positive sliding surface parameter, i.e., $a > 0$, the system is asymptotically stable with the equilibrium point at $e = 0$, $\dot{e} = 0$, and the convergence rate of the system can be controlled by the choice of parameter a.

To determine the control law that drives the system states onto the sliding surface and maintains them there, the derivative of s is taken as:

$$\dot{s} = \dot{e} + a\dot{v} = v + \frac{a}{M}\left[(A_1 + A_2)u + F_f\right] \tag{3.14}$$

Note that the friction force F_f, though depending on the position x, velocity v, or even time t, is a physical quantity and is upper bounded. Also note that the target system with appropriate control will be stable, which means the velocity v is upper bounded. Hence, the following inequality holds:

$$\left|\frac{Mv + aF_f}{a(A_1 + A_2)}\right| \leq f(e,\, v), \qquad \forall\,(e,\, v) \in R^2 \tag{3.15}$$

for some know function $f(e,\, v)$. With $V = \frac{1}{2}s^2$ as a Lyapunov function candidate for (3.14), its derivative can be written as:

$$\dot{V} = s\dot{s} = s\left(v + \frac{a}{M}F_f\right) + \frac{a(A_1 + A_2)}{M}su \tag{3.16}$$

$$\leq \frac{a(A_1 + A_2)}{M}|s|f(e,\, v) + \frac{a(A_1 + A_2)}{M}su \tag{3.17}$$

Taking

$$u = -\beta(e,\, v)\mathrm{sgn}(s) \tag{3.18}$$

where $\beta(e,\, v) \geq f(e,\, v) + \beta_0$ and $\beta_0 > 0$, with

$$\mathrm{sgn}(s) = \begin{cases} 1, & s > 0 \\ 0, & s = 0 \\ -1, & s < 0 \end{cases} \tag{3.19}$$

yields

$$\dot{V} \leq \frac{a(A_1 + A_2)}{M}|s|f(e,\, v) - \frac{a(A_1 + A_2)}{M}\left[f(e,\, v) + \beta_0\right] s \cdot \mathrm{sgn}(s) \tag{3.20}$$

$$= -\frac{a(A_1 + A_2)}{M}\beta_0|s| \tag{3.21}$$

Thus, $W = \sqrt{2V} = |s|$ satisfies the differential inequality

$$D^+W \leq -\frac{a(A_1 + A_2)}{M}\beta_0 \tag{3.22}$$

and the comparison lemma shows that

$$W(s(t)) \leq W(s(0)) - \frac{a(A_1 + A_2)}{M}\beta_0 t \tag{3.23}$$

Thus, the system states reach the sliding surface $s = 0$ in finite time and, once on the sliding surface, they will stay on it, as seen from (3.21). This ensures the stability of the system. Letting $\beta_1 \geq \beta(e,\, v)$ be the upper bound of $\beta(e,\, v)$, the control law can be further simplified to: $u = -\beta_1 \mathrm{sgn}(s)$.

The control law developed by SMC technique is known to induce chattering due

to the imperfections in switching devices and delays, and in this application, the slow response of the valve-transmission line. To address this problem, the signum function $\mathrm{sgn}(\cdot)$ is replaced by the saturation function, $\mathrm{sat}(\cdot)$, defined as:

$$\mathrm{sat}(y) = \begin{cases} y, & \text{if } |y| \leq 1 \\ \mathrm{sgn}(y), & \text{if } |y| > 1 \end{cases} \tag{3.24}$$

and the control law is given by:

$$u = -\beta_1 \mathrm{sat}\left(\frac{e + av}{\varepsilon}\right) \tag{3.25}$$

where ε is a positive constant that determines the thickness of boundary layer $\{|s| \leq \varepsilon\}$ for the sliding surface. This turns out to be a PD controller with saturation. The convergence rate of the system can be controlled by appropriately choosing a, which in effect limits the maximum speed of the needle, and the system position accuracy is determined by $\frac{1}{\varepsilon}$, which is effectively the proportional gain of the PD control once the system states reached and remained within the boundary layer $\{|s| \leq \varepsilon\}$. The saturation amplitude β_1 should be chosen large enough to ensure system stability under uncertainties, e.g., the friction force; but it should not be too large, because the control law is more vulnerable to slow valve-transmission line response and a large amplitude of the switching component can easily lead to system instability.

3.4.2 SMC-II

As mentioned in Section 3.4.1, large saturation amplitude, or large amplitude of the switching component makes the system more vulnerable to slow valve-transmission line response and should be avoided. In the design of SMC-I, the saturation amplitude is taken as the upper bound of $\beta(e,\, v)$, and that is a conservative estimate. Experimental observation shows that the dynamic friction force is significantly smaller than the static one. Hence, the following saturation amplitude definition can be used to improve the system stability:

$$\beta_1 = \begin{cases} \beta_2, & |v| \leq v_0 \\ \beta_3, & |v| > v_0 \end{cases} \tag{3.26}$$

where $0 < \beta_3 < \beta_2$.

3.4.3 SMC-III

To improve system stability, the saturation amplitude can also be reduced by dividing the control output into continuous and switching components. Taking

$$u' = -\frac{F}{A_1 + A_2} - \frac{M}{a(A_1 + A_2)}v + U \tag{3.27}$$

where $F = F_c \operatorname{sgn}(v)$ is an estimated friction force term and is of the form of coulomb friction with force amplitude F_c smaller than the minimum of the absolute value of the friction force observed. Now, the derivative of the sliding surface becomes:

$$\dot{s} = \frac{a}{M}\left[(A_1 + A_2)U + (F_f - F)\right] \tag{3.28}$$

and the upper bound of $|(F_f - F_c)/(A_1 + A_2)| = \beta_1' < \beta_1$. In consequence, the modified sliding mode control law can be written as:

$$u' = -\frac{F}{A_1 + A_2} - \frac{M}{a(A_1 + A_2)}v - \beta_1' \text{sat}\left(\frac{x + av}{\varepsilon}\right) \tag{3.29}$$

3.5 Experimental Evaluation of the SMC Controllers

All three SMC controllers designed in Section 3.4 gave good performance in simulation. To test the robustness of the controllers in real system and evaluate their control performance, experiments were conducted on the 1-DOF prototype device implemented. All three SMC controllers were tuned with trial and error to account for the parameter discrepancies between the simulation model and the actual system, and reasonably good dynamic response to step input were achieved for all controllers, as shown in Figure 3.9.

Though better accuracy could be obtained by fine-tuning the parameters, a positioning accuracy of only $1\,\text{mm}$ was achieved finally, since the position resolution of the MR images was in the order of $1\,\text{mm}$. Such positioning accuracy also helped to ensure the system stability by requiring lower controller gains. The saturation amplitudes of the SMC controllers were also chosen carefully, such that the maximum acceleration of the slider, or equivalently the needle, was limited and the slider would move slowly enough for the actuator of valve-transmission line to respond.

A same protocol was used to evaluate the performance of each controller. The 1-DOF prototype device started at 0 position, and its desired position was then set to be 25.4, 50.8, 76.2, $101.6\,\text{mm}$, in order. That was followed by the desired positions of 50.8,

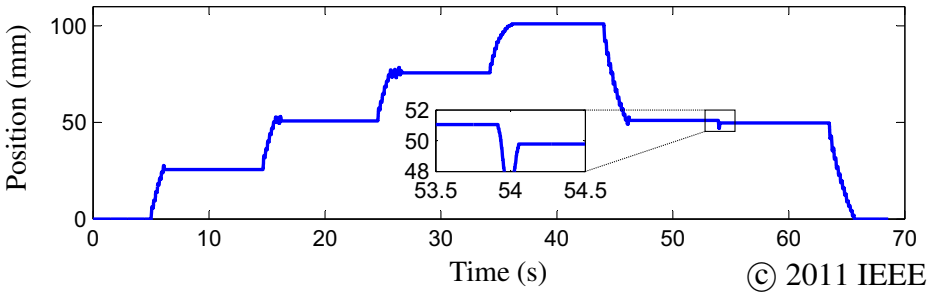

(a) Response curve of SMC-I

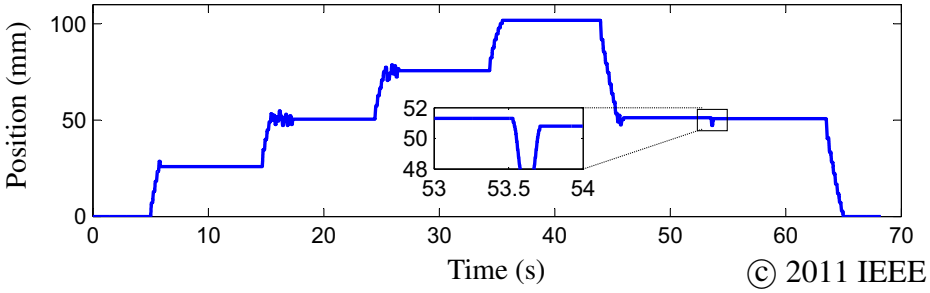

(b) Response curve of SMC-II

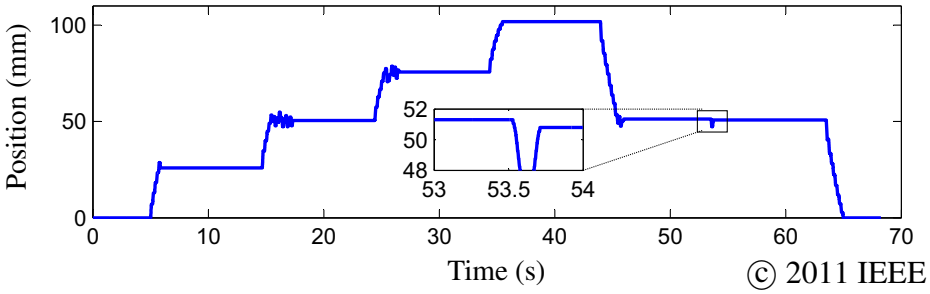

(c) Response curve of SMC-III

Figure 3.9: Experimental evaluation results of all three SMC controllers designed in Section 3.4. The commands given to all those controllers were similar, i.e., started from 0 position to 25.4, 50.8, 76.2, $101.2\,\mathrm{mm}$, and back to 50.8 and 0. Additional $1\,\mathrm{mm}$ amplitude step signals were commanded at about $55\,\mathrm{s}$ to each controller and zoom-in plots were shown in respective sub-figures. This showed that motion could be initiated for such small step input and the desired position would be reached within $1\,\mathrm{mm}$ accuracy. Reprint from [2], © IEEE.

and $0\,\mathrm{mm}$. Those commands tested the control performance in the large motion range. Prior to the final $0\,\mathrm{mm}$ position command, a small step command with amplitude of only $1\,\mathrm{mm}$ was sent after the device settled around the $50.8\,\mathrm{mm}$ location. That was to test if the desired $1\,\mathrm{mm}$ positioning resolution could be achieved.

As is shown in Figure 3.9, the step response curves differed slightly for different desired positions, despite that the distances traveled were the same. For example, the step response shown in Figure 3.9(a) exhibited a small overshoot when commanded from 0 to $25.4\,\mathrm{mm}$ while two and three cycles of oscillation existed for the step response when commanded from $25.4\,\mathrm{mm}$ to $50.8\,\mathrm{mm}$ and from $50.8\,\mathrm{mm}$ to $76.2\,\mathrm{mm}$, respectively. The step response from $76.2\,\mathrm{mm}$ to $101.6\,\mathrm{mm}$ even approached to the $101.6\,\mathrm{mm}$ position slowly without overshoot. Such a phenomenon was caused by the presence of non-uniform friction force along the guiding rods. As shown in Section 3.3.4, the friction force at one end of the guiding rods was higher than the other. Between the position at $50.8\,\mathrm{mm}$ and $76.2\,\mathrm{mm}$ the friction was relatively low and hence the system moved quickly and experienced oscillations. Around $101.6\,\mathrm{mm}$ the friction was higher, and the device moved slower and the overshoot was hence avoided. Those different dynamic responses (in the sense of overshoots and oscillations) showed the robustness of the SMC controllers against uncertainties, and all three controllers rendered stable and accurate position control over varying friction force / external disturbance.

It was notable from Figure 3.9 that stick-slip behavior was present in the result curves, which was consistent with the simulation results. Also observed were oscillations with small amplitudes at the desired locations and that was due to the SMC controllers behaving as stiff PD controllers when the system states had reached the boundary layers.

The observed peak-to-peak amplitudes of the oscillations prior to settlement at the desired locations, however, were small enough (less than $2.5\,\mathrm{mm}$ for SMC-I, and $5\,\mathrm{mm}$ for both SMC-II and SMC-III) and hence were acceptable.

The experiment conducted showed that the system could achieve a positioning accuracy of less than $1\,\mathrm{mm}$, and SMC-I performed best among all three controllers in the sense that it gave more uniform step response with smaller amplitude oscillation, which could be a result of parameter tuning.

3.6 MRI-Compatibility Evaluation of the 1-DOF Prototype Device

To verify the MRI-compatibility of the 1-DOF prototype device and its pneumatic actuation and to show the feasibility of accurate pneumatic actuation on MRI-compatible devices inside the MRI environment, a MRI test has been conducted using a Siemens $3\,\mathrm{T}$ Tim Trio MR scanner (Siemens Medical Solutions; Malvern, PA) and the experimental setup is shown in the top image of Figure 3.1.

The 1-DOF prototype device was first put into the MRI bore and actuated without performing MR imaging scans. This was followed by actuating the device with MR imaging performed during part of the actuation process. An identical step response as shown in Figure 3.9 was confirmed and no influence on the performance of the pneumatic actuation system due to the MRI environment was observed. This showed that good pneumatic actuation was feasible on MRI-compatible devices without being affected by the strong magnetic fields as well as the varying field generated during scanning.

A phantom test was then conducted to show that the device and its pneumatic ac-

tuation would not affect the quality of the MR images. This test also verified the system positioning accuracy with the MR images. The phantom used was a homemade phantom jelly, and it consisted of a mixture of $200\,\mathrm{ml}$ boiling water with $7.2\,\mathrm{g}$ gelatin powder (Knox gelatin, Kraft Foods Global Inc.). It was imaged using a T_1-weighted gradient echo acquisition with $T_\mathrm{E}/T_\mathrm{R} = 2.73/240\,\mathrm{ms}$, flip angle $= 90^\circ$, bandwidth $= 300\,\mathrm{Hz/pixel}$, FoV $= 120 \times 120\,\mathrm{mm}$, matrix $= 256 \times 256$, and slice thickness $= 3\,\mathrm{mm}$ to get the high-resolution static images shown in Figure 3.10(a) - Figure 3.10(c), and a T_1-weighted gradient echo acquisition with $T_\mathrm{E}/T_\mathrm{R} = 1.63/177.12\,\mathrm{ms}$, flip angle $= 90^\circ$, bandwidth $= 300\,\mathrm{Hz/pixel}$, FoV $= 120 \times 120\,\mathrm{mm}$, matrix $= 128 \times 128$, and slice thickness $= 3\,\mathrm{mm}$ to get a low-resolution image with short scanning time for dynamic imaging (5 frames per second), as shown in Figure 3.10(d).

No distortion due either to the 1-DOF prototype device or the pneumatic actuation was observed in the MR images acquired. Near the RFA needle tip in all images presented some blobs, which were resulted from the multiple sharp needle tips inside the RFA needle, since sharp edges could disturb the surrounding magnetic field and create artifacts in the MR images.

To further quantify the effect of the pneumatic system and its actuation on the MR image quality, SNR values were computed on the original DICOM images and the ROIs used for this calculation were indicated on the images with rectangles, as shown in Figure 3.10. The calculated SNRs were summarized in Table 3.1. Only slight SNR variation could be observed among the three high-resolution images, while their SNR values were significantly lower than that of the low-resolution image shown in Figure 3.10(d), due to their high image resolution in the same field of view as well as the difference in other

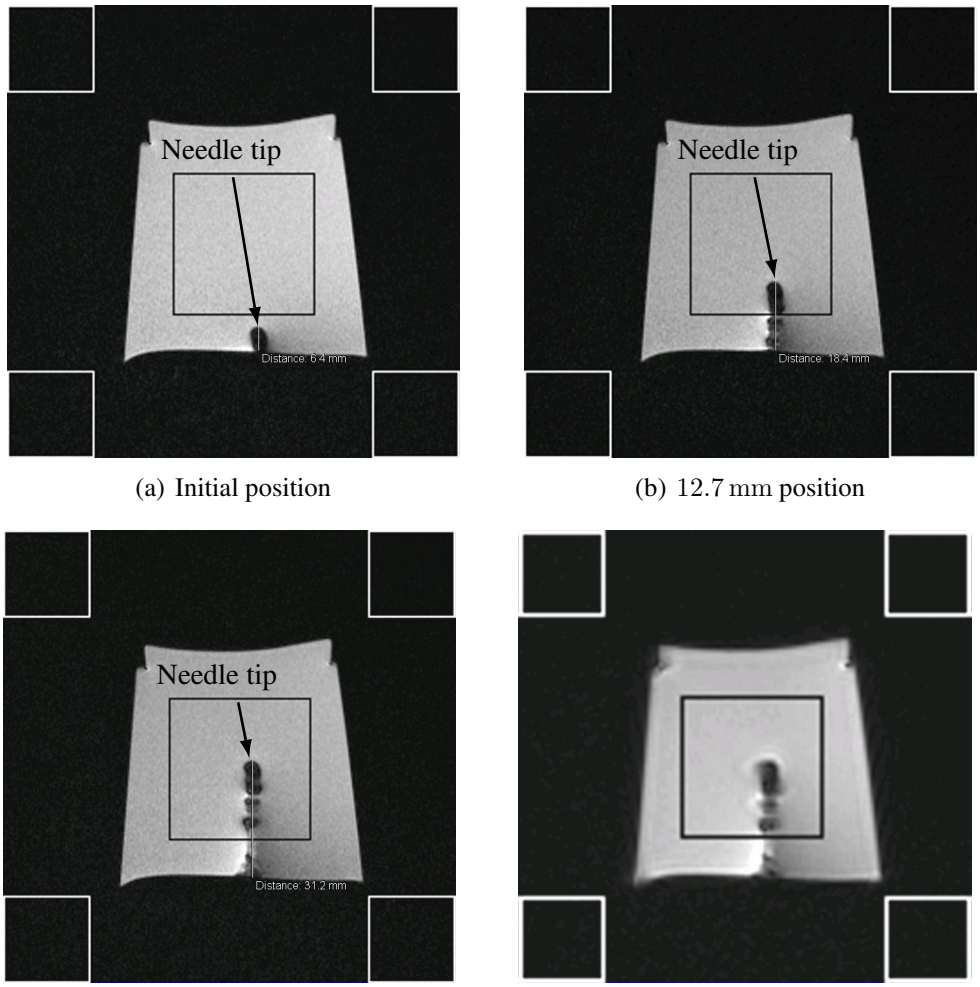

(a) Initial position

(b) $12.7\,\mathrm{mm}$ position

(c) $25.4\,\mathrm{mm}$ position

(d) Low-resolution MR image (for dynamic imaging)

Figure 3.10: MR images of phantom to evaluate pneumatic actuation accuracy and MRI-compatibility. (a)–(c) are the high resolution static images while (d) is the low resolution dynamic image. The rectangles indicate the ROIs used to calculate the SNR for each image.

imaging parameters. Since the final application would use the MR images to estimate the position of the device, the low-resolution dynamic image shown in Figure 3.10(d) further explained the reason why $1\,\mathrm{mm}$ was chosen as the desired positioning resolution.

The MR images shown in Figure 3.10(a) - Figure 3.10(c) were taken when the needle was at the initial position, the $12.7\,\mathrm{mm}$ position, and the $25.4\,\mathrm{mm}$ position, re-

Table 3.1: SNRs of the MR images with the 1-DOF prototype device

Experimental Setup	SNR Values
High-resolution image with needle at initial position	46.71
High-resolution image with needle at $12.7\,\mathrm{mm}$ position	45.47
High-resolution image with needle at $25.4\,\mathrm{mm}$ position	43.88
Low-resolution image with needle at $25.4\,\mathrm{mm}$ position	132.52

spectively. As clearly seen in those images, the positions measured from the MR images matched our desired positions closely. This demonstrated that the pneumatic actuation along with its validating 1-DOF prototype device was fully MRI-compatible and could position accurately as designed without any interference inside the MRI.

3.7 Pneumatic Control of the Cylinders of the Slave Robot

The work in the previous sections has shown that it is feasible to use pneumatic actuation through long transmission lines to achieve MRI-compatible actuation inside the MRI bore. With the inverse kinematics derived in Section 2.6, the length of each cylinder, including the three brass cylinders of the parallel mechanism and the two cable cylinders of the X-Y stage, can be computed for any desired pose. Then, the computed cylinder lengths will be sent to respective pneumatic controller to perform the accurate cylinder position control, actuating the slave robot.

The feasibility study of the pneumatic actuation was done over long transmission lines using proportional pressure valves, so that the complicated nonlinear orifice mass flow rate could be avoided and direct pressure command could be used. The proportional pressure valves used, though with a nominal reaction time of less than $10\,\mathrm{ms}$, took a much

longer time to establish the desired pressure at the output port. This was further affected by the long and relative thick ($3.175\,\mathrm{mm}$ or $1/8"$ ID) transmission lines, which added up to the cylinder chambers dead volume by several folds and resulted in the response time of the valve-transmission line in the order of $0.1\,\mathrm{s}$ or higher. To mitigate such issue, thinner transmission lines with $1.5875\,\mathrm{mm}$ ($1/16"$) ID and 3/5 proportional mass flow rate valves (Festo, MPYE-5-1/4-010-B) were used when the pneumatic actuation was applied to the slave robot.

Due to the slave robot configuration, the brass cylinders of the parallel mechanism have very small loads of a few hundred grams, which is mainly the mass of the cylinder piston rod, and the control law used is PI control with modified integration. Integration in PID control can eliminate positioning error by offsetting load disturbance such as cylinder stiction force, but at the risk of inducing overshoots or limit cycles. To take advantage of the merits of integration while avoiding its negative impact, a modified integration term has been adopted, with which the position error will only be integrated when it is larger than $0.5\,\mathrm{mm}$ and its derivative, i.e., the cylinder velocity, is less than $1\,\mathrm{mm/s}$. With a modest P gain with respect to the friction force level, the maximum cylinder velocity is limited so that the desired slow and smooth actuation without large overshoot can be ensured and a positioning accuracy of $0.5\,\mathrm{mm}$ is achieved. Experiments have been conducted with step signals to verify the effectiveness of this controller, and the response curves of one of the brass cylinders are shown in Figure 3.11.

As shown in Figure 3.11(a), a step signal from $45\,\mathrm{mm}$ to $75\,\mathrm{mm}$ was commanded at $t = 5\,\mathrm{s}$, and the cylinder responded quickly as a result of the large control output. Such large control output was due to the P term when the position error was large and

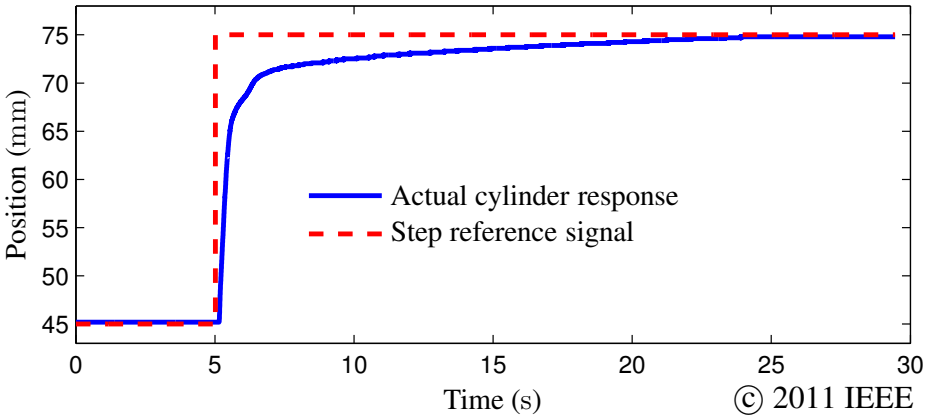

(a) Step response of a brass cylinder with mass flow rate valve

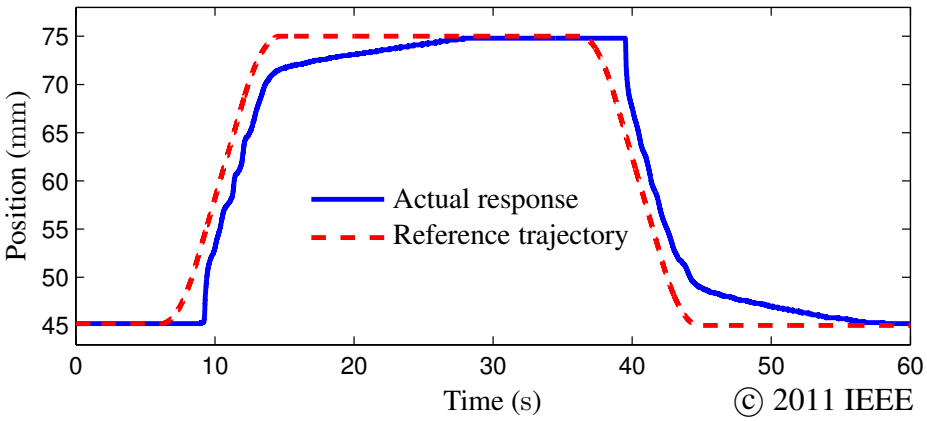

(b) Trajectory following response of a brass cylinder with mass flow rate valve

Figure 3.11: Experimental result of a brass cylinder controlled with a mass flow rate valve through long pneumatic transmission lines. Reprint from [2], © IEEE.

quick initial motion could also be attributed to the friction force drop after the stiction force had been overcome. As the position error decreased, the control output decreased with its P component, and the cylinder was slowed down by the friction force. Once the velocity of the moving cylinder dropped to the pre-set value, the integration term kicked in and maintained the control output while the position error was decreasing, effectively actuating the cylinder steadily towards the desired position without overshoot. To further improve the smoothness of the cylinder motion, a reference trajectory was generated with

$2\,\mathrm{mm/s^2}$ acceleration and $5\,\mathrm{mm/s}$ maximum velocity and was used as the commanded input of the modified PI controller. As expected, the cylinder moved smoothly with its maximum velocity confined, as shown in Figure 3.11(b). The cylinder stood still for about 3 seconds after the reference trajectory initiated due to the slow pressure build-up process along the long transmission lines. Then, it started to move at almost the same speed as the reference trajectory, and when it got near to the desired position (about $5\,\mathrm{mm}$), the modified integration term took effect and kept the cylinder moving slowly and steadily towards its final destination (within $0.5\,\mathrm{mm}$ positioning error) while avoiding the undesired overshoot.

Unlike brass cylinders, the cable cylinders of the X-Y stage had to carry the parallel mechanism and the load on the y-direction cable cylinder even reached up to $8\,\mathrm{kg}$. With such large payload, the friction force along these two cable cylinders increased significantly, mainly of the coulomb friction component. Hence, the control law used for the cable cylinders was PD control with fixed feed-forward friction compensation. The experimental result with step input signals were shown in Figure 3.12.

As shown in Figure 3.12(a), a step signal from $102\,\mathrm{mm}$ to $210\,\mathrm{mm}$ was commanded to the x-direction cable cylinder at $t = 3\,\mathrm{s}$. Smooth response with a small overshoot was achieved after about $0.6\,\mathrm{s}$ reaction time, which was the time needed to establish high enough pressures inside the cylinder chambers through the long transmission lines to overcome the large friction force. The controller easily achieved the $1\,\mathrm{mm}$ positioning accuracy thanks to the large payload. The response curve commanded by a reference trajectory generated with $50\,\mathrm{mm/s^2}$ acceleration and $50\,\mathrm{mm/s}$ maximum velocity was also presented in Figure 3.12(b). Compared to the case in Figure 3.12(a), the cylinder

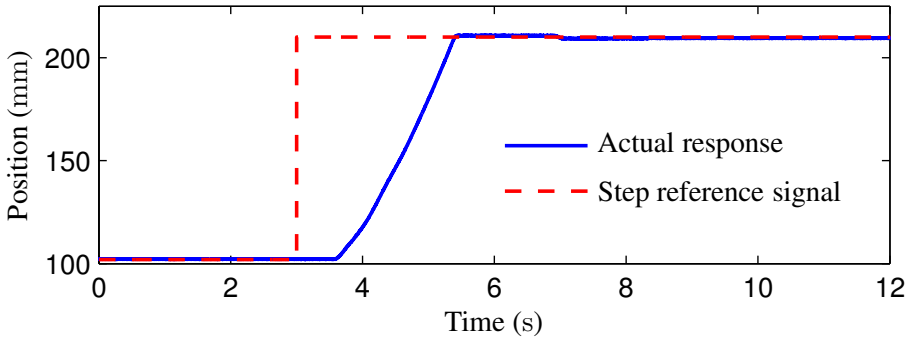

(a) Step response of the x-direction cable cylinder with mass flow rate valve

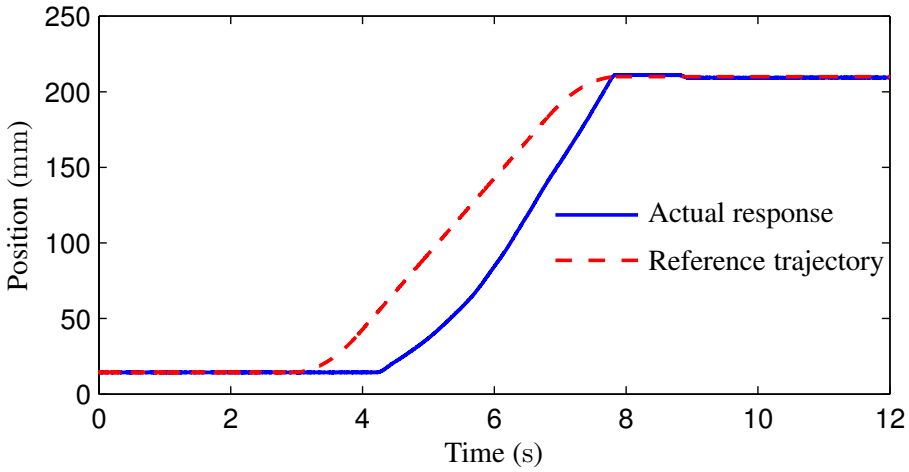

(b) Trajectory following response of the x-direction cable cylinder with mass flow rate valve

Figure 3.12: Experimental result of the x-direction cable cylinder controlled with a mass flow rate valve through long pneumatic transmission lines

started to respond after a longer pressure build-up process, since the position error were smaller at the initial phase and resulted in a smaller controller output. Then, the cylinder accelerated and caught up with the reference trajectory smoothly and finally reached its desired position as expected.

3.8 Summary

In this chapter, a MRI-compatible 1-DOF pneumatically actuated prototype device has been implemented, based on which the feasibility of pneumatic actuation with long transmission lines inside the MRI has been studied. A model of the pneumatic actuation system has been established, and various SMC controllers have been designed, implemented, and evaluated both inside and outside the MRI environment. Experimental results show that reasonably good control performance of the pneumatic actuation with positioning error of less than $1\,\mathrm{mm}$ is attainable with SMC controllers inside the MRI without affecting the quality of the MR images. Controllers for the pneumatic cylinders of the slave robot are then designed and implemented with good performance.

Followed by the MRI-compatible slave robot implementation and its pneumatic actuation, work on the design and implementation of the master robot will be discussed in the next chapter, with which a teleoperation system can be constructed.

Chapter 4

Design and Development of the Master Robot

With the MRI-compatible slave robot implemented in Chapter 2 and its corresponding pneumatic control strategy developed in Chapter 3, it is feasible to perform breast biopsy needle insertion inside the MRI scanner bore with continuous imaging guidance. However, the goal is not necessarily to replace the physician from such task, but to provide a means to assist the physician perform the needle insertion more efficiently and more accurately [21]. The physician should stay inside the MRI control room watching the MR images acquired in real-time and manipulate therein the slave robot to perform breast biopsy needle insertion procedures without the need of removing the patient from the MRI bore. In this way, the multiple iterations can be avoided and the sampling error can be minimized.

To manipulate the slave robot, the physician has to furnish the desired needle insertion depth, needle tip position and needle orientation to the slave robot controller so that each link variable can be solved. Even though that is an accurate way, it is very unintuitive to manipulate the slave robot in this manner, since the physician has to figure out those numbers from the available MR images by random guessing. This will adversely lead to a "trial and error" procedure that could require a long manipulation time. It is also not intuitive to have the needle-tissue interaction force sensed by the fiber-optic force sensor be displayed as numbers to let the physician "feel" the force. Therefore, it is necessary to

develop a manipulation capability, through which the slave robot can be manipulated as if the physician is operating the slave robot directly and can feel physically the insertion force exerted on the needle.

Such manipulation capability can be achieved with a master device that can act as a high resolution input device. It can read the position, orientation and push / pull commands from the physician while transmitting the needle-tissue interaction force cue to the physician [13]. The haptic feedback interface implemented in this way can also enable the physician to feel the puncture force when the needle penetrates various tissue membranes. That can be very helpful cues for an experienced physician to determine where the needle tip is and whether the needle has been inserted into the target tumor. Knowledge of such force is not only important for the practicing physician, but can also facilitate physician to train and understand the needle-tissue interaction force, which is one of the most difficult aspects of surgery to master [49].

In this chapter, an intuitive master manipulator that shares the similar structure of the slave robot is designed and implemented. It is haptic feedback enabled and can be used by the physician to control the slave robot inside the MRI bore. The details of the manipulator design and implementation is presented in Section 4.1, and its kinematics is described in Section 4.2. Section 4.3 discusses the control scheme of the master robot, and summaries are made in Section 4.4.

4.1 Design and Implementation of the Master Robot

Unlike the design of the slave robot that has to fit in a limited space and has to be actuated and sensed with MRI-compatible techniques, the design and implementation of the master robot is more flexible with respect to the choices of material, actuators, and sensors. Nonetheless, the master robot is to be used by the physician to manipulate the MRI-compatible slave robot implemented and perform the needle insertion task in an intuitive way. That means the manipulation of the master robot should be similar if not identical to the kinematic behavior of the slave robot. In addition, the information of the needle-tissue interaction force exerted on the needle is beneficial to the physician when inserting the needle into the tissue, and hence, should be reflected on the master robot along the needle insertion direction. According to these requirements, the master robot has been designed and implemented as shown in Figure 4.1 and the CAD drawing of each component is listed in Appendix B. It consists of a needle driver subsystem and a parallel mechanism subsystem, and these two subsystems correspond respectively to the two subsystems of the slave robot. They will help the physician perform the needle insertion task and the needle orientation adjustment task intuitively. The teleoperation of the X-Y stage of the slave robot can be achieved by directly using the keyboard for implementation simplicity, since the X-Y stage aligns with the world coordinate with decoupled actuation in horizontal and vertical directions and is simple and intuitive to manipulate.

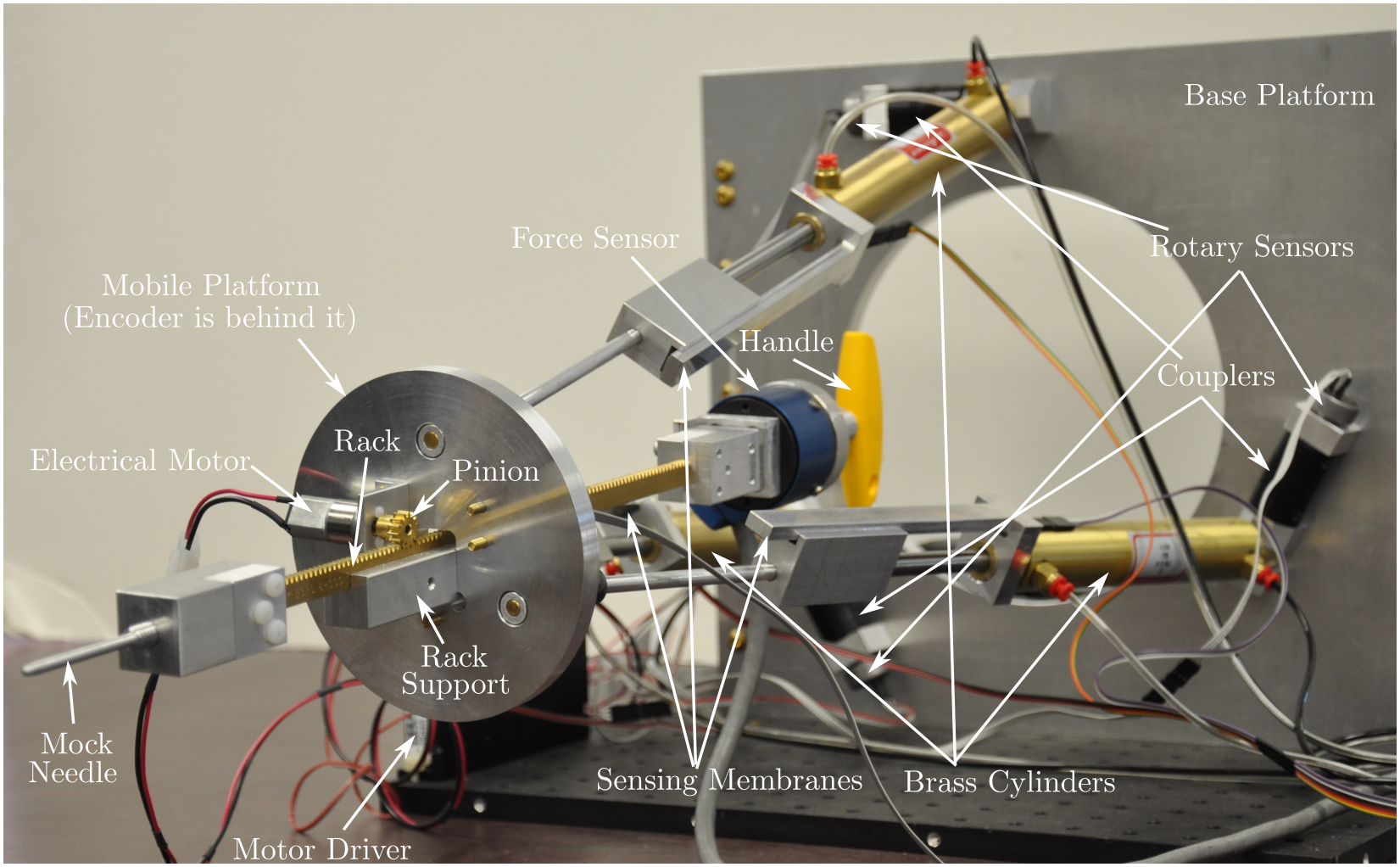

Figure 4.1: Photo of the actual master robot [97].

4.1.1 Needle Driver of the Master Robot

The design objective for the needle driver subsystem of the master robot is to duplicate the needle insertion and retraction motion while providing the desired needle insertion depth information to the needle driver of the slave robot and reflecting the needle insertion force measured by the force sensor of the slave robot to the physician.

To achieve the needle insertion and retraction motion, a rack and pinion structure is adopted. It has two pinions (McMaster, 7880K26) with an $11.1252\,\mathrm{mm}$ ($0.438"$) pitch diameter that push the rack (Quality Transmission Components, BSR0.8-300) against the rack support along a machined slot, as shown in Figure 4.1. An encoder (US Digital, S4-250-125-N-D) with 250 CPI resolution is attached to the pinion that locates at the back of the mobile platform and provides the position of the rack, or equivalently, the needle depth information with a resolution of $0.035\,\mathrm{mm}$.

To provide the desired haptic feedback force to the physician, the needle driver is actuated with en electrical motor (Sparkfun Electronics, ROB-08912) that attaches the other pinion in front of the mobile platform. The electrical motor is driven by a motor driver (Advanced Motion Controls, 25A8) and can provide torque up to $0.1836\,\mathrm{N}\cdot\mathrm{m}$ ($26\,\mathrm{oz}\cdot\mathrm{inches}$). That converts to over $30\,\mathrm{N}$ actuation force along the rack / needle insertion direction and is sufficient to generate the measured needle-tissue interaction force. When providing haptic feedback force, the electrical motor stalls and the excessive heat generated by such stall current could potentially burn the motor. Therefore, the motor driver has been tuned such that its output current limit is slightly lower than the rated stall current of the motor. The generated force is measured by a 6-DOF commercial force

sensor (JR3, 20E12A-I25) that connects the rack and the handle with adaptors, and closed loop control is used to ensure accurate force feedback.

The needle driver is attached to the mobile platform through the rack support as well as the brackets on which the electrical motor and the encoder mount. A mock needle is also manufactured and attached to the other side of the rack to improve intuitiveness of this needle driver.

4.1.2 Parallel Mechanism of the Master Robot

To ensure intuitive needle orientation adjusting operation, a similar three-link parallel mechanism is adopted for the master robot. However, the slave robot requires a compact design to fit into the limited space available inside the MRI bore, and hence the same small radius has been chosen for the mobile platform and the base platform, on which the extensible links lie. Duplicating the parallel mechanism of the slave robot for the master robot will leave little space among the extensible links, making it difficult for the physician to operate. Therefore, the extensible links of the master robot are intentionally attached to the base platform on a circle with larger radius, $139.7\,\mathrm{mm}$ ($5.5^{"}$). This design brings out sufficient room inside the structure for the physician to place his hand and manipulate the master robot. The circle radius on the mobile platform of the master robot, in contrast, is chosen to be identical to that of the slave robot. This is to ensure that the mobile platform of the master robot can translate along the x_b and y_b directions in the same coupled manner as that of the slave robot when the needle orientation is adjusted, since it has been shown in (2.40) and (2.41) that such coupling dependence is only on the

circle radius of the mobile platform, r, but not on the circle radius of the base platform, R.

To ensure the full workspace of the slave robot's parallel mechanism is covered by that of the master, the $101.6\,\mathrm{mm}$ ($4"$) stroke brass cylinders have been used (Allenair Brass Cylinder, C-7/8x4-BU-L-SZ), and their positions are measured by sensing membranes that measure up to $150\,\mathrm{mm}$ (spectrasymbol, TSP-L-0150-103-1%-RH). To facilitate solving for the orientation of the mock needle on the master robot and remove the numerical iterating computation process described in Section 2.6.2 in the case that those orientation information should be commanded to the slave robot, three rotary potentiometric sensors (Novotechnik, PL300 10k0 AA130 FK) are included to measure the rotation angles subtended between the extensible links and the base platform. Three couplers (McMaster, 6208K22) are used to connect the rotary sensors and the pins to which the cylinders are fixed to account for small misalignment during assembly and ensure accurate measurement of the rotation angles.

4.2 Kinematic Map of the Master Robot to the Slave Robot

With the similar kinematic structure as that of the slave robot, the kinematic analysis of the master robot can be performed based on the result derived in Section 2.6. Having identical circle radius on the mobile platform as that of the slave robot, the schematic of the parallel mechanism of the master robot overlaid with that of the slave robot is shown in Figure 4.2.

With the only difference of the extensible links being attached to the base platform

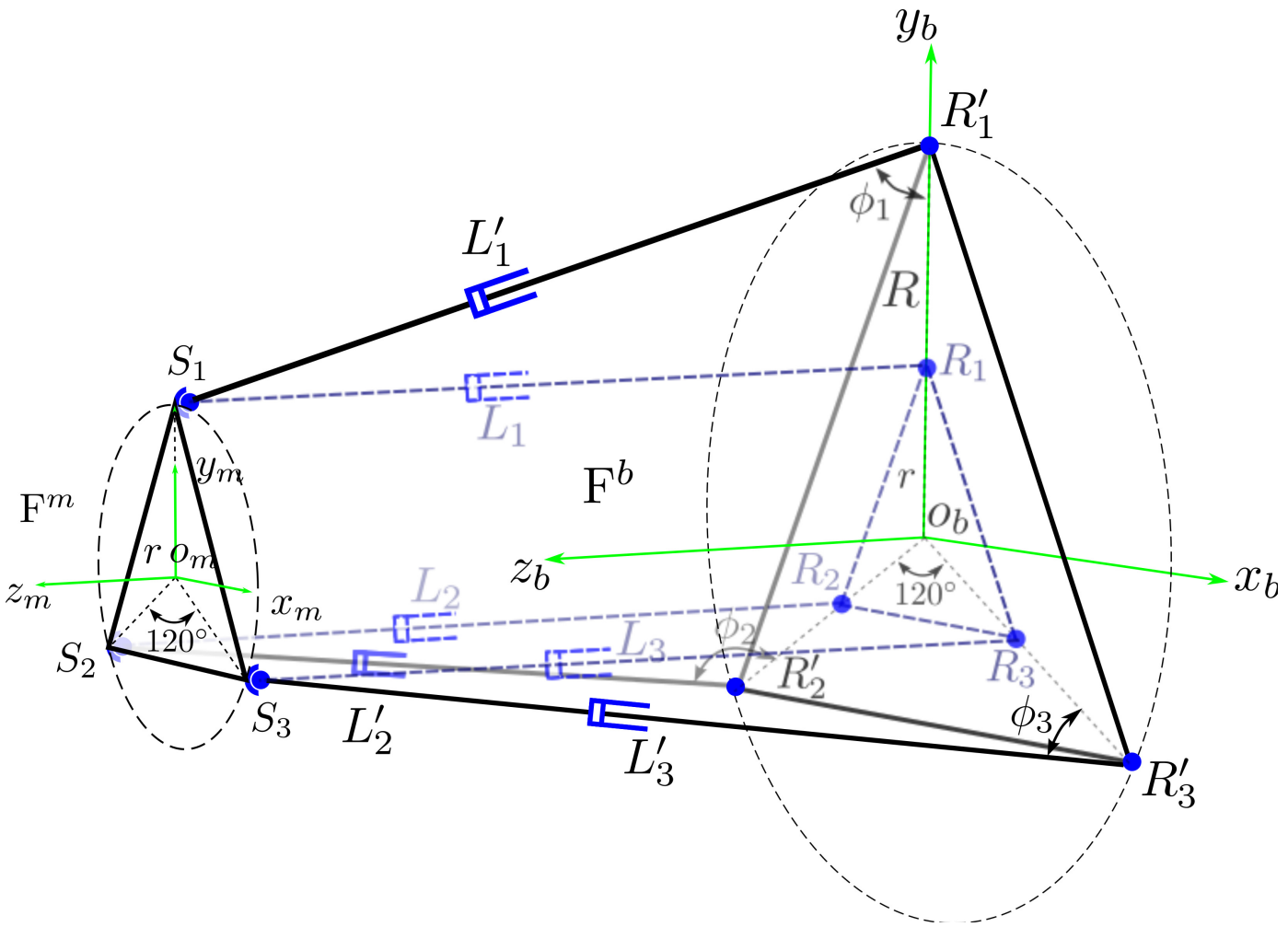

Figure 4.2: Schematic of the parallel mechanism of the master robot, overlapped with that of the slave robot in dotted lines. S_i represent the spherical joints on the mobile platform of both robots; R_i represent the revolute joints of the slave robot while R'_i represent the revolute joints of the master robot; θ_i are the angles subtend between the i^{th} link and the base platform $R'_1R'_2R'_3$; L_i and L'_i are the lengths of the extensible links of the slave and the master robot, respectively ($i = 1, 2, 3$). Both robots share the same frame definition of F^m and F^b.

along circles of different radii, it is possible to map the extensible link variables of the master robot to those of the slave robot directly. That can avoid the complicated and time-consuming computation of the forward kinematics of the master robot and the inverse kinematics of the slave robot. Since the spherical joints are evenly spaced along the circles on their respective mobile platforms and those circles are of the same radius, it is shown in (2.40) and (2.41) that the two parallel mechanisms could share a same kinematic behavior relative to their base platforms. Assuming that the base platforms coincide with each other and share the same base coordinate, as shown in Figure 4.2, the corresponding revolute joints R_i and R'_i ($i = 1, 2, 3$) are at a fixed distance (ΔR) away, and $\Delta R = R - r$. When the mobile platforms of the master robot and the slave robot achieve a same spatial position and orientation, the two mobile platforms will coincide with each other. Hence, the corresponding spherical joints will also coincide with each other at S_i ($i = 1, 2, 3$). Therefore, the point of S_i, R_i, and R'_i on link i form a triangle. By measuring the lengths of the extensible link on the master robot, L'_i ($i = 1, 2, 3$), and the corresponding angles θ_i ($i = 1, 2, 3$), the lengths of the extensible links on the slave robot, L_i ($i = 1, 2, 3$), can be computed using the cosine rule as:

$$L_i(L'_i,\ \theta_i) = \sqrt{{L'_i}^2 + \Delta R^2 - 2L'_i \Delta R \cos\theta_i} \tag{4.1}$$

Note that both parallel mechanisms attach their extensible links via revolute joints, which restricts the motion of the extensible links in the vertical plane about the base platform. Hence, the angle θ_i that subtends between $R'_i S_i$ and the base platform $R'_1 R'_2 R'_3$ is essentially the same rotation angle of link i and thus can be easily measured by the

corresponding rotary sensor.

4.3 Control of the Master Robot

The master robot is designed to be actuated only for its needle insertion DOF to reflect the needle-tissue interaction force. For the parallel mechanism that is mainly used as a interface to adjust the needle orientation while the slave robot is not contacting with its surrounding environment, only simple control strategy has been implemented for the cylinders so that the parallel mechanism can be locked in place as needed to help the physician perform the needle insertion task.

The locking of the brass cylinders of the parallel mechanism is achieved by pressurizing chambers at both sides of the cylinders before closing their connection ports. Two pressure valves (Hoerbiger, Tecno plus, PS120100-080-036) are used to change the air pressures inside the cylinder chambers in groups of three, since the effective piston areas on both sides are different. This is due to the presence of the cylinder rod at only one side of the cylinder, and different pressures have to be applied to avoid generating any net force. After the cylinder chambers are pressurized, six check valves (Festo, HGL-1/8 NPT) are used to close the connecting port of each cylinder chamber independently. By opening all the check valves and setting the pressure valve outputs at atmosphere pressure, air can flow into and out of the cylinder chambers freely, allowing the cylinders to move easily. This would allow the physician to adjust the needle orientation as needed. Once such orientation adjustment is done and the physician is ready to perform the needle insertion task, high pressures ($350\,\mathrm{kPa}$ in chambers on one side of each cylinder) are set

for the two pressure valves to pressurize the cylinder chambers. The check valves are then closed to lock the cylinders in place. This will help avoid the involuntary needle orientation change during the needle insertion phase and relieve the stress and fatigue experienced by the physician.

The actuation of the needle driver employs P control for both force and position control so that different control modes are available for different operation phases: when the physician is adjusting the needle orientation and is still preparing for needle insertion, position control can be activated to lock the needle in place and prevent unintentional needle insertion; when performing the needle insertion task, it is necessary to provide the needle-tissue interaction force feedback to the physician, and hence the force control is enabled. To improve the effectiveness of needle locking, the force measured by the force sensor is also used in the position control and fed forward to the electrical motor to compensate the force exerted by the physician and reduce the static positioning error. The control law is described as:

$$u_{\text{motor}} = \begin{cases} K_{px} e_x + K_{\text{pos}} F, & \text{Position control} \\ K_{pf} e_f, & \text{Force control} \end{cases} \tag{4.2}$$

where u_{motor} is the electrical motor input voltage, e_x and e_f are the respective position error and force error, and K_{px} and K_{pf} are the proportional gains for the position control and the force control, respectively. F is the force sensed by the master robot force sensor along the needle insertion direction and K_{pos} is the force compensation coefficient in the position control.

4.4 Summary

In this chapter, the design and implementation of the master robot, which serves as a high resolution input device and helps the physician manipulate the slave robot implemented in Chapter 2, is presented. Kinematic analysis that maps the master robot directly to the slave robot has been carried out, and the control strategy for the master robot has been discussed. The next chapter will discuss the integration of the master robot and the slave robot, as well as the control of the complete teleoperation system.

Chapter 5

Teleoperation Integration and the Graphic User Interface of the System

Based on the MRI-compatible slave robot developed in Chapter 2 with appropriate pneumatic actuation technique through long pneumatic transmission lines described in Chapter 3 and the master robot implemented in Chapter 4, a teleoperated surgical system could be constructed that would enable the physician sitting in the control room to manipulate the MRI-compatible slave robot located inside the MRI bore using the master robot. In this way, the physician could take advantage of the continuous MR images acquired in real-time and correct intuitively any needle positioning error shown in the images, using the master robot.

The technique of teleoperation enables the manipulation of mechatronic and robotic devices at a distance. It greatly extends the sensing and manipulation capability of the human operator and allows tasks under hazardous environment be performed while the human operator operates the device at a safe place. Sheridan reviewed the historical development of teleoperation prior to the 1980s and envisioned the thriving of teleoperation techniques in numerous fields [159]. Hollis et al. developed a 6-DOF fine motion wrist based on magnetically levitation [160]. Such wrist was then installed on a conventional manipulator to construct a teleoperation slave that would be applied in manipulation tasks requiring high precision and fine compliant motion with force-reflection capability [161]. Salcudean et al. studied the impedance control and applied it in a teleoperated mini exca-

vator to improve the completion time and task quality [162]. Fischer et al. applied teleoperation technique in the medical field and presented two different telerobotic devices for use in CT-and / or MRI-guided high precision radiological interventions [163]. Sitti et al. proposed a teleoperated nano-scale touching system with nano-forces scaling and such system would enable the study of nano-scale surface topography and contact [164]. Nguyen et al. presented a novel interface design for the intuitive teleoperation of wheeled and tracked vehicles [165]. Talasaz et al. incorporated haptic-enabled teleoperation into MIS tumor treatment to facilitate the physician to locate the tumor with tissue instrumentation force feel [166].

In this chapter, the teleoperation system that would enable the physician to perform breast biopsy needle insertion in the hard-to-reach space inside the MRI scanner bore will be developed, based on the aforementioned devices and actuation techniques. The system integration of the master and slave robots is described in Section 5.1; and the control strategy of the teleoperation system is presented in Section 5.2. The evaluation result of the integrated system is shown in Section 5.3 and Section 5.4 discusses the implemented GUI that facilitates the physician performing the task. Section 5.5 summarizes this chapter.

5.1 Integration of the Master System

As mentioned in Chapter 4, the master robot is specially designed to work with the MRI-compatible slave robot implemented in Chapter 2. It provides an intuitive means to the physician to adjust the needle orientation, whose kinematics is unintuitive and is governed by the parallel mechanism of the slave robot. The haptic-enabled master robot also

enables the physician to feel the needle insertion force while he or she is advancing the needle, and that is achieved by a fully actuated needle driver. In this way, the physician can control the needle orientation and insertion of the slave robot remotely, by manipulating the mock needle of the master robot.

The needle insertion / retraction can be done by pushing / pulling the handle of the master robot. Assisted by the electrical motor to overcome the device friction force, the rack slides smoothly and the needle depth information can be measured by the optical encoder. That corresponds to the desired needle depth for the slave robot. To adjust the needle orientation of the slave robot, the physician can change the orientation of the mock needle on the master robot, and the link lengths of the master robot change accordingly. With a similar structure to that of the slave robot's parallel mechanism subsystem, it is shown in Section 4.2 that the desired link lengths of the slave robot's parallel mechanism can be easily related to the corresponding link lengths of the master robot. Hence, the link lengths of the parallel mechanism at the slave robot side can be computed without solving the complicated forward and inverse kinematics of the parallel mechanisms. Therefore, the configuration map of the master and the slave robots can be conveniently reduced to actuator level one-to-one map. The corresponding structure of the master robot to the X-Y stage of the slave robot is intentionally omitted for implementation to reduce the complexity of the master robot, and keyboard input will be used to control the X-Y stage of the slave robot. This will not affect the intuitive operation of the teleoperation system, since the X-Y stage moves along the x and y axes of the world coordinate and is straightforward to adjust.

Based on the actuator level correlation described above, a teleoperation system can

be achieved. The master and the slave robot each has its dedicated DAQ cards (Sensoray, Model 626) and control computer, and the communication channel can be established through the network communication between the two control computers. The master control computer collects the actuator level configuration data of the master robot as well as accepting the commands for the X-Y stage from the keyboard and sends them to the slave control computer, where simple computation is carried out to get the commands for each actuator of the slave robot. Then, the slave control computer controls its actuators moving towards their commanded positions with the information acquired from the DAQ system. In the meanwhile, this slave configuration information is sent to the master control computer for data logging purpose as well as proper actuation of the master robot along the needle insertion DOF for haptic force feedback.

The implemented slave robot and the master are thus integrated as a teleoperated surgical system, based on which the control strategy of such teleoperation system can be developed.

5.2 Control Strategy for the Teleoperation System

With the actuator level one-to-one map achieved, the control scheme of the master-slave teleoperation system, as shown in Figure 5.1, is proposed. The only connection between the master and the slave robot systems is the network communication channel between the master and the slave control computer, both of which reside in the MRI control room. The dashed lines indicate actuator level virtual connections established with the information communicated through the network. With a fully actuated needle driver in the master

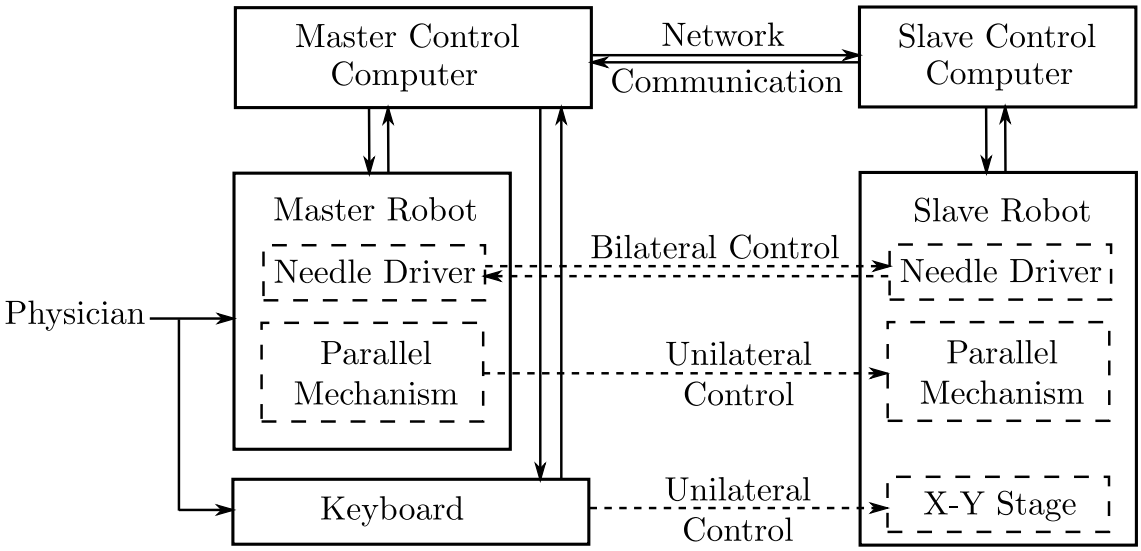

Figure 5.1: The control scheme of the master-slave teleoperation system. The only connection between the master and the slave robot systems is the network communication channel, and the dashed lines indicate actuator level virtual connections established with the information communicated through network [97].

robot, bilateral control is implemented for the needle insertion DOF to help the physician perform the needle insertion task with force feedback. For other DOFs, only unilateral control is implemented, since the parallel mechanism of the master robot cannot be fully actuated, and the counterpart of the slave robot's X-Y stage is not present in the current master robot implementation.

The two control computers of the master and the slave robot are both equipped with Intel® Core™ i5 $3.1\,\mathrm{GHz}$ CPU, $4\,\mathrm{GB}$ memory, and Intel® Gigabit Network Adaptors are used to establish the necessary network communication through a dedicated local router. Such network communication can potentially introduce time delays and deteriorate the control performance or even destroy the system stability. Extensive work has been done to address this issue [167–177]. Anderson and Spong studied the stability in a force-

reflecting bilateral teleoperation with substantial time delay, and the time delay was in the order of magnitude of $40\,\mathrm{ms}$ [167]. Niemeyer and Slotine pointed out the system stability could be compromised if the total time delay would provide more than a 90° phase shift at the frequency of a first-order system and utilized wave variables to develop adaptive tracking controller for control of remote robotic system [168]. Tzafestas et al. applied an adaptive impedance control scheme in a haptic teleoperation system to alleviate problems associated with the presence of time delay around $200\,\mathrm{ms}$. Xu et al. proposed two control methods to address the bilateral control of a car-like planetary rover under communication delay up to $900\,\mathrm{ms}$ [175]. Looking at a representative "median" time delay of $50\,\mathrm{ms}$, Lawrence studied the stability and transparency problems in bilateral teleoperation control, and believed that very small time delays such as $1\,\mathrm{ms}$ would cause little performance degradation [177]. Hence, it is necessary to determine the time delay introduced by the network communication.

To find the range of the time delay presented in the current system, an experiment was conducted as follows: A first data packet was sent by the slave control computer after a hardware timer had been initiated, and as soon as it arrived at the master control computer, a reply data packet was sent back. This reply packet was then replied by the slave control computer with another data packet, and such sending and replying iteration would be repeated until a preset number of iterations was reached at the slave control computer. The total time spent for this process would be recorded and used to compute the average time delay of a single trip, with the assumption that the time delays of both directions were of the same value. The data packets sent from both computers were the exact same ones used in actual communication, and a total of $10,000$ iterations were repeated for

Table 5.1: Experimental result of the network communication time delay

Test Number	Average Single Trip Time Delay (ms)	
	UDP	TCP
1	0.3946	0.1736
2	0.1863	0.3117
3	0.3165	0.2089
4	0.0786	0.4029
5	0.0723	0.0697
6	0.1685	0.1488
7	0.1872	0.1307
8	0.0605	0.0709
9	0.3644	0.3630
10	0.2134	0.3108
Average	0.2042 ± 0.1203	0.2191 ± 0.1205

each test. Ten tests had been performed with UDP and TCP protocols respectively, and the average single trip time delays are listed in Table 5.1.

The average time delays are computed to be $0.2191 \pm 0.1205\,\mathrm{ms}$ under TCP protocol and $0.2042 \pm 0.1203\,\mathrm{ms}$ under UDP protocol, and the highest time delay observed is no more than $0.5\,\mathrm{ms}$. These number are very small compared to the currently implemented $500\,\mathrm{Hz}$ sampling rate, not to mention the fact that the pressure wave delay along the 9 meters pneumatic transmission lines is in the order of $10\,\mathrm{ms}$. It also falls into the small time delay category that cause little system performance degradation as stated in [177]. Therefore, the time delay due to the network communication is neglected in the current implementation.

The UDP protocol is generally more suitable for real-time applications under complicated and unreliable network environment since dropping packets is preferable over waiting for delayed packets and smaller time delay is more desirable in those applications. However, the smaller time delay compared to that under TCP protocol is achieved at the cost of no guarantee of delivery, ordering, or packet duplication. The communication between the master and the slave robot control computers described here is implemented through a dedicated local router and the time delay under UDP protocol only shows marginal improvement compared to that under TCP protocol. Also considering that the communication of the teleoperation system includes data packets carrying special command for operation mode switching, TCP protocol is chosen for its implementation simplicity and reliability.

With such a teleoperation system, the physician can manipulate the master robot to first adjust the needle orientation and actuate the X-Y stage with a keyboard so that the needle is pointing along the desired orientation at the appropriate incision point. It is worth noting that the rotation center of the needle is neither on the needle tip nor on the mobile platform of the parallel mechanism, and the position of the needle tip as well as the center point of the mobile platform will change as a result of the needle orientation change, as shown in Section 2.6. To ensure an intuitive operation, the physician can optionally configure the control computers to automatically calculate the offsets and apply them to the X-Y stage as well as the needle driver such that the needle tip position is maintained. After the needle is adjusted to the right configuration in the positioning mode, the physician can lock up other DOFs except the needle insertion one and perform the needle insertion task in the insertion mode. Such separation of the "positioning" and

"insertion" modes could be an advantage since it gives extra safety on the overall system [21]. During the process of needle insertion, the physician can also switch back to the positioning mode and readjust the needle orientation as needed, though such adjustment is not encouraged since the steering of an 8 gauge ($4.191\,\mathrm{mm}$ in diameter) needle can cause excessive damage to the surrounding tissue.

5.3 Experimental Evaluation of the Teleoperation System

An experiment has been conducted to evaluate the teleoperation capability of the integrated teleoperated surgical system by manipulating the master and adjusting the needle orientation arbitrarily, and the commanded curves sensed by the master robot as well as the response curves measured at the slave robot are shown in Figure 5.2. The response curves of the X-Y stage of the slave robot are omitted here since their commands are formed with the keyboard of the master control computer, and the time delay experienced in the network communication is negligible compared to the slow response of the cable cylinder shown in Figure 3.12. This effectively implements a direct control of the X-Y stage, and same response as shown in Figure 3.12 should be expected.

The response curves of the slave robot shown in Figure 5.2 are the actual response curves of the brass cylinders of the parallel mechanism, while the curves of the master robot are computed using (4.1) and are the commanded inputs for the slave robot. As can be seen from the plots, the slave robot is able to follow the master robot's configuration with its pneumatic controllers and reasonable performance is achieved. Tracking errors can be observed in the response curves, and the error could be relatively large when fast

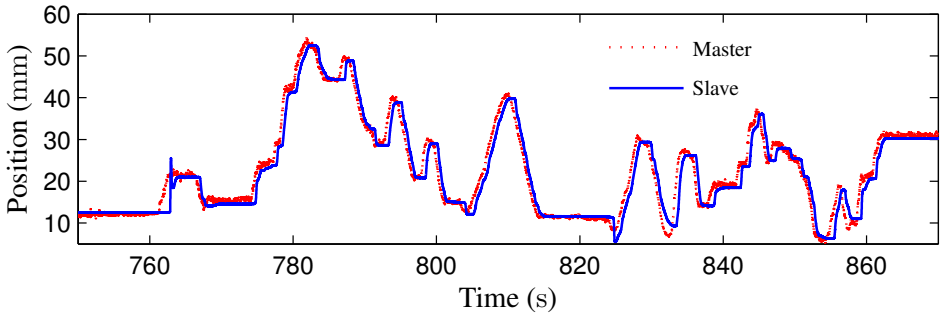

(a) Response of parallel mechanism cylinder 1

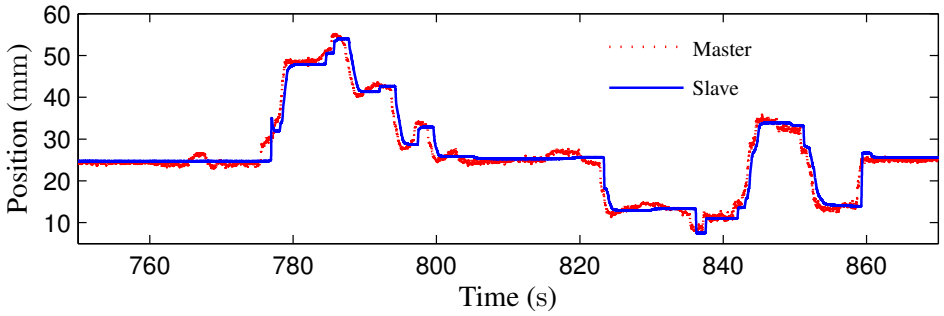

(b) Response of parallel mechanism cylinder 2

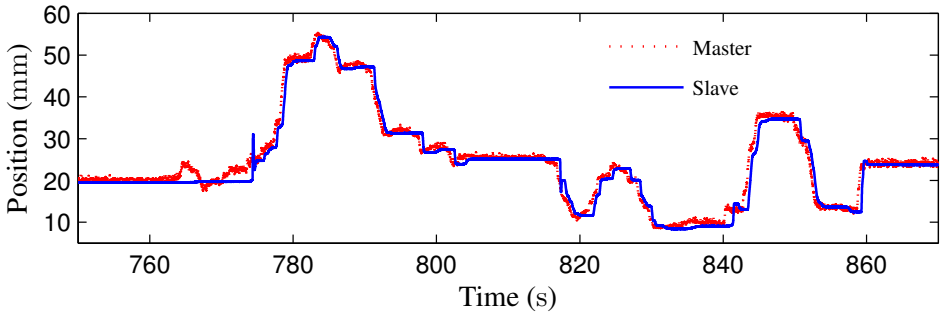

(c) Response of parallel mechanism cylinder 3

Figure 5.2: Experimental result of the teleoperation system under free manipulation for needle orientation [97].

varying commands with small change in amplitude are sent from the master robot. This is due to the combination of the slow dynamic response of the pneumatic controller and the nonlinear stiction friction force of the cylinders. However, such tracking performance might be beneficial in removing jerky motion at the master robot. In general, the slave robot is able to settle at the desired configuration after holding the master robot for several seconds and is able to follow the master robot's configuration.

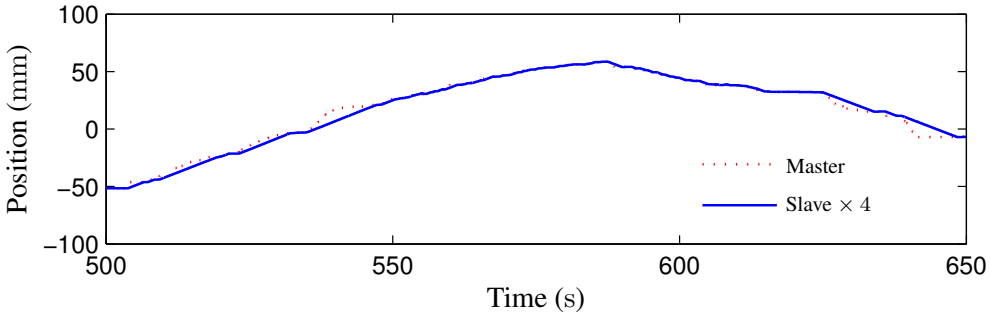

(a) Response of needle depth along insertion direction

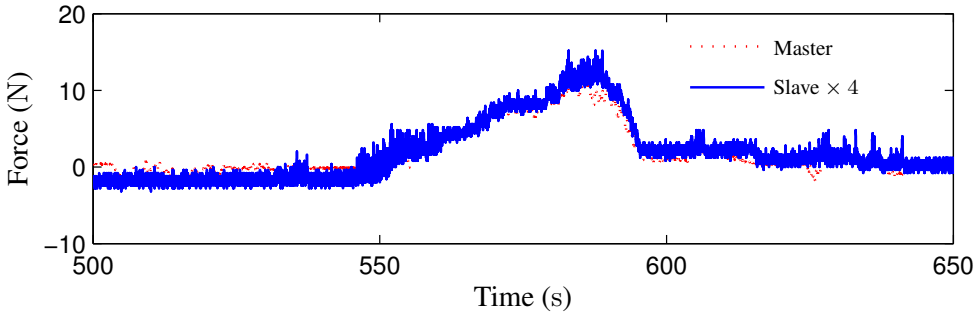

(b) Response of feedback force along insertion direction

Figure 5.3: Experimental result of the teleoperation system under free manipulation for needle insertion [97].

A needle insertion task has also been performed on a piece of foam (expanded polystyrene (EPS)). The needle used in this test is a customized 8 gauge aluminum needle and the resultant curves are shown in Figure 5.3. The slave insertion depth is scaled down by a factor of 4 since precise insertion depth is desired. This also mitigated the issue that the needle driver of the slave robot has a limited insertion speed, while tracking errors are still present during the process, as shown in Figure 5.3(a). To enhance the feedback force feeling during needle insertion, the force is scaled up by a factor of 4, and the noisy force data matches well in Figure 5.3(b).

These two experiments demonstrated the successful integration and control of the master and the slave robots to achieve the teleoperated surgical system.

5.4 Development of the GUI

The master robot provides an intuitive means for the physician to operate the slave robot; yet it is necessary to develop an appropriate graphical user interface (GUI) for the tele-operation system, since the master robot does not duplicate the motion of the slave robot and it is beneficial for the physician to be able to visualize the configuration of the slave robot.

A GUI program has been developed under the Qt framework, and a screenshot of this program is shown in Figure 5.4. The dialog interface is divided into three areas:

- The Graphical Display area: The CAD model of the slave robot is displayed here using Open Graphics Library (OpenGL). The configuration of the CAD model are determined either from the widgets in the Command Input area, or by the actual master robot configuration when network connection has been established between the master control PC and this program.

- The Command Input area: The widgets that can take input to change the behaviour of the program or the display of the slave CAD model are gathered here. The inputs implemented in the current version include the view point and view position parameters of the graphical display, the actuator parameters of the slave robot, and the button to establish network connection with the master control PC.

- The System Prompt area: The output messages that indicate the status of the program can be display here. Those messages are mainly for debugging purposes.

The primary function of this program is to display the CAD model of the slave robot

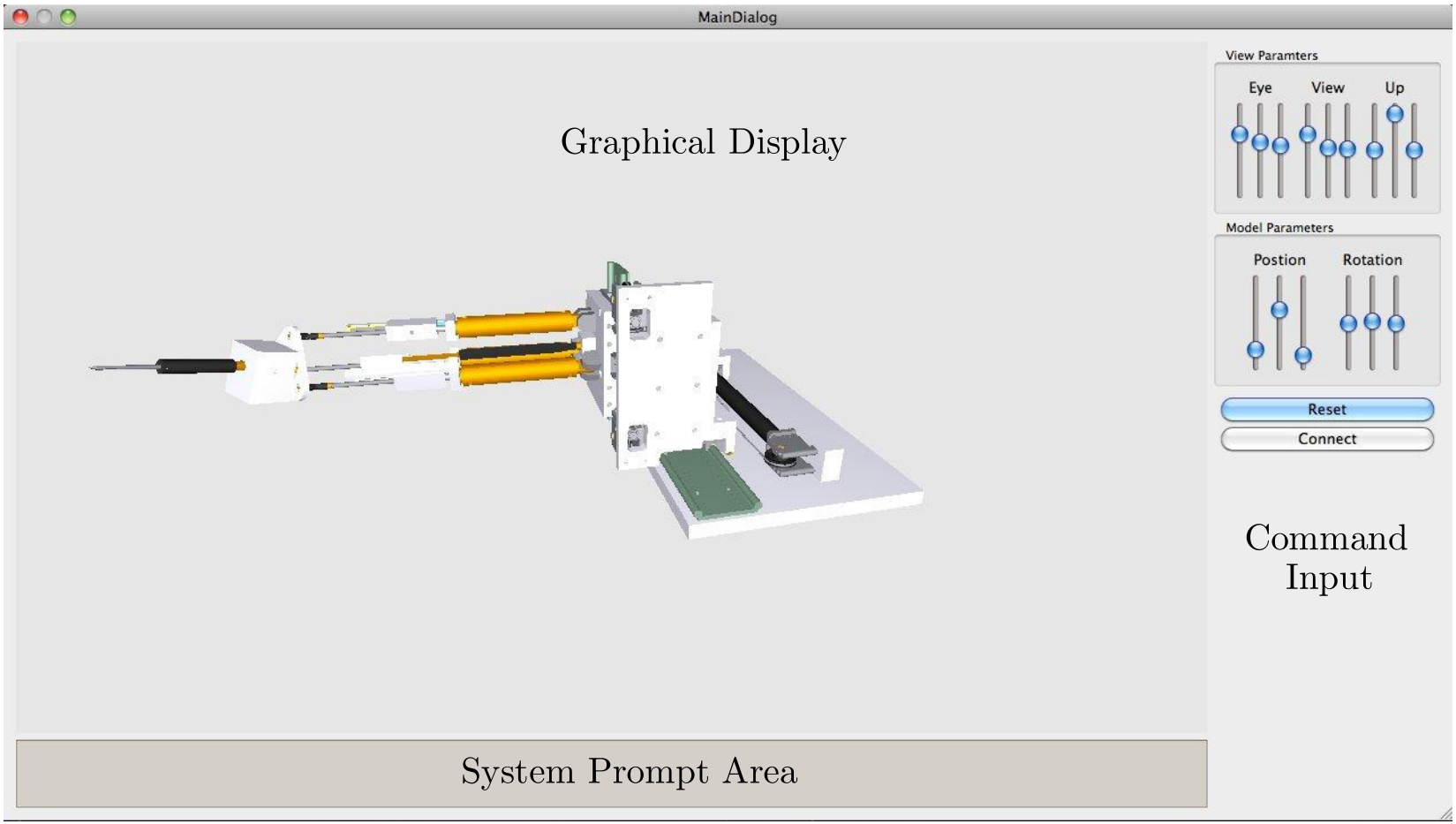

Figure 5.4: The graphical user interface of the teleoperation system

with configuration commanded by the master robot and provides intuitive visual feedback to the physician. This program is designed to be able to connect to both the master and the slave control PCs. When it is connected only to the slave control PC, the slave robot can also be controlled using this GUI program. If both the slave and the master control PCs are connected, this program displays the configuration of the slave robot in real-time for monitoring purpose only, and the slave robot is controlled using the master robot.

Potentially, this GUI can also display the target lesion with the surrounding tissue according to the MR images acquired, along with the CAD model of the slave robot using the configuration information acquired from the slave robot sensors. This can give the physician a better understanding of the relative position of the slave robot and its needle with respect to the target location. This program can also implement the feature that performs online simulation for the slave robot according to the instantaneous commanded configuration sent from the master robot. By superposition, both the simulated and the instantaneous configuration of the slave robot can be displayed together to compensate for the slow response of the slave robot due to its pneumatic actuation through long transmission lines, as suggested in [159]. Complicated kinematics computation can also be implemented such that the needle orientation change can be done by rotating the needle about any designated spatial point including the incision point.

The features mentioned above are the possible ways of taking advantage of this GUI. Along with the interface developed for the MRI scanner, this program can be very helpful to apply the teleoperation system in clinical applications.

5.5 Summary

In this chapter the integration of the master robot and the slave robot into a teleoperation system is presented, with which breast biopsy inside the MRI bore can be performed by manipulating it remotely from inside the control room. The control strategy of the teleoperation system has been discussed, and the experimental evaluation shows that the teleoperation system is operational with reasonable dynamic performance. A GUI program is then developed and can provide an intuitive visual feedback to the physician on the real-time configuration of the slave robot. Various possibilities to take advantage of the developed GUI program have also been presented in this chapter. Further experimental evaluation on the integrated master-slave surgical system will be present in the following chapter.

Chapter 6

Experimental Evaluation of the Master-Slave System

In the previous chapters, evaluation tests have been conducted on different aspects of the teleoperated master-slave surgical system. The MRI-compatibility examination of the slave robot has been performed in Chapter 2 and its pneumatic actuation via long transmission lines is presented in Chapter 3. In Chapter 5 the teleoperation system has been integrated and its function validation test has been carried out. Yet, further experiments on the complete teleoperation system needs to be executed to evaluate its overall performance.

To be able to perform the *ex vivo* phantom targeting test and the *in vivo* live animal targeting test, minor modifications on the needle driver of the slave robot has to be preformed. This chapter presents such modifications as well as the detailed results of the aforementioned experiments and is organized as follows: The modification of the slave robot and the MRI-compatibility study of the surgical system under dynamic MR imaging sequence are discussed in Section 6.1. Section 6.2 covers the result of the *ex vivo* phantom targeting experiment while Section 6.3 presents the result of the *in vivo* live animal experiment. Summaries are presented in Section 6.4.

6.1 MRI-Compatibility Evaluation under Dynamic MR Imaging

As shown in the MRI-compatibility evaluation result in Section 2.5, the slave robot does not induce any visually detectable artifact on the MR images. Hence, the position and orientation of the needle is unavailable from the MR images prior to its insertion into the target (tissue). Without such imaging feedback during the initial phase of needle insertion, it has been confirmed in actual prostate brachytherapy procedures that the necessary correction of needle insertion position and / or orientation could be delayed [95]. To acquire those information independent of the robotic device, Rea et al. proposed to apply passive microcoil fiducials on the device to generate artifacts in the MR images, so that the position information can be retrieved by real-time MR image processing [178]. In our implementation, the active MR tracking sensor, called EndoScout® sensor, has been adopted.

The EndoScout® sensor consists of three orthogonal coils. Specialized gradient pulses are embedded into the imaging pulse sequence, and the voltage from these pulses is captured by these coils and digitized at a rate of $20\,\mathrm{Hz}$ and converted to determine the location and orientation of the sensor [179–181]. The sensor, in conjunction with the pulse sequence, is pre-calibrated using a special grid that spans the entire diameter and the length of the MRI scanner bore and converts the signals to spatial location within the MRI machine. The induced voltages in the sensor during actual use are then compared by an optimization algorithm to a previously determined map of the field space to determine the tracking position and orientation of the sensor.

To mount the sensor onto the slave robot and to ensure its proper function, the nee-

dle driver implementation as well as the needle has been modified, as shown in Figure 6.1. Three modifications have been made in this implementation:

1. The fixing tube has been redesigned to mount the EndoScout® sensor;

2. The fixture has been replaced with a plastic version to avoid deteriorating the tracking accuracy of the EndoScout® sensor;

3. The customized 8 gauge aluminum needle is replaced by a needle that is customized from a 12 gauge high field MRI coaxial needle (Invivo, 9896 032 06491) for improved quality of MR images and good penetration capability.

After those modifications, MRI test is performed on the slave robot to verify its MRI-compatibility under dynamic imaging and its impact on the MR image quality. The experimental setup is shown in Figure 6.2 with the slave robot placed inside the MRI bore.

Testing is performed using a $3\,\mathrm{T}$ Tim Trio MR scanner (Siemens Medical Solutions; Malvern, PA) with a breast coil and the phantom used is chicken breast purchased at the local supermarket. Dynamic imaging is used for real-time monitoring of the needle insertion and the imaging sequence used is a rapid gradient echo sequence (FLASH sequence, $T_\mathrm{E}/T_\mathrm{R} = 1.5/4.1 - 8\,\mathrm{ms}$, flip angle $= 10^\circ$, bandwidth $= 1302\,\mathrm{Hz/pixel}$, FoV $= 300 \times 300\,\mathrm{mm}$, matrix $= 192 \times 192$, slice thickness $= 3\,\mathrm{mm}$). The dynamic MR images are acquired under various scenarios throughout the procedure of performing a needle insertion task, namely: a) when only the phantom is present in the MRI bore; b) when the robot is put in the MRI bore without any power; c) when the robot is powered on and holding its position; d) when the robot is actuated by its pneumatic actuators to

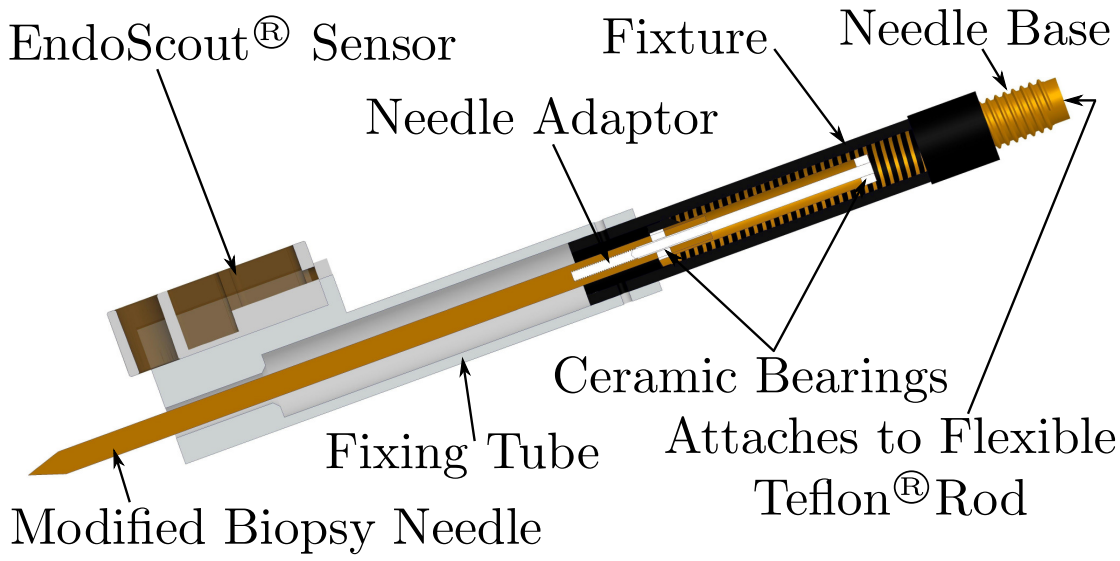

(a) The CAD drawing of the modified needle driver

(b) The actual photo of the modified needle driver

Figure 6.1: The modified needle driver that can mount the EndoScout® MR sensor

adjust the needle insertion position and orientation; e) when the piezo motor is actuated to perform needle insertion; f) when the robot is retracting the needle; g) when the needle is fully retracted from the phantom; and h) when the robot is powered off at the end of the procedure. All images can be clearly depicted with no visually-detectable distortion or difference, as shown in Figure 6.3.

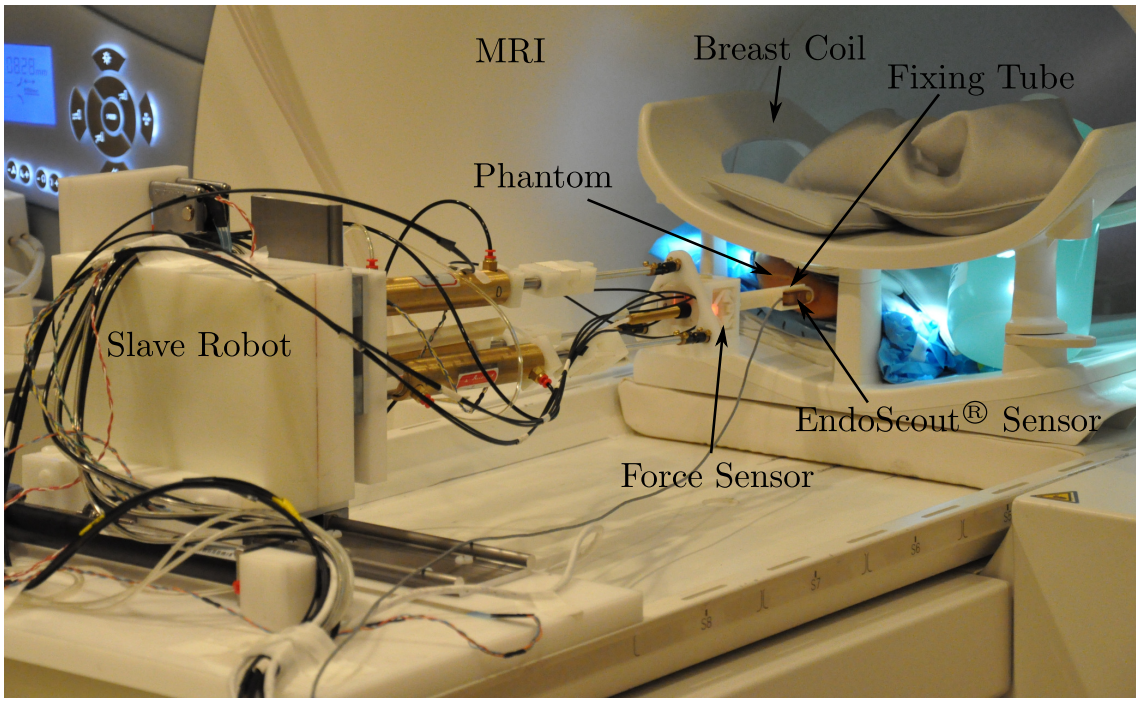

Figure 6.2: Experimental setup for the MRI-compatibility evaluation in the MRI

Table 6.1: SNRs of the dynamic MR images under various scenarios with ROIs defined in Figure 6.3

Scenarios	Dynamic Image SNR
a	18.85 ± 0.32
b	18.80 ± 0.34
c	18.45 ± 0.36
d	18.31 ± 0.32
e	18.78 ± 0.34
f	18.54 ± 0.29
g	19.63 ± 0.38
h	19.61 ± 0.14

The SNR values in Table 6.1 and the SNR curves in Figure 6.4 show consistent SNR change. When the robot is placed inside the MRI bore a negligible SNR drop can be

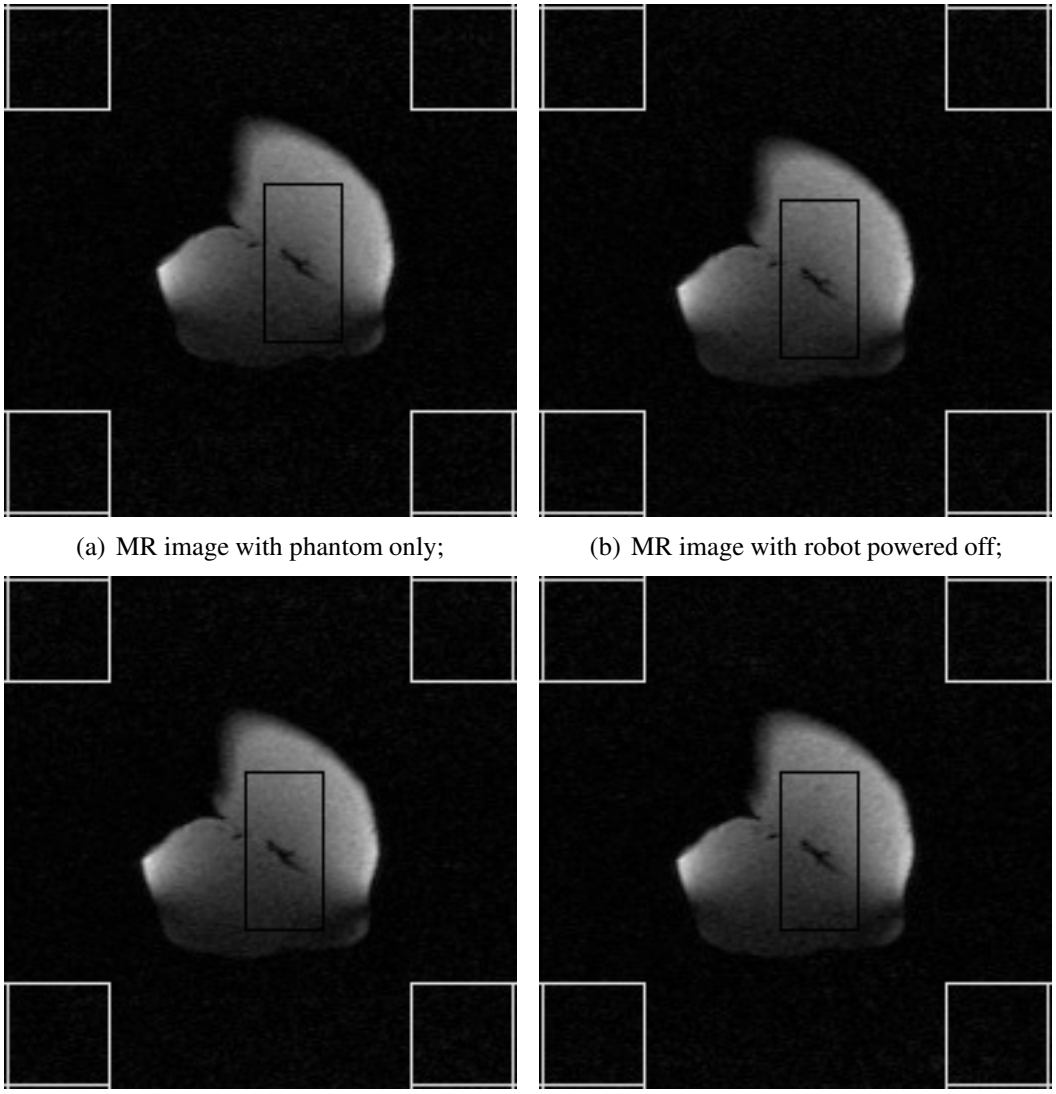

(a) MR image with phantom only; (b) MR image with robot powered off; (c) MR image with robot powered on; (d) MR image with robot targeting with pneumatic actuation;

Figure 6.3: Dynamic MR images under various scenarios throughout a needle insertion task. (continued)

observed. Powering on the robot and actuating the robot pneumatically also lead to SNR losses that are small enough to be neglected. The SNR values in Figure 6.4(e), (g) and (h) are slightly higher than those of the other five images. That is due to the $6\,\mathrm{mm}$ change of slice position at which the MR images are taken in order to make the needle in plane. Throughout the complete procedure under different actuation conditions, the variation of

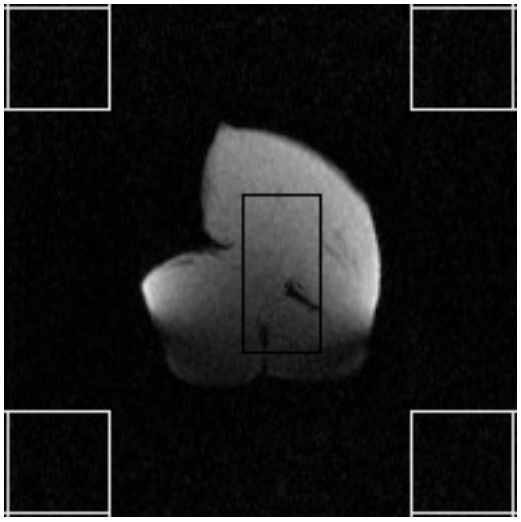

(e) MR image with robot inserting needle with piezo actuation;

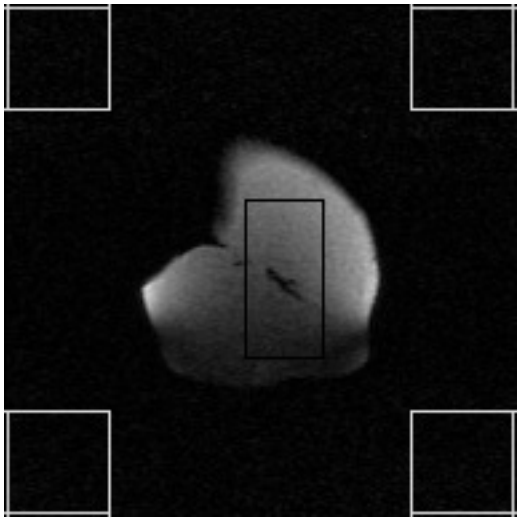

(f) MR image with robot retracting needle with piezo actuation;

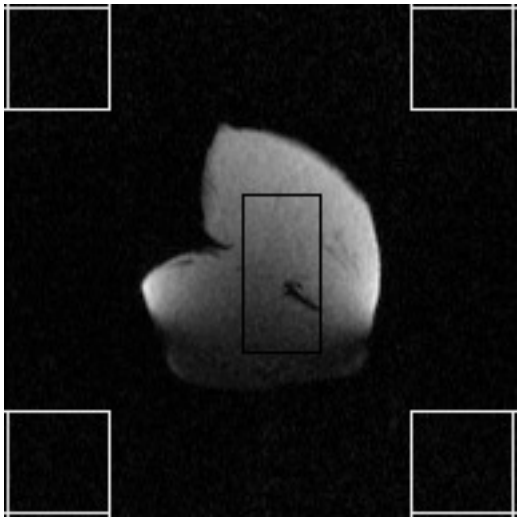

(g) MR image with robot retracted needle from the phantom;

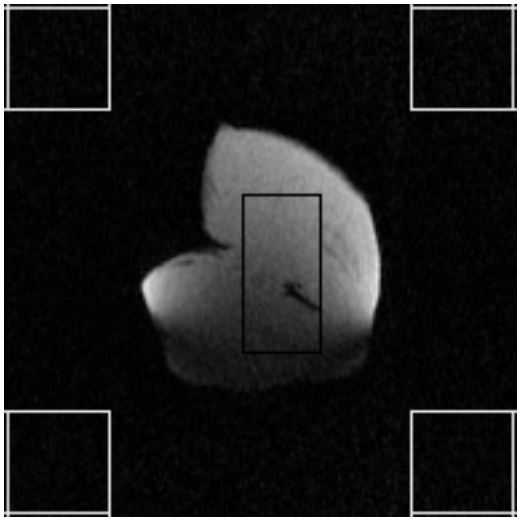

(h) MR image with robot powered off;

Figure 6.3: (continued) Dynamic MR images under various scenarios throughout a needle insertion task.

the SNR values is less than 8% even with the spatial variation present.

The acquired MR images and the SNR analysis show that the slave robot does not induce significant image distortion which cause severe degradation in the image quality. Hence, it can be safely operated inside the scanner with only minimal loss in SNR.

To further test the effect of the robot within the magnetic field with respect to the

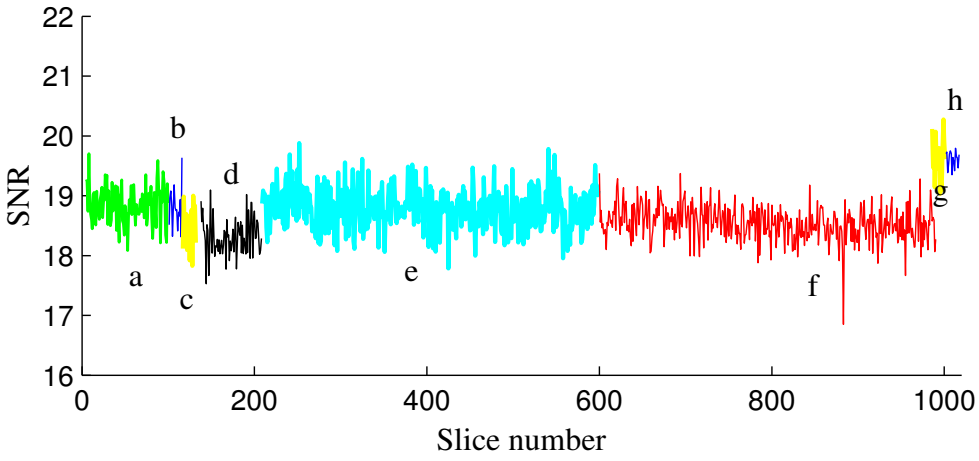

Figure 6.4: The SNR curve of the dynamic MR images throughout the MRI-compatibility test: the letters denote the aforementioned scenarios under which the dynamic images are acquired.

object being imaged, the field homogeneity maps are generated using a large uniform chicken breast and the distance of the slave robot to the slice being imaged are varied. The distance of the slave robot measured from the fixing tube of the needle driver towards the imaging volume varies from $25\,\mathrm{cm}$ to $5.5\,\mathrm{cm}$. Figure 6.5 shows the phase images from the chicken breast and are reflective of the field inhomogeneity. As can be seen from Figure 6.5 the field is very uniform (with frequency shift less than 10 part per million (ppm)) when the slave robot is not on the table (top left image) and when the slave robot is $25\,\mathrm{cm}$ away from the imaging slice. However, this uniformity is disturbed at the periphery of the phantom as the distance between the imaging volume and the slave robot decreases. The field inhomogeneities increase to as high as 40 ppm mainly at the periphery of the phantom while preserving the homogeneity at the center. Such field inhomogeneities have the potential to induce error greater than $5\,\mathrm{mm}$ into the tracking sensor.

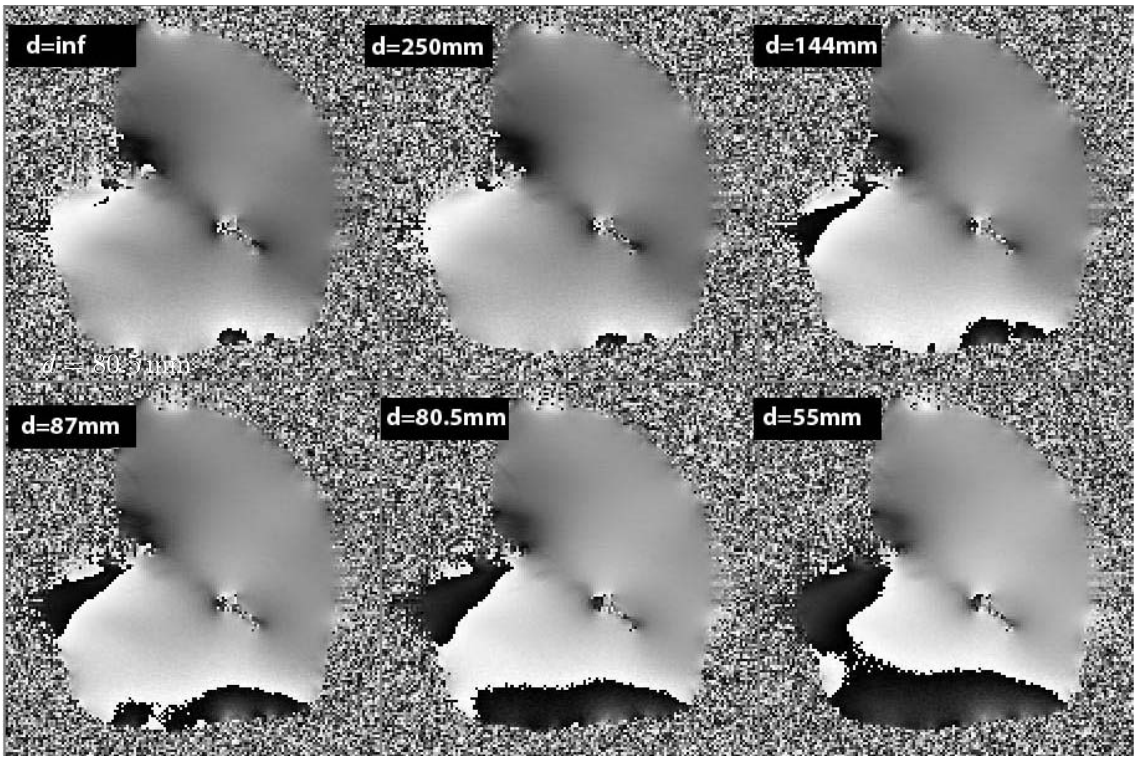

Figure 6.5: Phase images of the chicken breast with the slave robot at various distances from the phantom. Note that the base of the slave robot is $56.5\,\mathrm{cm}$ from the tip of the fixing tube of the robot. Field inhomogeneities increase as the distance between the slave robot and the imaging area of interest decreases. Changes in field homogeneity also affect the tracking accuracy of the EndoScout®.

6.2 *Ex Vivo* Targeting Test under MR Guidance

Along with the experimental confirmation of the MRI-compatibility of the slave robot, experiments have been performed multiple times using samples of either the chicken breast (three insertions) or a pig's thigh (four insertions) bought at the local supermarket that fit between the top and bottom part of a 4-channel breast coil. Markers are placed into the meat samples by placing $\mathrm{M4} \times 0.7 \times 15\,\mathrm{mm}$ plastic screws (three in the chicken breast and four in the pig thigh sample) at various locations. The leading tip of the plastic screw is considered the target and these targets are approached through robotic intervention from different angles. To perform robot-assisted biopsy under MRI guidance, a series of high resolution anatomical images are acquired and used to identify a target location in three orthogonal planes ($T_\mathrm{E}/T_\mathrm{R} = 2.46/440\,\mathrm{ms}$, flip angle $= 87^\circ$, matrix $= 192 \times 192 \times 35$, slice thickness $= 3\,\mathrm{mm}$, $0.78\,\mathrm{mm}$ in-plane resolution). From these images, along with identifying the target point, the point of insertion is also identified. Once the MRI coordinates for the point of insertion are determined, the robot is directed to that location in a manner that the trajectory of the robot is in line with the point of entry and the target within the image. Throughout this process, the location of the fixing tube is continuously monitored from the EndoScout® sensor as shown in Figure 6.6.

Once the robot is in place, additional imaging is performed to determine the plane of traversal for the needle towards the target using the same high-resolution imaging as described above. Tracking is then performed using rapid gradient echo sequence using 1-3 slices (FLASH sequence, $T_\mathrm{E}/T_\mathrm{R} = 1.5/4.1{-}8\,\mathrm{ms}$, flip angle $= 10^\circ$, matrix $= 192 \times 192$, slice thickness $= 3\,\mathrm{mm}$, $1.56\,\mathrm{mm}$ in-plane resolution) to ensure that the needle reaches

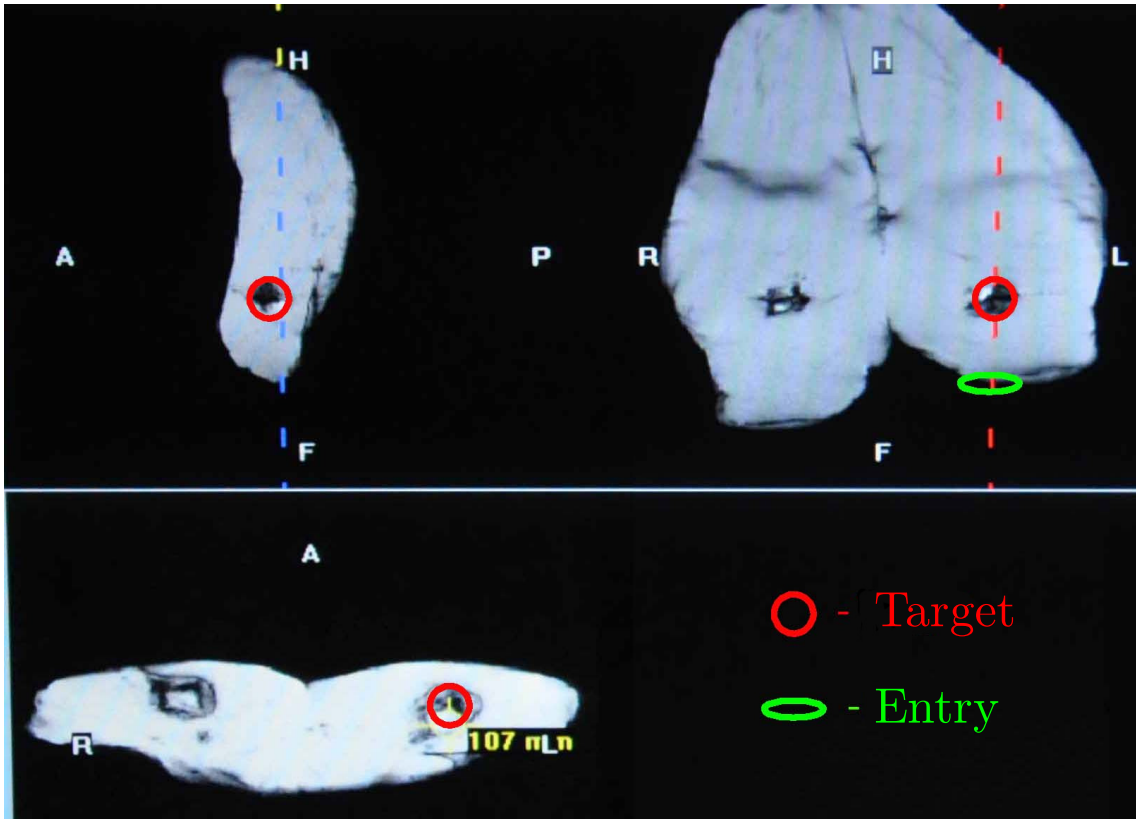

Figure 6.6: Sagittal (top left), coronal (top right), and axial (bottom) MR images displaying the target in red circle within chick breast. The green oval shows the entry point where the robot is guided to in a manner that it is directed towards the target as shown in the coronal image.

its target. The result of the last trial insertion into the chicken breast to reach the target point from the surface of the skin is shown in Figure 6.7.

As shown in Figure 6.7, the top left image presents the embedded plastic screw, the tip of which serves as the target, as well as the entry point for the robot. Advancement of the needle is shown under continuous MRI imaging guidance in the next few frames. Image on the bottom left shows the needle reaching the target with excellent accuracy, and further advancement of the needle tilts the target as shown by the blue arrows in subsequent frames. The targeting error is considered as $0\,\mathrm{mm}$, and the time it takes from

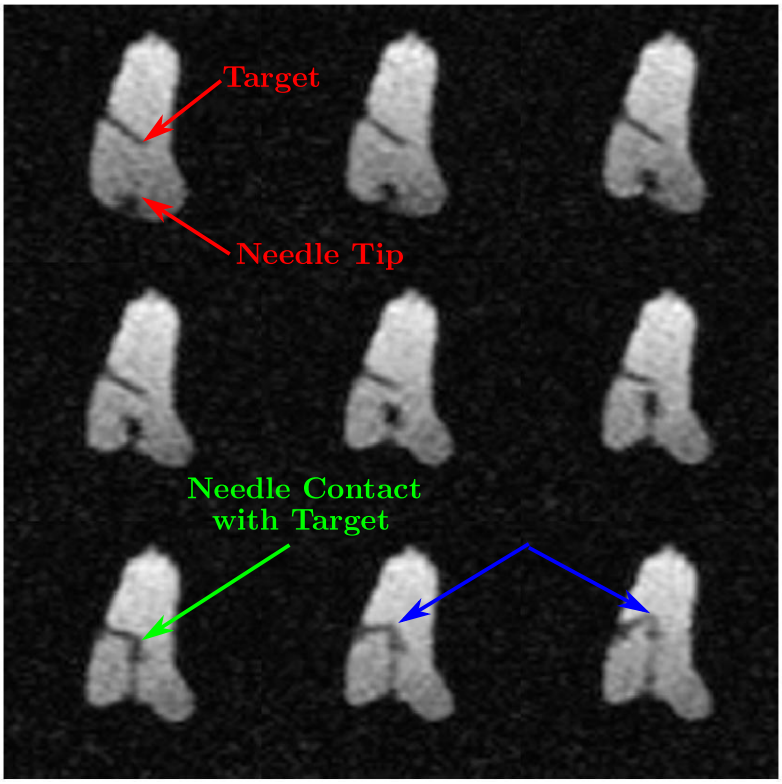

Figure 6.7: Selected nine frames from continuous MRI as the needle approaches the target. The Invivo MRI coaxial needle hits the target directly in the bottom left image.

taking the registration MR images till the needle hit the target is approximately 21 minutes in this trial.

Prior to the aforementioned needle insertion experiment, six insertion trials have been performed in total. The first four trials have been performed on a pig's thigh mainly to evaluate the targeting accuracy of the surgical system, while the other two trials along with the one described above have been performed on the chicken breast to evaluate the procedure time of the surgical system in addition to its targeting accuracy. The result of each insertion is listed as follows:

1. The experimental result of the first trial insertion is shown in Figure 6.8. Figure 6.8(a) shows three representative frames from the continuous MR images monitoring in the sagittal view as the needle approaches the target: the left image shows the target screw along with the needle at the entry point; the middle image shows the needle touches the tip of the embedded screw; and the right image shows that the screw has been pushed by the needle and tilts towards the direction of needle insertion. The axial MR image and the zoom-in sagittal MR image shown in Figure 6.8(b) and (c) further confirm that the needle is in contact with the target screw. This demonstrates the accurate targeting capability considering the $5\,\mathrm{mm}$ slice thickness of the tracking MR images and the $4\,\mathrm{mm}$ diameter of the target screw. The needle is deemed to slip away from the screw after contact and the targeting error is determined to be $0\,\mathrm{mm}$.

2. The experimental result of the second trial insertion is shown in Figure 6.9. Figure 6.9(a) shows three representative frames from the continuous MR images monitoring in the coronal view as the needle approaches the target of the screw tip: the left image shows the target screw along with the needle at the entry point; the middle image shows the needle touches the embedded screw; and the right image shows that the screw has been pushed by the needle and moves along the direction of needle insertion. The static MR images taken in the axial and coronal views shown in Figure 6.9(b) and (c) further confirm that the needle is in contact with the target screw. Figure 6.9(b) shows that the needle reaches the target screw in the center along its length and is measured to be $8.2\,\mathrm{mm}$ above the targeted screw tip.

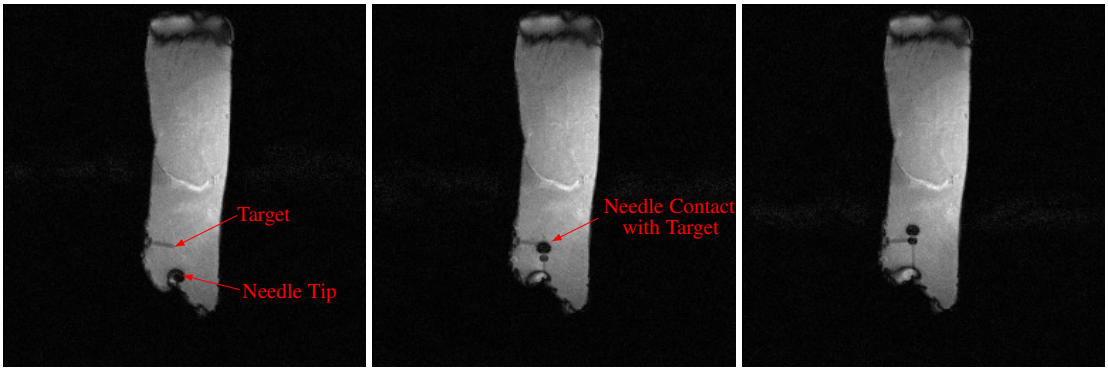

(a) Selected three frames from continuous MRI monitoring in the sagittal view as the needle approaches the target. The imaging sequence parameters are $T_{\mathrm{E}}/T_{\mathrm{R}} = 1.89/3.77\,\mathrm{ms}$, flip angle $= 45°$, bandwidth $= 977\,\mathrm{Hz/pixel}$, FoV $= 256 \times 256\,\mathrm{mm}$, matrix $= 256 \times 256$, slice thickness $= 5\,\mathrm{mm}$.

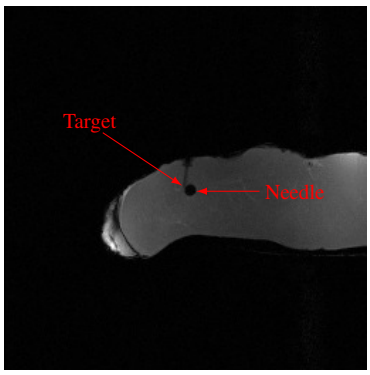

(b) The axial MR image that verifies the needle scraping against the screw. The imaging sequence parameters are $T_{\mathrm{E}}/T_{\mathrm{R}} = 1.89/3.77\,\mathrm{ms}$, flip angle $= 45°$, bandwidth $= 977\,\mathrm{Hz/pixel}$, FoV $= 256 \times 256\,\mathrm{mm}$, matrix $= 256 \times 256$, slice thickness $= 5\,\mathrm{mm}$.

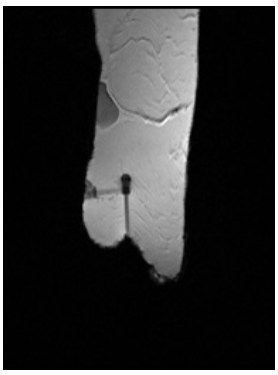

(c) The sagittal MR image that verifies the needle scraping against the needle. The imaging sequence parameters are $T_{\mathrm{E}}/T_{\mathrm{R}} = 2.46/440\,\mathrm{ms}$, flip angle $= 87°$, bandwidth $= 320\,\mathrm{Hz/pixel}$, FoV $= 150 \times 200\,\mathrm{mm}$, matrix $= 192 \times 256$, slice thickness $= 3\,\mathrm{mm}$.

Figure 6.8: MR images taken as the needle approaches the target in the pig's thigh in the first insertion trial.

This is reasonable considering the fact that the needle is able to reach the screw accurately in the tracking image plane, as shown in Figure 6.9(c). This can also be excused by the fact that the slice thickness of the tracking MR images is $5\,\mathrm{mm}$, yet it suggests that single plane MR image tracking is not sufficient to ensure accurate needle insertion. The targeting error in this trial is determined to be $8.2\,\mathrm{mm}$.

3. The experimental result of the third trial insertion is shown in Figure 6.10. Fig-

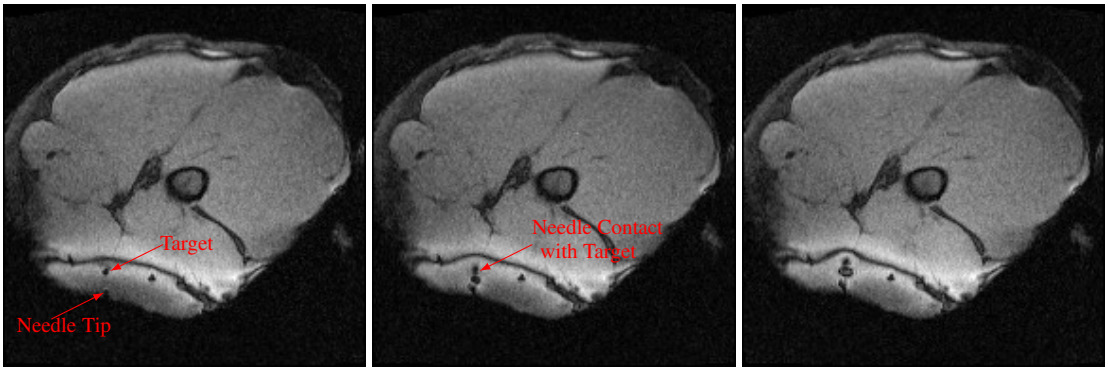

(a) Selected three frames from continuous MRI monitoring in the coronal view as the needle approaches the target. The imaging sequence parameters are $T_{\mathrm{E}}/T_{\mathrm{R}}/T_{\mathrm{I}} = 1.15/2452.7/2200\,\mathrm{ms}$, flip angle $= 20^{\circ}$, bandwidth $= 1532\,\mathrm{Hz/pixel}$, FoV $= 300 \times 300\,\mathrm{mm}$, matrix $= 192 \times 192$, slice thickness $= 5\,\mathrm{mm}$.

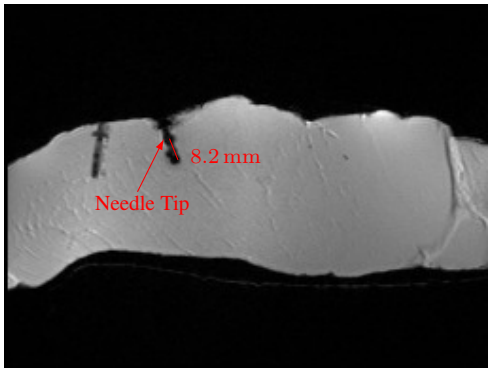

(b) The axial MR image that verifies the needle pushes against the screw at its center in length. The distance from the needle to the tip of the screw is measured to be $8.2\,\mathrm{mm}$. The imaging sequence parameters are $T_{\mathrm{E}}/T_{\mathrm{R}} = 2.46/440\,\mathrm{ms}$, flip angle $= 87^{\circ}$, bandwidth $= 320\,\mathrm{Hz/pixel}$, FoV $= 200 \times 150\,\mathrm{mm}$, matrix $= 256 \times 192$, slice thickness $= 3\,\mathrm{mm}$.

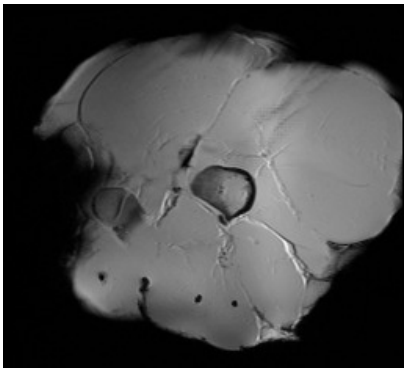

(c) The coronal MR image that verifies the needle pushes against the needle. The imaging sequence parameters are $T_{\mathrm{E}}/T_{\mathrm{R}} = 2.46/440\,\mathrm{ms}$, flip angle $= 90^{\circ}$, bandwidth $= 320\,\mathrm{Hz/pixel}$, FoV $= 253 \times 280\,\mathrm{mm}$, matrix $= 232 \times 256$, slice thickness $= 3\,\mathrm{mm}$.

Figure 6.9: MR images taken as the needle approaches the target in the pig's thigh in the second insertion trial.

ure 6.10(a) shows one of the continuous MR images monitoring in the coronal view. As shown in the image, the needle is slightly off the target screw and passes by it with an offset. This is shown more evidently in Figure 6.10(b) where a static MR image in the same coronal view but with a higher resolution has been taken after the needle was further inserted into the phantom. The targeting error in this case is measured to be $3.6\,\mathrm{mm}$.

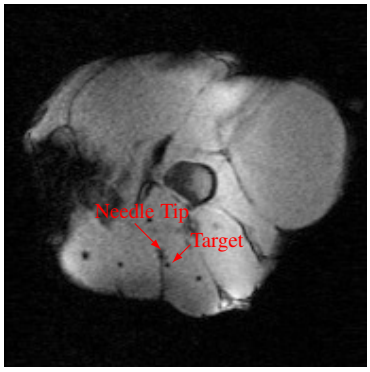

(a) The dynamic coronal MR image taken after the needle passes by at $3.6\,\mathrm{mm}$ from the target screw. The imaging sequence parameters are $T_\mathrm{E}/T_\mathrm{R} = 1.51/4.1\,\mathrm{ms}$, flip angle $= 10°$, bandwidth $= 1302\,\mathrm{Hz/pixel}$, FoV $= 300 \times 300\,\mathrm{mm}$, matrix $= 192 \times 192$, slice thickness $= 3\,\mathrm{mm}$.

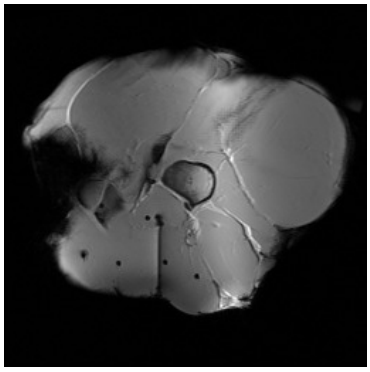

(b) The static coronal MR image that verifies the relative position of the needle with respect to the target screw. The imaging sequence parameters are $T_\mathrm{E}/T_\mathrm{R} = 2.46/440\,\mathrm{ms}$, flip angle $= 87°$, bandwidth $= 320\,\mathrm{Hz/pixel}$, FoV $= 300 \times 300\,\mathrm{mm}$, matrix $= 256 \times 256$, slice thickness $= 3\,\mathrm{mm}$.

Figure 6.10: MR images taken as the needle approaches the target in the pig's thigh in the third insertion trial.

4. The experimental result of the fourth trial insertion is shown in Figure 6.11. Figure 6.11(a) shows three representative frames from the continuous MR images monitoring in the sagittal view as the needle approaches the target of the screw tip: the left image shows the target screw along with the needle at the entry point; the middle image shows the needle touches the embedded screw; and the right image shows that the screw has been pushed by the needle and moves along the direction of needle insertion. The needle is vaguely shown in these images since it is slightly off the imaging plane, as shown in Figure 6.11(b) and (c). The static MR images taken in the coronal view shown in Figure 6.11(b) confirms that the needle is in close proximity with the target screw. This is further verified in Figure 6.11(c) where the needle was replaced with an MRI marker to capture a clearer needle trace. The targeting error in this trial is determined to be $3.2\,\mathrm{mm}$.

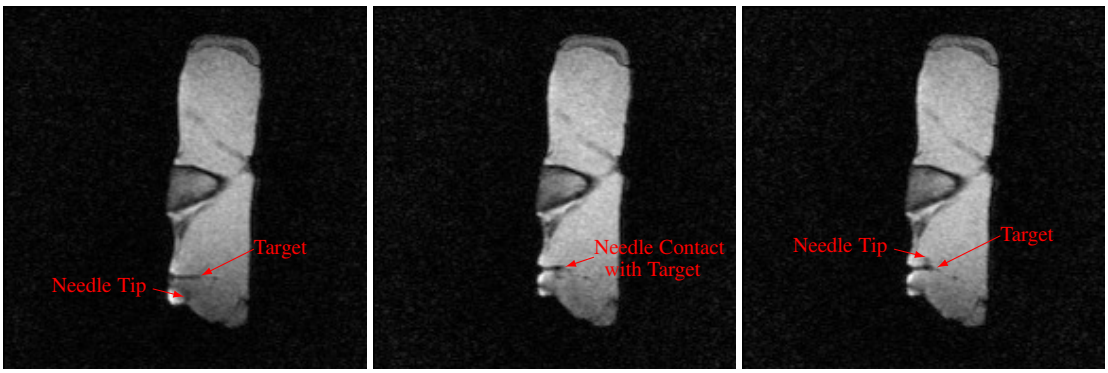

(a) Selected three frames from continuous MRI monitoring in the sagittal view as the needle approaches the target. The imaging sequence parameters are $T_{\mathrm{E}}/T_{\mathrm{R}} = 1.51/4.1\,\mathrm{ms}$, flip angle $= 10°$, bandwidth $= 1302\,\mathrm{Hz/pixel}$, FoV $= 300 \times 300\,\mathrm{mm}$, matrix $= 192 \times 192$, slice thickness $= 3\,\mathrm{mm}$.

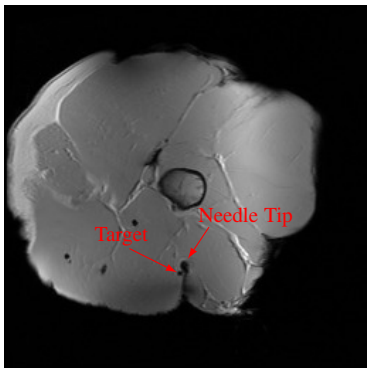

(b) The coronal MR image that shows the relative position of the needle with respect to the target screw. The imaging sequence parameters are $T_{\mathrm{E}}/T_{\mathrm{R}} = 2.46/440\,\mathrm{ms}$, flip angle $= 87°$, bandwidth $= 320\,\mathrm{Hz/pixel}$, FoV $= 300 \times 300\,\mathrm{mm}$, matrix $= 256 \times 256$, slice thickness $= 3\,\mathrm{mm}$.

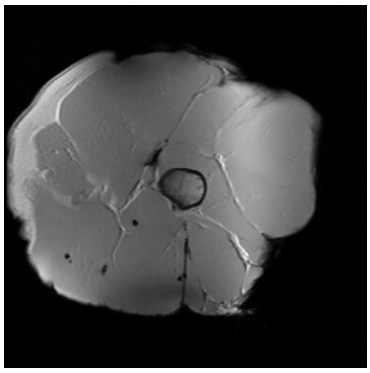

(c) The coronal MR image that confirms the needle position after replacing the needle with an MRI marker through the guiding cannula. The imaging sequence parameters are $T_{\mathrm{E}}/T_{\mathrm{R}} = 2.46/440\,\mathrm{ms}$, flip angle $= 87°$, bandwidth $= 320\,\mathrm{Hz/pixel}$, FoV $= 300 \times 300\,\mathrm{mm}$, matrix $= 256 \times 256$, slice thickness $= 3\,\mathrm{mm}$.

Figure 6.11: MR images taken as the needle approaches the target in the pig's thigh in the fourth insertion trial.

5. The experimental result of the fifth trial insertion is shown in Figure 6.12. Figure 6.12(a) shows three representative frames from the continuous MR images monitoring in the sagittal view as the needle approaches the target of the screw tip: the left image shows the target screw along with the needle at the entry point; the middle image shows the needle touches the embedded screw; and the right image shows that the screw has been pushed by the needle and moves along the direc-

tion of needle insertion. The static MR images taken in the coronal view shown in Figure 6.12(b) and in the sagittal view shown in Figure 6.12(c) confirm the needle position relative to the target by replacing the needle with an MRI marker through the guiding cannula. The targeting error in this trial is determined to be $0\,\mathrm{mm}$ and the procedure time from taking the registration MR images till the needle hit the target is approximately 24 minutes.

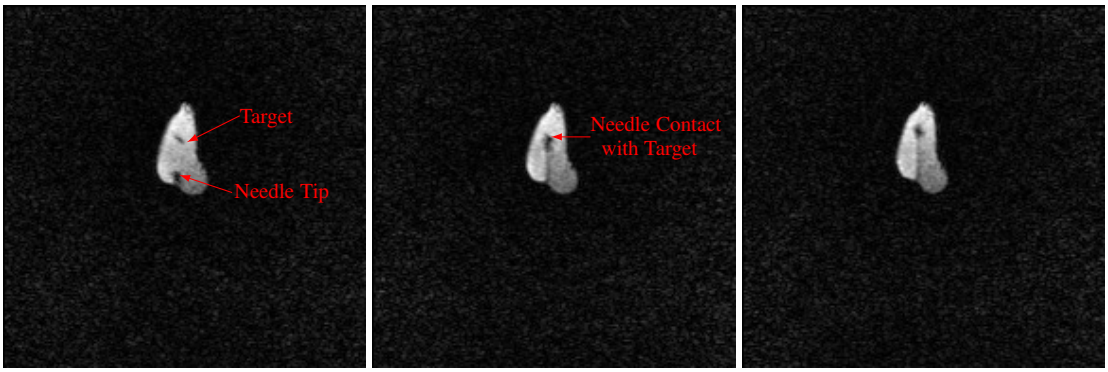

(a) Selected three frames from continuous MRI monitoring in the sagittal view as the needle approaches the target. The imaging sequence parameters are $T_\mathrm{E}/T_\mathrm{R} = 1.51/4.1\,\mathrm{ms}$, flip angle $= 10^\circ$, bandwidth $= 1302\,\mathrm{Hz/pixel}$, FoV $= 300 \times 300\,\mathrm{mm}$, matrix $= 192 \times 192$, slice thickness $= 3\,\mathrm{mm}$.

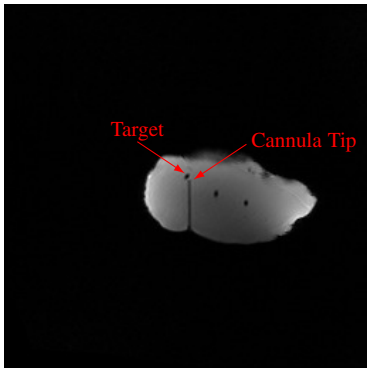

(b) The coronal MR image that verifies the needle position after replacing the needle with an MRI marker through the guiding cannula. The imaging sequence parameters are $T_\mathrm{E}/T_\mathrm{R} = 2.46/440\,\mathrm{ms}$, flip angle $= 87^\circ$, bandwidth $= 320\,\mathrm{Hz/pixel}$, FoV $= 300 \times 300\,\mathrm{mm}$, matrix $= 256 \times 256$, slice thickness $= 3\,\mathrm{mm}$.

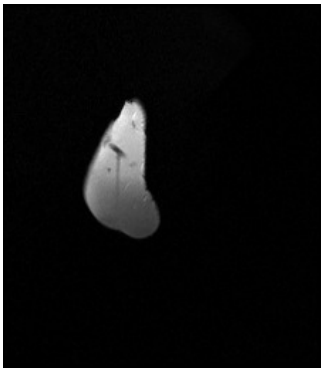

(c) The sagittal MR image that verifies the needle position after replacing the needle with an MRI marker through the guiding cannula. The imaging sequence parameters are $T_\mathrm{E}/T_\mathrm{R} = 2.46/440\,\mathrm{ms}$, flip angle $= 90^\circ$, bandwidth $= 320\,\mathrm{Hz/pixel}$, FoV $= 175 \times 200\,\mathrm{mm}$, matrix $= 224 \times 256$, slice thickness $= 4\,\mathrm{mm}$.

Figure 6.12: MR images taken as the needle approaches the target in the chicken breast in the fifth insertion trial.

6. The experimental result of the sixth trial insertion is shown in Figure 6.13. Figure 6.13(a) shows three representative frames from the continuous MR images monitoring in the sagittal view as the needle approaches the target of the screw tip: the left image shows the target screw along with the needle at the entry point; the middle image shows the needle touches the embedded screw; and the right image shows that the screw has been scraped by the needle and moves along the direction of needle insertion. The static MR images taken in the coronal view with the needle shown in Figure 6.13(b) and with the MRI marker inserted through the guiding cannula shown in Figure 6.13(c) confirm the needle position relative to the target. The targeting error in this trial is determined to be $0\,\mathrm{mm}$ and the procedure time from taking the registration MR images till the needle hit the target is approximately 17 minutes.

As summarized in Table 6.2, the robot comes within $4\,\mathrm{mm}$ of the target location six times during the seven trials, with the targeting being perfect four times as shown in Figure 6.7, 6.8, 6.12, and 6.13. During the second trial, the target is missed by about $8.2\,\mathrm{mm}$. This error can be attributed to the tissue deformation and movement during the robotic manipulation. The average time from initial imaging to hitting the target for the three trials performed on the chicken breast is 20.67 ± 3.51 minutes.

Force feedback data has also been collected during the seven *ex vivo* targeting trials. Figure 6.14 shows a typical force profile that was obtained in the second trial when the needle was inserted into the pig's thigh. The force along the direction of needle insertion remains zero prior to the needle tissue contact and rises quickly around $t = 3200\,\mathrm{s}$ when

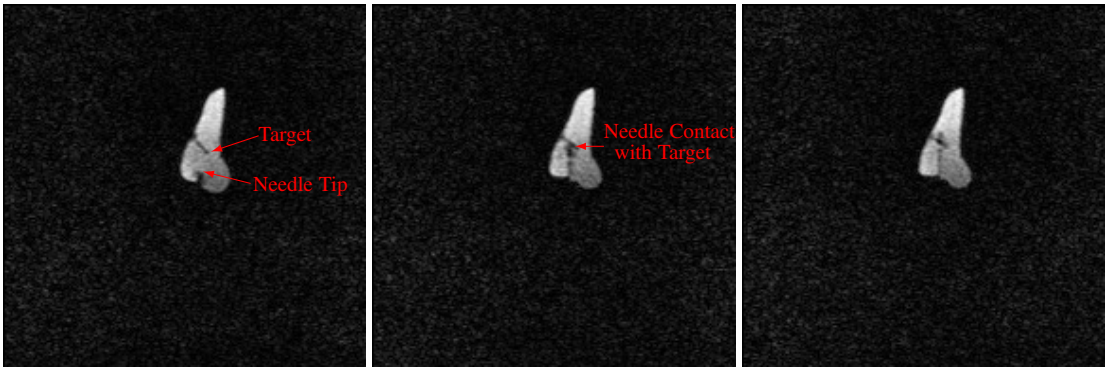

(a) Selected three frames from continuous MRI monitoring in the sagittal view as the needle approaches the target. The imaging sequence parameters are $T_{\mathrm{E}}/T_{\mathrm{R}} = 1.51/4.1\,\mathrm{ms}$, flip angle $= 10^{\circ}$, bandwidth $= 1302\,\mathrm{Hz/pixel}$, FoV $= 300 \times 300\,\mathrm{mm}$, matrix $= 192 \times 192$, slice thickness $= 3\,\mathrm{mm}$.

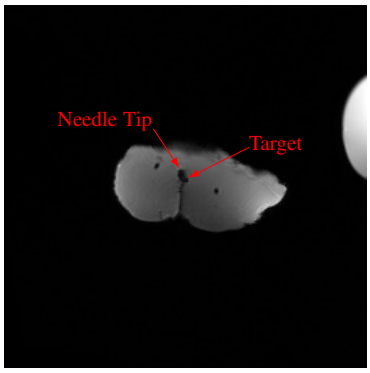

(b) The coronal MR image that shows the needle position relative to the target screw. The imaging sequence parameters are $T_{\mathrm{E}}/T_{\mathrm{R}} = 2.46/440\,\mathrm{ms}$, flip angle $= 87^{\circ}$, bandwidth $= 320\,\mathrm{Hz/pixel}$, FoV $= 300 \times 300\,\mathrm{mm}$, matrix $= 256 \times 256$, slice thickness $= 3\,\mathrm{mm}$.

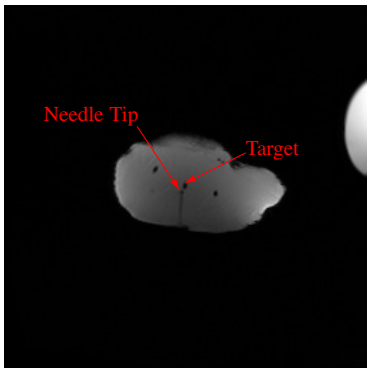

(c) The coronal MR image that verifies the needle position after replacing the needle with an MRI marker. The imaging sequence parameters are $T_{\mathrm{E}}/T_{\mathrm{R}} = 2.46/440\,\mathrm{ms}$, flip angle $= 87^{\circ}$, bandwidth $= 320\,\mathrm{Hz/pixel}$, FoV $= 300 \times 300\,\mathrm{mm}$, matrix $= 256 \times 256$, slice thickness $= 3\,\mathrm{mm}$.

Figure 6.13: MR images taken as the needle approaches the target in the chicken breast in the sixth insertion trial.

the needle is inserted into the tissue. The peak force observed is approximately $1.5\,\mathrm{N}$. After about $t = 1700\,\mathrm{s}$ force drop is observed due to the tissue relaxation and the needle penetrating further into the tissue layers.

Table 6.2: Summary of the seven evaluation tests for the surgical system performing needle insertion under continuous MRI guidance

(a) Targeting error of the seven trials

Trial No.	Error (mm)
1	0.0
2	8.2
3	3.6
4	3.2
5	0.0
6	0.0
7	0.0
Average	2.14 ± 3.12

(b) Procedure time of the last three trials

Trial No.	Time (min)
5	24
6	17
7	21
Average	20.67 ± 3.51

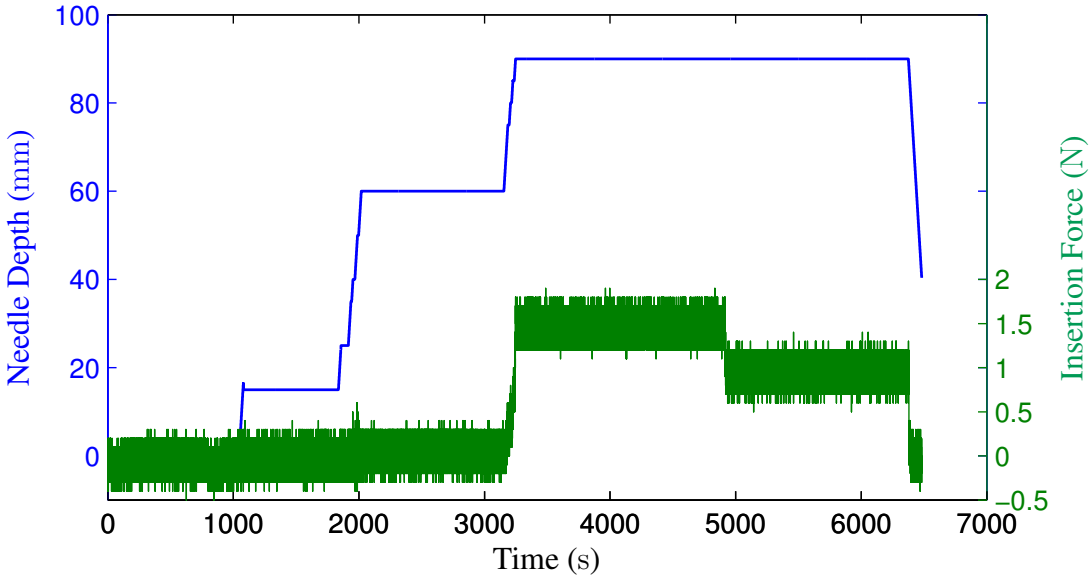

Figure 6.14: Insertion force profile measured when the needle is inserted into the pig's thigh

6.3 *In Vivo* Targeting Test under MR Guidance

After extensive *ex vivo* experiments have been performed using either pig's thigh or chicken breast, *in vivo* experiment using live animal has been conducted to evaluate the master-slave system. Though a few *in vivo* experiments have been conducted and more than one successful experiment has been performed, this section presents the data for only one successful experiment. A Yorkshire pig weighing approximately $48\,\mathrm{kg}$ is used and the protocol has been approved by the Institutional Animal Care and Use Committee (IACUC). The pig is anesthetized using Telazol + xylazine with 0.25% bipuvacaine prior to transporting to the MRI center. Anesthesia is continued as needed while the veterinarian staff monitored the animal during the course of the complete experiment by periodic measurement of blood pressure, heart rate, etc. The pig is placed in the magnet sideways in the head first position as shown in Figure 6.15 and the robotic system is placed at the edge of the magnet on the table top in its default position. An MR visible marker is also attached to the tip of the fixing tube of the slave robot so that identification of its location is possible through MR. An 8-channel body array coil is used to image the pig.

High-resolution images of the thigh muscles of the hind leg are obtained using T_1-weighted FLASH sequence ($T_\mathrm{E}/T_\mathrm{R} = 2.46/440\,\mathrm{ms}$, flip angle $= 87^\circ$, matrix $= 192 \times 192 \times 35$, slice thickness $= 3\,\mathrm{mm}$, $0.78\,\mathrm{mm}$ in-plane resolution), and the targeting location is chosen to be $1.5\,\mathrm{cm}$ anterior to the femoral bone as shown in Figure 6.16(A) in both the coronal and sagittal planes.

Once the target is determined, the best trajectory to the target is chosen and the

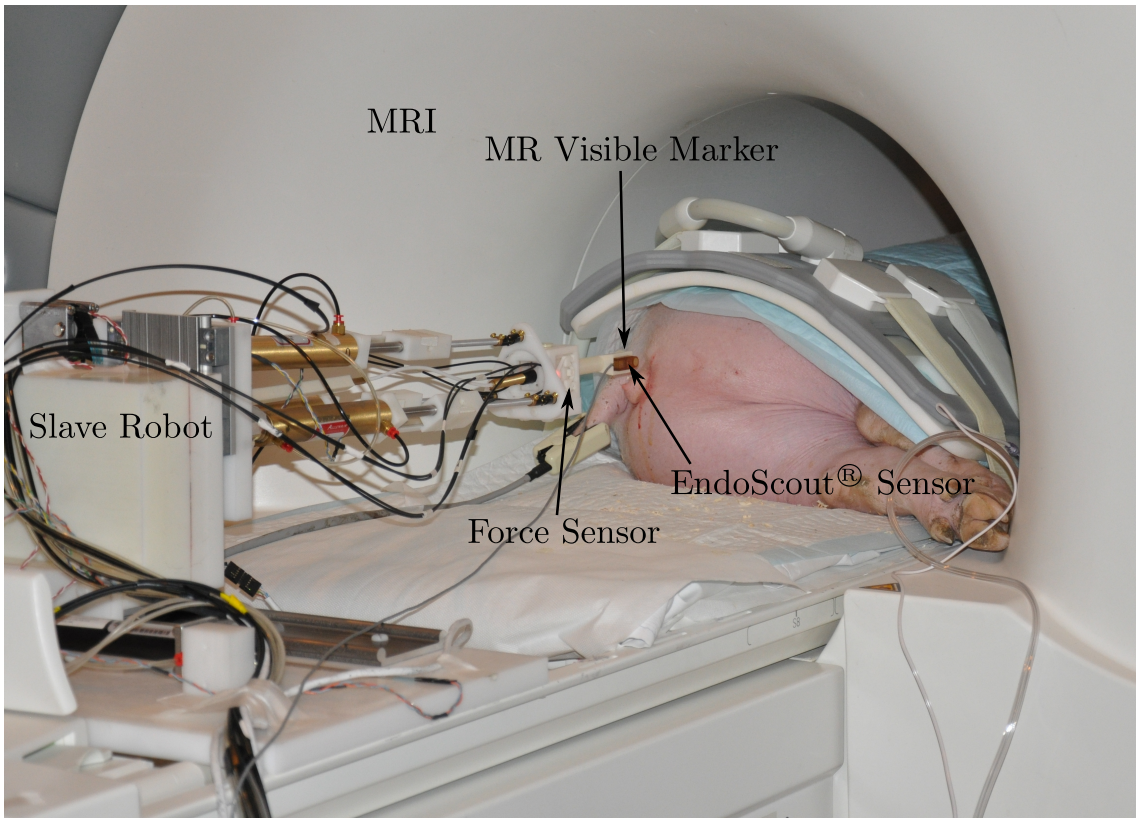

Figure 6.15: *In vivo* experimental setup in the MRI targeting the femoral bone

slave robot is actuated to line up with the target. Figure 6.16 shows the MR visible marker (circled in cyan) in line with the target (circled in red). Also shown in the images is the entry point (green oval) on the pig skin. Once the slave robot is aligned with the target, the MR table is retracted from the center of the magnet bore and an incision is made in the skin at the location the robot is pointing. After the incision is made the pig along with the robot is moved back into the scanner and imaging is resumed. High resolution images are obtained to ensure that the slave robot is still in position to advance the needle towards the target. Dynamic images are then obtained with the slave robot while advancing the needle to the target using rapid imaging sequence (FLASH sequence,

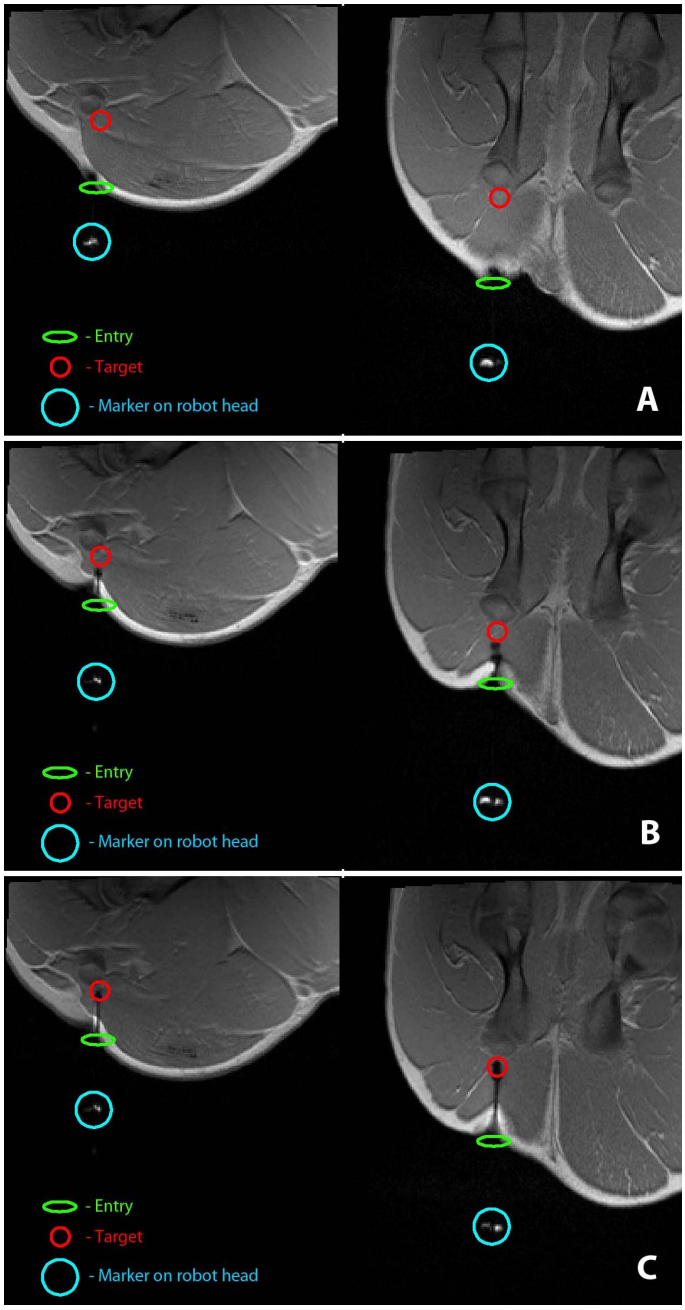

Figure 6.16: High-resolution coronal (left) and sagittal (right) spot images at different phases of targeting: (A) target (red circle) being identified and the robot moved into position to move towards the target; (B) mid-point of targeting; (C) needle reaching the final target location.

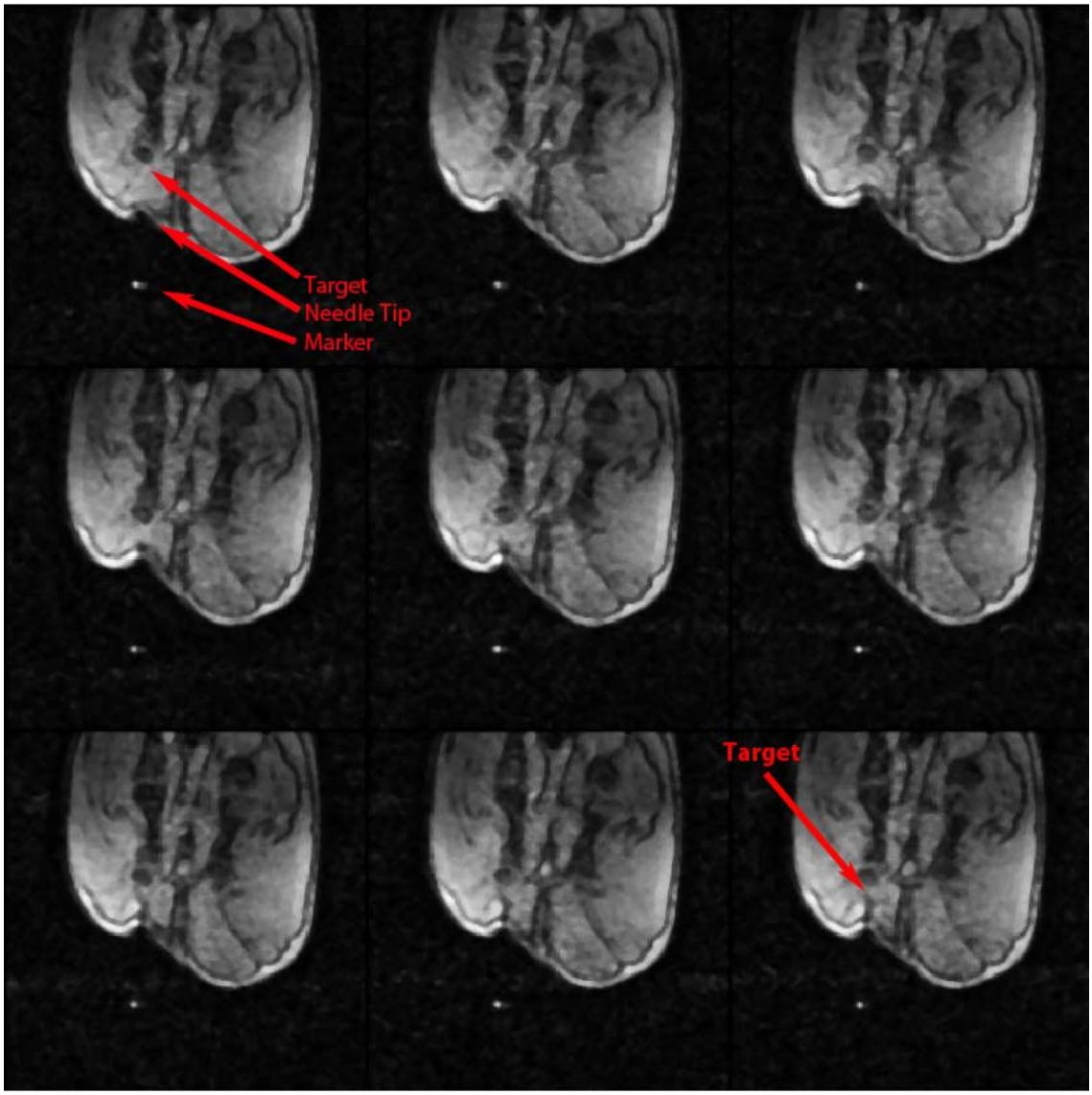

Figure 6.17: Sample dynamic images in the sagittal plane as the needle is advanced towards the target.

$T_{\mathrm{E}}/T_{\mathrm{R}} = 1.5/4.1-8\,\mathrm{ms}$, flip angle $= 10^{\circ}$, matrix $= 192 \times 192$, slice thickness $= 3\,\mathrm{mm}$, $1.56\,\mathrm{mm}$ in-plane resolution) with a frame rate of 2.5 frames per second. Figure 6.17 shows some frames from the dynamic session where the needle is advancing towards the target.

Figure 6.16(B) shows the spot high-resolution images with the needle at the mid-

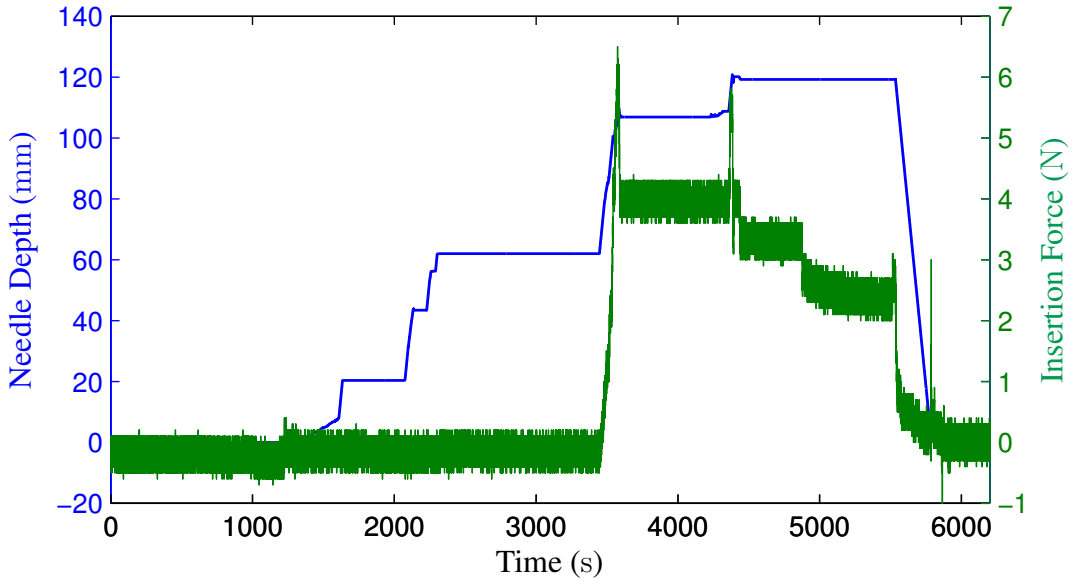

Figure 6.18: Insertion force profile measured when the needle is inserted into the thigh muscles of the hind leg of the live pig

point towards the target and Figure 6.16(C) shows successful targeting of the planned location.

Figure 6.18 shows the force feedback data. Similar to the results observed in the *ex vivo* experiments, the needle insertion force is zero prior to the needle tissue contact and rises sharply when the needle is inserted into the tissue. Peak force over $6\,\mathrm{N}$ is observed which is much higher compared to the peak force observed in the *ex vivo* experiments and shorter relaxation time is also observed in the *in vivo* experiment. The total time taken from setting up the system to reaching the target takes slightly more than 50 minutes.

6.4 Summary

In this chapter, the results of the evaluation experiments have been presented in detail. The MRI-compatibility test shows that the operation of the teleoperated surgical system

does not induce any visually-detectable artifact though the robot might induce field inhomogeneities at the periphery of the phantom. Under continuous MRI guidance, the *ex vivo* targeting experiment can achieve over 85% success rate, and the *in vivo* targeting experiment on a live pig has been performed successfully using about 50 minutes. These experimental results verify the effectiveness of the developed teleoperated master-slave surgical system.

Chapter 7

Conclusions and Future Works

7.1 Conclusions

The goal of this project is to develop a teleoperated master-slave surgical system with a MRI-compatible slave robot that can enable the physician to perform needle-based breast biopsy under continuous MRI guidance. Active work has been carried out by multiple researchers to develop MRI-compatible surgical robots for various applications, and the MRI-compatible slave robot developed here is one of the few that has the potential to perform breast biopsies. It employs pneumatic actuation for the majority of the DOFs and is teleoperated using a dedicated master robot. The teleoperation system also uses a GUI program that can assist the physician performing the needle insertion task in an intuitive way. Thorough evaluation experiments have been conducted, including *ex vivo* phantom test and *in vivo* animal test. Based on the research work done and experimental results obtained in this project, the following conclusions can be made:

- Polymer materials such as Delrin® and Teflon® are the most preferred materials for applications inside the MRI since they are both nonmagnetic and dielectric. For structural parts that require higher mechanical stiffness and strength that polymer materials cannot provide, titanium is the most ideal material when manufacturing cost and machining capability are less of a concern. The economical alternatives are brass (Alloy 360) and aluminum (Alloy 3601) that render limited magnetic field

interference in the MRI environment. However, when using those non-magnetic materials, the metal volume should be minimized and be placed as far away from the scanning center as possible.

- Pneumatic actuation leads to least magnetic field interference compared to other actuation techniques and causes negligible MR image quality degradation and SNR loss, though achieving dynamic performance and millimeter-scale positioning accuracy can be a challenge. Piezo motor can provide better dynamics and positioning accuracy at the cost of modest image quality degradation and SNR loss in the MR images, and should be placed as far away from the scanner center as permitted. Also, the actuation force and speed of the piezo motor is limited.

- The slave robot and its prototype, both of which are developed with the aforementioned materials and actuation techniques, are MRI-compatible based on the results of the MRI experiments.

- The kinematic analysis shows that the developed slave robot has 6 DOFs. The three-link parallel mechanism can provide one translational DOF and two rotational DOFs and is accompanied by two additional coupled translational DOFs, and hence, moves the mobile platform in 6-D space. The slave robot can be used to adjust the needle orientation and position to perform needle insertion tasks.

- The most challenging aspect of pneumatic actuation inside the MRI environment is the slow response due to the long transmission lines and the nonlinear friction force. Despite these challenges, accurate positioning of $1\,\mathrm{mm}$ can be achieved with

controllers based on SMC control or PID with friction compensation.

- With negligible time delay introduced by the local network communication, the master and the slave robot of the teleoperation system can be directly connected with reasonable dynamic performance.

- Based on the *ex vivo* and *in vivo* MRI experiments, the developed teleoperated surgical system can fulfil its designed functions and perform needle insertion tasks with high success rate (over 85%). Such surgical system can potentially be used in clinical applications with further development.

7.2 Contributions

To the best of my knowledge, this is the first MRI-compatible master-slave robotic system that has been developed to enable breast biopsy under continuous MRI using long pneumatic transmission lines. Though the robotic system is not yet suitable for clinical trials, this dissertation presents extensive work that has been done towards achieving that goal. The contributions presented in this dissertation can be summarized as follows:

- Designed and developed the MRI-compatible breast biopsy slave robot:
  - Developed a prototype MRI-compatible slave robot consisting of a three-link parallel mechanism that could provide needle orientation adjustment and a needle driver that could perform needle insertion using screw motion;
  - Based on the prototype robot, developed a 6-DOF slave robot that is able to assist the physician perform breast biopsy needle insertion inside the MRI;

  - Derived the inverse kinematics of the three-link parallel mechanism using screw theory and presented the forward kinematics with detailed result.

- Studied the pneumatic control over long transmission lines for applications inside the MRI based on a 1-DOF prototype device:
  - Developed pneumatic controllers using SMC technique for proportional pressure valves;
  - Developed pneumatic controllers using PID technique with friction compensation for proportional mass flow rate valve.

- Developed the master robot for intuitive operation of the slave robot:
  - Established actuator level kinematics map between the master and the slave robot;
  - Developed the control strategy for the master robot to work as an intuitive manipulation interface to the slave robot.

- Developed the GUI program for visualization of the slave robot and assembled the virtual components in the OpenGL environment using the derived kinematics.

- Evaluated of the master-slave surgical system experimentally:
  - Conducted experiments to validate the MRI-compatibility of the slave robot;
  - Performed *ex vivo* phantom targeting tests and achieved six successful needle insertions out of seven trials;
  - Carried out *in vivo* targeting experiments successfully.

7.3 Future Works

The possible directions for future work in this area are:

- Improve the engineering design of the slave robot to make it smaller and more rigid with less metal components. Work can also be carried out to increase the mobility of the slave robot, such as installing it on a mobile table, so that the burden of preparing the robot on the MRI scanner bed would be lessened;
- Redesign the needle driver of the slave robot so that standard clinical instruments can be mounted with quick-release capability;
- Investigate the design of the slave robot for redundant sensing and actuation, as well as the incorporation of safety mechanisms.
- Improve the design of the master robot to make its size smaller and its operation more intuitive;
- Further investigate the control of pneumatic cylinders over long transmission lines. Mechanical damping mechanism can also be included to facilitate controller design;
- Incorporate more features in the GUI program to facilitate the operation of the surgical system, such as: a) communicating with the MRI scanner to render the MR images along with the CAD model of the robot, b) performing online simulation for the slave robot according to the instantaneous commanded configuration from the master to compensate the slow response of the slave robot, c) providing trajectory planning for the needle insertion, and d) enabling the rotation of the needle about any spatial point specified by the user.

Appendix A

CAD Drawings of the Slave Robot

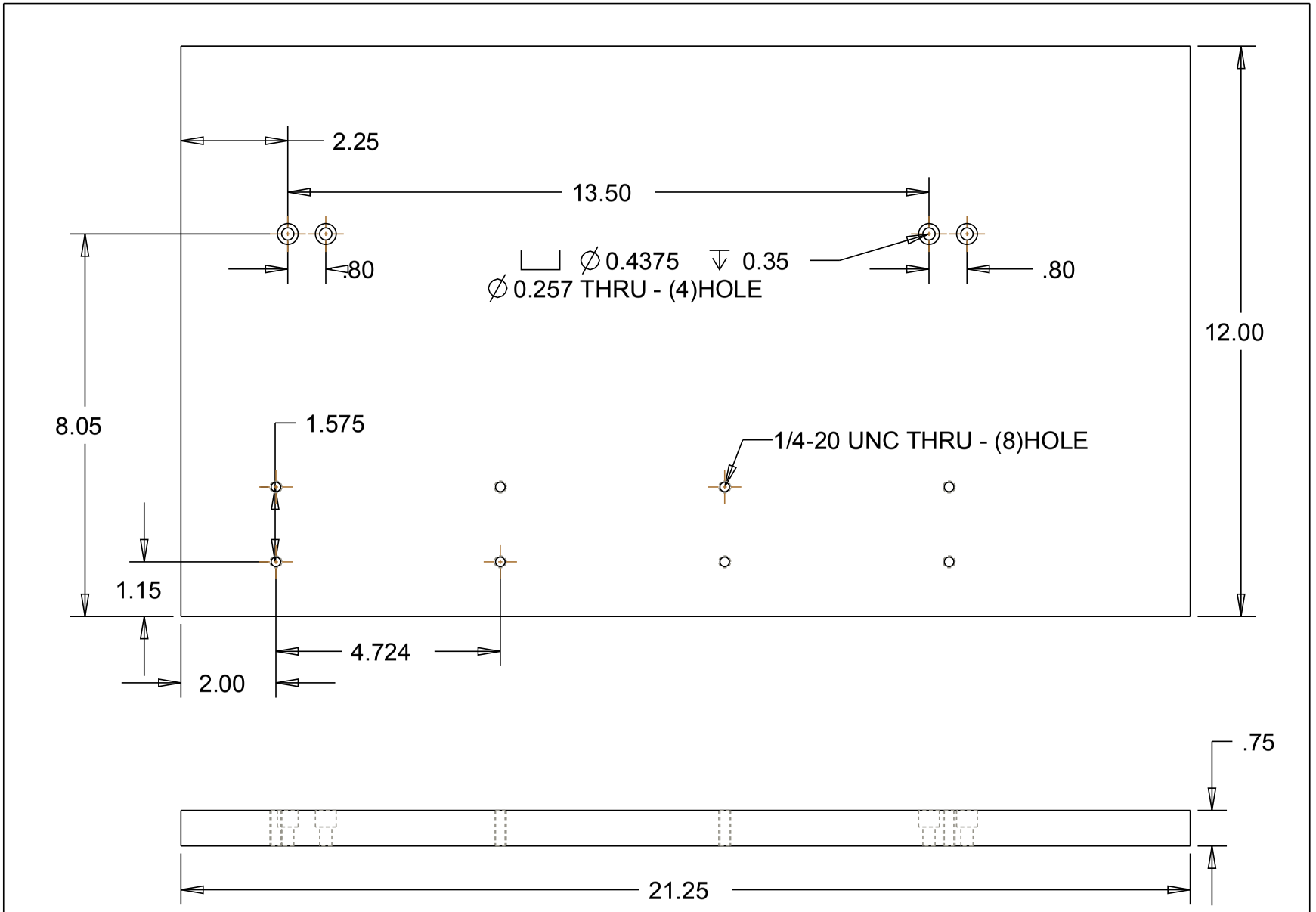

Part Name: Base	Unit: Inches	Author: YANG Bo
Material: Derlin	Quantity: 1	Data: 20110218

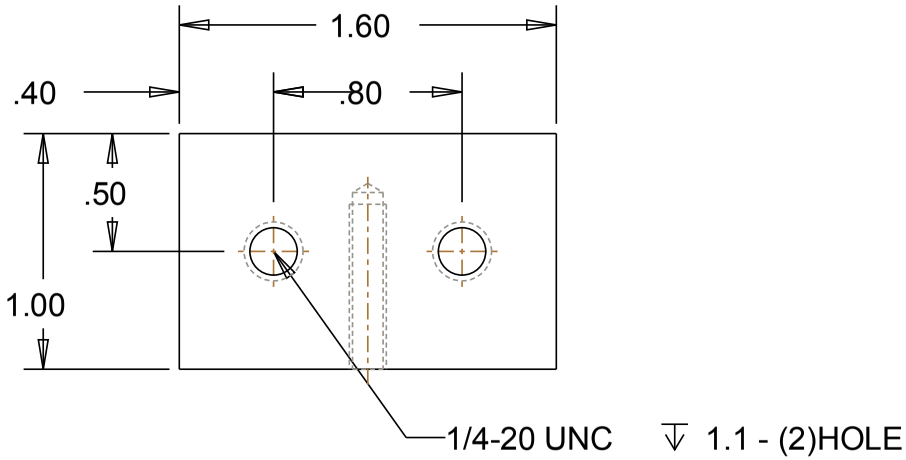

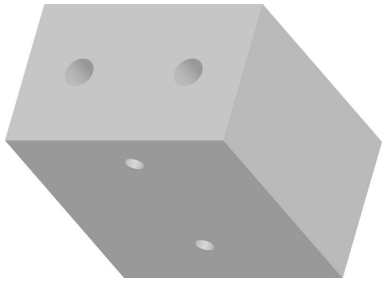

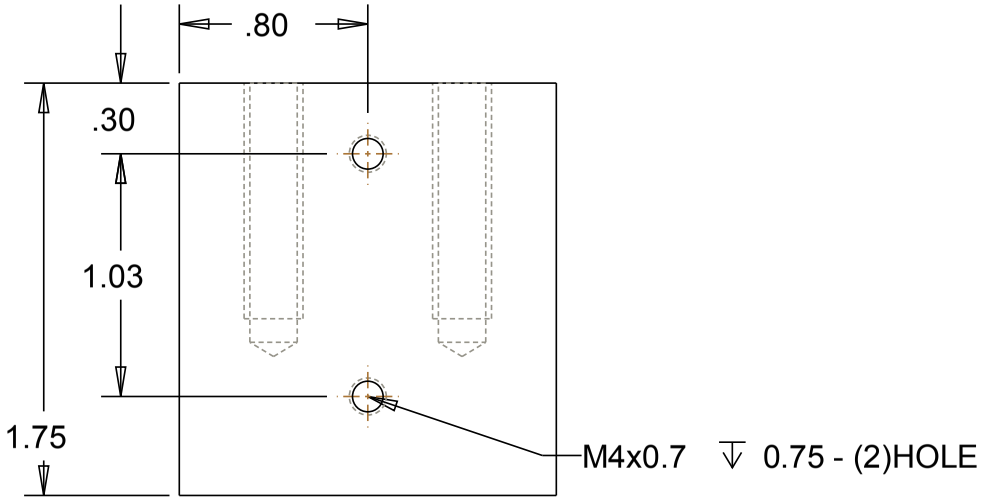

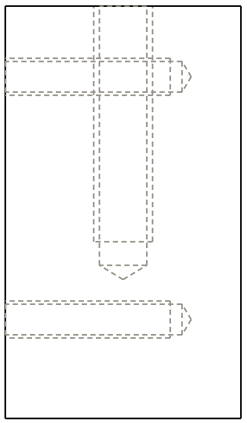

Part Name: Cylinder Mount X	Unit: Inches	Author: YANG Bo
Material: Derlin	Quantity: 2	Data: 20110218

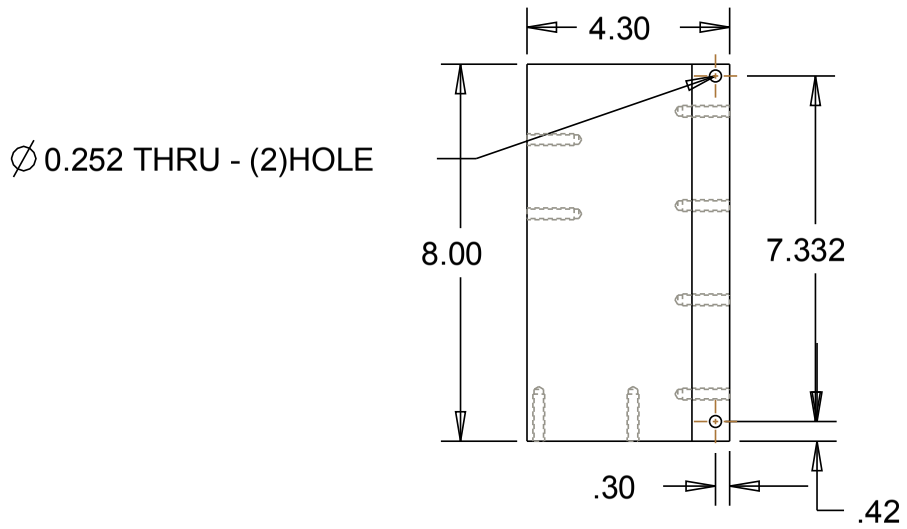

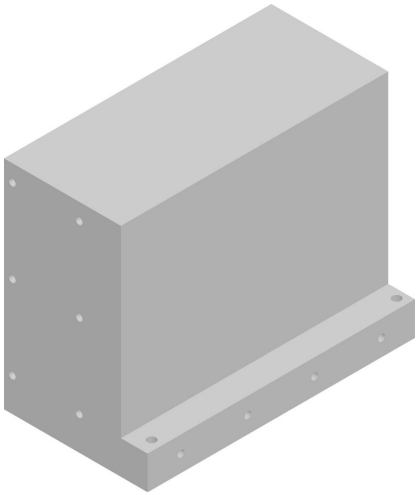

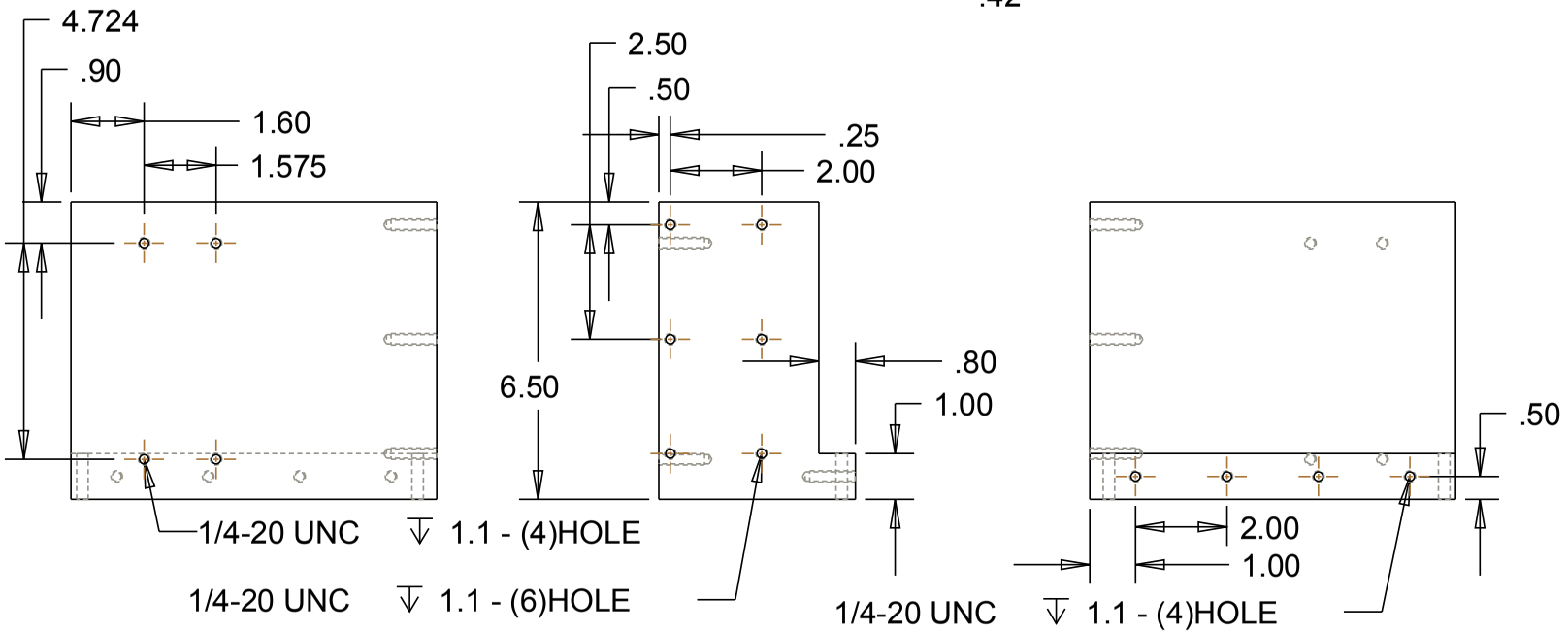

Part Name: Table angle	Unit: Inches	Author: YANG Bo
Material: Derlin	Quantity: 1	Data: 20110218

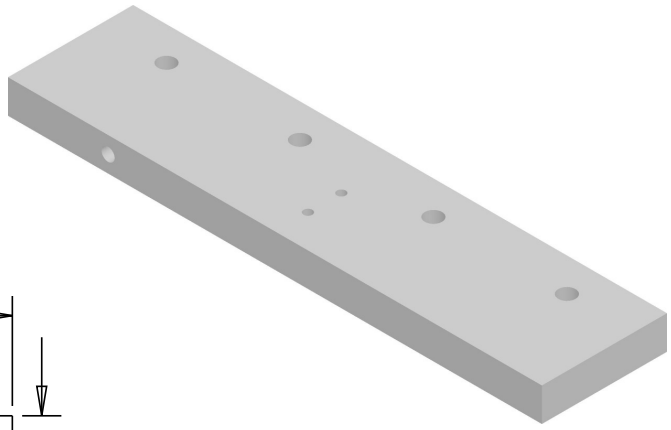

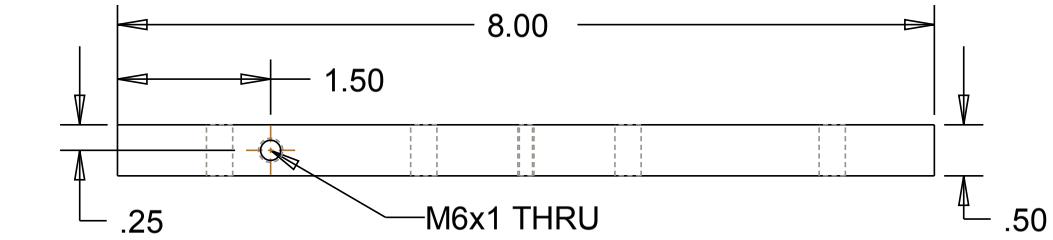

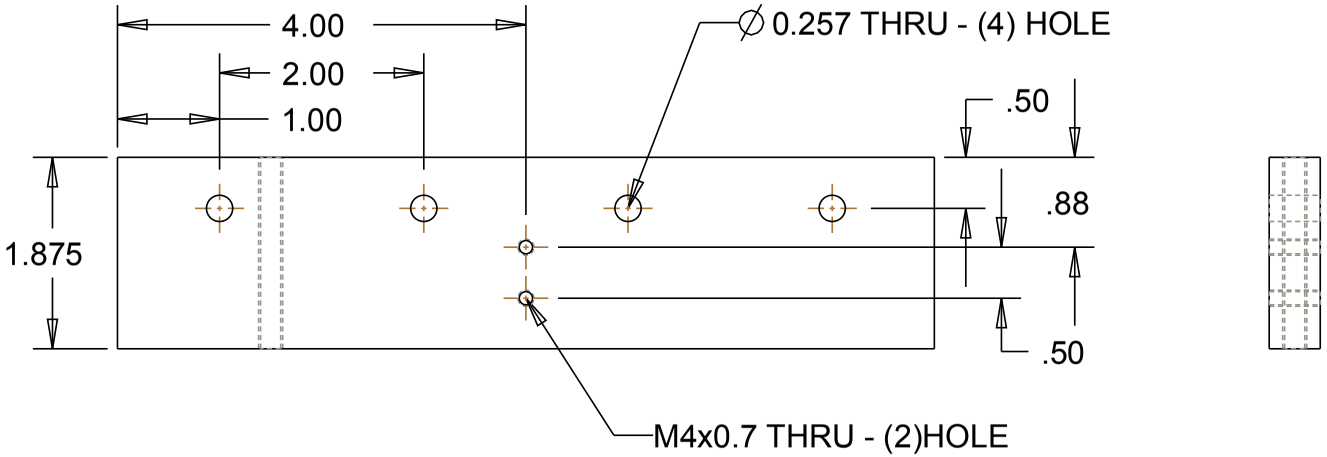

Part Name: Support X	Unit: Inches	Author: YANG Bo
Material: Derlin	Quantity: 1	Data: 20110218

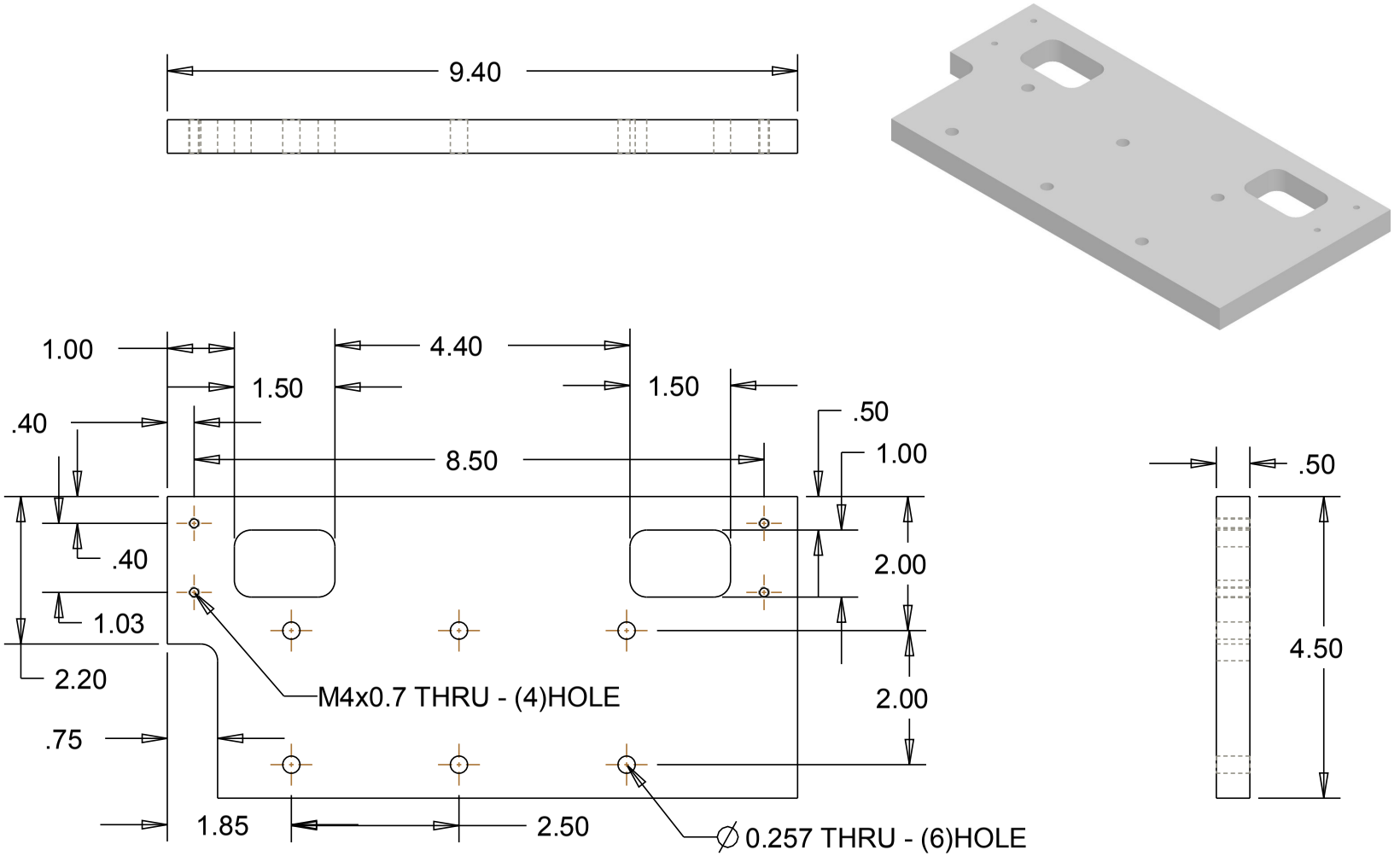

Part Name: Cylinder Mount Y	Unit: Inches	Author: YANG Bo
Material: Derlin	Quantity: 1	Data: 20110218

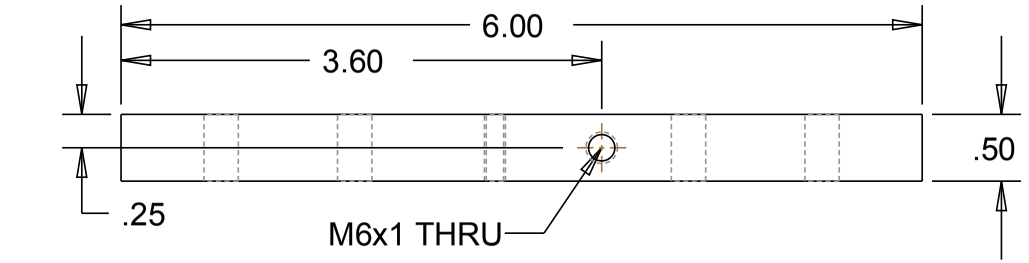

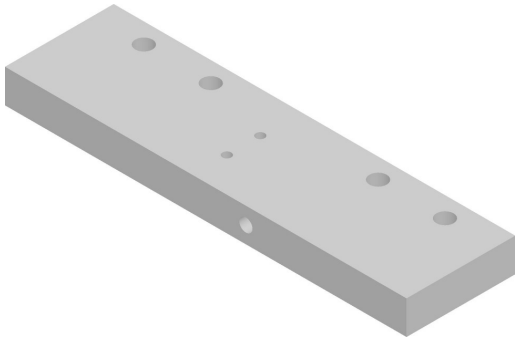

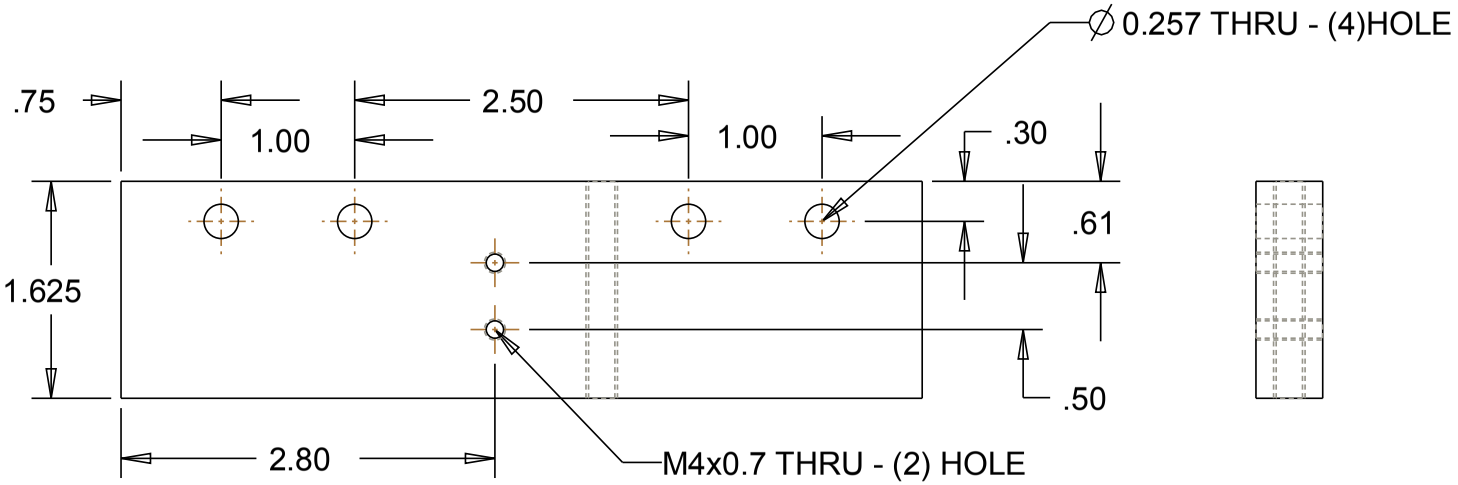

Part Name: Support Y	Unit: Inches	Author: YANG Bo
Material: Derlin	Quantity: 1	Data: 20110218

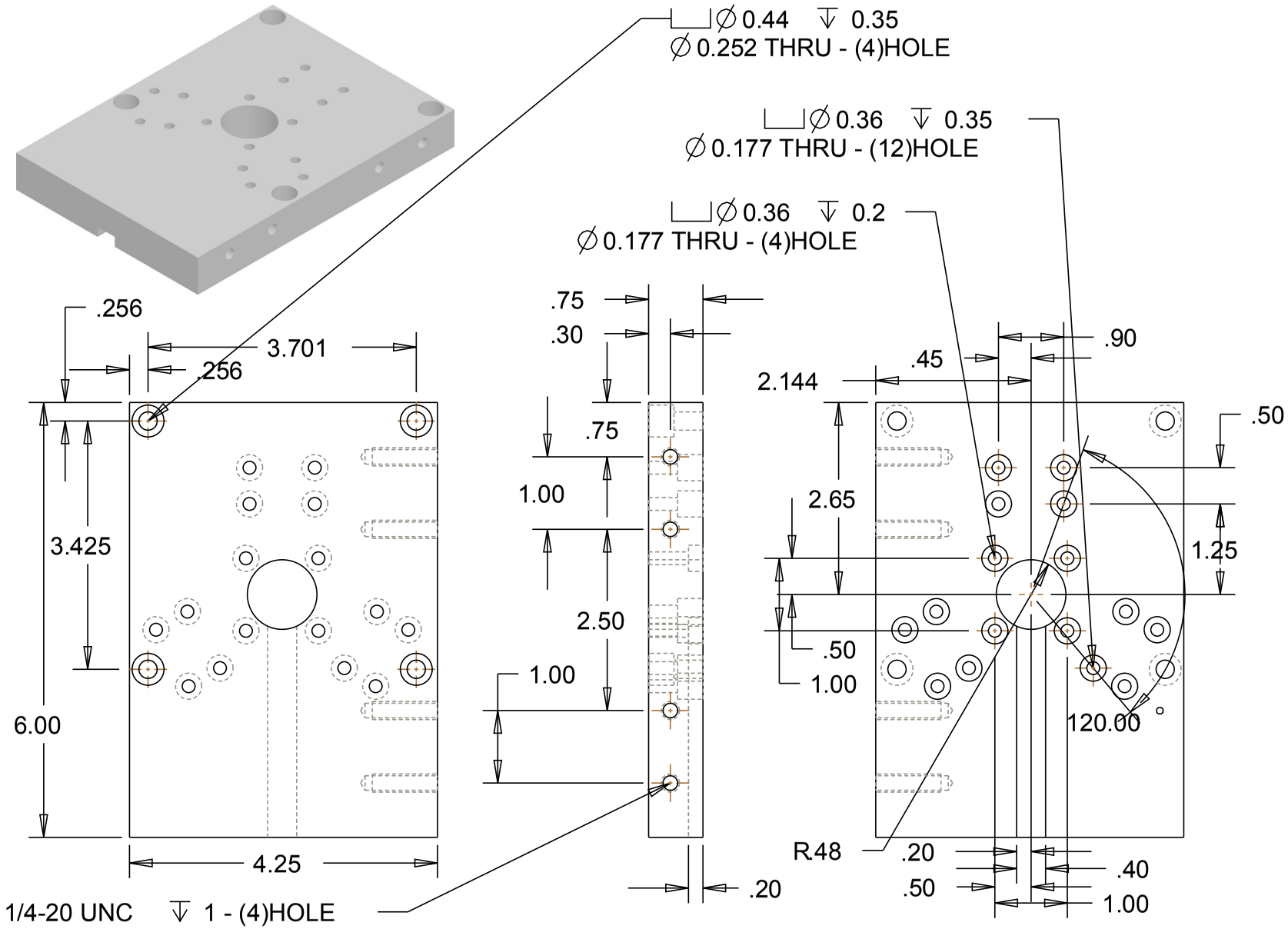

Part Name: Stewart base	Unit: Inches	Author: YANG Bo
Material: Derlin	Quantity: 1	Data: 20110415

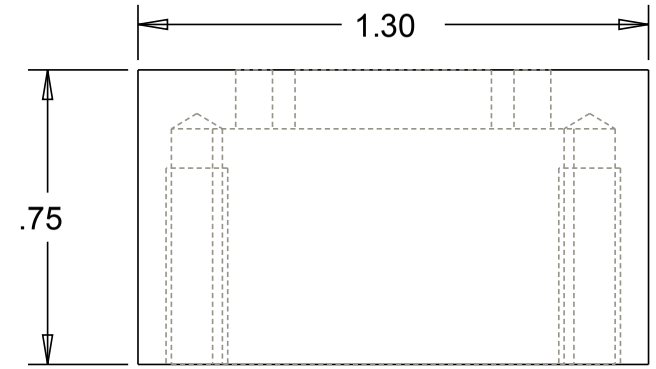

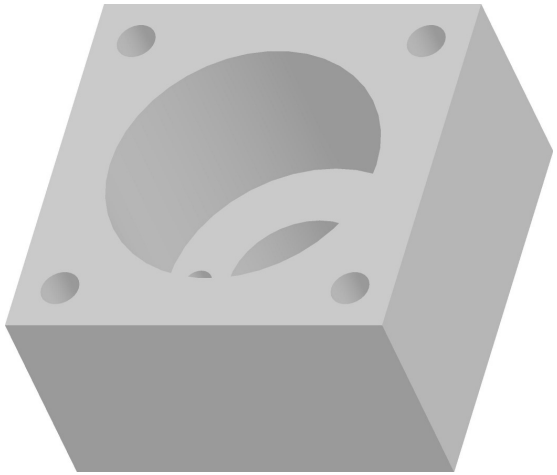

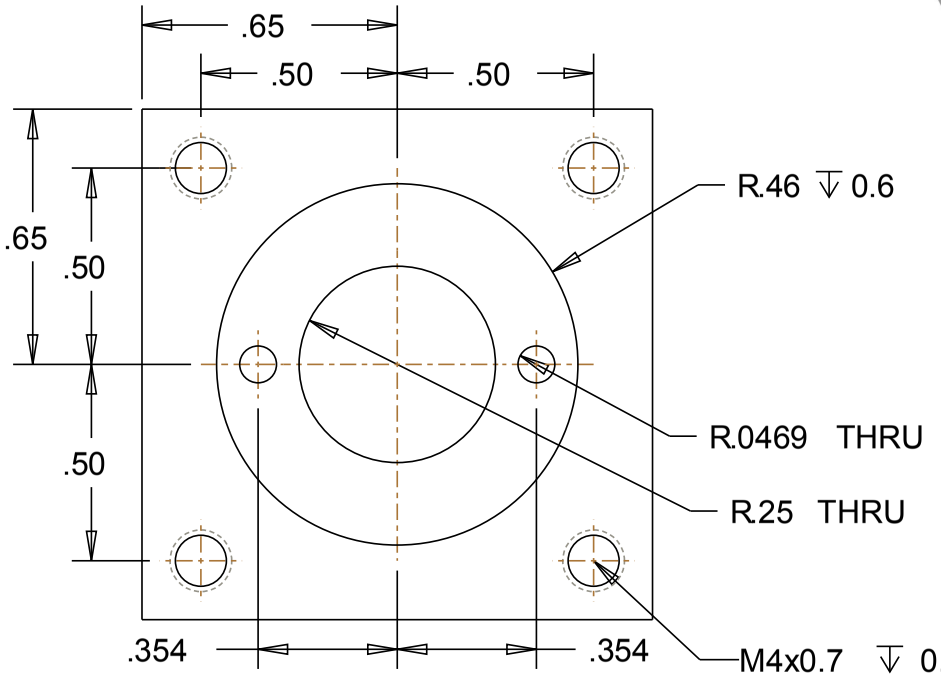

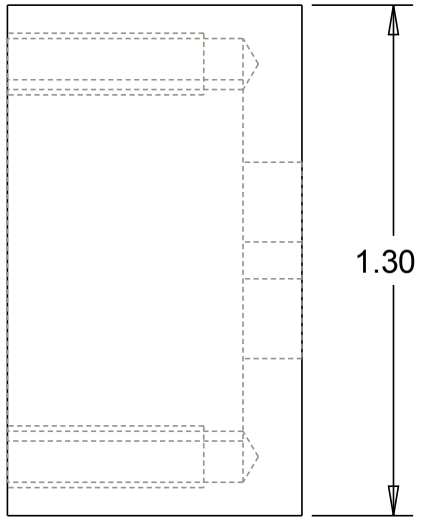

Part Name: Motor Casing	Unit: Inches	Author: YANG Bo
Material: Derlin	Quantity: 1	Data: 20110603

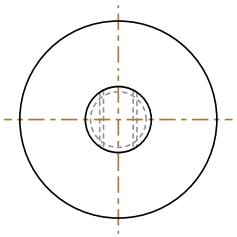

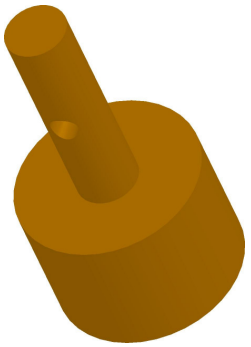

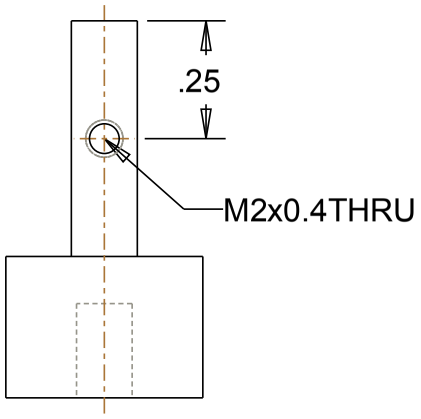

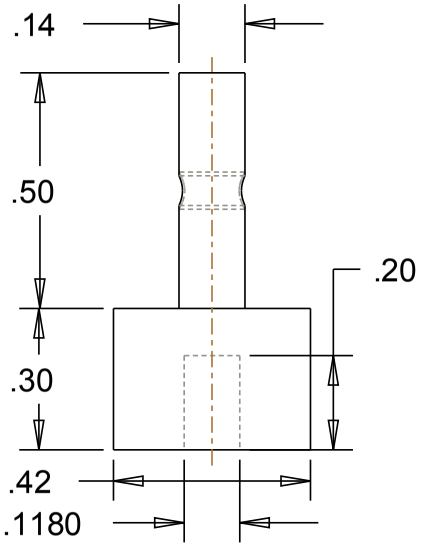

PRESS FIT WITH 3mm OD MOTOR SHAFT

Part Name: Motor Coupler	Unit: Inches	Author: YANG Bo
Material: Brass (Alloy 360)	Quantity: 1	Data: 20110623

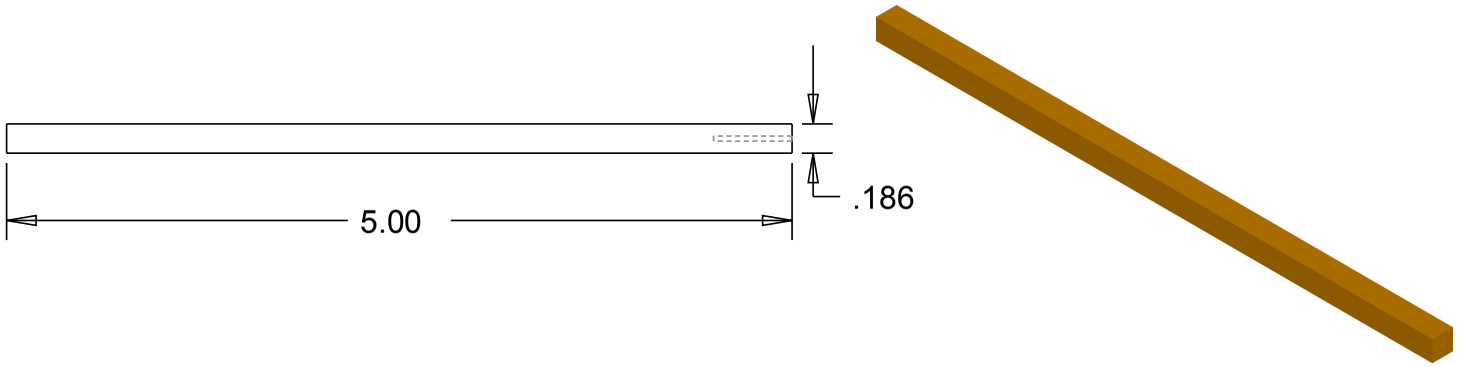

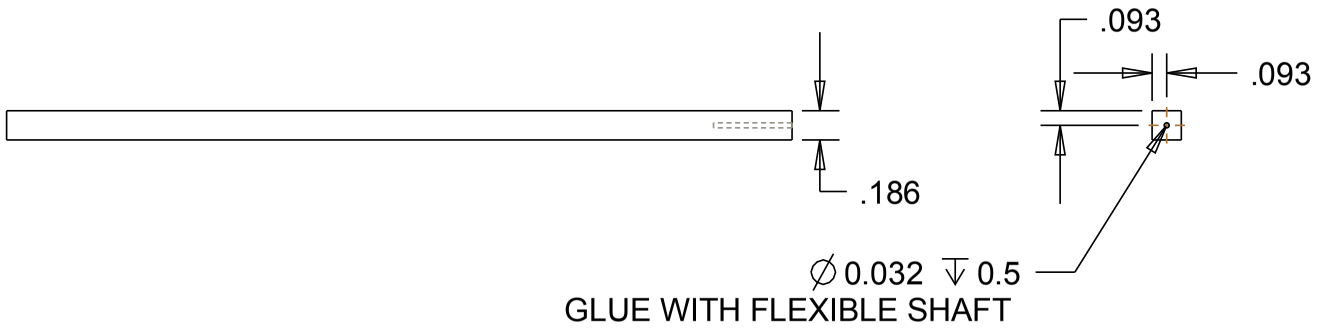

Part Name: Transmission Rod	Unit: Inches	Author: YANG Bo
Material: Brass (Alloy 360)	Quantity: 1	Data: 20110623

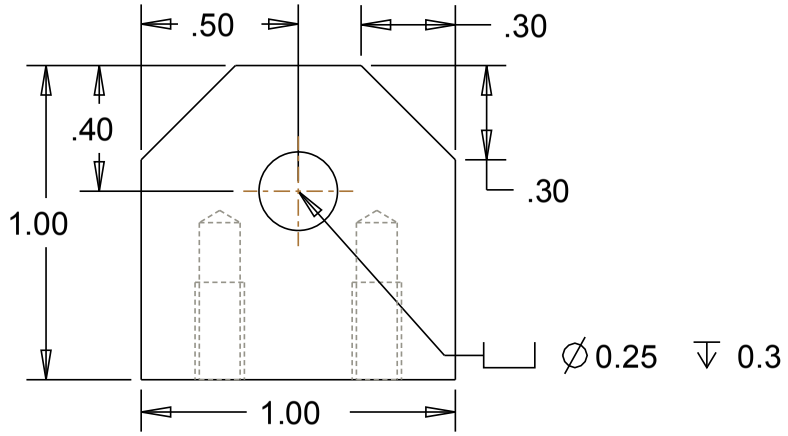

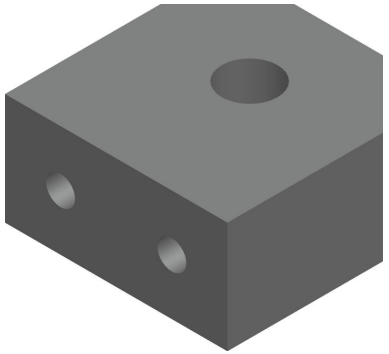

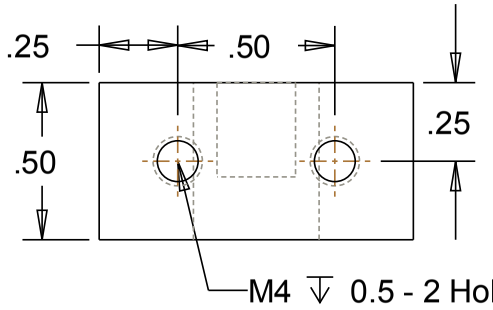

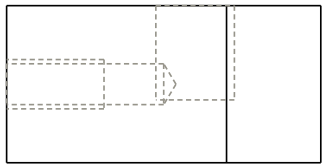

Part Name: Pin Support Alt	Unit: Inches	Author: YANG Bo
Material: Aluminium (6061)	Quantity: 6	Data: 20100721

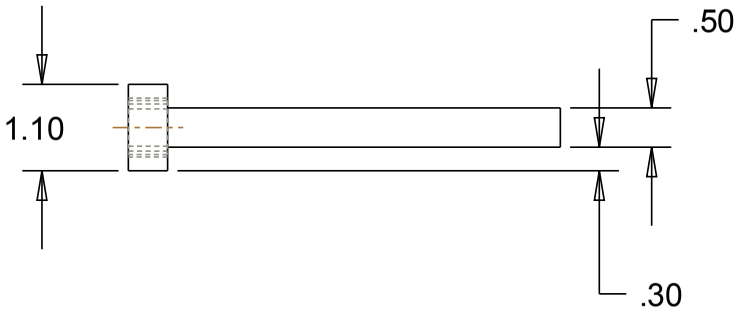

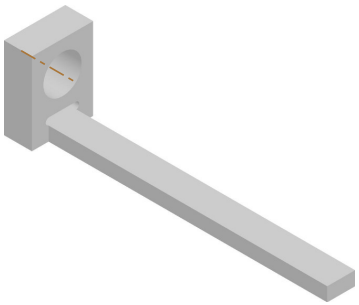

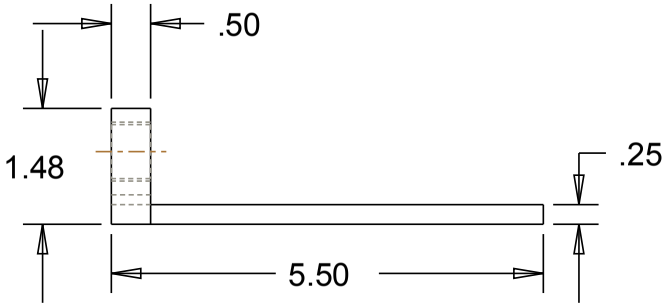

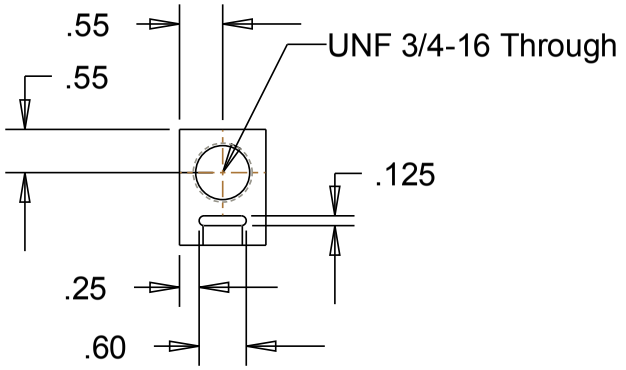

Part Name: Strip support	Unit: Inches	Author: YANG Bo
Material: Derlin	Quantity: 3	Date: 20100619

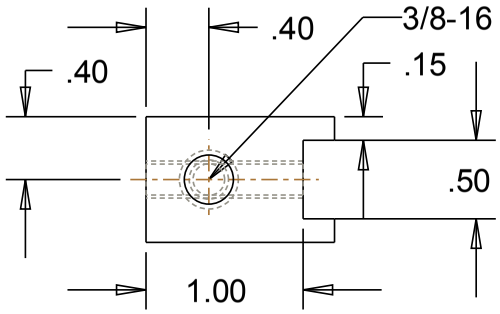

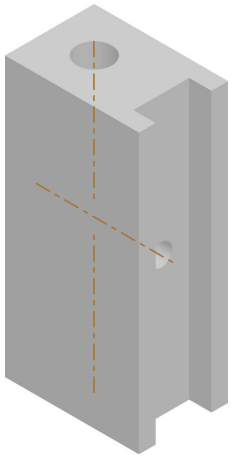

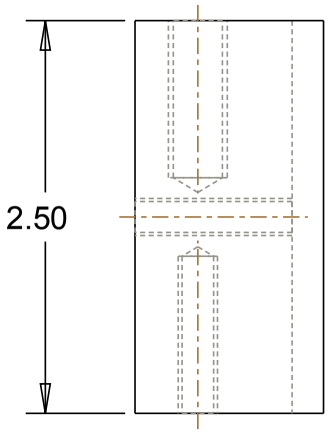

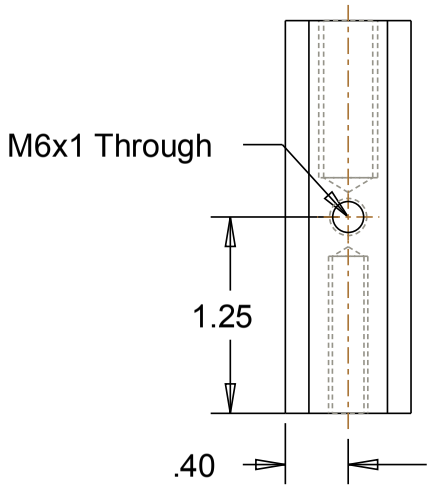

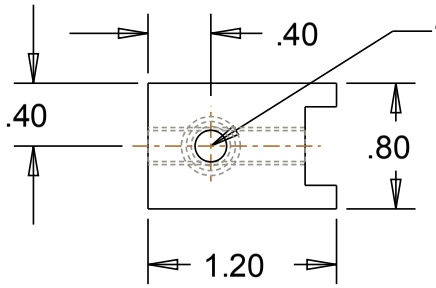

Part Name: Wiper housing	Unit: Inches	Author: YANG Bo
Material: Derlin	Quantity: 3	Date: 20100619

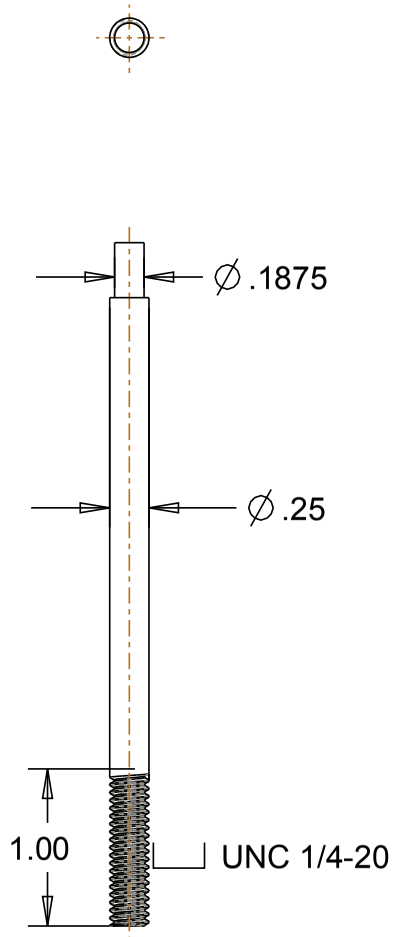

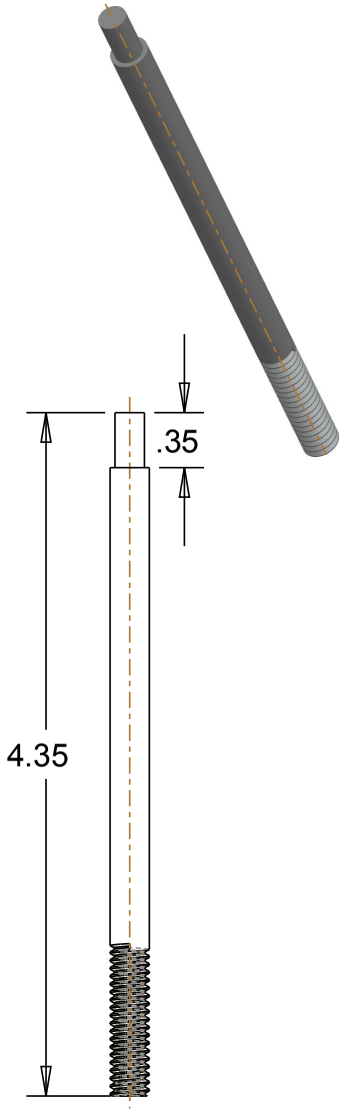

Part Name: Leg rod	Unit: Inches	Author: YANG Bo
Material: Aluminium (6061)	Quantity: 3	Date: 20100721

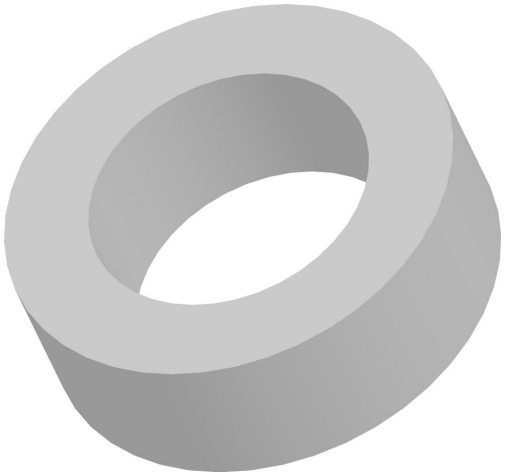

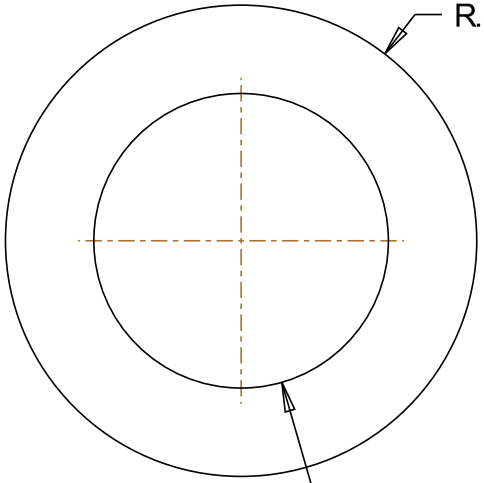

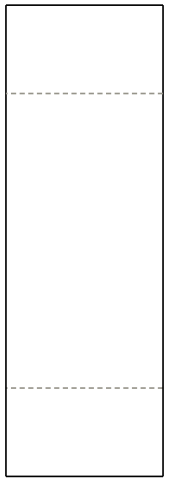

Part Name: Roller Pin Fix	Unit: Inches	Author: YANG Bo
Material: Derlin	Quantity: 3	Data: 20110218

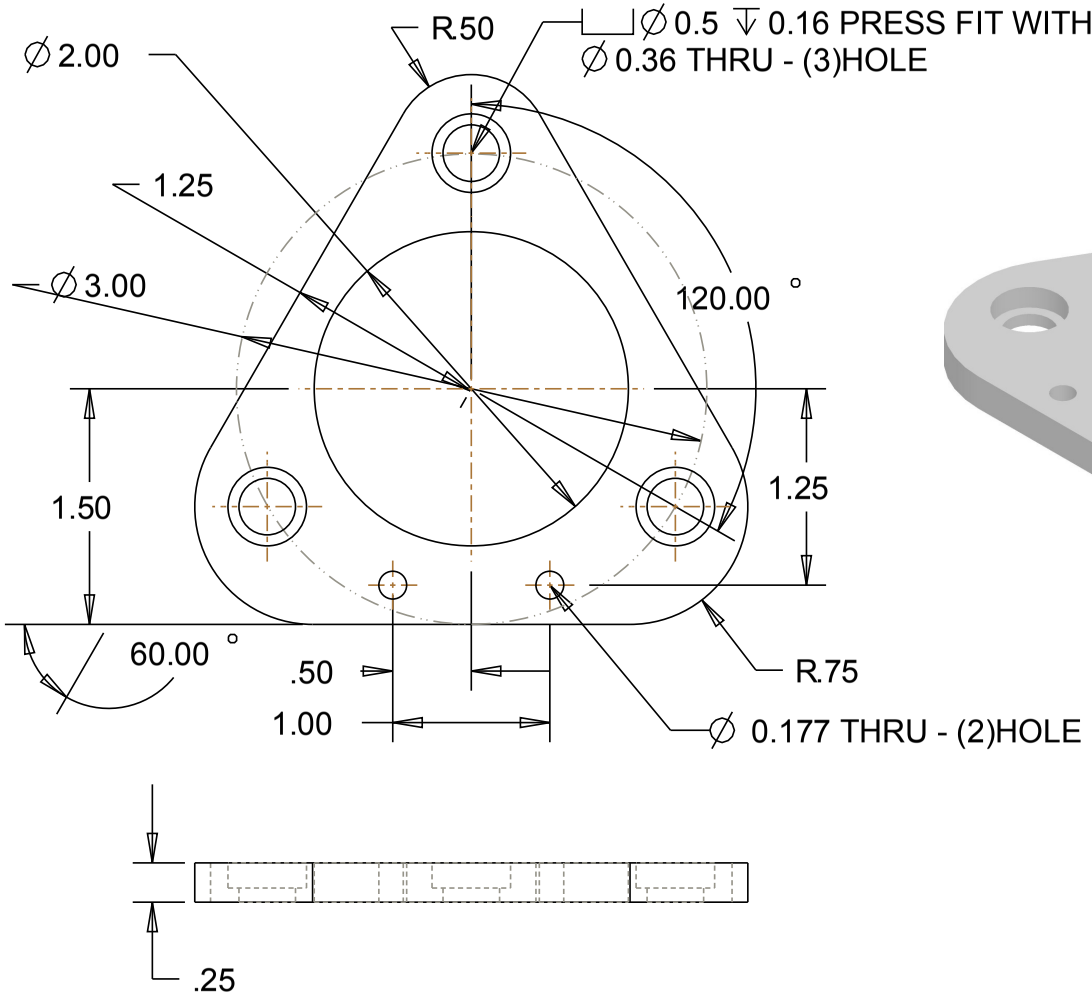

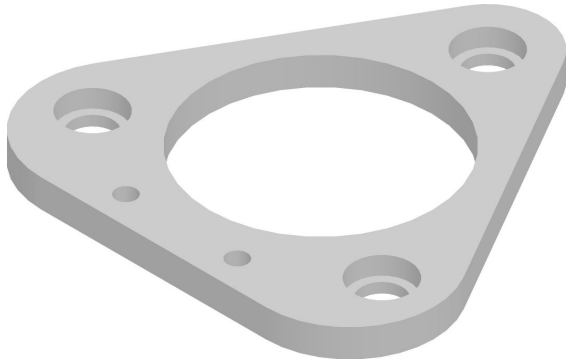

Part Name: Stewart Platform	Unit: Inches	Author: YANG Bo
Material: Derlin	Quantity: 1	Date: 20110218

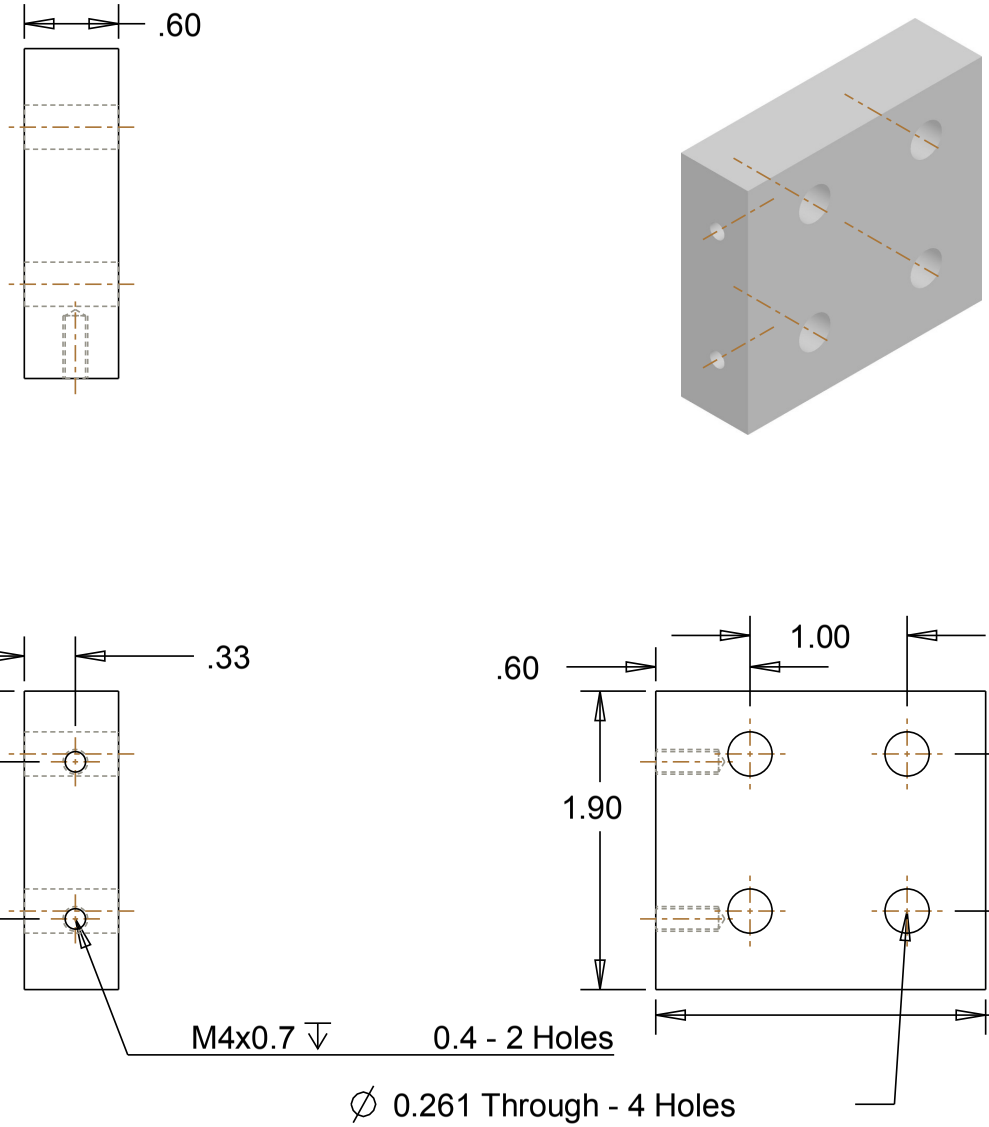

Part Name: Sensor Support	Unit: Inches	Author: YANG Bo
Material: Derlin	Quantity: 1	Data: 20100618

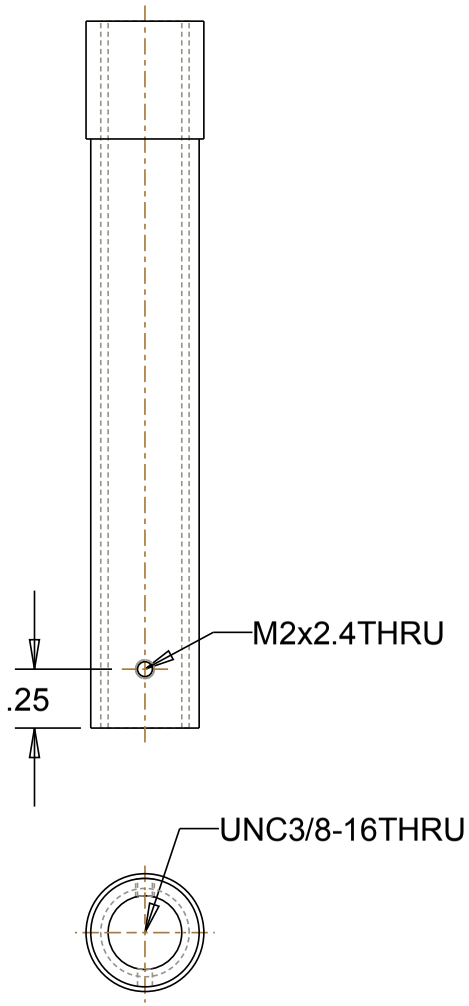

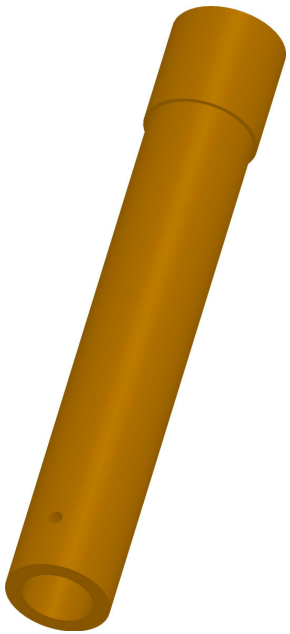

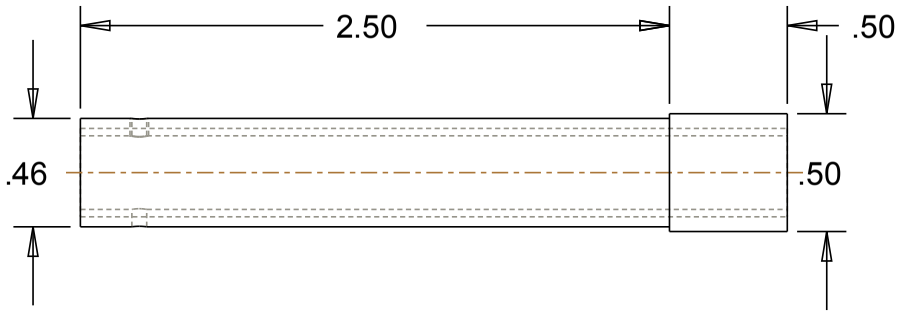

Part Name: Needle Housing	Unit: Inches	Author: YANG Bo
Material: Brass (Alloy 360)	Quantity: 1	Data: 20110622

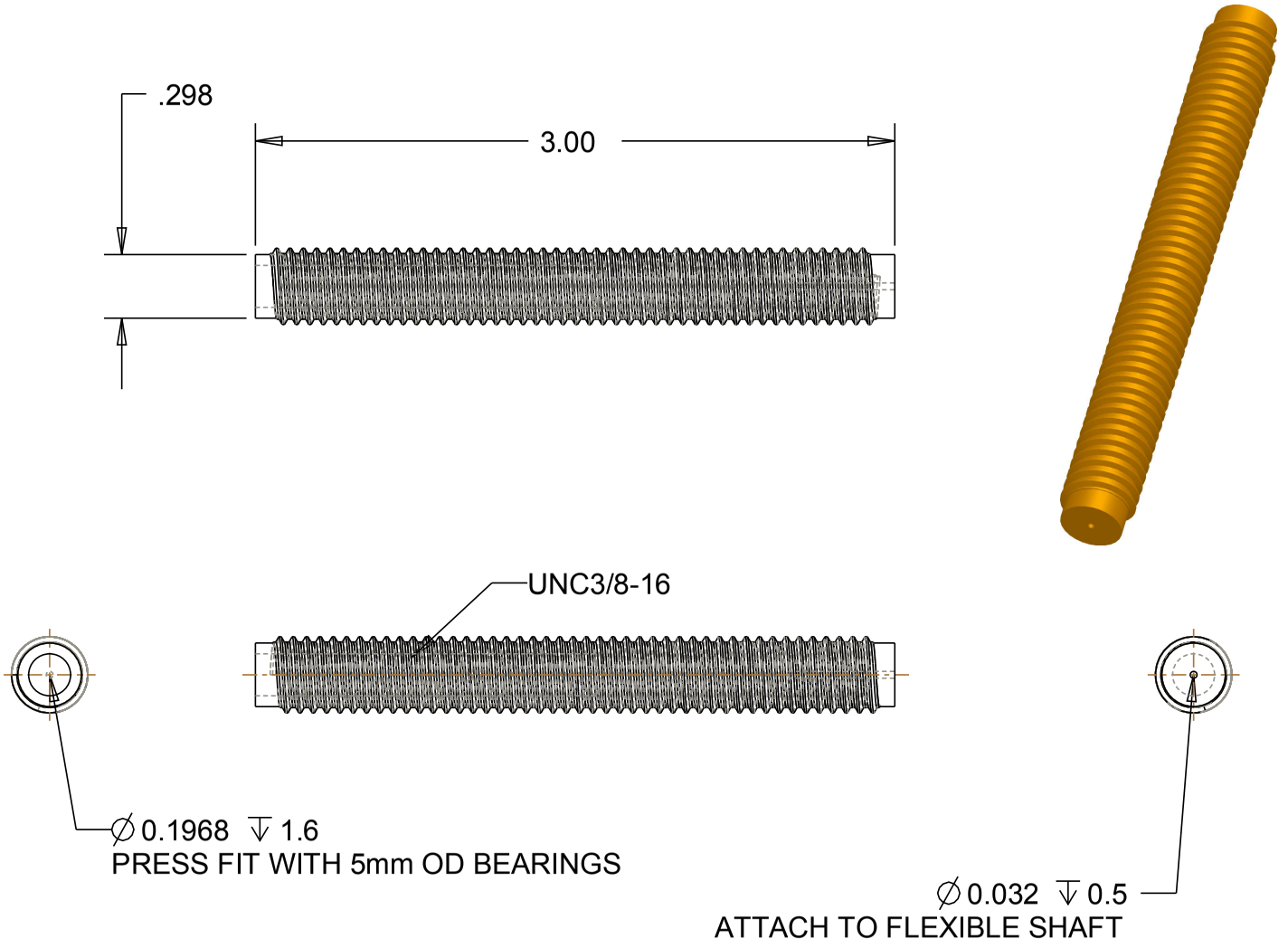

Part Name: Needle Holder	Unit: Inches	Author: YANG Bo
Material: Brass (Alloy 360)	Quantity: 1	Data: 20110622

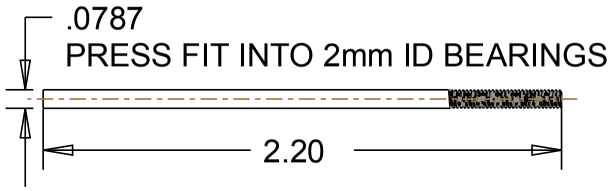

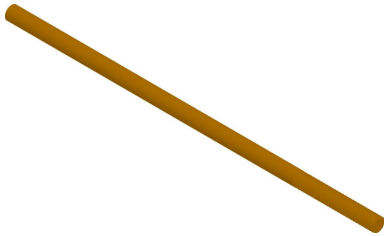

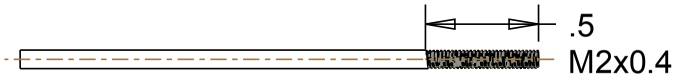

Part Name: Needle Shaft	Unit: Inches	Author: YANG Bo
Material: Brass (Alloy 360)	Quantity: 1	Data: 20110623

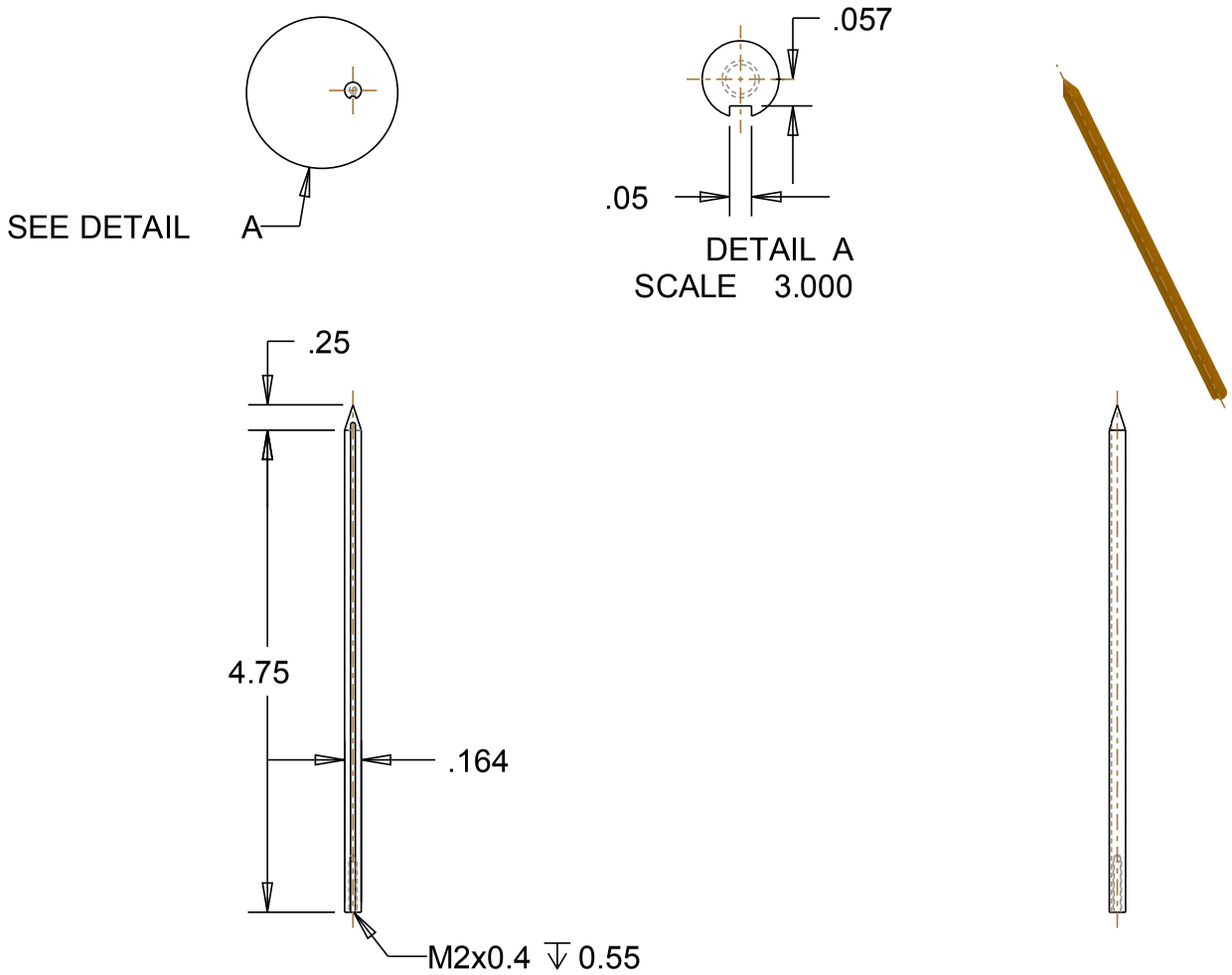

Part Name: Needle	Unit: Inches	Author: YANG Bo
Material: Brass (Alloy 360)	Quantity: 1	Data: 20110622

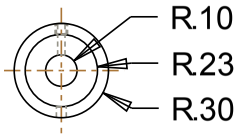

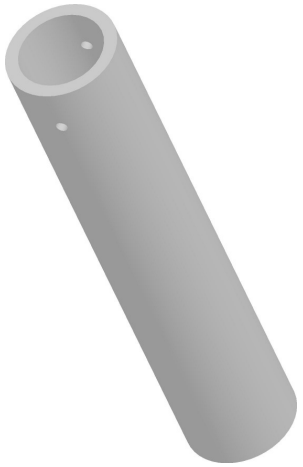

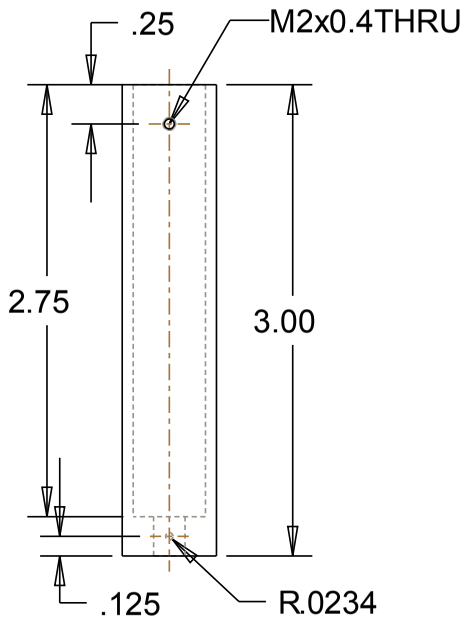

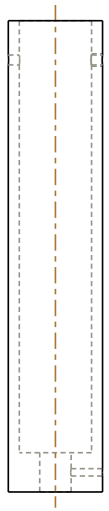

Part Name: Needle Fix	Unit: Inches	Author: YANG Bo
Material: Derlin	Quantity: 1	Data: 20110622

Appendix B

CAD Drawings of the Master Robot

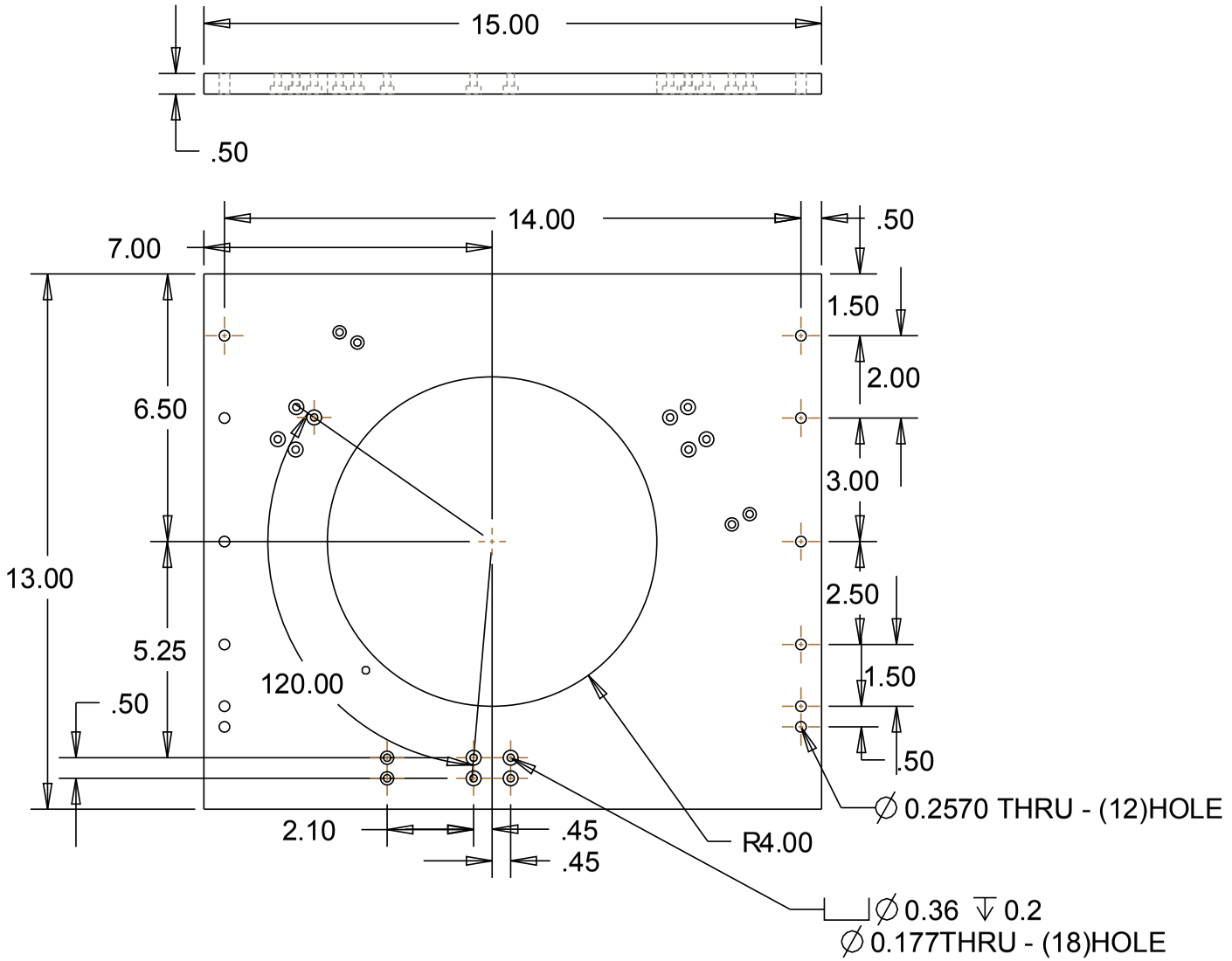

Part Name: Base	Unit: Inches	Author: YANG Bo
Material: Aluminum	Quantity: 1	Data: 20110602

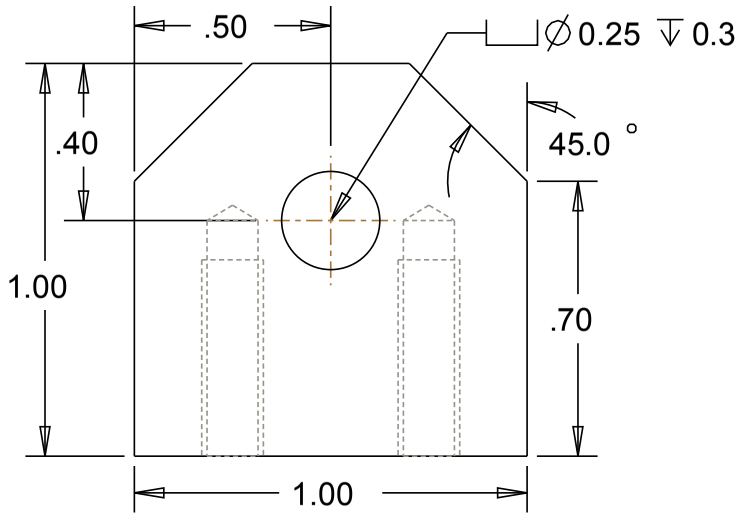

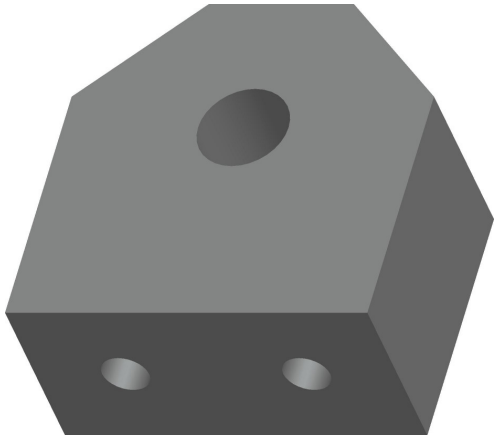

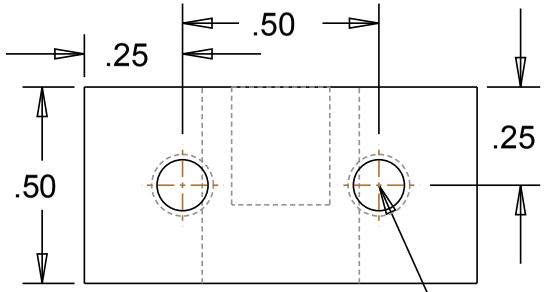

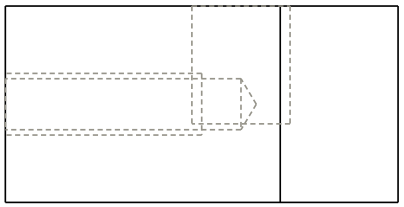

M4x0.7 ↧ 0.6-(2)HOLE

Part Name: Pin Support Close	Unit: Inches	Author: YANG Bo
Material: Aluminum	Quantity: 3	Data: 20110404

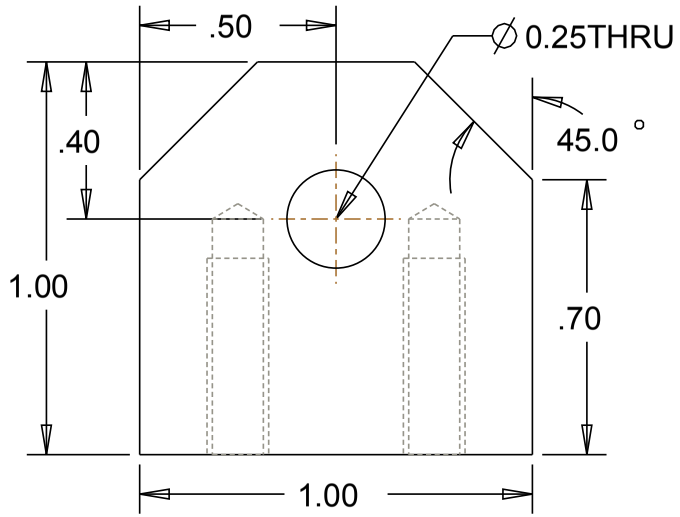

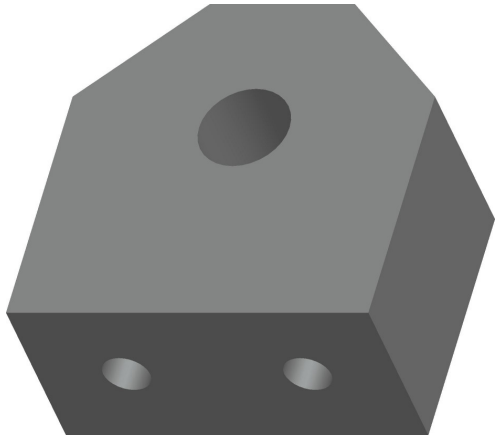

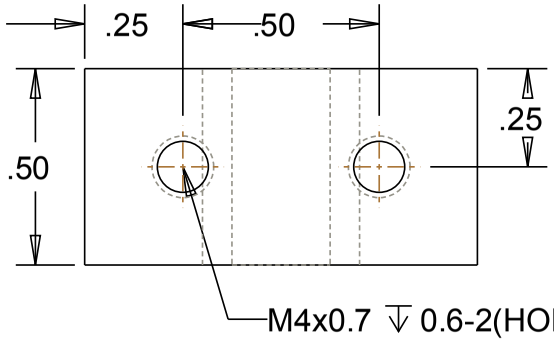

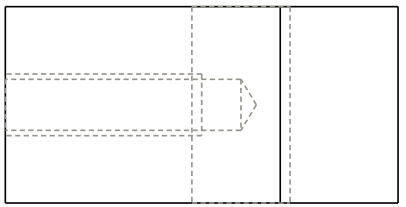

Part Name: Pin Support Open	Unit: Inches	Author: YANG Bo
Material: Aluminum	Quantity: 3	Data: 20110404

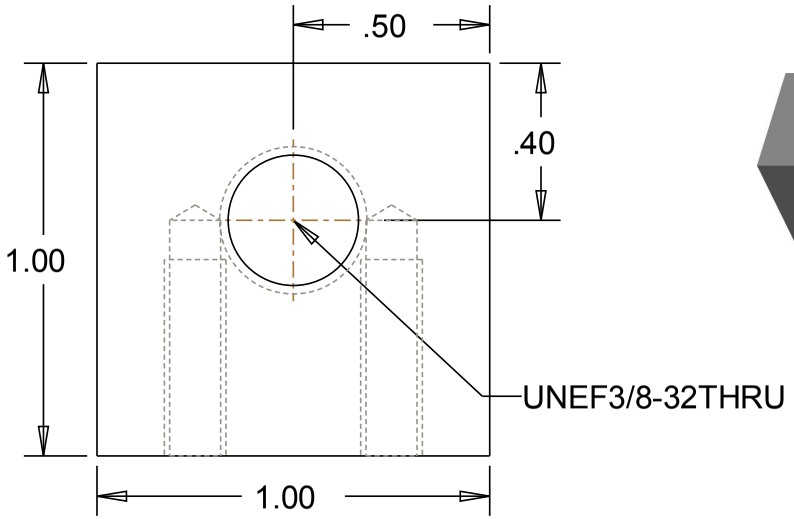

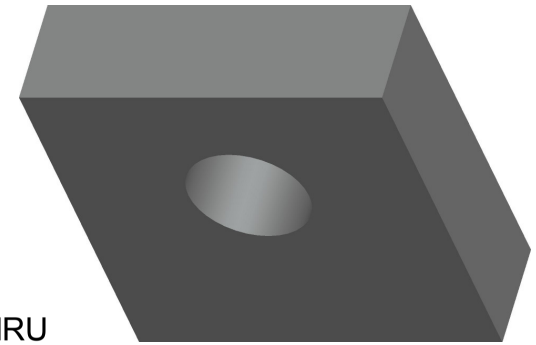

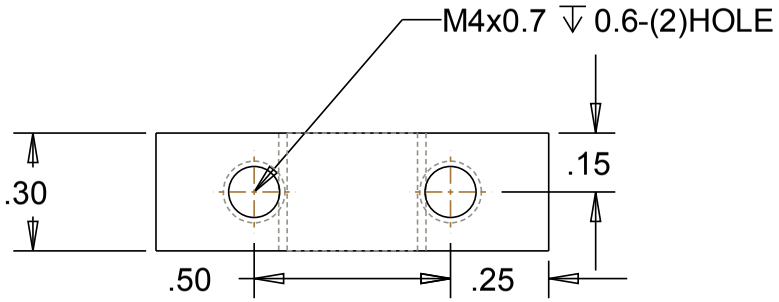

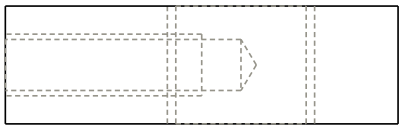

Part Name: Encoder Frame	Unit: Inches	Author: YANG Bo
Material: Aluminum	Quantity: 3	Data: 20110421

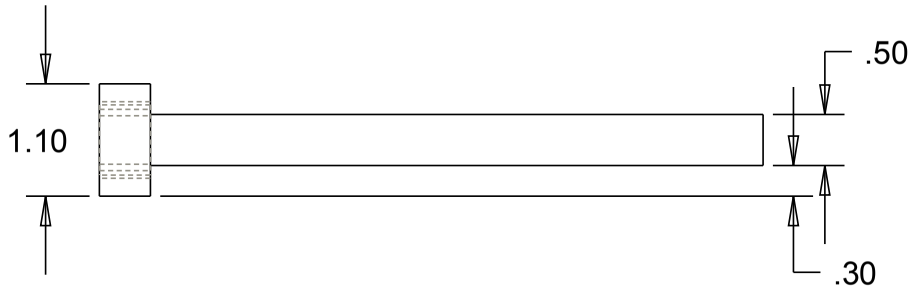

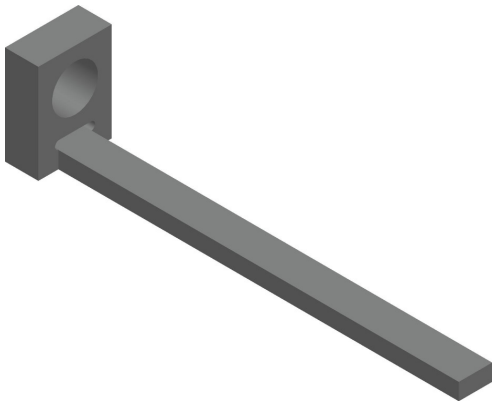

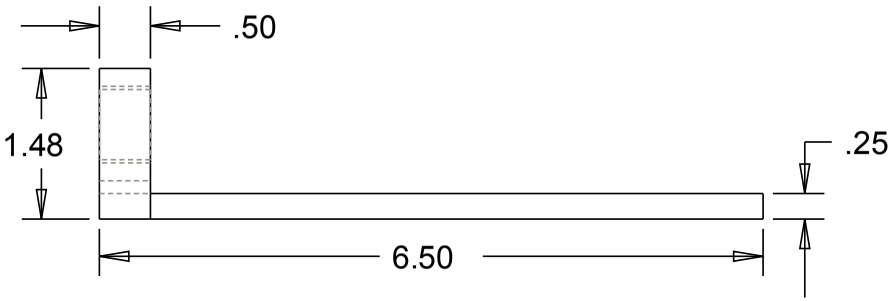

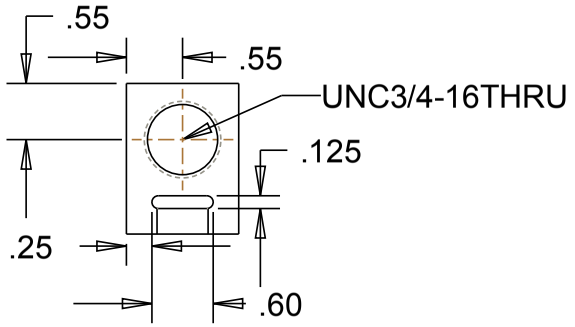

Part Name: Strip Support 150mm	Unit: Inches	Author: YANG Bo
Material: Aluminum	Quantity: 3	Data: 20110404

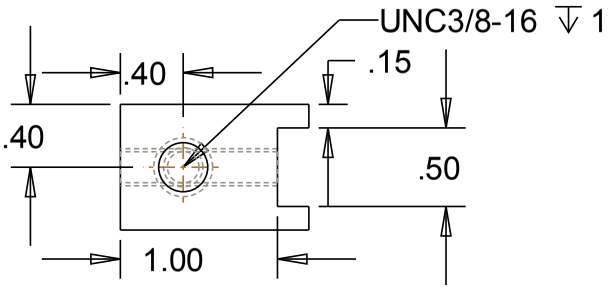

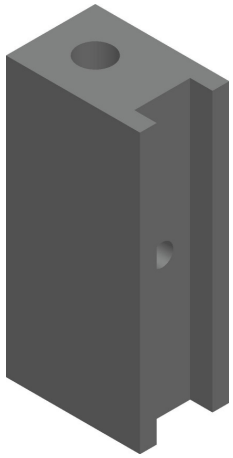

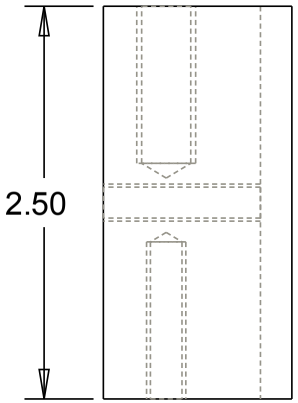

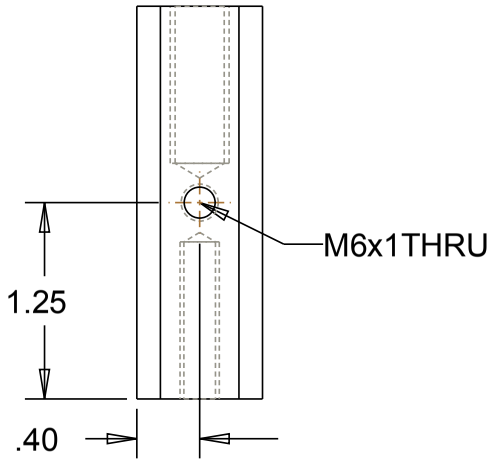

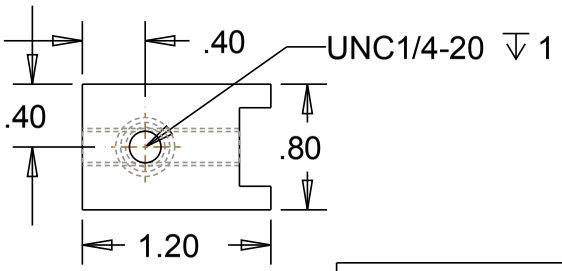

Part Name: Wiper Housing	Unit: Inches	Author: YANG Bo
Material: Aluminum	Quantity: 3	Data: 20110404

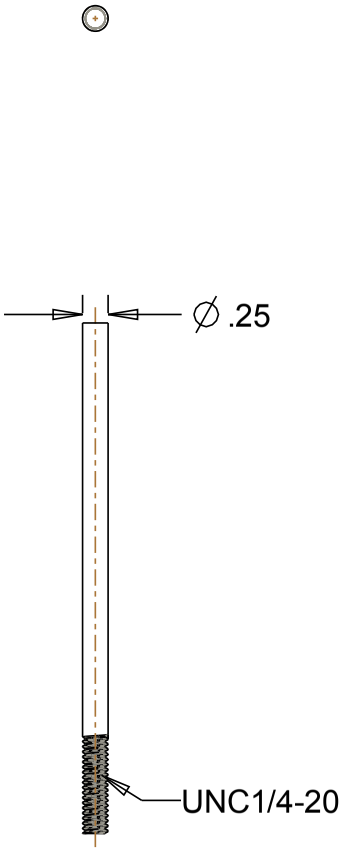

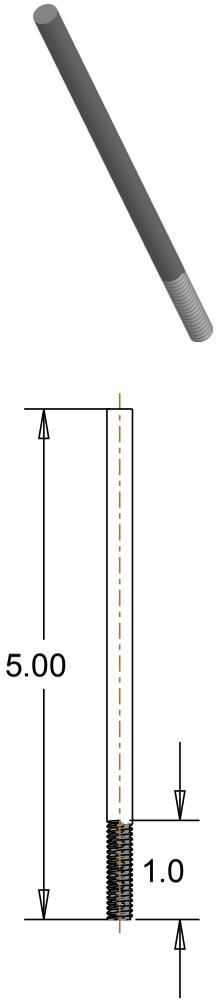

Part Name: Leg Rod	Unit: Inches	Author: YANG Bo
Material: Aluminum	Quantity: 3	Data: 20110404

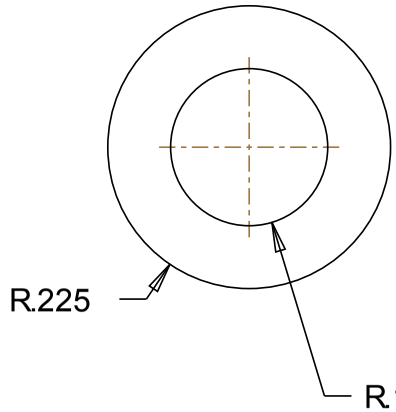

Press Fit with

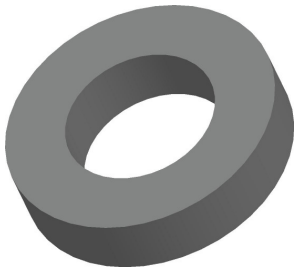

∅ 1/4 Pin

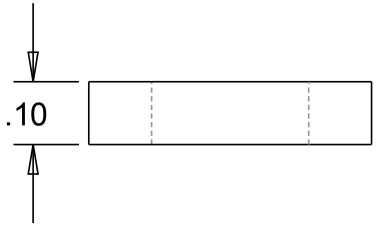

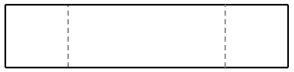

Part Name: Ball Pin Fix	Unit: Inches	Author: YANG Bo
Material: Aluminum	Quantity: 3	Data: 20110404

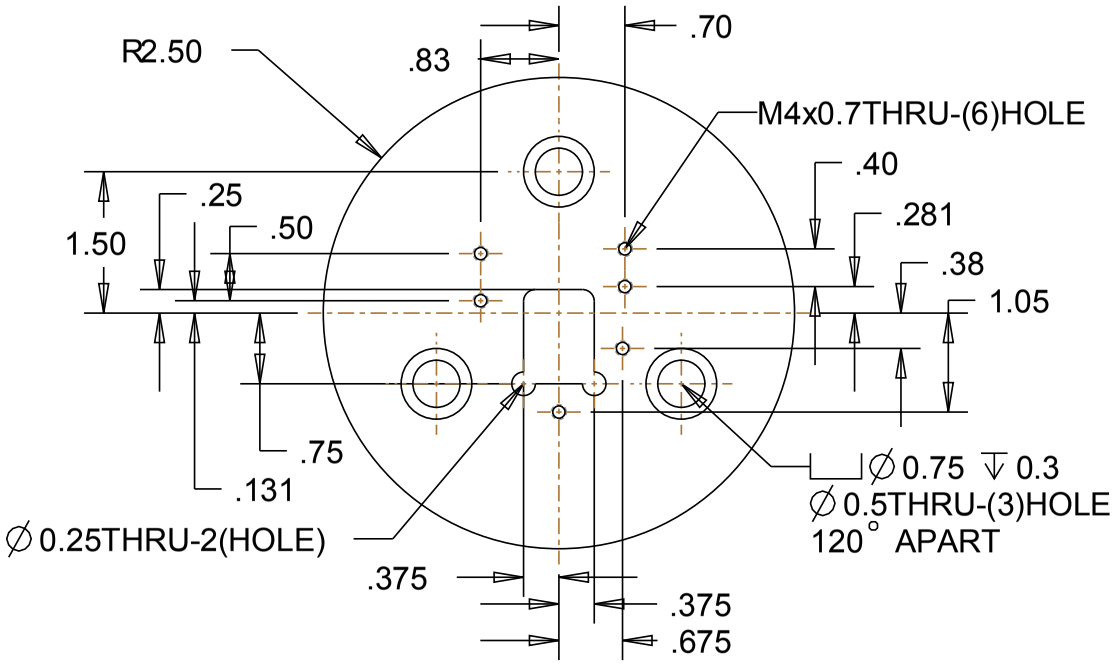

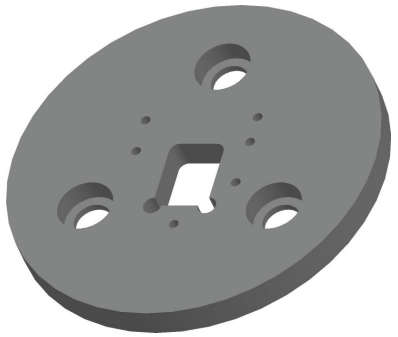

Part Name: Master Platform	Unit: Inches	Author: YANG Bo
Material: Aluminum	Quantity: 1	Data: 20110404

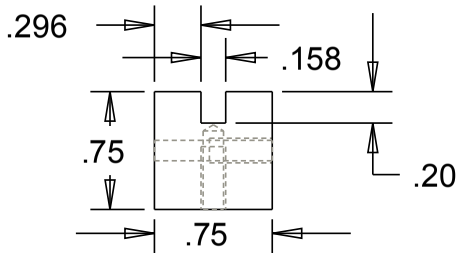

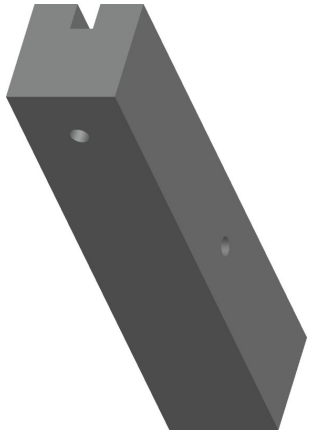

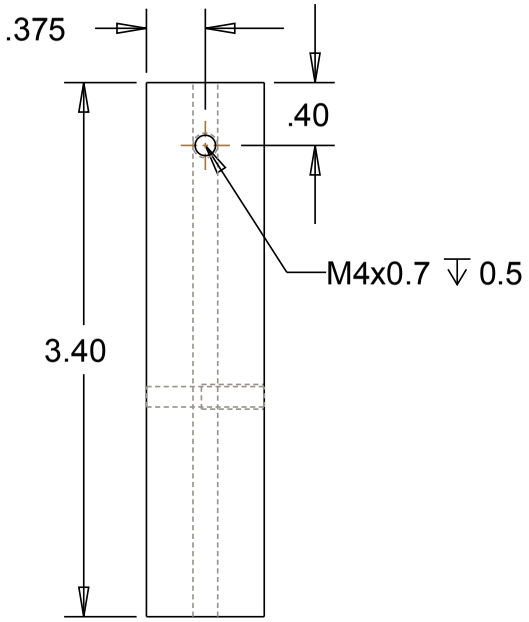

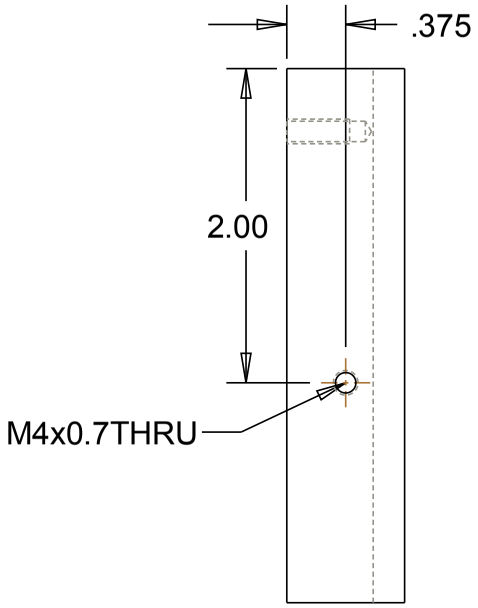

Part Name: Rack Support	Unit: Inches	Author: YANG Bo
Material: Aluminum	Quantity: 1	Data: 20110404

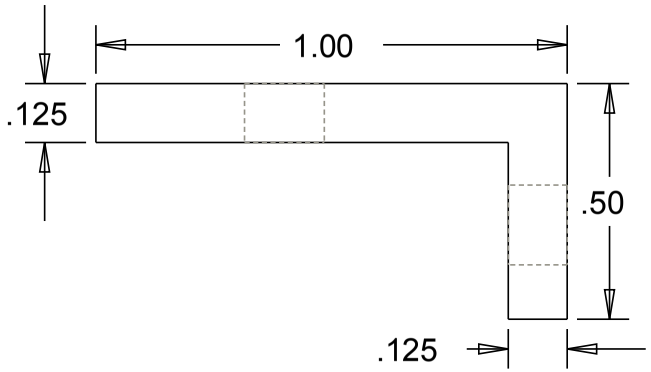

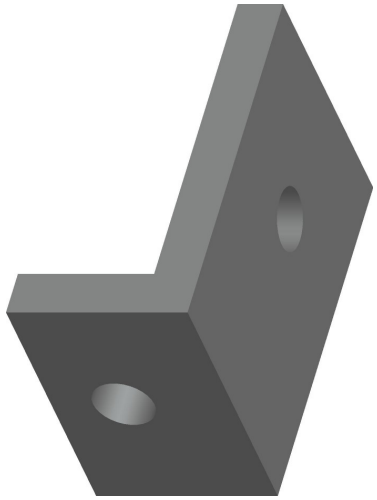

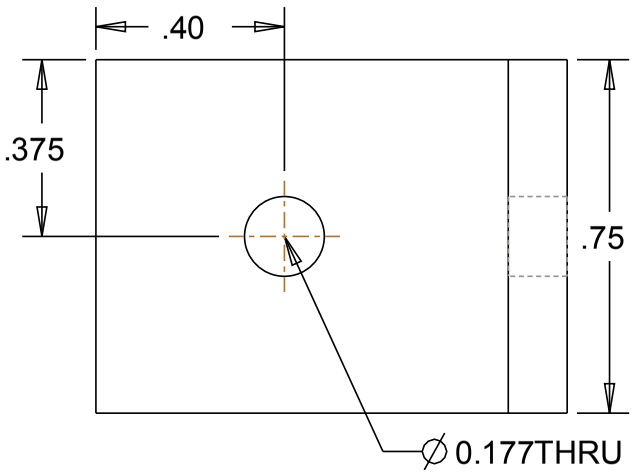

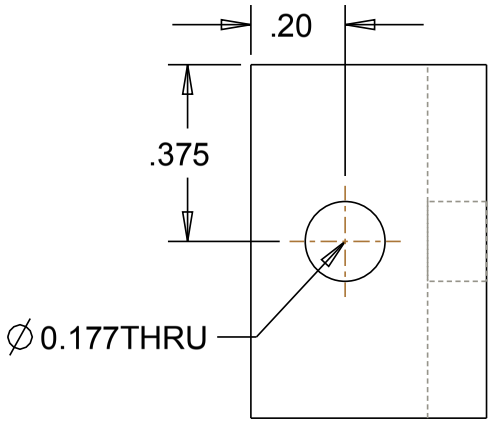

Part Name: Angle	Unit: Inches	Author: YANG Bo
Material: Aluminum	Quantity: 2	Data: 20110404

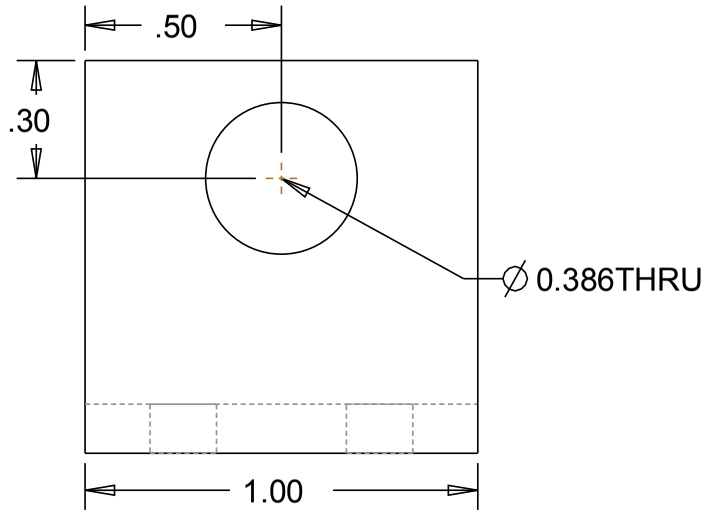

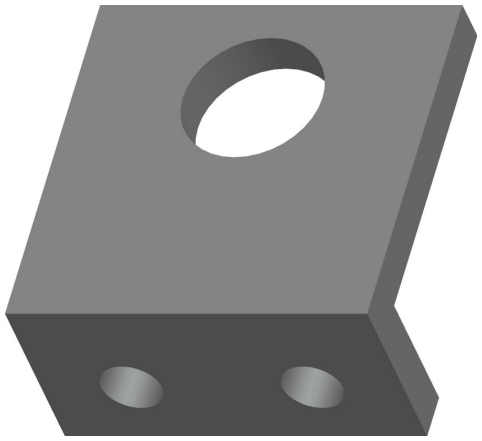

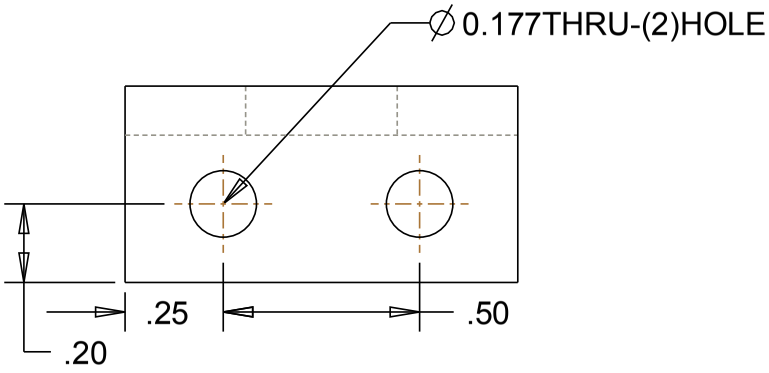

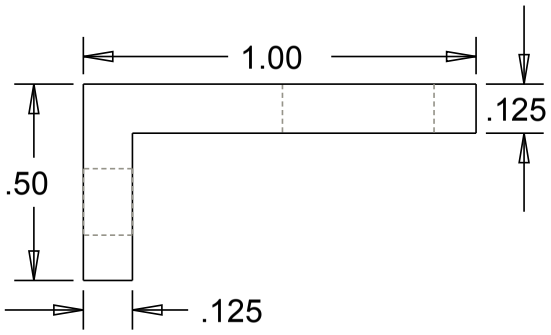

Part Name: Encoder Angle	Unit: Inches	Author: YANG Bo
Material: Aluminum	Quantity: 1	Data: 20110404

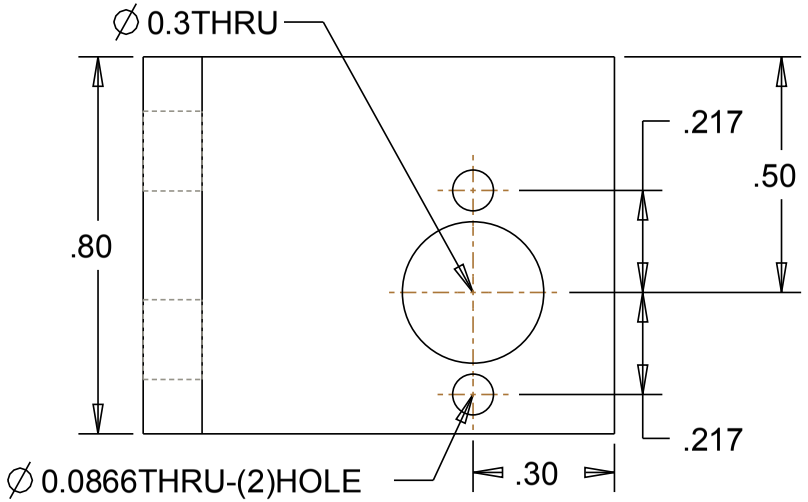

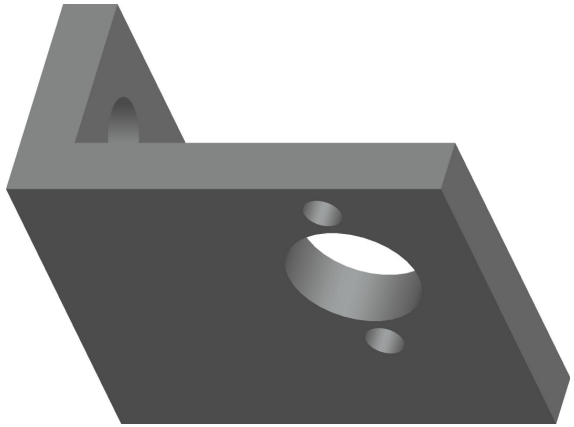

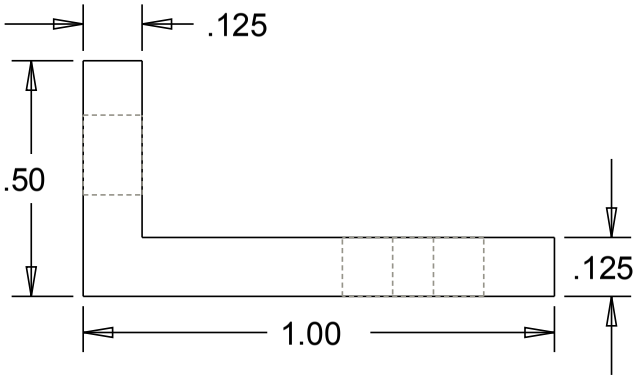

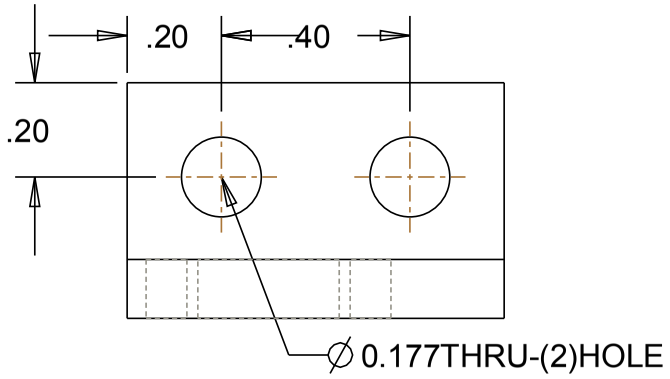

Part Name: Motor Angle	Unit: Inches	Author: YANG Bo
Material: Aluminum	Quantity: 1	Data: 20110404

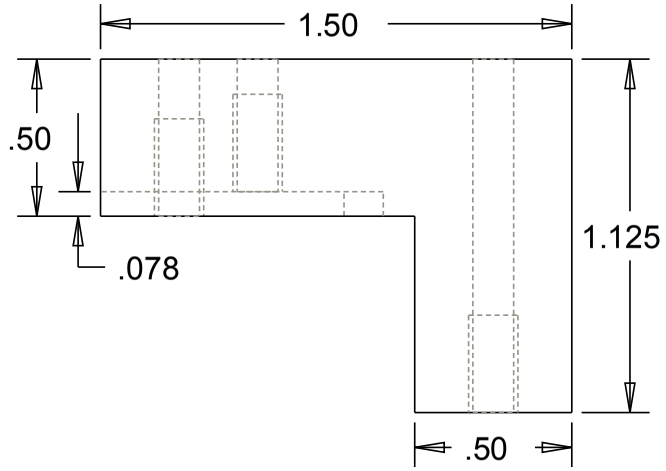

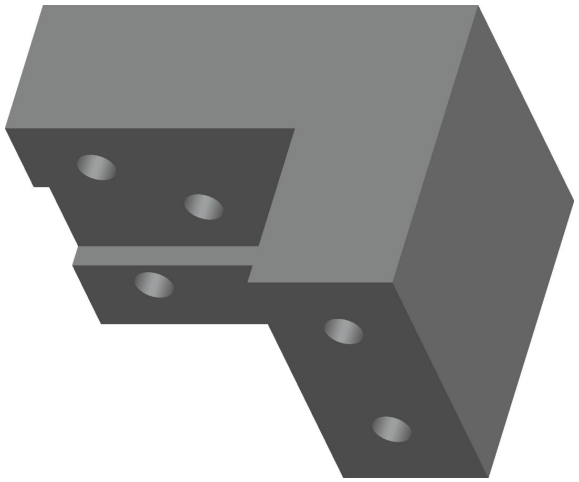

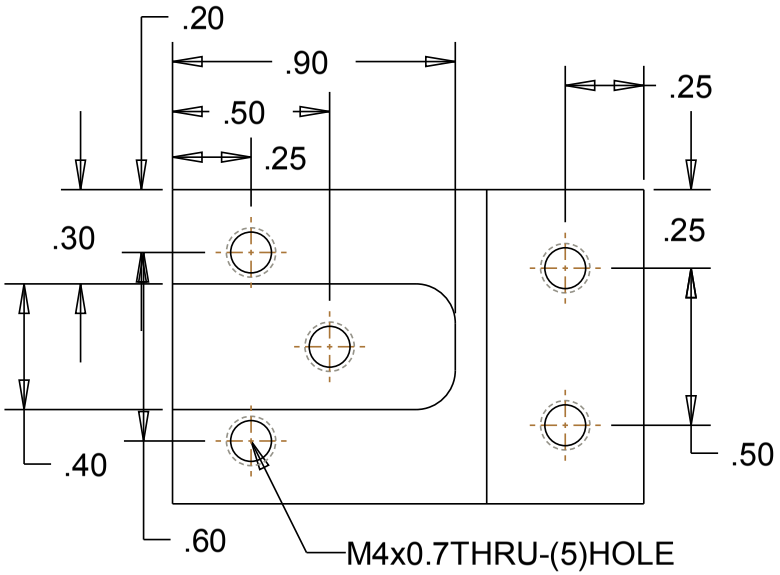

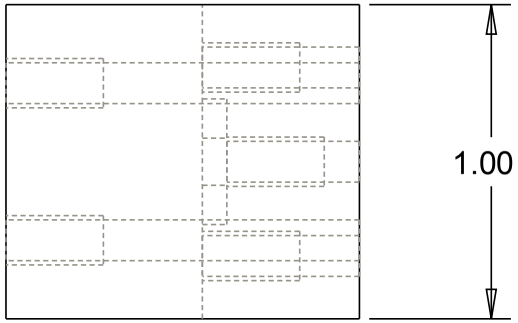

Part Name: Rack Rear Conn	Unit: Inches	Author: YANG Bo
Material: Aluminum	Quantity: 1	Data: 20110428

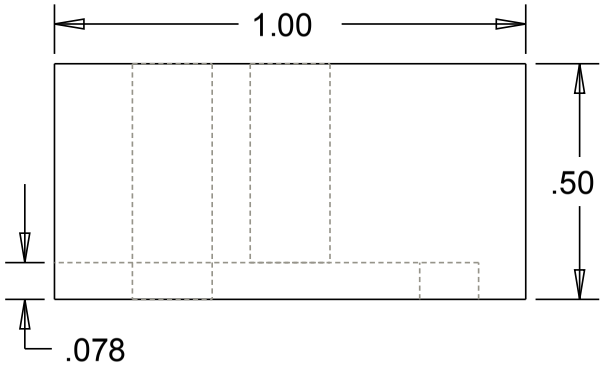

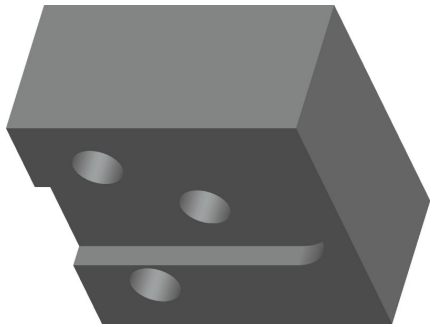

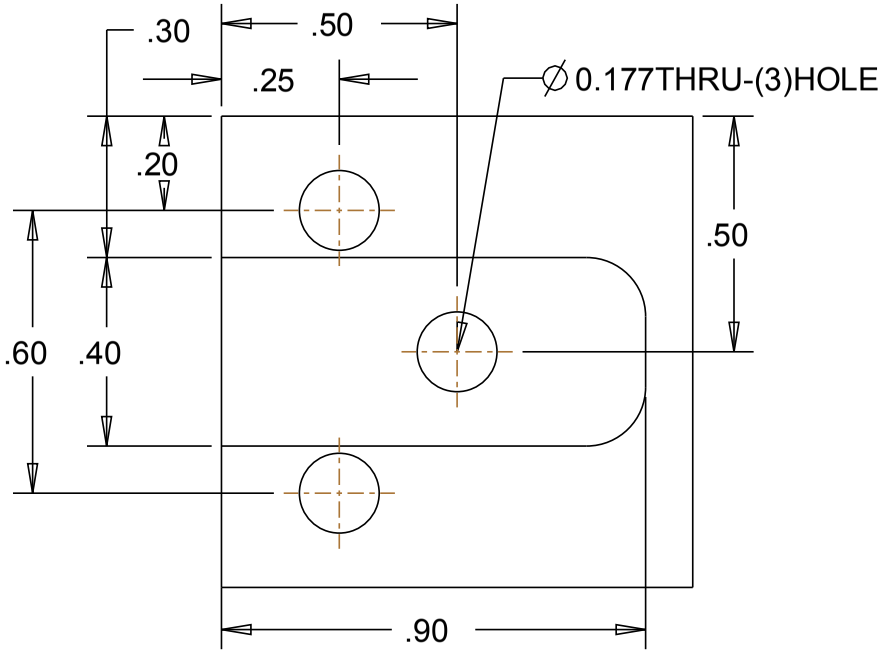

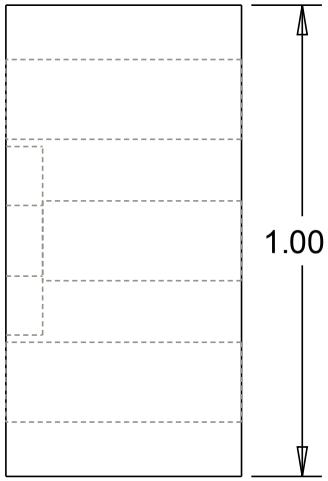

Part Name: Rack Lock	Unit: Inches	Author: YANG Bo
Material: Aluminum	Quantity: 2	Data: 20110404

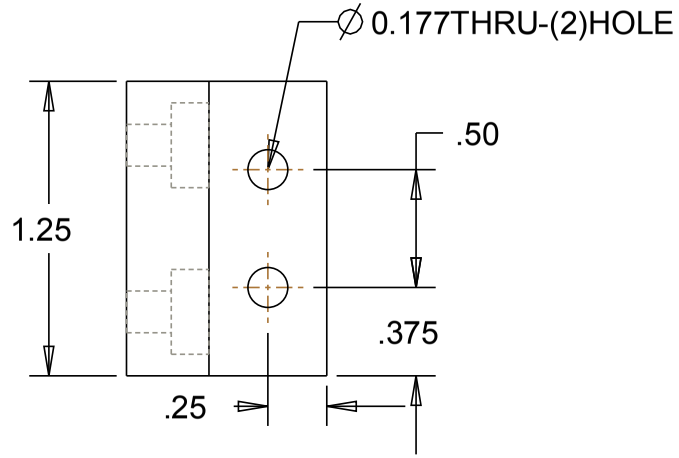

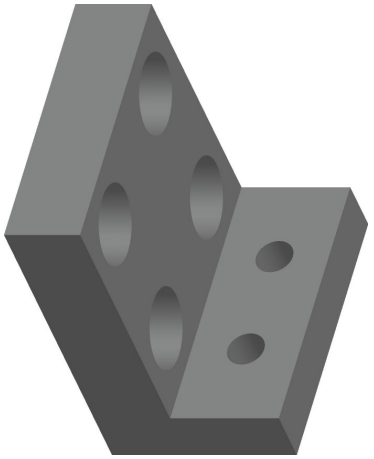

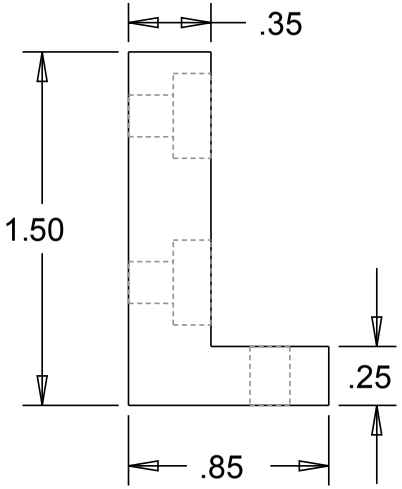

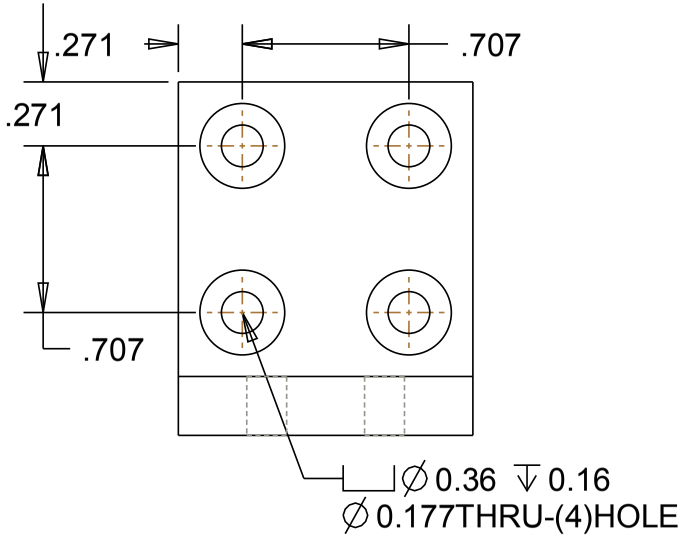

Part Name: FS Angle	Unit: Inches	Author: YANG Bo
Material: Aluminum	Quantity: 1	Data: 20110428

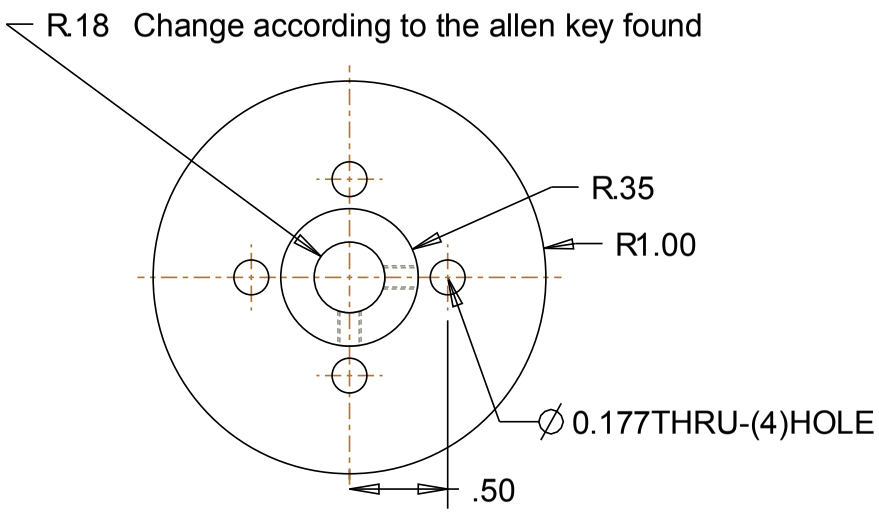

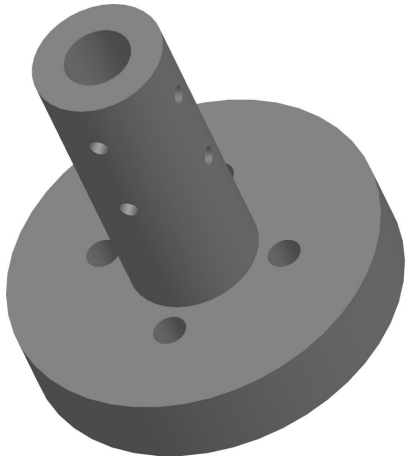

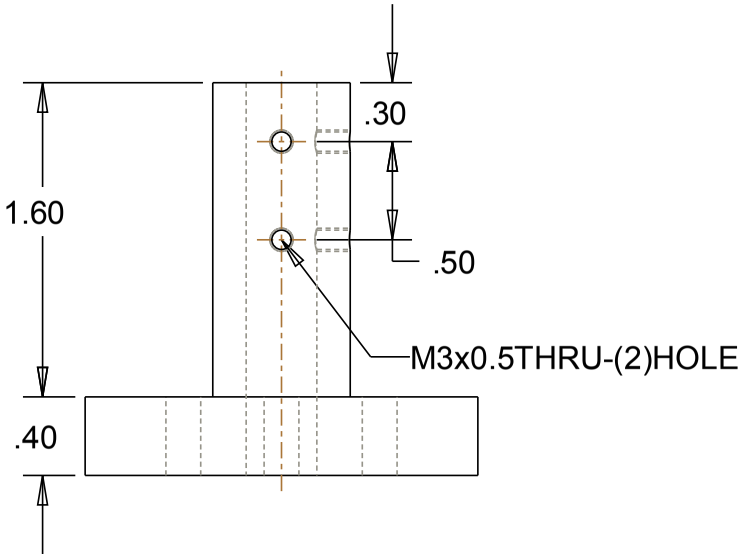

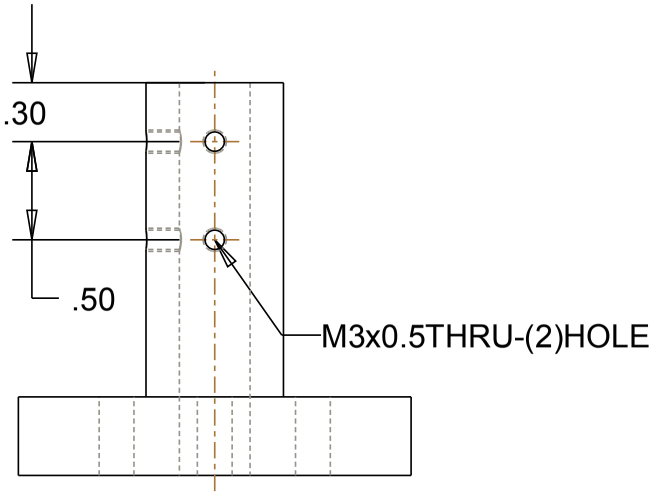

Part Name: Handle Mount	Unit: Inches	Author: YANG Bo
Material: Aluminum	Quantity: 1	Data: 20110428

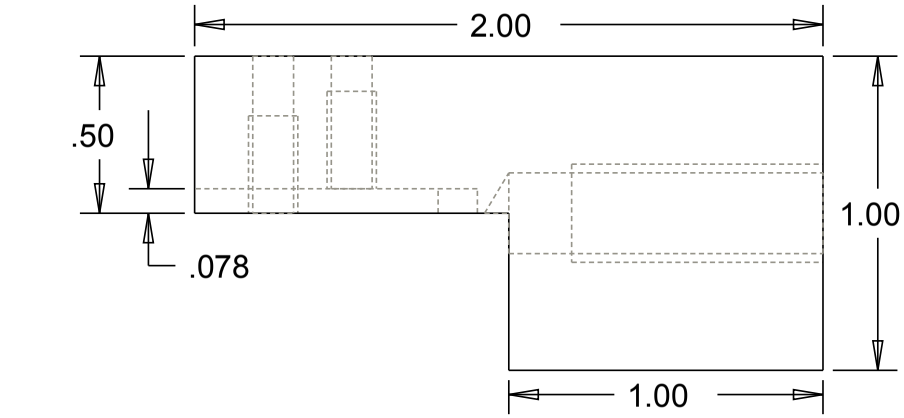

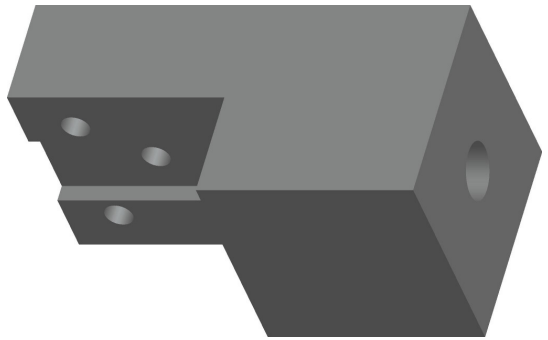

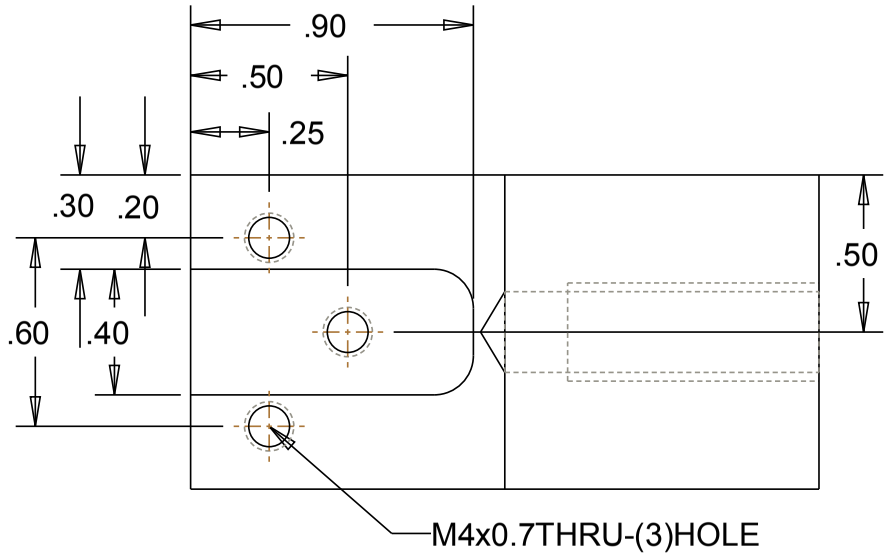

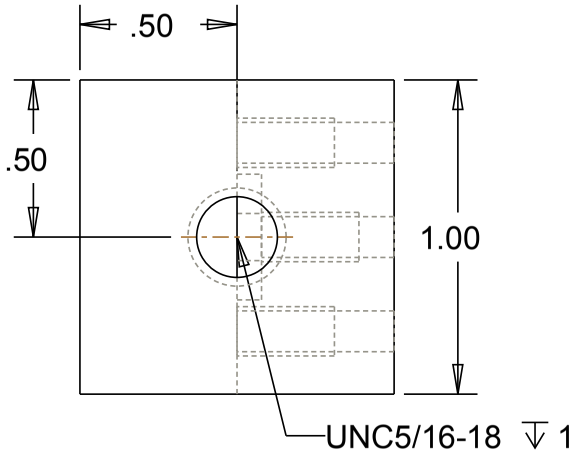

Part Name: Rack Needle Conn	Unit: Inches	Author: YANG Bo
Material: Aluminum	Quantity: 1	Data: 20110404

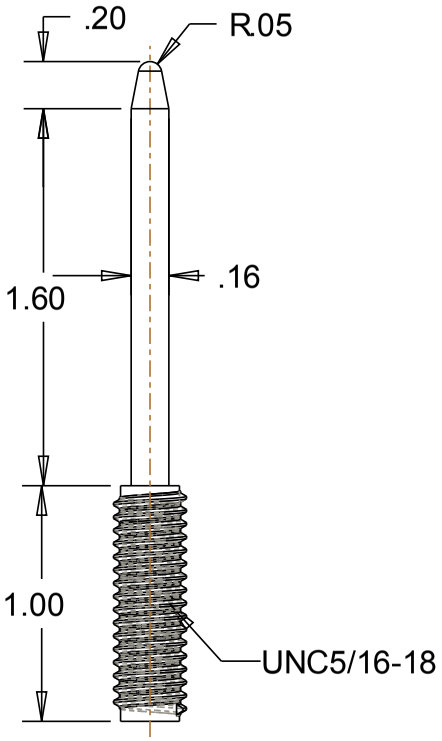

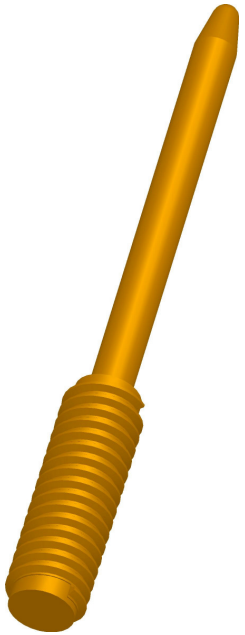

Part Name: Needle	Unit: Inches	Author: YANG Bo
Material: Aluminum	Quantity: 1	Data: 20110421

Bibliography

[1] Bo Yang, U-Xuan Tan, Alan McMillan, Rao Gullapalli, and Jaydev P. Desai. Design and implementation of a pneumatically-actuated robot for breast biopsy under continuous MRI. In *IEEE International Conference on Robotics and Automation*, pages 674–679, Shanghai, China, May 2011.

[2] Bo Yang, U-Xuan Tan, Alan McMillan, Rao Gullapalli, and Jaydev P. Desai. Design and control of a 1-DOF MRI compatible pneumatically actuated robot with long transmission lines. *IEEE/ASME Transactions on Mechatronics*, 16(6):1040–1048, December 2011.

[3] American Cancer Society. Breast cancer facts & figures 2011–2012. American Cancer Society, Inc., Atlanta, Georgia, 2011.

[4] American Cancer Society. Cancer Facts & Figures 2012. American Cancer Society, Atlanta, 2012.

[5] Andreas Melzer. Image-guided robotics and navigation. *Minimally Invasive Therapy*, 16(4):194–195, 2007.

[6] Constance D. Lehman, Constantine Gatsonis, Christinae K. Kuhl, R. Edward Hendrick, Etta D. Pisano, Lucy Hanna, Sue Peacock, Stanley F. Smazal, Daniel D. Maki, Thomas B. Julian, Elizabeth R. DePeri, David A. Bluemke, and Mitchell D. Schnall. MRI evaluation of the contralateral breast in women with recently diagnosed breast cancer. *The New England Journal of Medicine*, 356(13):1295–1303, March 2007.

[7] Christiane K. Kuhl, Simone Schrading, Heribert B. Bieling, Eva Wardelmann, Claudia C. Leutner, Roy Koenig, Walther Kuhn, and Hans H. Schild. MRI for diagnosis of pure ductal carcinoma in situ: a prospective observational study. *The Lancet*, 370(9586):485–492, August 2007.

[8] Elias A. Zerhouni. Major trends in the imaging sciences: 2007 eugene p. pendergrass new horizons lecture. *Radiology*, 249(2):403–409, September 2008.

[9] U.S. FDA. A primer on medical device interactions with magnetic resonance imaging systems. pages 1–9, 1997.

[10] Garnette R. Sutherland, Taro Kaibara, Deon Louw, David I. Hoult, Boguslaw Tomanek, and John Saunders. A mobile high-field magnetic resonance system for neurosurgery. *Journal of Neurosurgery*, 91(5):804–813, November 1999.

[11] Yik San Kwoh, Joahin Hou, Edmond A. Jonckheere, and Samad Hayati. A robot with improved absolute positioning accuracy for CT guided stereotactic brain surgery. *IEEE Transactions on Biomedical Engineering*, 35(2):153–160, February 1988.

[12] Peter Kazanzides, Brent D. Mittelstadt, Bela L. Musits, William L. Bargar, Joel F. Zuhars, Bill Williamson, Phillip W. Cain, and Emily J. Carbone. An integrated system for cementless hip replacement. *IEEE Engineering in Medicine and Biology Magazine*, 14(3):307–313, May 1995.

[13] Gary S. Guthart and J. Kenneth Salisbury, Jr. The intuitive^{TM} telesurgery system: overview and application. In *IEEE International Conference on Robotics and Automation*, volume 1, pages 618–621, San Francisco, CA, April 2000.

[14] Ana Luisa Trejos, Rajni V. Patel, and Richard A. Malthaner. A device for robot-assisted minimally-invasive lung brachytherapy. In *IEEE International Conference on Robotics and Automation*, pages 4187–4192, Orlando, Florida, May 2006.

[15] Rafael Martínez-Monge, Cristina Garrán, Isabel Vivas, and José María López-Picazo. Percutaneous CT-guided ^{103}Pd implantation for the medically inoperable patient with T1N0M0 non-small cell lung cancer: a case study. *Brachytherapy*, 3(3):179–181, 2004.

[16] Amir Degani, Howie Choset, Alon Wolf, and Marco A. Zenati. Highly articulated robotic probe for minimally invasive surgery. In *IEEE International Conference on Robotics and Automation*, pages 4167–4172, Orlando, Florida, May 2006.

[17] Kodak Tadano and Kenji Kawashima. Development of a master slave system with force sensing using pneumatic servo system for laparoscopic surgery. In *IEEE International Conference on Robotics and Automation*, pages 947–952, Roma, Italy, April 2007.

[18] Jacques Marescaux, Joel Leroy, Michel Gagner, Francesco Rubino, Didier Mutter, Michel Vix, Steven E. Butner, and Michelle K. Smith. Transatlantic robot-assisted telesurgery. *Nature*, 413:379–380, May 2001.

[19] Ana Luisa Trejos, A. W. Lin, M. P. Pytel, Rajni V. Patel, and Richard A. Malthaner. Robot-assisted minimally invasive lung brachytherapy. *The International Journal of Medical Robotics and Computer Assisted Surgery*, 3:41–51, March 2007.

[20] Julianna Pisch, Scott J. Belsley, Robert Ashton, Lin Wang, Rudolph Woode, and Cliff Connery. Placement of ^{125}I implants with the da Vinci robotic system after video-assisted thoracoscopic wedge resection: a feasibility study. *International Journal of Radiation Oncology · Biology · Physics*, 60(3):928–932, November 2004.

[21] B. Maurin, O. Piccin, B. Bayle, J. Gangloff, M. de Mathelin, L. Soler, and A. Gangi. A new robotic system for CT-guided percutaneous procedures with haptic feedback. *International Congress Series*, 1268:515–520, June 2004.

[22] Dan Stoianovici, Jeffrey A. Cadeddu, Roger D. Demaree, Stephen A. Basile, Russell H. Taylor, Louis L. Whitcomb, William N. Sharpe, and Louis R. Kavoussi. A

novel mechanical transmission applied to percutaneous renal access. In *Proceedings of the ASME Dynamic Systems and Control Division, DSC*, volume 61, pages 401–406, 1997.

[23] Dan Stoianovici, Jeffrey A. Cadeddu, Roger D. Demaree, Stephen A. Basile, Russell H. Taylor, Louis L. Whitcomb, William N. Sharpe, and Louis R. Kavoussi. An efficient needle injection technique and radiological guidance method for percutaneous procedures. In Jocelyne Troccaz, Eric Grimson, and Ralph Mösges, editors, *CVRMed-MRCAS'97*, volume 1205 of *Lecture Notes in Computer Science*, pages 295–298. Springer Berlin / Heidelberg, 1997.

[24] Dan Stoianovici, Kevin Cleary, Alexandru Patriciu, Dumitru Mazilu, Alexandru Stanimir, Nicolae Craciunoiu, Vance Watson, and Louis Kavoussi. AcuBot: a robot for radiological interventions. *IEEE Transactions on Robotics and Automation*, 19(5):927–930, October 2003.

[25] Stephen B. Solomon, Alexandru Patriciu, Mark E. Bohlman, Louis R. Kavoussi, and Dan Stoianovici. Robotically driven interventions: a method of using CT fluoroscopy without radiation exposure to the physician. *Radiology*, 255(1):277–282, October 2002.

[26] Stephen B. Solomon, Alexandru Patriciu, and Dan S. Stoianovici. Tumor ablation treatment planning coupled to robotic implementation: a feasibility study. *Journal of Vascular and Interventinal Radiology*, 17(5):903–907, May 2006.

[27] Zhouping Wei, Mingyue Ding, Donal Downey, and Aaron Fenster. 3D TRUS guided robot assisted prostate brachytherapy. In James Duncan and Guido Gerig, editors, *International Conference on Medical Image Computing and Computer Assisted Intervention*, volume 3750 of *Lecture Notes in Computer Science*, pages 17–24. Springer Berlin / Heidelberg, 2005.

[28] Louis Phee, Di Xiao, John Yuen, Chee Fatt Chan, Henry Ho, Choon Hua Thng, Christopher Cheng, and Wan Sing Ng. Ultrasound guided robotic system for transperineal biopsy of the prostate. In *IEEE International Conference on Robotics and Automation*, pages 1315–1320, Barcelona, Spain, April 2005.

[29] Septimiu E. Salcudean, Thomas D. Prananta, William J. Morris, and Ingrid Spadinger. A robotic needle guide for prostate brachytherapy. In *IEEE International Conference on Robotics and Automation*, pages 2975–2981, Pasadena, CA, USA, May 2008.

[30] Kevin Cleary, Andreas Melzer, Vance Watson, Gernot Kronreif, and Dan Stoianovici. Interventional robotic systems: applications and technology state-of-the-art. *Minimally Invasive Therapy*, 15(2):101–113, 2006.

[31] Ken Masamune, Etsuko Kobayashi, Yoshitaka Masutani, Makoto Suzuki, Takeyoshi Dohi, Hiroshi Iseki, and Kintomo Takakura. Development of an MRI-compatible needle insertion manipulator for stereotactic neurosurgery. *Journal of Image Guided Surgery*, 1(4):242–248, 1995.

[32] Azadeh Khanicheh, Nikolaos Tsekos, and Constantinos Mavroidis. Guest editorial Introduction to the focused section on mechatronic systems for MRI applications. *IEEE/ASME Transactions on Mechatronics*, 13(3):265–267, June 2008.

[33] H. Elhawary, A. Zivanovic, B. Davies, and M. Lampérth. A review of magnetic resonance imaging compatible manipulators in surgery. *Proceedings of the Institution of Mechanical Engineers. Part H, Journal of Engineering in Medicine*, 220(3):413–424, 2006.

[34] Mingyen Ho, Michael Koltz, J. Marc Simard, Rao Gullapalli, and Jaydev P. Desai. Towards a MR image-guided SMA-actuated neurosurgical robot. In *IEEE International Conference on Robotics and Automation*, pages 1153–1158, Shanghai, China, May 2011.

[35] Haythem Elhawary, Aleksander Zivanovic, Marc Rea, Brain Davis, Collin Besant, Donald McRobbie, Nandita de Souza, Ian Young, and Michael Lampérth. The feasibility of MR-image guided prostate biopsy using piezoceramic motors inside or near to the magnet isocentre. In Rasmus Larsen, Mads Nielsen, and Jon Sporring, editors, *International Conference on Medical Image Computing and Computer Assisted Intervention*, volume 4190 of *Lecture Notes in Computer Science*, pages 519–526. Springer Berlin / Heidelberg, September 2006.

[36] Gregory S. Fischer, Axel Krieger, Iulian Iordachita, Csaba Csoma, Louis L. Whitcomb, and Gabor Fichtinger. MRI compatibility of robot actuation techniques - a comparative study. In *International Conference on Medical Image Computing and Computer Assisted Intervention*, pages 509–517, 2008.

[37] Andrew A. Goldenberg, John Trachtenberg, Walter Kucharczyk, Yang Yi, Masoom Haider, Leo Ma, Robert Weersink, and Cyrus Raoufi. Robotic system for closed-bore MRI-guided prostatic interventions. *IEEE/ASME Transactions on Mechatronics*, 13(3):374–379, June 2008.

[38] Axel Krieger, Iulian Iordachita, Sang-Eun Song, Nathan B. Cho, Peter Guion, Gabor Fichtinger, and Louis L. Whitcomb. Development and preliminary evaluation of an actuated MRI-compatible robotic device for MRI-guided prostate intervention. In *IEEE International Conference on Robotics and Automation*, pages 1066–1073, Anchorage, Alaska, USA, May 2010.

[39] Blake T. Larson, Nikolaos V. Tsekos, and Arthur G. Erdman. A robotic device for minimally invasive breast interventions with real-time MRI guidance. In *Bioinformatics and Bioengineering, 2003. Proceedings. Third IEEE Symposium on*, pages 190–197, March 2003.

[40] Takashi Suzuki, Hongen Liao, Etsuko Kobayashi, and Ichiro Sakuma. Ultrasonic motor driving method for EMI-free image in MR image-guided surgical robotic system. In *IEEE/RSJ International Conference on Intelligent Robots and Systems*, pages 522–527, San Diego, CA, October 29 – November 2 2007.

[41] Hao Su, Michael Zervas, Gregory A. Cole, Cosme Furlong, and Gregory S. Fischer. Real-time MRI-guided needle placement robot with integrated fiber optic force sensing. In *IEEE International Conference on Robotics and Automation*, pages 1583–1588, Shanghai, China, May 2011.

[42] Ningbo Yu, Christoph Hollnagel, Armin Blickenstorfer, Spyros S. Kollias, and Robert Riener. Comparison of MRI-compatible mechatronic systems with hydrodynamic and pneumatic actuation. *IEEE/ASME Transactions on Mechatronics*, 13(3):268–277, June 2008.

[43] Dan Stoianovici, Alexandru Patriciu, Doru Petrisor, Dumitru Mazilu, and Louis Kavoussi. A new type of motor: pneumatic step motor. *IEEE/ASME Transactions on Mechatronics*, 12(1):98–106, February 2007.

[44] Hiroyuki Sajima, Ikuma Sato, Hiromasa Yamashita, Takeyoshi Dohi, and Ken Masamune. Two-DOF non-metal manipulator with pneumatic stepping actuators for needle puncturing inside open-type MRI. In *World Automation Congress*, Kobe, Japan, September 19-23 2010. TSI Press.

[45] Kiyoyuki Chinzei, Nobuhiko Hata, Ferenc A. Jolesz, and Ron Kikinis. MR compatible surgical assist robot: system integration and preliminary feasibility study. *International Conference on Medical Image Computing and Computer Assisted Intervention*, 3:921–930, October 2000.

[46] Axel Krieger, R. C. Susil, Gabor Fichtinger, E. Atalar, and Louis L. Whitcomb. Design of a novel MRI compatible manipulator for image guided prostate intervention. In *IEEE International Conference on Robotics and Automation*, volume 1, pages 377–382, New Orleans, LA, USA, April 2004.

[47] R. Moser, R. Gassert, E. Burdet, L. Sache, H. R. Woodtli, J. Erni, W. Maeder, and H. Bleuler. An MR compatible robot technology. In *IEEE International Conference on Robotics and Automation*, pages 670–675, Taipei, Taiwan, September 2003.

[48] Roger Gassert, Roland Moser, Etienne Burdet, and Hannes Bleuler. MRI/fMRI-compatible robotics system with force feedback for interaction with human motion. *IEEE/ASME Transactions on Mechatronics*, 11(2):216–224, April 2006.

[49] Garnette R. Sutherland, Isabelle Latour, Alexander D. Greer, Tim Fielding, Georg Feil, and Perry Newhook. An image-guided magnetic resonance-compatible surgical robot. *Journal of Neurosurgery*, 62(2):286–292, February 2008.

[50] Dan Stoianovici, Danny Song, Doru Petrisor, Daniel Ursu, Dumitru Mazilu, Michael Mutener, Michael Schar, and Alexandru Patriciu. "MRI Stealth" robot for prostate interventions. *Minimally Invasive Therapy*, 16(4):241–248, 2007.

[51] Gregory S. Fischer, Iulian Iordachita, Csaba Csoma, Junichi Tokuda, Simon P. DiMaio, Clare M. Tempany, Nobuhiko Hata, and Gabor Fichtinger. MRI-compatible

pneumatic robot for transperineal prostate needle placement. *IEEE/ASME Transactions on Mechatronics*, 13(3):295–305, June 2008.

[52] Sang-Eun Song, Nathan B. Cho, Nobuhito Hata, Clare Tempany, Gabor Fichtinger, and Iulian Iordachita. Development of a pneumatic robot for MRI-guided transperineal prostate biopsy and brachytherapy: new approaches. In *IEEE International Conference on Robotics and Automation*, pages 2580–2585, Anchorage, AK, May 2010.

[53] Werner A. Kaiser, Harald Fischer, Jeorg Vagner, and Manfred Selig. Robotic system for biopsy and therapy of breast lesions in a high-field whole-body magnetic resonance tomography unit. *Investigative Radiology*, 35(8):513–519, August 2000.

[54] Blake T. Larson, Arthur G. Erdman, Nikolaos V. Tsekos, Essa Yacoub, Panagiotis V. Tsekos, and Ioannis G. Koutlas. Design of an MRI-compatible robotic stereotactic device for minimally invasive interventions in the breast. *Journal of Biomechanical Engineering*, 126(4):458–465, August 2004.

[55] Rebecca Kokes, Kevin Lister, Rao Gullapalli, Bao Zhang, Howard Richard, and Jaydev P. Desai. Towards a needle driver robot for radiofrequency ablation of tumors under continuous MRI. In *IEEE International Conference on Robotics and Automation*, pages 2509–2514, Pasadena, CA, USA, May 2008.

[56] Rebecca Kokes, Kevin Lister, Rao Gullapalli, Bao Zhang, Alan McMillan, Howard Richard, and Jaydev P. Desai. Towards a teleoperated needle driver robot with haptic feedback for RFA of breast tumors under continuous MRI. *Medical Image Analysis*, 13(3):445–455, June 2009.

[57] Cyrus Raoufi, Pinhas Ben-Tzvi, Andrew A. Goldenberg, and Walter Kucharczyk. A MR-compatible tele-robotic system for MRI-guided intervention: system overview and mechanical design. In *IEEE/RSJ International Conference on Intelligent Robots and Systems*, pages 1795–1800, San Diego, CA, USA, November 2007.

[58] Cyrus Raoufi, Andrew A. Goldenberg, and Walter Kucharczyk. Control paradigm and design for a novel MR-compatible tele-robotic system for MRI-guided neurosurgery. In *Mechatronics and Automation, 2007. ICMA 2007. International Conference on*, pages 1445–1451, Harbin, China, August 2007.

[59] Cyrus Raoufi, Andrew A. Goldenberg, and Walter Kucharczyk. Design and control of a novel hydraulically/pneumatically actuated robotic system for MRI-guided neurosurgery. *Journal of Biomedical Science and Engineering*, 1(1):68–74, May 2008.

[60] Nabil Zemiti, Ivan Bricault, Céline Fouard, Bénédicte Sanchez, and Philippe Cinquin. LPR: A CT and MR-compatible puncture robot to enhance accuracy and safety of image-guided interventions. *IEEE/ASME Transactions on Mechatronics*, 13(3):306–315, June 2008.

[61] Nicholas Pappafotis, Wojciech Bejgerowski, Rao Gullapalli, J. Marc Simard, Satyandra K. Gupta, and Jaydev P. Desai. Towards design and fabrication of a miniature MRI-compatible robot for applications in neurosurgery. *32nd Mechanisms and Robotics Conference, Parts A and B*, 2:747–754, 2008.

[62] Nikolaos V. Tsekos, Azadeh Khanicheh, Eftychios Christoforou, and Constantinos Mavroidis. Magnetic resonance-compatible robotic and mechatronics systems for image-guided interventions and rehabilitation: A review study. *Annual Review of Biomedical Engineering*, 9:351–387, August 2007.

[63] Wensheng Hou, Shan Shen, and A. Sterr. An MRI compatible visual force-feedback system for the study of force control mechanics. *Engineering in Medicine and Biology Society, 2005. IEEE-EMBS 2005. 27th Annual International Conference of the*, pages 3687–3690, January 2005.

[64] Zion Tsz Ho Tse, Haytham Elhawary, Aleksandar Zivanovic, Marc Rea, Martyn Paley, Graeme Bydder, Brian L. Davies, Ian Young, and Michael U. Lampérth. A 3-DOF MR-compatible device for magic angle related *in vivo* experiments. *IEEE/ASME Transactions on Mechatronics*, 13(3):316–324, June 2008.

[65] Ningbo Yu, Roger Gassert, and Robert Riener. Mutual interferences and design principles for mechatronic devices in magnetic resonance imaging. *International Journal of Computer Assisted Radiology and Surgery*, 6(4):473–488, July 2011.

[66] John F. Schenck. The role of magnetic susceptibility in magnetic resonance imaging: MRI magnetic compatibility of the first and second kinds. *Medical Physics*, 23(6):815–850, June 1996.

[67] Takashi Kubota, Kouhei Tada, and Yasuharu Kunii. Smart manipulator actuated by ultra-sonic motors for lunar exploration. In *IEEE International Conference on Robotics and Automation*, pages 3576–3581, Pasadena, CA, USA, May 2008.

[68] Ningbo Yu and R. Riener. Review on MR-compatible robotics systems. *Biomedical Robotics and Biomechatronics, 2006. BioRob 2006. The First IEEE/RAS-EMBS International Conference on*, pages 661–665, February 2006.

[69] Gregory S. Fischer, Iulian Iordachita, Csaba Csoma, Junichi Tokuda, Philip W. Mewes, Clare M. Tempany, Nobuhiko Hata, and Gabor Fichtinger. Pneumatically operated MRI-compatible needle placement robot for prostate interventions. In *IEEE International Conference on Robotics and Automation*, pages 2489–2495, Pasadena, CA, USA, May 2008.

[70] Roger Gassert, Dominique Chapuis, Hannes Bleuler, and Etienne Burdet. Sensors for application in magnetic resonance environments. *IEEE/ASME Transactions on Mechatronics*, 13(3):335–344, June 2008.

[71] U-Xuan Tan, Bo Yang, Rao Gullapalli, and Jaydev P. Desai. Triaxial MRI-compatible fiber-optic force sensor. *IEEE Transactions on Robotics*, 27(1):65–74, February 2011.

[72] George H. Pfreundschuh, Vijay Kumar, and Thomas G. Sugar. Design and control of a 3-DOF in-parallel actuated manipulator. In *IEEE International Conference on Robotics and Automation*, volume 2, pages 1659–1664, Sacramento, California, USA, April 1991.

[73] Vijay Kumar, Thomas G. Sugar, and George H. Pfreundschuh. A three degree-of-freedom in-parallel actuated manipulator. In A. Morecki, G. Bianchi, and K. Jaworek, editors, *Proceedings of the Ninth CISM-IFToMM Symposium on Theory and Practice of Robots and Manipulators*, volume 187 of *Lecture Notes in Control and Information Sciences*, pages 215–226. Springer Berlin / Heidelberg, 1993.

[74] Septimiu E. Salcudean, P. A. Drexel, D. Ben-Dov, A. J. Taylor, and P. D. Lawrence. A six degree-of-freedom, hydraulic, one person motion simulator. In *IEEE International Conference on Robotics and Automation*, volume 3, pages 2437–2443, San Diego, CA, USA, May 1994.

[75] George H. Pfreundschuh, Thomas G. Sugar, and Vijay Kumar. Design and control of a three-degrees-of-freedom, in-parallel, actuated manipulator. *Journal of Robotic Systems*, 11(2):103–115, 1994.

[76] Roelof G. van Silfhout. High-precision hydraulic Stewart platform. *Review of Scientific Instruments*, 70(8):3488–3494, August 1999.

[77] Steve Hadden, Torey Davis, Paul Buchele, Jim Boyd, and Tim Hintz. Heavy load vibration isolation system for airborne payloads. In *Smart Structures and Materials 2001: Industrial and Commercial Applications of Smart Structures Technologies*, volume 4332, pages 171–182, Newport Beach, CA, USA, March 2001. SPIE.

[78] R. Aracil, R. Saltarén, and O. Reinoso. Parallel robots for autonomous climbing along tubular structures. *Robotics and Autonomous System*, 42(2):125–134, February 2003.

[79] R. F. Boian, M. Bouzit, G. C. Burdea, and J. E. Deutsch. Dual Stewart platform mobility simulator. In *Engineering in Medicine and Biology Society, 2004. IEMBS '04. 26th Annual International Conference of the IEEE*, pages 4848–4851, San Francisco, CA, USA, September 1–5 2004.

[80] R. F. Boian, M. Bouzit, G. C. Burdea, J. Lewis, and J. E. Deutsch. Dual Stewart platform mobility simulator. In *Rehabilitation Robotics, 2005. ICORR 2005. 9th International Conference on*, pages 500–555, Chicago, IL, USA, June 28–July 1 2005.

[81] Kejun Ning, Mingyang Zhao, and Jie Liu. A new wire-driven three degree-of-freedom parallel manipulator. *Journal of Manufacturing Science and Engineering*, 128(3):816–819, August 2006.

[82] Yoshito Tanaka, Isao Yokomichi, Toshiaki Makino, and Yaobao Yin. Study of force-driven pneumatic joystick. In *Proceedings of the 7th World Congress on*

Intelligent Control and Automation (WCICA 2008), pages 3669–3672, Chongqing, China, June 25–27 2008.

[83] S. D'Angella, A. Khan, F. Cepolina, and M. Zoppi. Modeling and control of a parallel robot for needle surgery. In *IEEE International Conference on Robotics and Automation*, pages 3388–3393, Shanghai, China, May 2011.

[84] D. Li and Septimiu E. Salcudean. Modeling, simulation, and control of a hydraulic Stewart platform. In *IEEE International Conference on Robotics and Automation*, volume 4, pages 3360–2266, Albuquerque, New Mexico, USA, April 1997.

[85] Michael J. Girone, Grigore C. Burdea, and Mourad Bouzit. The "Rutgers ankle" orthopedic rehabilitation interface. In *Proceedings of the ASME Haptics Symposium, DSC*, volume 67, pages 305–312, November 1999.

[86] M. Girone, G. Burdea, M. Bouzit, V. Popescu, and J. E. Deutsch. Orthopedic rehabilitation using the "Rutgers ankle" interface. In *Proceedings of Medicine Meets Virtual Reality 2000, IOS*, pages 89–95, January 2000.

[87] Michael Girone, Grigore Burdea, Mourad Bouzit, Vlorel G. Popescu, and Judlth Deutsch. A Stewart platform-based system for ankle telerehabilitation. *Autonomous Robots*, 10(2):203–212, March 2001.

[88] Jungwon Yoon, Jeha Ryu, Girgore Burdea, and Rares Boian. Control of the Rutgers ankle rehabilitation interface. In *Proceedings of IMECE 2002. ASME International Mechanical Engineering Congress & Exposition*, volume 71, pages 787–794, New Orleans, LA, USA, November 17–22 2002.

[89] Judith E. Deutsch, Jason Latonio, Grigore Burdea, and Rares Boian. Rehabilitation of musculoskeletal injuries using the Rutgers ankle haptic interface: three case reports. In *Proceedings of EuroHaptics Conference*, pages 11–16, UK, July 1–4 2001.

[90] Prabjot Nanua, Kenneth J. Waldron, and Vasudeva Murthy. Direct kinematic solution of a Stewart platform. *IEEE Transactions on Robotics and Automation*, 6(4):438–444, August 1990.

[91] Kai Liu, John M. Fitzgerald, and Frank L. Lewis. Kinematic analysis of a Stewart platform manipulator. *IEEE Transactions on Industrial Electronics*, 40(2):282–293, April 1993.

[92] Terenziano Raparelli, Pierluigi Beomonte Zobel, and Francesco Durante. Mechanical design of a 3-dof parallel robot actuated by smart wires. In Marco Ceccarelli, editor, *Proceedings of EUCOMES 08*, pages 271–278. Springer Netherlands, 2009.

[93] Kok-Meng Lee and Shankar Arjunan. A three-degrees-of-freedom micromotion in-parallel actuated manipulator. *IEEE Transactions on Robotics and Automation*, 7(5):634–641, October 1991.

[94] S. Shah, A. Kapoor, J. Ding, P. Guion, D. Petrisor, J. Karanian, W. F. Pritchard, D. Stoianovici, B. J. Wood, and K. Cleary. Robotically assisted needle driver: evaluation of safty release, force profiles, and needle spin in a swine abdominal model. *International Journal of Computer Assisted Radiology and Surgery*, 3(1-2):173–179, 2008.

[95] Niki Abolhassani and Rajni V. Patel. Teleoperated master-slave needle insertion. *The International Journal of Medical Robotics and Computer Assisted Surgery*, 5(4):398–405, December 2009.

[96] Basem Yousef, Rajni V. Patel, and Mehrdad Moallem. A macro-robot manipulator for medical applications. In *IEEE International Conference on Systems, Man, and Cybernetics*, volume 1, pages 530–535, Taipei, Taiwan, October 2006.

[97] Bo Yang, U-Xuan Tan, Alan McMillan, Rao Gullapalli, and Jaydev P. Desai. Towards the development of a master-slave surgical system for breast biopsy under continous MRI. In *the 13th International Symposium on Experimental Robotics*, Québec City, Canada, June 17–21 2012. (In Press).

[98] Niki Abolhassani, Rajni Patel, and Mehrdad Moallem. Experimental study of robotic needle insertion in soft tissue. *International Congress Series*, 1268:797–802, 2004.

[99] Kok-Meng Lee and Dharman K. Shah. Kinematic analysis of a three-degrees-of-freedom in-parallel actuated manipulator. *IEEE Journal of Robotics and Automation*, 4(3):354–360, June 1988.

[100] Thomas G. Sugar. Desian and control of an in-parallel pneumatically-actuated manipulator. Technical report, University of Pennsylvania, May 1992.

[101] Kok-Meng Lee and Dharman K. Shah. Dynamic analysis of a three-degrees-of-freedom in-parallel actuated manipulator. *IEEE Journal of Robotics and Automation*, 4(3):361–367, June 1988.

[102] D. Ben-Dov and Septimiu E. Salcudean. A force-controlled pneumatic actuator for use in teleoperation masters. In *IEEE International Conference on Robotics and Automation*, volume 3, pages 938–943, May 1993.

[103] D. Ben-Dov and Septimiu E. Salcudean. A force-controlled pneumatic actuator. *IEEE Transactions on Robotics and Automation*, 11(6):906–911, December 1995.

[104] Septimiu E. Salcudean, S. Bachmann, and D. Ben-Dov. A six degree-of-freedom wrist with pneumatic suspension. In *IEEE International Conference on Robotics and Automation*, volume 3, pages 2444–2450, San Diego, CA, USA, May 1994.

[105] Björn Verrelst, Ronald Van Ham, Bram Vanderborght, Dirk Lefeber, Frank Daerden, and Michaël Van Damme. Second generation pleated pneumatic artificial muscle and its robotic applications. *Advanced Robotics*, 20(7):783–805, 2006.

[106] Houxiang Zhang, Jianwei Zhang, Wei Wang, Rong Liu, and Guanghua Zong. A series of pneumatic glass-wall cleaning robots for high-rise buildings. *Industrial Robot: An International Journal*, 34(2):150–160, 2007.

[107] Venkat Durbha and Perry Y. Li. Passive bilateral tele-operation and human power amplification with pneumatic actuators. In *Proceedings of the ASME 2009 Dynamic Systems and Control Conference, DSCC 2009*, Hollywood, California, USA, October 2009.

[108] Kenichi Narioka and Koh Hosoda. Motor development of an pneumatic musculoskeletal infant robot. In *IEEE International Conference on Robotics and Automation*, pages 963–968, Shanghai, China, May 2011.

[109] Keith W. Wait and Michael Goldfarb. Design and control of a pneumatic quadrupedal walking robot. In *IEEE International Conference on Robotics and Automation*, pages 587–592. Shanghai, China, May 2011.

[110] Michael Pearce. Is there an alternative to fluid power? [electrically driven linear motion technology]. *Computing Control Engineering Journal*, 16(2):8–11, April–May 2005.

[111] Edmond Richer and Yildirim Hurmuzlu. A high performance pneumatic force actuator system: part 1 — nonlinear mathematical model. *Journal of dynamic systems, measurement, and control*, 122(3):416–425, September 2000.

[112] Eric J. Barth, Jianlong Zhang, and Michael Goldfarb. Sliding mode approach to PWM-controlled pneumatic systems. In *American Control Conference*, volume 3, pages 2362–2367, Anchorage, AK, May 2002.

[113] Tienan Zhao, Kiahmok Goh, Weidong Lin, and Gunther Ehlert. Parameter identification using orthogonal polynomials and its application on a pneumatic position servo. In *Control and Automation, 2003. ICCA'03. Proceedings. 4th International Conference on*, pages 385–388. Montreal, Canada, June 2003.

[114] Massimo Sorli, Giorgio Figliolini, and Stefano Pastorelli. Dynamic model and experimental investigation of a pneumatic proportional pressure valve. *IEEE/ASME Transactions on Mechatronics*, 9(1):78–86, 2004.

[115] Bo Lu, Guoliang Tao, Zhong Xiang, and Wei Zhong. Modeling and control of the pneumatic constant pressure system for zero gravity simulation. In *Advanced Intelligent Mechatronics, 2008. AIM 2008. IEEE/ASME International Conference on*, pages 688–693, Xi'an, China, July 2008.

[116] James E. Bobrow and F. Jabbari. Adaptive pneumatic force actuation and position control. *Journal of Dynamic Systems, Measurement, and Control*, 113(2):267–272, June 1991.

[117] B. W. McDonell and J. E. Bobrow. Adaptive tracking control of an air powered robot actuator. *Journal of Dynamic Systems, Measurement, and Control*, 115(3):427–433, September 1993.

[118] K. Hamiti, A. Voda-Besançon, and H. Roux-Buisson. Position control of a pneumatic actuator under the influence of stiction. *Control Engineering Practice*, 4(8):1079–1088, August 1996.

[119] X. Brun, M. Belgharbi, S. Sesmat, D. Thomasset, and S. Scavarda. Control of an electropneumatic actuator: comparison between some linear and non-linear control laws. *Proceedings of the Institution of Mechanical Engineers, Part I: Journal of System and Control Engineering*, 213(5):387–406, 1999.

[120] Pascal Bigras, Karim Khayati, and Tony Wong. Modified feedback linearization controller for pneumatic system with non negligible connection port restriction. *Systems, Man and Cybernetics, 2002 IEEE International Conference on*, 2:227–231, October 2002.

[121] Shu Ning and Gary M. Bone. High steady-state accuracy pneumatic servo positioning system with PVA/PV control and friction compensation. In *IEEE International Conference on Robotics and Automation*, volume 3, pages 2824–2829, Wachington, DC, USA, May 2002.

[122] S. Davis, J. Canderle, P. Artrit, N. Tsagarakis, and Darwin G. Caldwell. Enhanved dynamics performance in pneumatic muscle actuators. In *IEEE International Conference on Robotics and Automation*, volume 3, pages 2836–2841. Washington, DC, May 2002.

[123] Yong Zhu and Eric J. Barth. Impedance control of a pneumatic actuator for contact tasks. In *IEEE International Conference on Robotics and Automation*, pages 987–992, Barcelona, Spain, April 2005.

[124] Edmond Richer and Yildirim Hurmuzlu. A high performance pneumatic force actuator system: part 2 — nonlinear controller design. *Journal of dynamic systems, measurement, and control*, 122(3):426–434, September 2000.

[125] John H. Lilly and Peter M. Quesada. A two-input sliding-mode controller for a planar arm actuated by four pneumatic muscle groups. *IEEE Transactions on Neural Systems and Rehabilitation Engineering*, 12(3):349–359, September 2004.

[126] Hong Zhao, Pinhas Ben-Tzvi, Tingqi Lin, and Andrew A. Goldenberg. Two-layer sliding mode control of pneumatic position synchro system with feedback linearization based on friction compensation. In *Robotic and Sensors Environments, 2008. ROSE 2008. International Workshop on*, pages 41–45, Ottawa, Canada, October 2008.

[127] Michaël Van Damme, Bram Vanderborght, Ronald Van Ham, Björn Verrelst, Frank Daerden, and Dirk Lefeber. Sliding mode control of a 2DOF planar pneumatic manipulator. *Journal of Dynamic Systems, Measurement, and Control*, 131(2):021013, March 2009.

[128] Jianhui Wu, Michael Goldfarb, and Eric J. Barth. The role of pressure sensors in the servo control of pneumatic actuators. In *American Control Conference*, volume 2, pages 1710–1714, Denver, Colorado, June 2003.

[129] Navneet Gulati and Eric J. Barth. Non-linear pressure observer design for pneumatic actuators. In *Advanced Intelligent Mechatronics. Proceedings, 2005 IEEE/ASME International Conference on*, pages 783–788, Monterey, CA, USA, July 2005.

[130] Navneet Gulati and Eric J. Barth. Pressure observer based servo control of pneumatic actuators. In *Advanced Intelligent Mechatronics. Proceedings, 2005 IEEE/ASME International Conference on*, pages 498–503, Monterey, CA, USA, July 2005.

[131] Navneet Gulati and Eric J. Barth. A globally stable, load-independent pressure observer for the servo control of pneumatic actuators. *IEEE/ASME Transactions on Mechatronics*, 14(3):295–306, June 2009.

[132] Robert B. van Varseveld and Gary M. Bone. Accurate position control of a pneumatic actuator using on/off solenoid valves. *IEEE/ASME Transactions on Mechatronics*, 2(3):195–204, September 1997.

[133] Ying Chen, Jia-fan Zhang, Can-jun Yang, and Bin Niu. Design and hybrid control of the pneumatic force-feedback systems for Arm-Exoskeleton by using on/off valve. *Mechatronics*, 17(6):325–335, April 2007.

[134] M. Q. Le, M. T. Pham, M. Tavakoli, and R. Moreau. Development of a hybrid control for a pneumatic teleoperation system using on/off solenoid valves. In *IEEE/RSJ International Conference on Intelligent Robots and Systems*, pages 5818–5823, Taipei, Taiwan, October 2010.

[135] M. Q. Le, M. T. Pham, R. Moreau, and T. Redarce. Transparency of a pneumatic teleoperation system using on/off solenoid valves. In *19th IEEE International Symposium on Robot and Human Interactive Communication*, pages 15–20, Viareggio, Italy, September 2010.

[136] C. B. Schuder and R. C. Binder. The response of pneumatic transmission lines to step inputs. *Journal of Basic Engineering*, 81:578–584, December 1959.

[137] S. Goldstein. On diffusion by discontinuous movements, and on the telegraph equation. *The Quarterly Journal of Mechanics and Applied Mathematics*, 4(2):129–156, 1951.

[138] M. A. Abdou. Adomian decomposition method for solving the telegraph equation in charged particle transport. *Journal of Quantitative Spectroscopy and Radiative Transfer*, 95(3):407–414, October 2005.

[139] H. A. Abdusalam and E. S. Fahmy. Exact solution for the generalized telegraph Fisher's equation. *Chaos, Solitons and Fractals*, 41(3):1550–1556, August 2009.

[140] David J. Evans and Hasan Bulut. The numerical solution of the telegraph equation by the alternating group explicit (AGE) method. *International Journal of Computer Mathematics*, 80(10):1289–1297, October 2003.

[141] R. K. Mohanty. An unconditionally stable finite difference formula for a linear second order one space dimensional hyperbolic equation with variable coefficients. *Applied Mathematics and Compution*, 165(1):229–236, June 2005.

[142] R. Aloy, M. C. Casabán, L. A. Caudillo-Mata, and L. Jódar. Computing the variable coefficient telegraph equation using a discrete eigenfunctions method. *Computers and Mathematics with Applications*, 54(3):448–458, August 2007.

[143] J. Biazar and H. Ebrahimi. An approximation to the solution of telegraph equation by Adomian decomposition method. In *International Mathematical Forum*, volume 2 of *45*, pages 2231–2236, 2007.

[144] Mark W. Coffey and Gabriel G. Colburn. Quantum lattice gas algorithm for the telegraph equation. *Physical Review E*, 79(6):066707, June 2009.

[145] J. S. Stecki and S. C. Davis. Fluid transmission lines — distributed parameter models part 1: a review of the state of the art. In *Proceedings of the Institution of Mechanical Engineers, Part A: Journal of Power and Energy*, volume 200, pages 215–228, 1986.

[146] Craig D. Walrath. Adaptive bearing friction compensation based on recent knowledge of dynamic friction. *Automatica*, 20(6):717–727, 1984.

[147] Brian Armstrong-Hélouvry. Stick slip and control in low-speed motion. *Automatic Control, IEEE Transactions on*, 38(10):1483–1496, October 1993.

[148] Pierre E. Dupont and D. Bapna. Stability of sliding frictional surfaces with varying normal force. *Journal of Vibration and Acoustics*, 116(2):237–242, April 1994.

[149] Pierre E. Dupont and Eric P. Dunlap. Friction modeling and PD compensation at very low velocity. *Journal of Dynamic Systems, Measurement, and Control*, 117(1):8–14, March 1995.

[150] Brian Armstrong-Hélouvry, Pierre Dupont, and Carlos Canudas de Wit. A survey of models, analysis tools and compensation methods for the control of machines with friction. *Automatica*, 30(7):1083–1138, July 1994.

[151] Brian Armstrong-Hélouvry, Pierre Dupont, and Carlos Canudas de Wit. Friction in servo machines: analysis and control methodes. *Applied Mechanics Reviews, Special Issue on Friction Induced Vibration*, 47(7):275–305, July 1994.

[152] Naomi Elizabeth Ehrich. An investigation of control strategies for friction compensation. Master's Thesis, Systems Research Center, University of Maryland, College Park, MD, April 1991.

[153] Naomi Ehrich Leonard and P. S. Krishnaprasad. Adaptive friction compensation for bi-directional low-velocity position tracking. In *Decision and Control, 1992. Proceedings of the 31st IEEE Conference on*, Tucson, AZ, USA, December 1992.

[154] Bernard Friedland and Young-Jin Park. On adaptive friction compensation. *Automatic Control, IEEE Transactions on*, 37(10):1609–1612, October 1992.

[155] Pierre E. Dupont. Avoiding stick-slip through PD control. *Automatic Control, IEEE Transactions on*, 39(5):1094–1097, May 1994.

[156] R Kelly, V Santibañez, and E González. Adaptive friction compensation in mechanisms using the Dahl model. In *Proceedings of the Institution of Mechanical Engineers, Part I: Journal of Systems and Control Engineering*, volume 218, pages 53–57, 2004.

[157] Tong Heng Lee, Kik Kiong Tan, and Sunan Huang. Adaptive friction compensation with a dynamical friction model. *IEEE/ASME Transactions on Mechatronics*, PP(99):1–8, February 2010.

[158] Zhan Gao, Kevin Lister, and Jaydev P. Desai. Constitutive modeling of liver tissue: experiment and theory. *Annals of Biomedical Engineering*, 38(2):505–516, February 2010.

[159] Thomas B. Sheridan. Telerobotics. *Automatica*, 25(4):487–507, July 1989.

[160] Ralph L. Hollis, Septimiu E. Salcudean, and A. Peter Allan. A six-degree-of-freedom magnetically levitated variable compliance fine-motion wrist: design, modeling, and control. *IEEE Transactions on Robotics and Automation*, 7(3):320–332, June 1991.

[161] Septimiu E. Salcudean, N. M. Wong, and Ralph L. Hollis. Design and control of a force-reflecting teleoperation system with magnetically levitated master and wrist. *IEEE Transactions on Robotics and Automation*, 11(6):844–858, December 1995.

[162] Septimiu E. Salcudean, S. Tafazoli, P. D. Lawrence, and I. Chau. Impedance control of a teleoperated mini excavator. In *Advanced Robotics, 1997. ICAR 97. Proceedings., 8th International Conference on*, pages 19–25, Monterey, CA, USA, July 1997.

[163] H. Fischer, E. Hempel, J. Vagner, L. Gumb, W. A. Kaiser, and A. Melzer. Telerobotics for high precise radiological interventions. In *VDE World Microtechnologies Congress*, volume 2, pages 387–394, Hannover, Germany, September 2000.

[164] Metin Sitti and Hideki Hashimoto. Teleoperated touch feedback from the surfaces at the nanoscale: modeling and experiments. *IEEE/ASME Transactions on Mechatronics*, 8(2):287–298, June 2003.

[165] Ba-Hai Nguyen and Jee-Hwan Ryu. Design of a master device for the teleoperation of wheeled and tracked vehicles. In *IEEE International Conference on Control, Automation and Systems*, pages 1643–1648, Gyeonggi-do, Korea, October 2010.

[166] A. Talasaz, Rajni V. Patel, and M. D. Naish. Haptics-enabled teleoperation for robot-assited tumor localization. In *IEEE International Conference on Robotics and Automation*, pages 5340–5345, Anchorage, Alaska, USA, May 2010.

[167] Robert J. Anderson and Mark W. Spong. Bilateral control of teleoperators with time delay. *IEEE Transactions on Automatic Control*, 34(5):494–501, May 1989.

[168] Günter Niemeyer and Jean-Jacques E. Slotine. Stable adaptive teleoperation. *IEEE Journal of Oceanic Engineering*, 16(1):152–162, January 1991.

[169] Thomas B. Sheridan. Space teleoperation through time delay: Review and prognosis. *IEEE Transactions on Robotics and Automation*, 9(5):592–606, October 1993.

[170] Rogelio Lozano, Nikhil Chopra, and Mark W. Spong. Passivation of force reflecting bilateral teleoperators with time varying delay. In *Proceedings of the 8. Mechatronics Forum*, pages 24–26, Entschede, Netherlands, 2002.

[171] Keyvan Hashtrudi-Zaad and Septimiu E. Salcudean. Transparency in time-dalayed systems and the effect of local force feedback for transparent teleoperation. *IEEE Transactions on Robotics and Automation*, 18(1):108–114, February 2002.

[172] Peter F. Hokayem and Mark W. Spong. Bilateral teleoperation: An historical survey. *Automatica*, 42(12):2035–2057, December 2006.

[173] Costas Tzafestas, Spyros Velanas, and George Fakiridis. Adaptive impedance control in haptic teleoperation to improve transparency under time-delay. In *IEEE International Conference on Robotics and Automation*, pages 212–219, Pasadena, CA, USA, May 2008.

[174] Erick J. Rodríguez-Seda, Dongjun Lee, and Mark W. Spong. Experimental comparison study of control architectures for bilateral teleoperators. *IEEE Transactions on Robotics*, 25(6):1304–1318, December 2009.

[175] Zhihao Xu, Lei Ma, and Klaus Schilling. Passive bilateral teleoperation of a carlike mobile robot. In *17th Mediterranean Conference on Control and Automation*, pages 790–796, Makedonia Palace, Thessaloniki, Greece, June 2009.

[176] Emmanuel Nuño, Luis Basañez, Romeo Ortega, and Guillermo Obregón-Pulido. Position traking using adaptive control for bilateral teleoperators with time-delays. In *IEEE International Conference on Robotics and Automation*, pages 5370–5375, Anchorage, AK, May 2010.

[177] Dale A. Lawrence. Stability and transparency in bilateral teleoperation. *IEEE Transactions on Robotics and Automation*, 9(5):624–637, October 1993.

[178] Marc Rea, Donald McRobbie, Haytham Elhawary, Zion Tsz Ho Tse, Michael Lampérth, and Ian Young. System for 3-D real-time tracking of MRI-compatible devices by image processing. *IEEE/ASME Transactions on Mechatronics*, 13(3):379–382, June 2008.

[179] J. Hong, N. Hata, K. Konishi, and M. Hashizume. Real-time magnetic resonance imaging driven by electromagnetic locator for interventional procedure and endoscopic therapy. *Surgical Endoscopy*, 22(2):552–556, 2008.

[180] Y. Kurumi, T. Tani, S. Naka, H. Shiomi, T. Shimizu, H. Abe, Y. Endo, and S. Morikawa. MR-guided microwave ablation for malignancies. *International Journal of Clinical Oncology / Japan Society of Clinical Oncology*, 12(2):85–93, 2007.

[181] A. M. Tang, D. F. Kacher, E. Y. Lam, K. K. Wong, F. A. Jolesz, and E. S. Yang. Simultaneous ultrasound and MRI system for breast biopsy: compatibility assessment and demonstration in a dual modality phantom. *IEEE Transactions on Medical Imaging*, 27(2):247–254, 2008.